Electrochemically assisted generation of oriented and nanostructured silica-based thin films : functionalization via click chemistry, characterization and applications

Cheryl Karman

To cite this version:

Cheryl Karman. Electrochemically assisted generation of oriented and nanostructured silica-based thin films : functionalization via click chemistry, characterization and applications. Material chemistry. Université de Lorraine, 2017. English. NNT : 2017LORR0218 . tel-01816029

HAL Id: tel-01816029

https://theses.hal.science/tel-01816029

Submitted on 14 Jun 2018

Sujet de thèse:

Génération électrochimiquement assistée de films sol-gel nanostructurés orientés: fonctionnalisation par « chimie click », caractérisation et applications

Par

Cheryl KARMAN

Pour l'obtention de titre de **Docteur**

Soutenance publique prévue le **26 Octobre 2017** devant le jury:

Directeur :
Dr. Alain Walcarius - Directeur de Recherche (LCPME, Villers-lès-Nancy, France)

Co-directeur :
Dr. Neus Vilà Cusco – Maître de Conférences (LCPME, Villers-lès-Nancy, France)

Rapporteurs :
Prof. Frank Marken - Professeur (University of Bath, Bath, Royaume-Uni)

Prof. Jean-Christophe Lacroix - Professeur (Université Paris Diderot, Paris, France)

Examinateurs :

Prof. Iluminada Gallardo García – Professeur (Universitat Autonoma de Barcelona, Barcelone, Espagne)

Dr. Sophie Legeai - Maître de Conférences (IJL, Metz, France)

Laboratoire de Chimie Physique et Microbiologie pour l'Environnement (LCPME)
Unité mixte de recherche – UMR 756
405 Rue de Vandoeuvre, 54600, Villers-lès-Nancy, France

A thesis:

Electrochemically assisted generation of oriented and nanostructured silica-based thin films: functionalization via click chemistry, characterization and applications

By

Cheryl KARMAN

For obtaining a **Doctoral** title

Public defense planned on **October 26th 2017** in front of the jury:

Supervisor :
Dr. Alain Walcarius – Research Director (LCPME, Villers-lès-Nancy, France)

Co-supervisor :
Dr. Neus Vilà Cusco – Lecturer (LCPME, Villers-lès-Nancy, France)

Reviewers :
Prof. Frank Marken – Professor (University of Bath, Bath, United Kingdom)
Prof. Jean-Christophe Lacroix – Professor (Université Paris Diderot, Paris, France)

Examiners :

Prof. Iluminada Gallardo García – Professor (Universitat Autonoma de Barcelona, Barcelone, Spain)

Dr. Sophie Legeai - Lecturer (IJL, Metz, France)

Laboratory of Physical Chemistry and Microbiology for the Environment

UMR 756

405 Rue de Vandoeuvre, 54600, Villers-lès-Nancy, France

To ***Ho Peng Yam****, mijn lieve Opa,*

my forever role model,

for your bright intelligence and unconditional kindness.

You feed the soul that resonates within me.

-ii-

Acknowledgements

First and foremost, I would like to express my biggest gratitude to both of my supervisors. **Alain Walcarius**, since the day when you drew and showed me molecules during my Skype interview, I knew that you would be a great person to work with. Thank you for the unending and uncountable great ideas, inspiration and challenges you had given me. **Neus Vilà**, thank you for your constant presence and guidance in the lab, as well as your patience when I had almost no clue on the basics of electrochemistry and sometimes chemistry in general. I am also very grateful for all the compounds you have synthesized and the TEM sessions you went to for this work.

Secondly, I would like to address my appreciation to the colleagues who contributed a lot in this work. **Alonso Gamero-Quijano**, I dedicate Chapter 6 for you, thank you for being not just a great co-author, but also a friend and an unofficial mentor. Thank you for all the discussions and ideas, as well as patience with my impatience. **Christelle Despas**, for the help and discussion about ion chromatography, as well as the electrochemistry lessons that you gave in the faculty. **Grégoire Herzog,** for the ideas and organization of the experiments in Chapter 6.

Next in the row are my labmates. **Martha Collins**, the ultimate lab, office, and housemate. Thanks for sharing so many things with me, mostly raclettes during the good times and tubs and tubs of ice cream through the bad times. **Lin Zhang**, for our vast discussions, from shoes shopping to charge transfer, from Asian food to covalent bonds. **Maciej Mierzwa**, for all the fun facts, dry jokes, criticism, and ECL measurements. My fellow South East Asian, **Najwa Jajuli**, for sharing lunch times together. **Samuel Ahoulou**, for sharing interesting results and discussions about your experiments. **Salima Mesli,** for your encouragement when I needed the most. Also other labmates and fellow PhD students **Tauquir Nasir**, **Christelle Ghazaly**, **Lukasz Poltorak**, **Ievgen Mazurenko**, **Ileana Pavel**, **Sijin Li**, **Grace Ham**, and **Mbola Robinson**.

Furthermore, thank you for the people who have helped me with several measurements, **Jaafar Ghanbaja** for TEM images, **Jérôme Grausem** for FTIR set-up, **Manuel Dossot** for the Spectrofluorimeter experiments, **Emmanuel Aubert** for GIXD measurements, and **Grégory Francius** for AFM images. As well as other people in LCPME and Université de Lorraine, **Jean-Paul Moulin** and **Gérard Paquot** for the homemade cells and other equipments. **Claire Genois** and **Patrick Bombardier** for the technical support. **Marie Tercier**, **Christelle Charbaut**, **Jacqueline Druon**, and **Severine Bonenberger** for the administrative matters. Not to forget **Mathieu Etienne**, **Marc Hebrant**, **Michel Perdicakis**, and **Liang Liu** for the inputs and discussions both during group meetings and daily encounters.

Lastly, I would like to express my gratitude to my family and friends. **Mama** and **Papa** for your constant long-distant support. **Arlene Karman** and **Amber Rasjidgandha**, my favorite girls and sane keepers. My girls, **Felicia Isadora** the ultimate sane keeper and spiritual/conscious-living junkie, thank you for keeping me grounded and seeing the clear blue sky despite all the clouds and the fireworks, **Adysti Raissa** my partner in fickle-minded moments, **Agnes Pranindita**, and **Zaskya Mansur**. **Silvia Lasala**, for living with me during the first 9 months and then coming back to Nancy, being there for me through the good and the hard times in Amorino, Japonais, la Pep, Vivier, couscouserie, etc. **Boris Martinez** for keeping me focused on the thesis during the first 2 years and finally to my support system during the most difficult moments, **Grisel Castillo**, **Dominikus Savio**, and **Edgardo Herrera**.

Table of Content

Abstract

In this work, we exploited the vertically-aligned mesoporous silica thin films generated by electro-assisted self-assembly (EASA). First of all, we present a study about the amplification of charge transfer of a repulsed anionic redox probes [i.e. $Fe(CN)_6^{3-/4-}$] through the negatively charged silica film by using neutrally or positively charged redox probes [$Fc(MeOH)_2$ or $Ru(NH_3)_6^{3+}$ respectively] through redox mediating processes.

Furthermore, the functionalization can be conducted by combining EASA method to obtain azide-functionalized silica film and further letting it react with an ethynyl-bearing reactant (e.g. ethynyl-ferrocene) according Huisgen click chemistry. The resulting ferrocene-functionalized silica films are electroactive, involving an electron hopping mechanism between adjacent ferrocene moieties. The electrochemical oxidation of ferrocene into ferricinium ion generates positive charges that are compensated by the ingress of anions into the film, opening the door to possible indirect amperometric detection of non-electroactive anions by flow injection analysis. Operating in an electrolyte-free flow, each injection of an anion (e.g., NO_3^-) at an electrode biased at a suitable positive potential (i.e., +0.5 V) gave rise to an amperometric response proportional to the anion concentration. However, to avoid the decrease of the electrochemical signal due to the progressive consumption of ferrocene in multiple successive analyses, it was necessary to regenerate the electrode by reduction of ferricinium moieties, which can be achieved in-situ by square wave amperometry. The feasibility to apply such indirect amperometric detection scheme in suppressed ion chromatography (for detecting anions in mixture) was also demonstrated.

The oriented mesoporous film can also be functionalized with ruthenium(II)bipyridyl complex $[Ru(bpy)_2(bpy')]^{2+}$ using the same method. Optimization of the functionalization level is controlled electrochemically by cyclic voltammetry (CV) and monitored through the UV-vis spectra. Further study is conducted upon the charge transfer (electron hopping along the adjacent sites) and the mass transfer of the compensating counter anion through the mesochannels by varying the CV potential scan rate. The emission of the $[Ru(bpy)_2(bpy')]^{2+}$-functionalized film and its quenching in the presence of oxygen are evidenced in both aqueous and organic solvent, giving opportunities to apply the film for different application, such as electrochemiluminescence sensor and oxygen detection.

Lastly, the vertically-aligned mesoporous silica film is used as a hard template to grow polyanilinine nanofilaments. The growth of ordered polyaniline nanofilaments is controlled by potentiostatic polymerization. In such small pore template (2 nm in diameter), quasi-single PANI chains are likely to be produced. From chronoamperometric experiments and using films of various thicknesses (100–200 nm) it is possible to evidence the electropolymerization transients, wherein each stage of polymerization (induction period, growth, and overgrowth of polyaniline on mesoporous silica films) is clearly identified. The advantageous effect of mesostructured silica thin films as hard templates for the generation of isolated polyaniline nanofilaments is demonstrated from enhancement of the reversibility between the conductive and the nonconductive states of polyaniline and the higher electroactive surface areas displayed for all mesoporous silica/PANI composites. The possibility to control and tailor the growth of conducting polymer nanofilaments offers numerous opportunities for applications in various fields including energy, sensors and biosensors, photovoltaics, nanophotonics, or nanoelectronics.

Keywords: *functionalized mesoporous silica based material*, *electrochemistry*, *click chemistry.*

Résumé

Dans ce travail, plusieurs applications des films minces à base de silice mésoporeuse fonctionnalisée, générés par auto-assemblage électrochimiquement-assisté (EASA), organisés et orientés, ont été développées. Au préalable, avant de se concentrer sur les films fonctionnalisés proprement dits, nous avons caractérisé les propriétés de perméabilité de tels films vis-à-vis de sondes redox en solution différemment chargées (neutre, $Fc(MeOH)_2$, positive, $Ru(NH_3)_6^{3+}$, négatives, $Fe(CN)_6^{3-/4-}$), démontrant une limitation électrostatique pour les anions. Ceci nous a amené à étudier l'amplification de la réponse électrochimique des sondes électroactives anioniques ($Fe(CN)_6^{3-/4-}$) en présence d'un film de silice chargé négativement sur la surface de l'électrode en ayant recours à des médiateurs neutres ou chargés positivement**.**

La fonctionnalisation de ces films minces de silice a été effectuée en combinant la méthode EASA pour obtenir un film de silice fonctionnalisé par de groupements azoture avec une réaction de couplage avec un groupe alcyne (l'éthynyl-ferrocène dans ce cas). La réponse électrochimique obtenue pour ces films isolants fonctionnalisés par des groupes ferrocene électroactifs est due à un mécanisme de saut d'électrons entre les sites électroactifs adjacents. L'oxydation électrochimique du ferrocène en ion ferricinium génère des charges positives qui sont compensées par l'entrée d'anions permettant une éventuelle détection ampérométrique indirecte d'anions non électroactifs. L'injection d'anions non-électroactifs dans une cellule électrochimique constituée par une électrode de travail fonctionnalisée par ces films de silice porteurs de groupements ferrocène, soumise à l'imposition d'un potentiel positif (+0,5 V), a donné lieu à une réponse ampérométrique

proportionnelle à la concentration d'anions. La régénération de l’électrode par réduction du ferricinium était nécessaire afin d’éviter la diminution du signal électrochimique dû à la consommation progressive du ferrocène par des multiples analyses successives. Cette régénération a été réalisée in situ par une méthode ampérométrique à onde carrée.

Le films mésoporeux orientés peuvent également être fonctionnalisés par des complexes à base de ruthénium du type $[Ru(bpy)_2(bpy')]^{2+}$ en adaptant la méthode décrite auparavant. Le succès de la fonctionnalisation est vérifié par électrochimie et aussi par spectroscopie UV-Vis au travers de la bande MLCT caractéristique du complexe immobilisé. Une étude plus approfondie est effectuée lors du transfert de charge (saut d'électrons le long des sites adjacents) et le transport de masse de l’anion compensateur de charge au travers des canaux mésoporeux en faisant varier la vitesse de balayage en potentiel. Les propriétés de luminescence de ces films ont été étudiées en présence et en absence d’oxygène, évaluant la possibilité d'utiliser ce type de film pour des applications telles que l'électrochimiluminescence ou la détection d’oxygène.

Finalement, ces films à base silice orientés ont été utilisés pour la croissance de nanofilaments de polyaniline (PANI). Ces nanofilaments de polyaniline ordonnée sont générés par voie électrochimique de manière contrôlée. Etant donnée la taille des mésopores (2 nm de diamètre), des chaînes PANI quasi-uniques sont vraisemblablement produites. À partir d'expériences de chronoampérométrie, sur base de films de différentes épaisseurs (100-200 nm), il est possible de prouver l’existence de plusieurs étapes d'électropolymérisation. Chaque étape de la formation du polymère (période d'induction, croissance de la polyaniline au sein et en dehors des canaux mésoporeux) est clairement identifiée. La génération de nanofilaments de polyaniline isolés est démontrée par

l'amélioration de la réversibilité entre les états conducteurs et non-conducteurs de la polyaniline. La possibilité de contrôler et d'adapter la croissance des nanofilaments polymères conducteurs offre de nombreuses possibilités d'application dans divers domaines, y compris l'énergie, capteurs et biocapteurs, photovoltaïque, nanophotonique ou nanoélectronique.

Mots clés: *matériau à base de silice mésoporeuse fonctionnalisée*, *électrochimie*, *chimie click*.

Chapter I

Bibliographical Introduction

1.1 Mesoporous silica

1.1.1 Introduction

Porous materials have been one of the most important research topics in the twenty-first century due to their large surface area, excellent in many applications acting as adsorbents, catalysts, carriers (catalyst supports), ion - exchange agents and nanoreactors.[1] Mesoporous materials, in particular, are the ones possessing pore diameters in the 2 – 50 nm range according to IUPAC classification. Among them, mesoporous silica (namely Mobil Oil Corp.'s M41S[2]) was considered the pioneer of this class of materials, since Kresge *et al* reported their findings in 1992.[3–6] Subsequently, the amount of research focused on the subject of mesoporous silica has increased significantly as shown in **Fig. 1.1**.

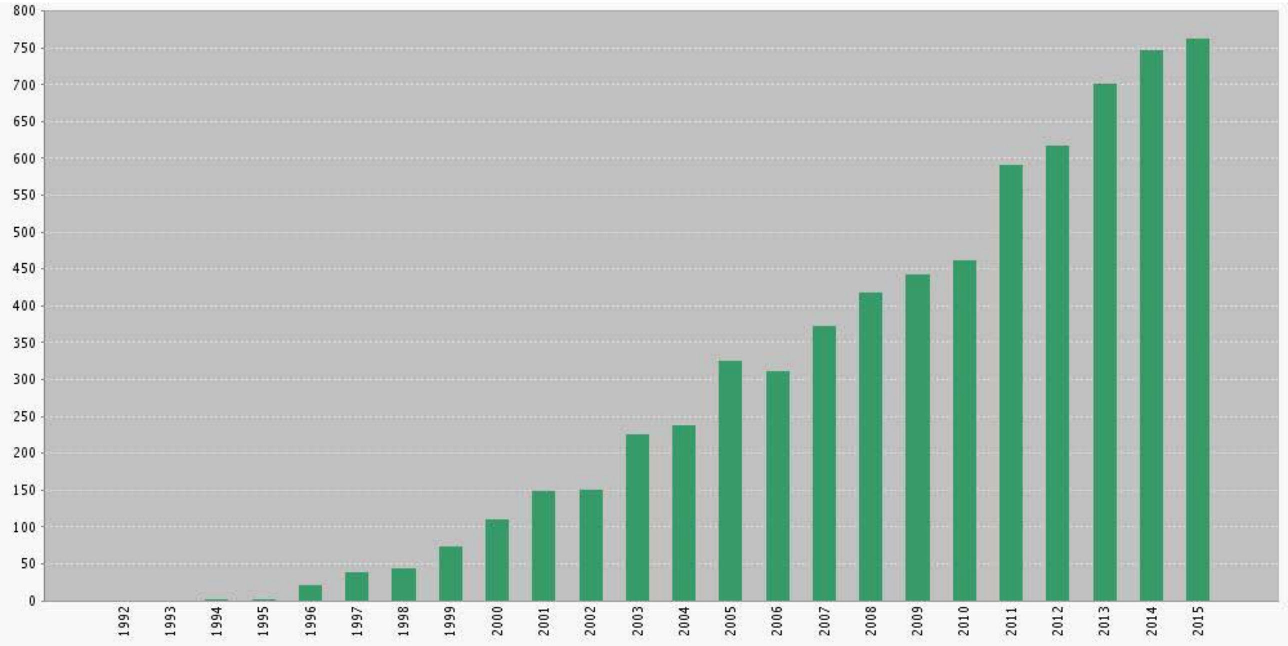

Figure 1.1 The number of published papers entitled "mesoporous silica" since 1992. Source: Web of Science

1.1.2 Sol-gel process

The synthesis of silica materials is commonly conducted via sol-gel method[7], which is a two-step process consisting of hydrolysis followed by condensation of the silane precursors. Typical precursors of this process are alkoxysilanes ($Si(OR)_4$), with OR corresponding to different alkoxy groups, typically methoxy (tetramethoxysilane/TMOS $Si(OCH_3)_4$) and ethoxy (tetraethoxysilane/TEOS $Si(OCH_2H_5)_4$). The reactions forming part of sol-gel process are depicted by **Eqs. 1.1 – 1.3**.

The hydrolysis of alkoxysilane forming silanol and alcohol is presented in **Eq. 1.1**, in which n represents the degree of hydrolysis that reaches completion at n = 4.

$$Si(OR)_4 + n\ H_2O \rightarrow Si(OR)_{4-n}\ (OH)_n + n\ ROH \qquad \textbf{Eq. 1.1}$$

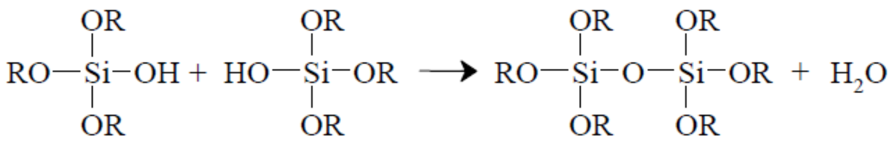

$$RO-\underset{OR}{\overset{OR}{Si}}-OH + HO-\underset{OR}{\overset{OR}{Si}}-OR \longrightarrow RO-\underset{OR}{\overset{OR}{Si}}-O-\underset{OR}{\overset{OR}{Si}}-OR + H_2O$$

q. 1.2

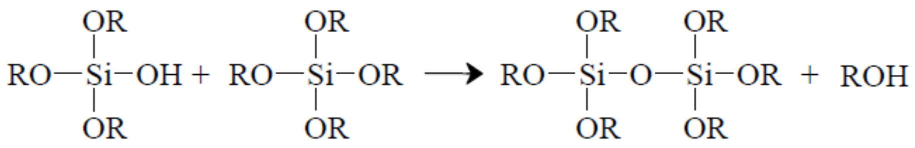

$$RO-\underset{OR}{\overset{OR}{Si}}-OH + RO-\underset{OR}{\overset{OR}{Si}}-OR \longrightarrow RO-\underset{OR}{\overset{OR}{Si}}-O-\underset{OR}{\overset{OR}{Si}}-OR + ROH$$

Eq. 1.3

The succeeding reaction can be categorized in water producing and alcohol producing condensation, presented in **Eqs. 1.2** and **1.3** respectively. Both cases result in the formation of siloxane network. Continuous polycondensation reaction (aging process) is in charge to densify the material forming gel structure of silica. Evaporation of the solvent leads to solid silica network.

The hydrolysis and condensation reaction kinetics is pH dependent[7–9], where at acidic pH the hydrolysis process is catalyzed with an optimum at pH 3 and the condensation process is most effectively catalyzed at pH 8 as presented in **Fig. 1.2**.

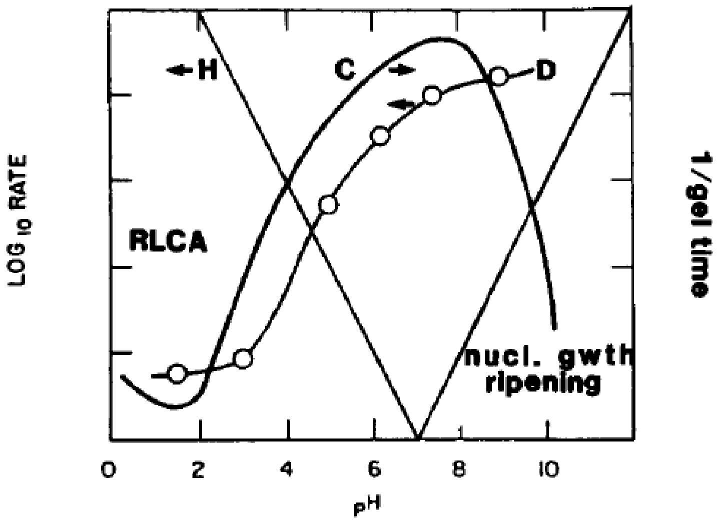

Figure 1.2 Schematic representation of pH influences in the hydrolysis (H), condensation (C), and depolymerization (D) rates.[9]

1.1.3 Mesostructuration

In order to achieve the mesoporosity of silica, several pathways can be choosen. The first one is hard-templating method, also called nanocasting, which has the similar principle as traditional casting developed 6000 years ago.[1,10] The mesostructuration in this case is formed by a preformed mesoporous template material (silicates or carbons). Another method is dealumination of zeolites, although it produces non-ordered mesopores.[11]

A more elegant method is soft-templating method where ordered mesoporosity can be achieved using structure directing agent (SDA) molecules as template. During the synthesis, the SDAs form mesostructured assembly while the silica precursors condense around the structure. Here, the use of different types of SDA (e.g. cationic, anionic, or nonionic surfactants, and block-copolymers) can tune the pore size, structure, and morphology of the resulting mesoporous silica.

The mechanism of this method was first proposed by Kresge *et al*[3,6] concerning the formation of the hexagonally arranged MCM-41 shown in **Fig. 1.3**. In the true liquid-crystal template mechanism (pathway a), highly concentrated surfactant molecules aggregate and form a hexagonal array of cylindrical micelles. Subsequently, silica precursor is added and condenses around its structure. Nowadays, a concerted self-assembly mechanism is mostly accepted, where a mixture of surfactant molecules and silica precursor undergoes a cooperative assembly and form the same final mesostructure (pathway b). In both cases, mesoporosity is obtained upon removal of the tensioactive molecules by calcination or extraction.

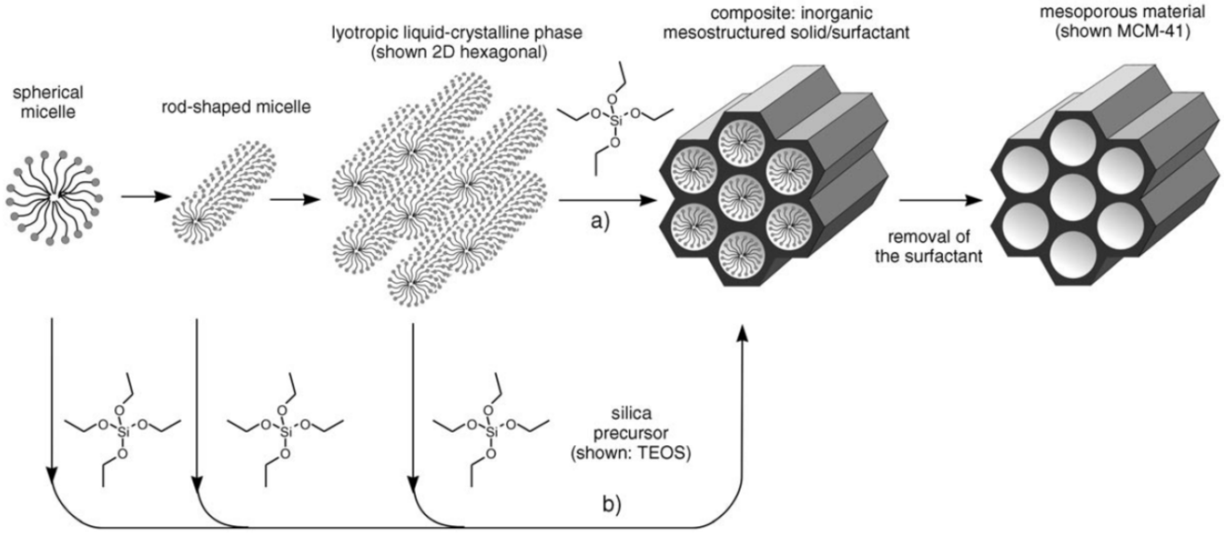

Figure 1.3 Mechanistic pathways for MCM-41 formation as proposed by the founders in Mobil Oil Corp. a) true liquid-crystal template mechanism, b) cooperative liquid- crystal template mechanism.[12]

The arrangement of the resulting mesopores can be changed by varying the concentration of the surfactant as it can change the arrangement of the micelles from spherical, cylindrical up to planar bilayer form giving various pore geometries, such as 2D hexagonal, cubic and lamellar structures (see **Fig. 1.4**).

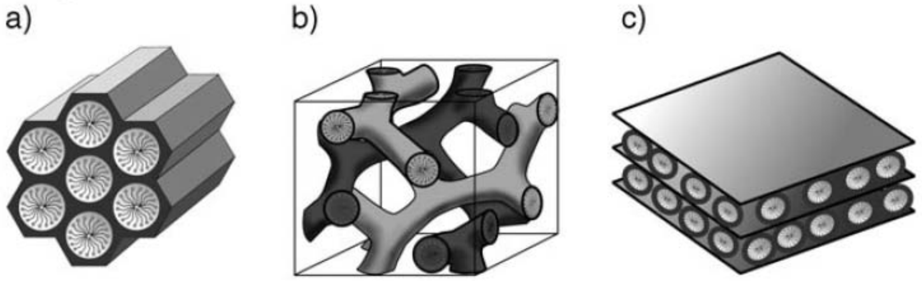

Figure 1.4 Differents structures of mesoporous M41S materials: a) MCM-41 (2D hexagonal *p6mm*), b) MCM-48 (cubic *Ia3d*), and c) MCM-50 (lamellar *p2*).[12]

1.1.4 Morphology

As previously mentioned, the pore geometry can be tuned by changing the surfactant/silica ratio. In addition, the final morphology of the material can also be controlled to form typical shapes such as fibers and rods, monoliths, single crystals, spheres, and thin films depending on the experimental conditions and the type of surfactant employed for the synthesis (see **Fig. 1.5**). Controlling the morphology of silica is important to fit it with the desired application and this objective is achievable by manipulating some parameters such as types of silica precursors, types of the surfactant micelles, interactions between silicate species and surfactants, and additives (inorganic salts, organic swelling agents, cosolvents and cosurfactants).[1]

In the area of catalysis, separation and water treatment, mesoporous silica monoliths can be directly used as reactors. The synthesis uses amphiphilic block copolymers as a soft-templating agent and as reported by Göltner *et al.*[13], it can produce crack-free transparent mesoporous silica monoliths which can be applied in optical devices application.

Another important research field is the development of materials for drug delivery application. In such field, mesoporous silica hollow spherical particles have been exploited.[14] Besides, mesoporous silica spheres have also been employed a lot in chromatography and electroanalysis.[14,15] They have been used in high-performance liquid chromatograpy (HPLC) packing for the separation of aromatic molecules[16,17] and large biomolecules such as proteins,[17,18] as well as in electrochemical detection of analytes further describe in **Section 1.2.3**. Depending on the type of application, both particle and pore size can be adjusted by control of experimental conditions.[15]

Fibril structure is also quite popular in the field of mesoporous materials. Huo *et al.*[19] managed to optimize the yield of mesoporous silica fibers (d = 1-100 µm) synthesis by changing the common TEOS precursor to tetrabutoxysilane (TBOS). Some researchers have also succeeded in the formation of nanorods and helical or chiral mesoporous silica fibers.[20–22]

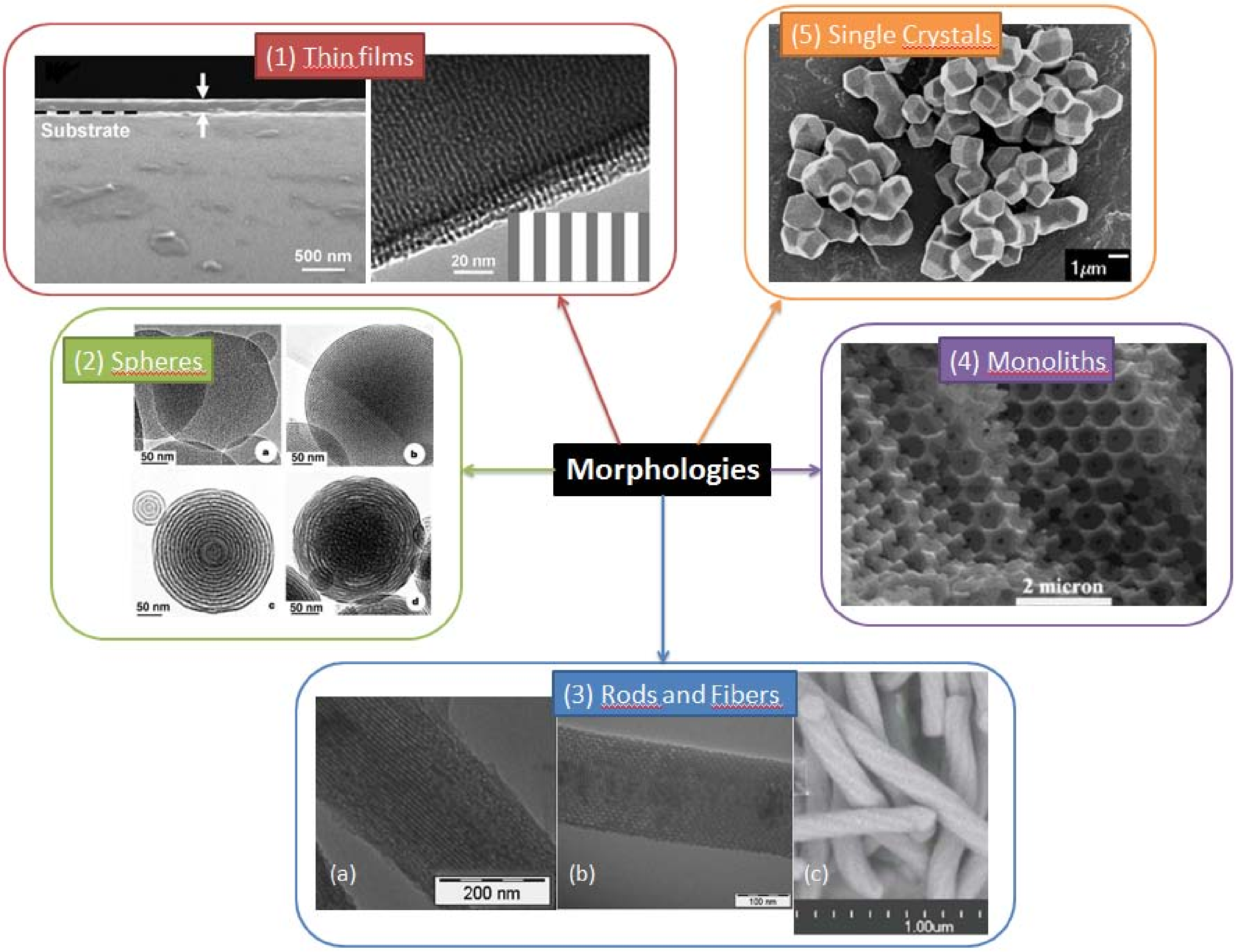

Figure 1.5 Various morphologies of mesoporous silica materials. (1)Thin films[23], (2) spheres[24], (3) rods[20] and fibers[21], (4) monoliths[25], and (5) single crystals[26].

Aside from the three morphologies described above, mesoporous silica thin films cover the broadest categories of applications from coatings and insulators, membrane and separation science, photocatalysis, sensors and preconcentration analysis, up to (nano)bio and biomedical applications, etc.[15,27] They are generally prepared by evaporation induced self-assembly (EISA) method first reported by Brinker's[28] and Ozin's[29] groups in the late 1990s, and then largely developed notably by the group of Grosso and Sanchez[30]. By its name it is clear that the polycondensation of silica precursors around the supramolecular template in EISA is driven by solvent evaporation and the process consists of four main steps illustrated in **Fig. 1.6**.

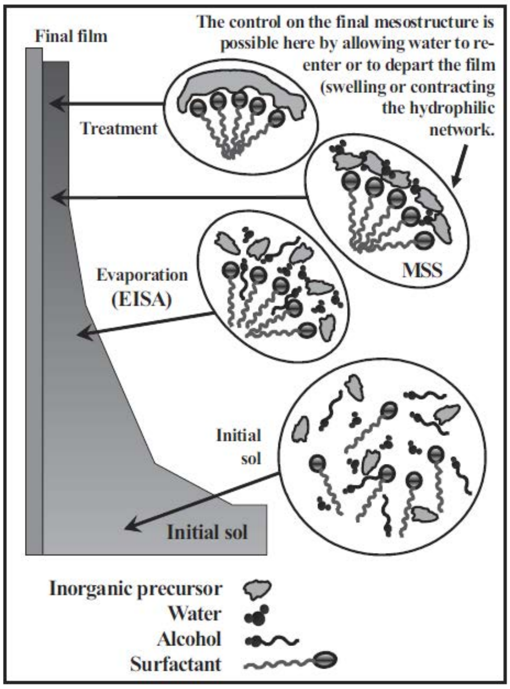

Figure 1.6 Schematic representation of EISA of mesoporous inorganic material by dip coating.[30]

- Step 1: Diluted initial sol solution contains the silica precursors, the surfactant molecules, and solvent. It has a significantly slow rate of condensation
- Step 2: Upon evaporation of the solvent, CMC of the surfactant molecules is reached and micelles are started to be formed
- Step 3: Evaporation is complete. Here, the mesostructure can be tuned by relative humidity (RH) adjustment
- Step 4: Inorganic condensation and stabilization of the mesostructured silica network.

A control of the synthesis condition leads to the generation of mesoporous thin film with well-defined pore geometry.[30]

1.2 Modified electrodes

Since the 1970s, Murray *et al.* have pioneered the research in chemically modified electrodes, where procedures were developed in immobilizing mono/multilayer of electroactive species on the surface of the electrode.[31–33] Ever since, the field of interest increased and expanded to modification with thicker polymeric and inorganic films, conductive polymers and organic metals, biological materials, up to complex structures such as composite, multilayers, and arrays.

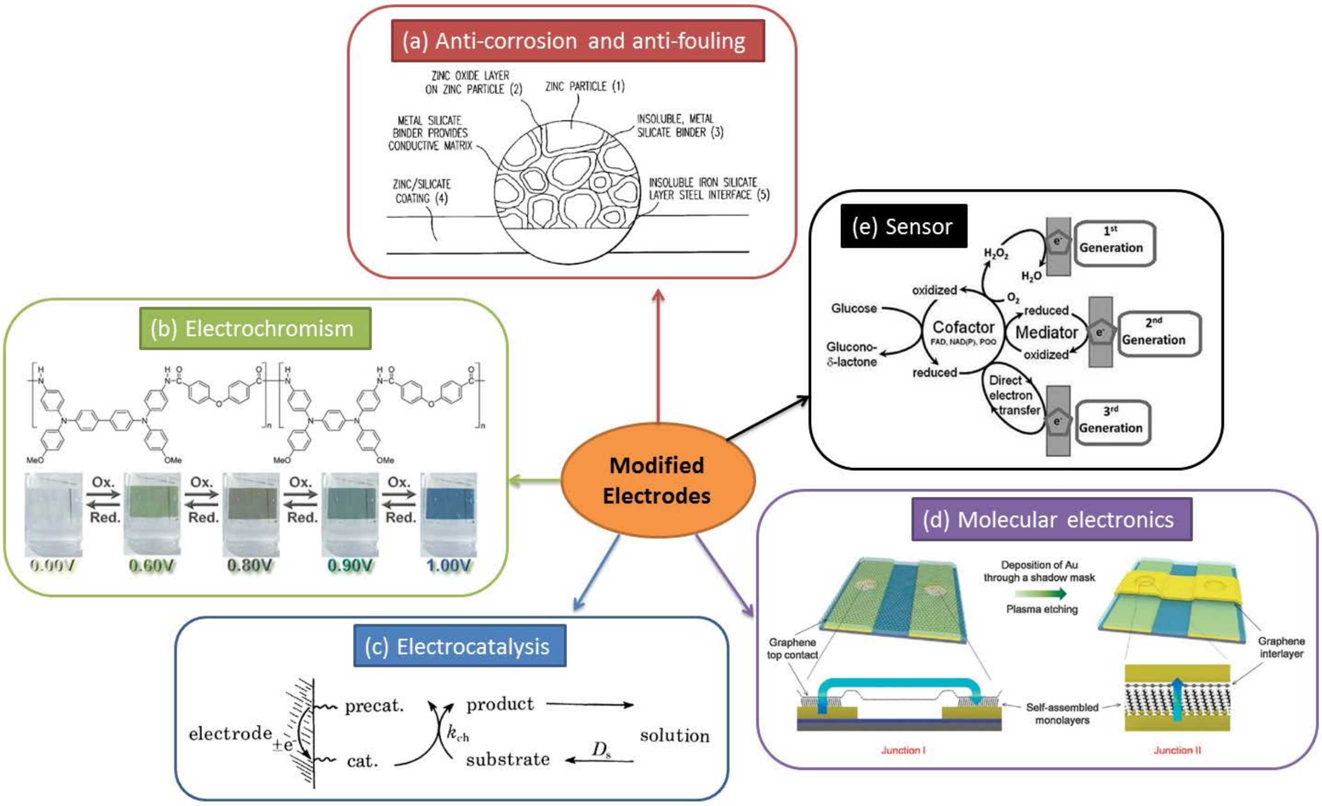

Figure 1.7 The use of modified electrodes in various applications; (a) anti-corrosion and anti-fouling[34], (b) electrochromic material[35], (c) electrocatalysis[36], (d) molecular junctions[37], (e) electrochemical sensor[38].

The objective of electrode modification is to enhance the properties of the electrode for its use in many applications, such as electrocatalysis, electrochromic device, corrosion protection, anti-fouling coating, analytical sensor, and molecular electronic device, as represented in **Fig. 1.7**.

1.2.1 Thin films on electrodes

Monolayer of electroactive species can be formed via adsorption or covalent attachment to the surface of the electrode by techniques like Langmuir-Blodgett or self-assembly method.[32]

A typical example of adsorbed layer is a sulfur-containing species on the surface of gold or mercury, due to strong metal-sulfur interaction.[32] Other specific adsorbed species on electrodes are depicted in **Fig. 1.8**, including olefin on platinum, Langmuir-Blodgett film on gold, and metal ion or complex on mercury surface.[32]

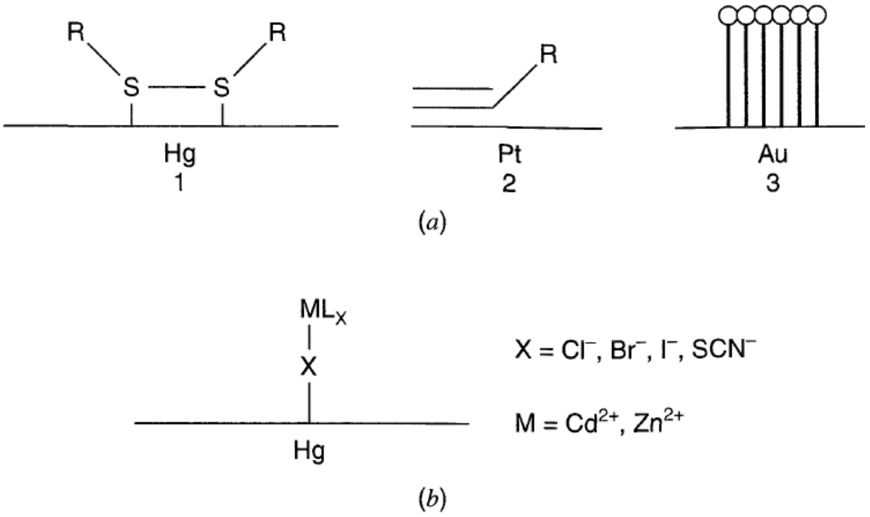

Figure 1.8 (a) Adsorption of a disulfide on Hg (1), an olefin on Pt (2), and a Langmuir-Blodgett film on Au (3). (b) Adsorption of a metal ion or complex through an anionic ligand bridge on Hg.[32]

In the case of covalent bounded species, linking agents, such as organosilanes, are frequently used to bind electroactive species such as ferrocenes[39], viologens[40], and pyridine-based metal complexes[41] on the electrode surface. Cyclic voltammograms of each of these covalently-linked species are presented in **Fig. 1.9**.

Polymer films can be deposited on electrode surface by various methods ranging from evaporation induced coating, thermal deposition, electrodeposition, electro/photopolymerization, up to plasma deposition.[32] There are many types of polymeric electrode modifier; the most common falls to conducting polymers (e.g. polypyrrole[42], polyaniline[43]) and electroactive polymers[44] (e.g. poly(vinylferrocene) and polymerized $Ru(vbpy)^{3+}$). Other types are ion-exchange polymer (e.g. Nafion[45]) and biological polymers[46] (e.g. enzymes and other proteins) for biosensing application.

For applications which demand well-defined structures as well as high thermal and chemical stability, inorganic films (i.e. metal oxides, silica, clay, and zeolites) provide the answer. Generally, metal oxide films are formed by anodization of metal electrodes (e.g. Al_2O_3 formation upon immersion of Al anode in H_3PO_4 solution)[47]. Oxides from other metals such as Ti, W, Mo, and Ta can also be deposited by chemical vapor deposition (CVD),[48] vacuum evaporation and sputtering,[49] and deposition from colloidal solution[50]. These metal oxides are valuable in electrocatalysis application.[36,51] On the other hand, silica, clay, or zeolite modified electrodes possess hosting,[15] molecular sieving,[52] and ion-exchange properties[53] which are important in the field of electroanalysis. These films are commonly deposited by EISA method which includes various coating techniques (i.e. dip coating, spin coating, drop coating, etc).[54]

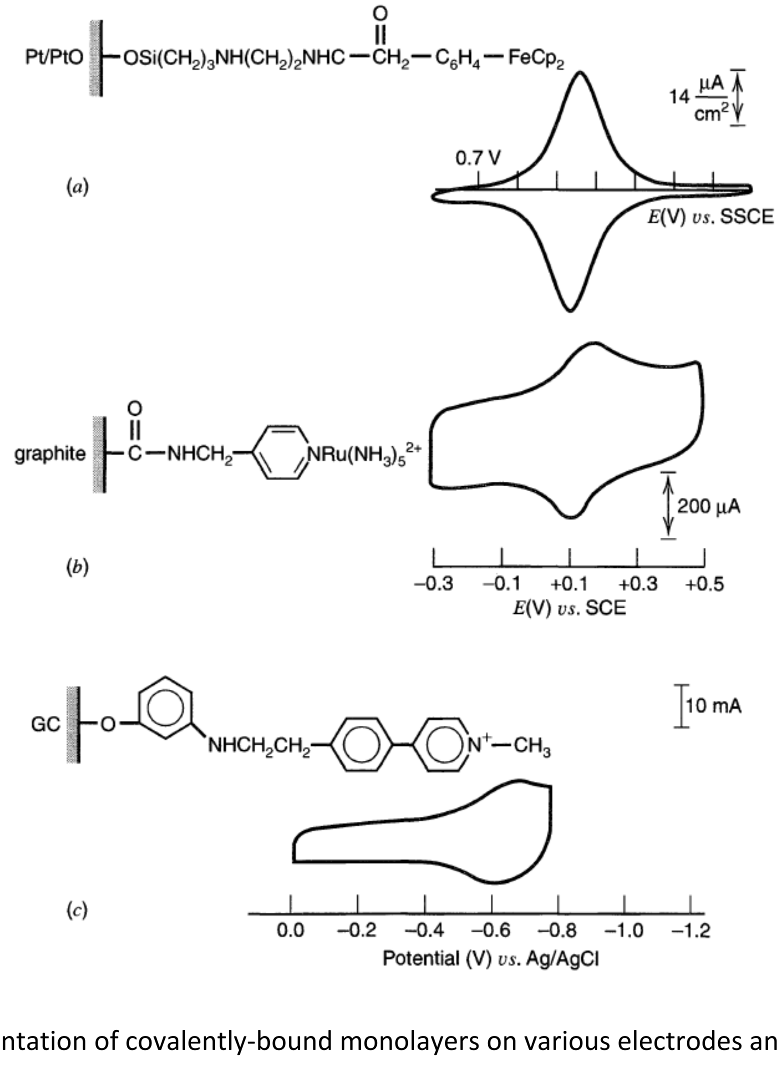

Figure 1.9 Representation of covalently-bound monolayers on various electrodes and their cyclic voltammograms. (a) Ferrocene on Pt, ν = 200 mV/s, (b) py-$Ru(NH_3)_5$ on graphite, ν = 5 V/s, and (c) viologen on glassy carbon, ν = 100 mV/s.[32]

1.2.2 Composite electrodes

Immobilization of chemical modifiers, especially the ones in the form of solid particles, onto flat electrodes can be tricky and unstable. Carbon paste matrix can be used to host vast types of either inorganic or organic/organometallic materials to form composite electrodes.[55] It is basically done by binding the graphite powder and the modifier particles together using an inert liquid binder, as represented in **Fig. 1.10**.

Inorganic particles such as Prussian-Blue derrivatives[56,57] and polyoxometallates,[59,60] for examples, offer an attractive electrocatalytic purpose. Natural clays,[60,61] zeolites[62,63] and silica-based materials[54,64] possess high surface area which is interesting for preconcentration analysis, as well as both molecular sieving and ion-exchange properties used in detection of inorganic ions, molecules, and environmental speciation. Catalytic behavior for the detection of various species can be also provided by non-siliceous metal oxides (RuO_2,[65] Cu_2O,[66] MnO_2,[67] etc) or metal elements (Ru, Pt, Rh,[68] Ir,[69] and bimetallic Ru-Pt[70]).

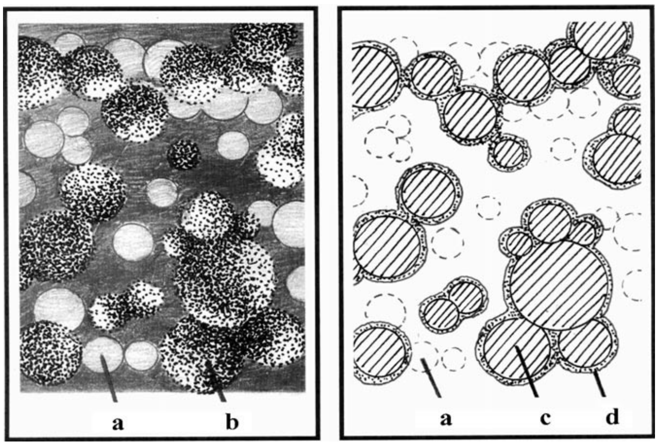

Figure 1.10 Microstructure of carbon paste (left) made of glassy carbon powder with spherical particles and the respective cross section (right). a) Carbon paste bulk revealing graphite particles coated with pasting liquid, b) the respective outer layer, c) graphite particles alone, d) thin film of liquid binder.[71]

Organic modifiers of CPEs can be generally classified into different types. First, there are organic ligands containing molecule sites to preconcentrate analytes, such as N- or S-based complexing centers to preconcentrate metals or cup-shaped macrocyclic compounds to host the target analytes.[55] Then there are organic catalysts like quinones,[72] phenothiazines,[73] phenoxanines,[74] and phenazines[75] and organometallic catalysts such as ferrocenes[72] and complexes of phthalocyanine derrivatives[76] who act as charge transfer mediators which are important for electroanalysis. Furthermore, to achieve electrode selectivity based on hydrophobic interactions, amphiphilic[77] and lipophilic[78] compounds can be mixed to the CPE matrix. Lastly, different types of polymers and macromolecules can be incorporated, such as functionalized resins to bind metal ions,[79] ion exchange resins[80] and permselective polymers for selectivity,[81] redox polymers for catalytic purposes,[82] and conducting polymers[83] to maintain electronic conductivity of the composite electrodes.

1.2.3 Interest of mesoporous silica in electrochemistry

The combination between electrochemistry and mesoporous silica gives different aspects of advantages. In the first place, it is possible to use electrochemistry to characterize the material, i.e. estimation of electroactive surface areas and double layer capacities, analysis of the behavior of surface-confined redox probes, and quantification of mass and charge transport processes inside such confined environments.[15] Cyclic voltammetry is a common electrochemical technique to test the permeability of mesoporous silica film on the surface of electrodes (as shown in **Fig. 1.11**), by using solution-phase redox probes which penetrates across the film before reaching the underlying electrode surface. Using probes with different charges and sizes (e.g. hexacyanoferrate ($Fe(CN)_6^{3-}$), ferrocenemethanol (FcMeOH), hexamineruthenium ($Ru(NH_3)_6^{3+}$), etc) can also characterize the film permselectivity based on electrostatic interactions.[84,85] Another permeability test of mesoporous silica with different mesostructures has been shown by using electrochemical impedance spectroscopy. Mass transport (diffusion coefficient) of redox species across the mesoporous silica film can be evaluated by hydrodynamic voltammetry technique using rotating disk electrode[86] or wall-jet cell[85]. In addition to the voltammetric method, scanning electrochemical microscopy analysis and imaging has been used as well to study transfer processes through the film.[87]

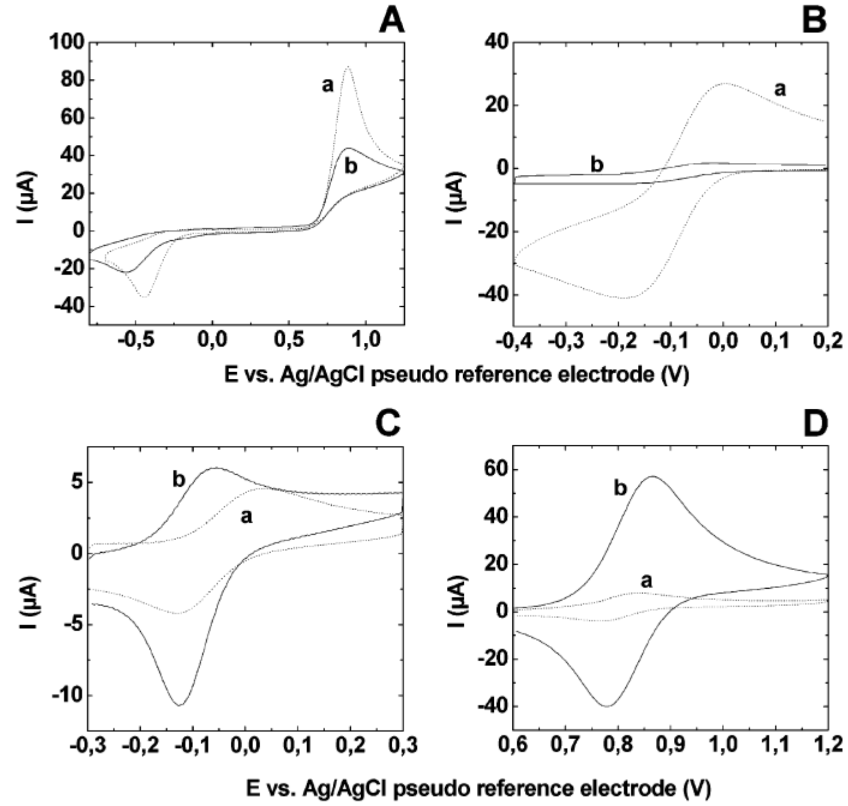

Figure 1.11 Cyclic voltammetric (CV) permeability tests of an ITO electrode coated with surfactant-extracted mesoporous silica thin film with cubic symmetry (plain lines, curves b) compared to bare ITO electrode (dotted lines, curves a). CV curves recorded in 0.05 mol L^{-1} hydrogen phthalate solutions (pH 4.1) containing (A) 0.5 mmol L^{-1} KI, (B) 0.5 mmol L^{-1} $Fe(CN)_6^{3-}$,(C)50 µmol L^{-1} FcMeOH, and (D) 50 µmol L^{-1} $Ru(bpy)_3^{2+}$; scan rate was 20 mV s^{-1}, and potentials are given versus a Ag/ AgCl reference electrode.

Furthermore, the mesoporous silica material itself offers the possibility to modify electrodes, providing properties interesting in many applications. The main application of mesoporous silica modified electrodes in electrochemistry is in electroanalysis, covering direct/indirect detection and electrocatalysis, preconcentration analysis, biosensing, and other sensors.[15] For the purpose of direct detection, electronically insulating mesoporous silica is commonly used to immobilize conducting nanoparticles (NPs), such as gold[88] and silver[89] NPs for the detection of glucose and H_2O_2 respectively. Preconcentration analysis is basically accumulation of target species from a diluted solution to the surface of the electrode prior to the electrochemical detection to increase the detection sensitivity. Based on this concept, mesoporous silica is a great candidate for its high surface area and the possibility to functionalize its surface for increased selectivity to certain target species. Some examples are the selective detection of Hg(II),[90] Cu(II),[91] and Pb(II)[92] using electrodes modified with mesoporous silica functionalized with amine or thiol, cyclam, and amide-cyclam groups respectively.

For the same intrinsic properties of mesoporous silica mentioned above, it is interesting to employ the material for the means of biosensing. Immobilization of different types of biomolecules has been conducted to detect other related species, for example the enzymes (e.g. glucose oxidase or horseradish peroxidase)[93,94] as first-generation biosensors are used to detect the enzymatically-generated products. Another example is immobilized heme proteins for the detection of H_2O_2[95] and hemoglobin (Hb) in different silica mesostructures[96] (**Fig. 1.12**). Besides the analytical techniques described above, there are other detection technique which take advantage of mesoporous silica, such as electrochemiluminescence (ECL)[97] and humidity[98] detections.

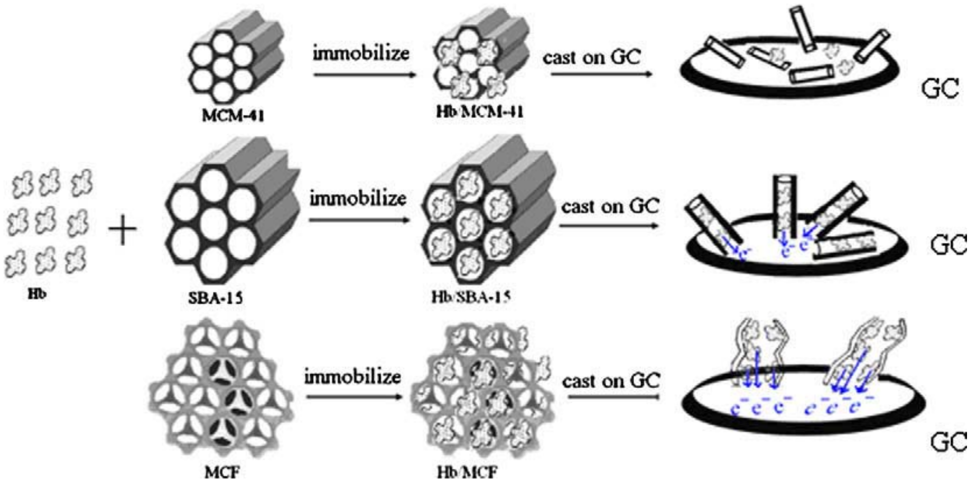

Figure 1.12 Schematic representation of Hb immobilized on different structures of mesoporous silica and the electron transfer between Hb and GC electrode.[96]

Ultimately, it has been proven[99,100] that electrochemistry can be utilized to generate ordered mesoporous silica deposit on the surface of electrodes. This part will be furthermore elaborated in **Section 1.3.2** below.

1.3 Mesoporous silica thin films on electrode

As mentioned previously, mesoporous silica has been an attractive material in electrochemical applications. It generally exists in two forms,[85] i.e.:

- Bulk composite electrodes (mesoporous silica particles dispersed in conductive matrix).
- Mesoporous silica thin film deposited on solid electrodes.

The thin film configuration is considered advantageous because it is binder-free. Therefore, in this section, attention will be drawn towards the modification of electrodes by specifically mesoporous silica thin films.

As described in **Section 1.1.4**, mesoporous silica thin films can be easily formed on the surface of a substrate by EISA method. This method has been successfully applied to modify electrode surfaces, such as gold, platinum, and glassy carbon electrodes by spin-coating,[101] as well as ITO[85] and FTO[102] electrodes , and silicon and alumina substrates with interdigitated electrodes[103] by dip-coating.

Although mesoporous silica film deposition can be easily formed by EISA, its application as electrode modifier can have some challenges. First of all, there is a necessity of continuous crack-free and stable film deposition. Thermal aging and calcination step of mesoporous silica coating can produce cracks and shrinkage respectively.[102,104,105] Secondly, and the most importantly, is that the pores of the film are preferably accessible from the film surface. EISA technique induces deposition of silica thin films with the mesochannels parallel to the electrode surface. Hence, films with mesochanels oriented normal to the electrode surface has become of particular interest as it enhances the pore accessibility and favors faster mass transfer from/to the solution.[104,105]

1.3.1 Vertically aligned mesoporous silica film on electrode

Many scientists have reported methods to obtain surface-accessible mesoporous silica film. The first goes back to the 1998, where Zhao *et al.*[106] reported the formation of continuous mesoporous silica thin films with 3D-accessible pore structure.

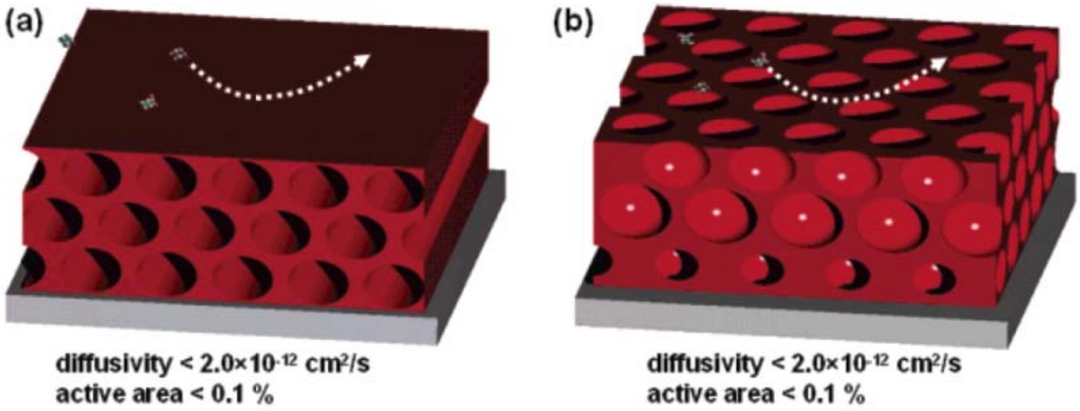

Figure 1.13 Representation of poor mass transport access of species through (a) 2D hexagonal silica film and (b) face-centered cubic silica film.[102]

For vertical alignment, Teng *et al.*[23] have proven that Stöber solution (a mixture of TEOS, CTAB, ethanol, and ammonia) can be used for the growth of silica films with continuous 2D-ordered channels perpendicular to the substrate. In this method, CTA^+ can be attached and form spherical micelles on the negatively charged substrate. Subsequently, the hydrolyzed TEOS condenses on the surface of the micelles. The role of ammonia here is to catalyze the transformation of spherical shape of the silica-CTAB structure to cylindrical, giving vertical growth normal to the substrate surface.

Other attempts have been reported, such as epitaxial-like growth on a patterned substrate,[107] the scanning electrochemical microscopy,[108] the use of external fields, such as magnetic field[109] and radio frequency,[110] and the addition of decane in the sol mixture.[111] Despite of the vertical alignment achievements, these methods presented some drawbacks; i.e. sophisticated processes, time-consuming and complex substrate pre-treatments, low level of pore orientation, and restricted choice of support type or geometry.[112] Moreover, they were restricted to bigger pore diameters (above 5-6 nm) and none have reported functionalization of the film surface.[112]

In the following sections, focus will be drawn to a particular strategy in obtaining such oriented mesochannels, called the Electrochemically-assisted Self-assembly (EASA)[113] method as it is the basis of this thesis work.

1.3.2 Electrochemically-assisted self-assembly (EASA) method

Walcarius group first reported in 2007[113] that mesoporous silica film with vertically oriented mesochannels sizing around 2-3 nm of diameter can be obtained using EASA method and deposited in various type of conductive substrate, such as gold, glassy carbon, platinum, copper and indium tin oxide (ITO) coated glass.[113,114]

The principle of this technique (as illustrated in **Fig. 1.14**) is basically applying a suitable cathodic potential to an electrode immersed in a hydrolyzed sol solution containing a surfactant template (i.e. CTAB). Such negative potential (commonly -1.3 V) induces two important occurrences. First, it drives self-assembly of surfactants onto the electrode surface. Concurrently, it also generates hydroxide ions in the interface between the electrode surface and the solution, causing therefore local pH increase high enough to catalyze polycondensation of silica network growing normal to the underlying substrate around the formed surfactant assemblies.

The pore organization and vertical orientation of the mesoporous silica film generated by EASA is controlled by the CTAB/TEOS ratio. A detailed study conducted by Goux *et al*.[114] had been done on this matter, resulting in three main pore organization based on CTAB/TEOS ratio; i.e. amorphous (non-organized), weakly organized (wormlike structure), and highly organized and oriented hexagonal structure obtained in the CTAB/TEOS ratio range from 0.16 up to 0.64. By keeping the applied cathodic potential (i.e. -1.3 V) and the deposition time (i.e. 20s) constant, the thickness of the film can be controlled by varying the concentration of TEOS (50 – 350 mM) in the sol solution and it ranges from 25 to 150 nm.

1.3.3 Surface functionalization

Alongside the importance of material structuration, surface functionalization has also caught many attentions in research in order to add certain specific properties and reactivity of the materials for different applications. In the case of mesoporous silica, pore walls functionalization is important to modify the properties of the material for the applications of interest, such as electrochemical sensing, molecular sieving, or other nanomaterial synthesis templating. Several strategies to answer to this challenge are described below.

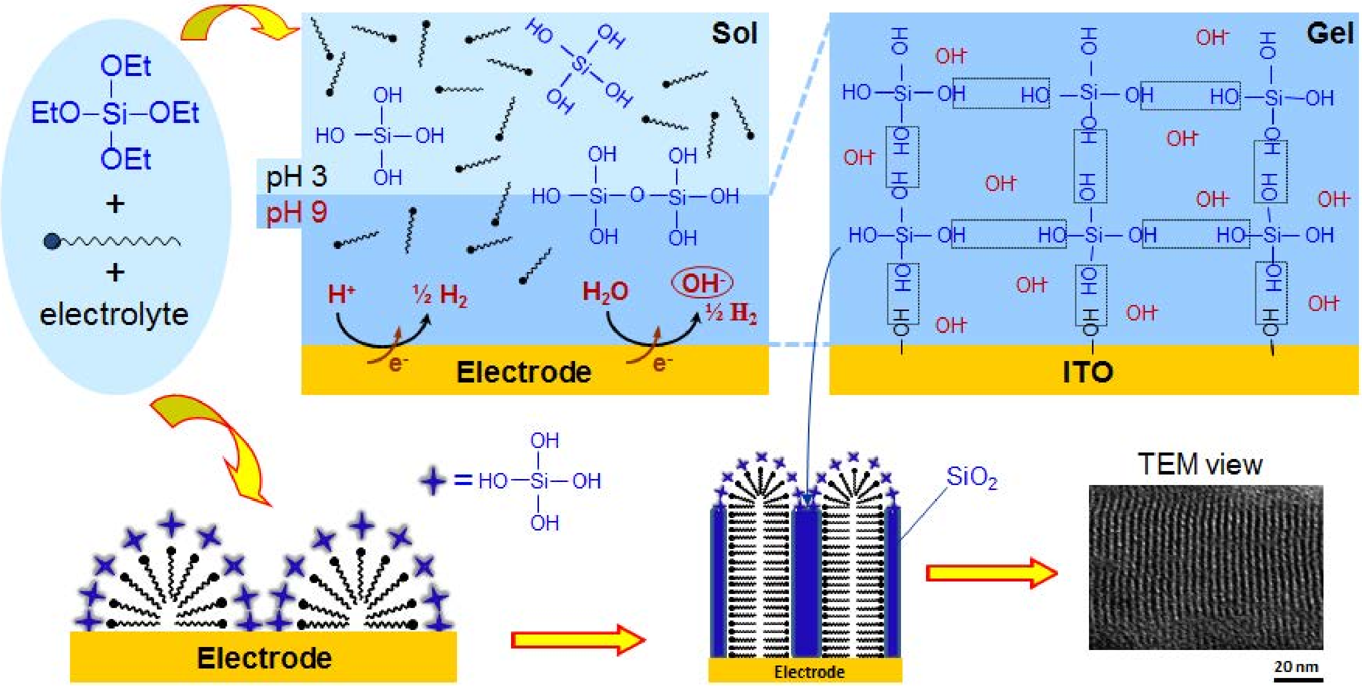

Figure 1.14 Schematic representation of the Electro-assisted Self-assembly (EASA) method used to generate ordered and vertically-oriented mesoporous silica thin films.[115]

Post-synthesis grafting method could be applied for this purpose. However, most of the time, attempts resulted in dramatic blocking effect. Some successful result was found to graft hydroquinone[116], ammonium[117], and ferrocene groups[118]. Nonetheless, non-uniform spatial distribution of grafting was found, with more grafting in the pore entrance than inside the channels.

Blocking effect can be defeated by an alternative approach which called co-condensation method. In principle, it can be done by adding alkoxy/organosilane to the silica precursor solution. With this method, simple organofunctional groups, such as amine[86], methyl[87], octyl or hexadecyl[119], thiol[120], ethylenediamine[121], and azide[112], can be incorporated in the mesochannels. However, high concentration of organosilane in the precursor solution leads to disordered structure. To maintain high order and vertical alignment of the film, there are different maximum percentage of organosilane content that can be bonded, such as 10% for amine[86] and thiol[120], 60% for methyl[87], 20% for octyl[119], 5% for hexadecyl[119], 8% for ethylenediamine[121], and 40% for azide groups[112].

Two-step synthesis can also be conducted to obtain more versatile functionalization. One example is by using as-synthesized amine-functionalized silica film to post-functionalize it with catechol moieties via electrochemical generation of reactive *o*-quinone followed by covalent bonding to the anchored amine groups.[122] Hydroquinone groups were also attached by post-derivatization of amine-functionalized silica film with a certain dioxopyrrolidin-hydroquinone-based reagent.[116]

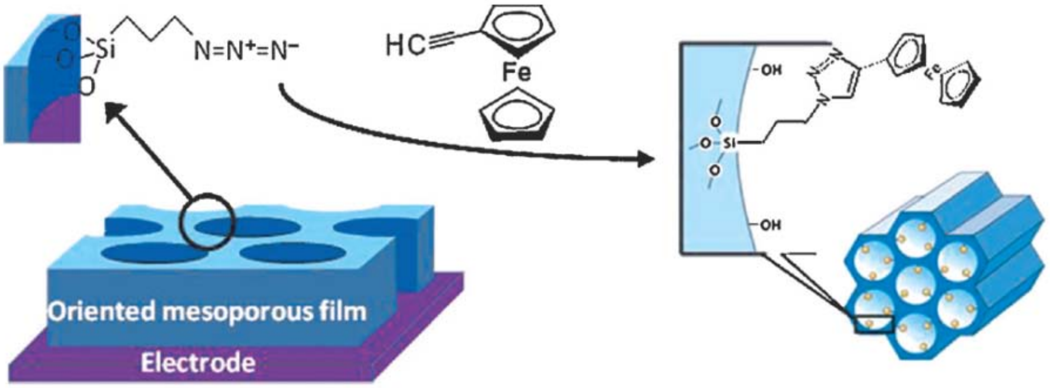

Figure 1.15 Schematic representation of a Huisgen click reaction between covalently-bound azide groups on silica surface with ethynyl bearing ferrocene group.[123]

Another novel and even more versatile two-step functionalization is by using Huisgen (azide-alkyne) and thiol-ene click chemistry to post-functionalize, respectively, azide and thiol-functionalized silica film. For Huisgen click reaction, the idea is the possibility to covalently link any species bearing ethynyl functional group to the pre-attached azide groups (schematically shown in **Fig. 1.15**). Vila *et al.* have managed to "click" ferrocene[123] and tetrazine[124] groups on azide-functionalized silica film. As for the thiol-ene reaction, the same principle applies for any species bearing vinyl functional groups and thiol-functionalized silica film. It was demonstrated that this reaction can facilitate ferrocene functionalization, even bifunctionalization was successful using silica film functionalized with both azide and thiol groups. Upon reaction with ethynylcobaltocene and vinylferrocene, bifunctionalized silica film was obtained, with controlled cobaltocene/ferrocene ratio.[125]

Chapter II

Experimental Part

This chapter contains detailed information concerning the list of chemicals and apparatus, the electrochemical set-ups, and the experimental protocols applied for the completion of this thesis. **Section 2.3** depicts the protocols which were largely repeated throughout the thesis; i.e. the vertically aligned silica film deposition, its methods of click-functionalization, and electrochemical characterizations. All other information regarding experiment details are mentioned later in the individual **Chapters III – VI**.

2.1 Chemicals

All chemicals used in the experiments are listed in **Table 2.1**. Some chemicals were synthesized in the lab according to the references noted in the table, and some of the protocols are described in **Section 2.3**.

Table 2.1 List of chemicals

Name	Abbreviation/ Formula	Source	Molecular Weight (g/mol)	Purity (%)
Silica precursors and template salt				
Tetraethoxysilane	TEOS	Alfa Aesar	208.33	98
(3-azidopropyl)trimethoxysilane	AzPTMS	Synthesized in the lab (see **Section 2.3.1**)	205	N/A
(3-chloropropyl)trimethoxysilane	ClPTMS	Alfa Aesar	197,5	97
Cetyltrimethylammonium bromide	CTAB	Acros Organics	364.45	99
Supporting electrolytes				
Sodium nitrate	$NaNO_3$	Prolabo	84.99	99
Phosphate Buffer Tablet pH 7.4	PBS	Sigma Aldrich	N/A	N/A
Tetrabutylammonium tetrafluoroborate	TBABF4	Sigma Aldrich	329.27	99

Table 2.1 List of chemicals (continued)

Redox probes				
Hexaammineruthenium (III) chloride	$Ru(NH_3)_6Cl_3$	Sigma Aldrich	309.61	98
Potassium Hexacyanoferrate (III)	$K_3Fe(CN)_6$	Fluka	329.25	99
Potassium Hexacyanoferrate (II)	$K_4Fe(CN)_6$	Fluka	368.35	99.5
1,1’-ferrocenedimethanol	$Fc(MeOH)_2$	Sigma Aldrich	246.08	97
Iron(II) sulfate	$FeSO_4$	Prolabo	278.01	N/A
Iron(III) sulfate pentahydrate	$Fe_2(SO_4)_3.5H_2O$	Acros Organics	489.94	97
Reactants and Catalysts				
Sodium azide	NaN_3	Sigma Aldrich	65.01	99
Tetra-n-butylammonium perchlorate	$TBAClO_4$	Fluka	341.91	98
Ethynyl ferrocene	EtynylFc	Sigma Aldrich	210.05	97
Copper (II) acetate	Cu(II)acetate	Prolabo	181.63	99
Copper (II) sulfate pentahydrate	$CuSO_4.5H_2O$	Prolabo	159.61	99
L+ascorbic acid	AA	Merck	176.12	99.7
Sodium diethyldithiocarbamate	NaDDTC	Sigma Aldrich	225.31	N/A
Ruthenium(2,2’-bipyridine)2-(4-[(2-propyn-1-yloxy)methyl]-4’-methyl-2,2’-bipyridine)	$Ru(bpy)_2(bpy')$	Synthesized in the lab	997	N/A
Tris (2,2’-bipyridyl) dichlororuthenium(II) hexahydrate	$Ru(bpy)_3$	Acros	748.62	98
Ethynyl-ruthenium bis-2,2’-bipyridine	Ethynyl-$Ru(bpy)_2$	Synthesized in the lab	493	N/A
cis-Dichlorobis (2,2’-bipyridine)ruthenium(II)	$Ru(bpy)_2$	Sigma Aldrich	484.34	97
2,2'-bipyridine	Bpy	Lancaster	156.18	99
Ethynyl-(2,2’-bipyridine)	Ethynyl-bpy	Synthesized in the lab		N/A
Cobalt (II) chloride	$CoCl_2$	Alfa Aesar	129.84	99.9
2,3-di(2-pyridyl)-5,6-diphenylpyrazine	dpdpz	Synthesized in the lab		N/A
4,4’-dimethyl-2,2’-dipyridyl	dmdp	Sigma Aldrich	184.24	99.5
1,4-dioxane	DEO	Sigma Aldrich	88.11	99.8
Selenium (IV) oxide	SeO_2	Alfa Aesar	110.96	99.4
Ruthenium (III) chloride trihydrate	$RuCl_3.3H_2O$	Sigma Aldrich	261.47	99.9
Lithium chloride	LiCl	Fluka	42.39	99
Aniline	Ani	Sigma Aldrich	93.13	99.5

Table 2.1 List of chemicals (continued)

Solvents				
Water	H_2O	Millipore Milli-Q system	18.02	N/A
Ethanol	EtOH	Merck	46.07	95-96
Acetone	AcOEt	Carlo Erba	58.08	99.8
N,N-dimethylformamide	DMF	Sigma Aldrich	73.09	99.8
Diethyl ether	DEE	Sigma Aldrich	74.12	99
Chloroform	$CHCl_3$	Sigma Aldrich	119.38	99.8
Dichloromethane	DCM	Prolabo	84.93	99.9
Acetonitrile	AcN	Biosolve	41.05	99.95
Others				
Hydrochloric acid (1 M)	HCl	Sigma Aldrich	36.46	37
Sodium carbonate	Na_2CO_3	Sigma Aldrich	105.99	99.5
Sodium bicarbonate	$NaHCO_3$	Sigma Aldrich	84.01	99
Multi-element standard solution of 1000µg/mL of F^-, NO_3^-, Br^-, Cl^-, SO_4^{2-} and PO_4^{3-}	N/A	SCP Science	N/A	N/A
Sulfuric acid	H_2SO_4	Sigma Aldrich	98.08	95-97
Nitric acid	HNO_3	Sigma Aldrich	63.01	65
Perchloric acid	$HClO_4$	Riedel de Haen	100.46	60
Hydrogen peroxide	H_2O_2	VWR Prolabo	34.01	30
Potassium permanganate	$KMnO_4$	Prolabo	158.03	99
Buffer solution pH 7	N/A	Riedel de Haen	N/A	N/A
Buffer solution pH 4	N/A	Prolabo	N/A	N/A
Tripropylamine	TPA	Sigma Aldrich	143.27	98

2.2 Instrumentations

2.2.1 Electrochemistry

- Potentiostats:

  All electrochemical measurements were conducted using either of three potentiostats, which are **PGSTAT 100**, **µAutolab III** (both monitored by either GPES or NOVA software), or **EmStat^{3+}** (monitored by PSTrace software).

2.2.2 Spectroscopy

- Fourier Transform Infra-red Spectroscopy:

  IR Spectra were recorded using **Nicolet 8700** apparatus equipped with a specular reflectance accessory.
- UV-vis Spectroscopy:

  Cary 60 UV–vis spectrophotometer was used to record the spectra.
- X-ray Photoelectron Spectroscopy:

  Analyses were completed using **KRATOS Axis Ultra X-ray photoelectron spectrometer** which was equipped with the monochromated AlKα X-ray source (hν = 1486.6 eV) operated at 150 W.
- Spectrofluorometer:

  Fluorescence and electrochemiluminescence measurements were conducted using **JASCO FP-8200** and **SAFAS Xenius XM** apparatuses, respectively.
- Grazing-incidence X-ray diffraction:

  Patterns were obtained using **Nonius Kappa CCD diffractometer** equipped with an ApexII CCD detector (copper cathode - λ K = 1.54184 Å).

2.2.3 Microscopy

- Optical Microscopy:

  Observation of surfaces was done using **Nikon Eclipse microscope** fitted with Nikon LHS-H100P-2 (12V; 100W) Halogen lamp and lenses with 5X, 10X, 20X, 50X, and 100X magnifications.
- Scanning Electron Microscopy:

  Top-view images of silica films were taken using **JEOL JSM-840 microscope**.
- Transmission Electron Microscopy:

  The morphology/mesostructure of the silica films (samples were carefully scratched from the ITO electrode and transferred to a TEM grid) was characterized using a **CM20 microscope** at an acceleration voltage of 200 kV equipped with an Energy Dispersive Spectroscopy (EDS) analyzer.
- Atomic Force Microscopy:

The evaluation of silica film surface roughness and rough estimation of its thickness were obtained using **Asylum MFP3D-Bio** apparatus.

2.2.4 Others

- pH Meter:

  pH of solutions was measured using **Radiometer Analytical PHM210 Standard pH Meter** equipped with a glass pH probe with Ag/AgCl as reference. pH meter was calibrated using buffer solutions of pH 7 and pH 4.
- Ion Chromatography:

  All analyses were carried out using a **Metrohm 882 Compact IC plus** instrument controlled by MagIC NetTM 3.1 software and equipped with chemical (Metrohm suppressor MSM II for chemical) and sequential (Metrohm CO_2 suppressor MCS) suppression modules and a conductivity detector. Separations were performed on a Metrosep A Supp 5-250/4.0 column packed with polyvinyl alcohol particles functionalized with quaternary ammonium group (5µm particles diameter) and associated with a guard column (Metrosep A supp 4/5 guard).
- Flow Injection Apparatus:

  All flow injection experiments were conducted using **BASi Epsilon LC-EC Detection injector and flow cell**, completed with RE-6 Ag/AgCl reference electrode with flexible connector

2.3 Experimental set-up and protocols

Various experimental set-ups and protocols were used throughout the dissertation. In this chapter, only largely repeated protocols are described. Among them are the organic synthesis of AzPTMS, electrochemically-assisted self-assembly (EASA) of silica thin films on an electrode surface, Huisgen click reaction, and electrochemical characterization of bare or modified electrodes.

2.3.1 Synthesis of (3-azidopropyl)trimethoxysilane (AzPTMS)

The synthesis of AzPTMS followed the protocols reported by Vilà *et al.*[112] A solution of NaN_3 (2.16 g, 33.2 mmol) and $TBAClO_4$ (1.290 g, 4 mmol) in dry AcN (100 mL) was bubbled by N_2 for 30 minutes. Subsequently, ClPTMS (4 g, 19.1 mmol) was added to the solution. The reaction mixture was stirred under reflux and kept under N_2 atmosphere for 48 h, as shown in **Fig. 2.1**. After this period, the solvent was reduced under vacuum pressure using a rotary evaporator. The resulting crude mixture was diluted in cyclohexane and filtered. The crude oil obtained from the filtration was finally distilled under vacuum pressure. Yield: 68%. Characterization: ^{1}H-NMR (400MHz, $CDCl_3$): δ 0.68 (s, 9H), 1.70 (m, 2H), 3.27 (t, 2H), 3.87 (m, 2H).

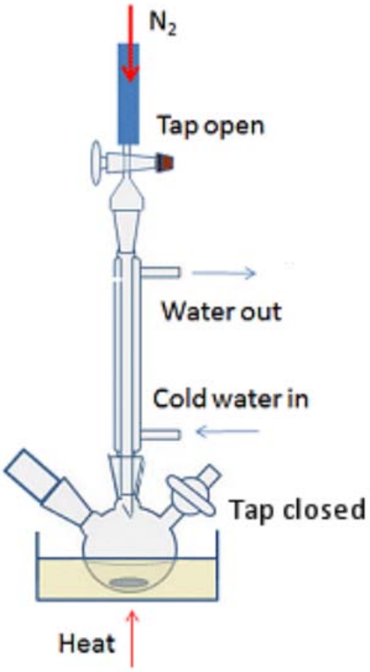

Figure 2.1 Organic synthesis set-up under reflux and N_2 atmosphere.[126]

2.3.2 Electrochemically-assisted self-assembly (EASA) of silica thin films

A Teflon home-made electrochemical cell was used for the EASA synthesis of the mesoporous silica films onto indium-tin oxide (ITO) plates (surface resistivity 8-12 Ω, Delta Technologies) connected as working electrodes by a tinned copper wire; a stainless steel counter- electrode and an AgCl-coated silver wire pseudo-reference were used to complete the three-electrode set-up shown in **Fig. 2.2**.

Ordered and perpendicularly oriented mesoporous silica thin films were electrodeposited on ITO by the method reported previously.[113,114,127] A typical sol was prepared containing 50-200 mM TEOS as the silica precursor, 16-64 mM CTAB as surfactant template (C_{CTAB}/C_{TEOS} was kept constant at 0.32) and 0.1 M $NaNO_3$ as supporting electrolyte. The sol pH was adjusted to 3 by the addition of 0.1 M HCl and stirred for 2.5 hours. The surface of the electrode was delimited by a round seal pictured in Fig. 2.2c (10 mm inner diameter) on top of which a Teflon cell containing the silica sol was placed. A cathodic potential of -1.3 V was applied on the ITO working electrode for 20 seconds. The electrode was then removed from the solution and rinsed with distilled water. The deposit was finally dried and aged overnight in an oven at 130°C. Surfactant extraction was carried out by immersing the film in an ethanol solution containing 0.1 M HCl for 10 minutes.

In the case of azide-functionalized mesoporous silica films synthesis, the same protocol was maintained. The differentiating point is that the sol contained a mixture of silane precursors (notably TEOS and AzPTMS), with a various ratio of C_{TEOS}/C_{AzPTMS}, typically 70-95/30-5. The amount of CTAB surfactant was maintained as previously[112] optimized ($C_{CTAB}/C_{total\text{-}silane}$ ratio = 0.32).

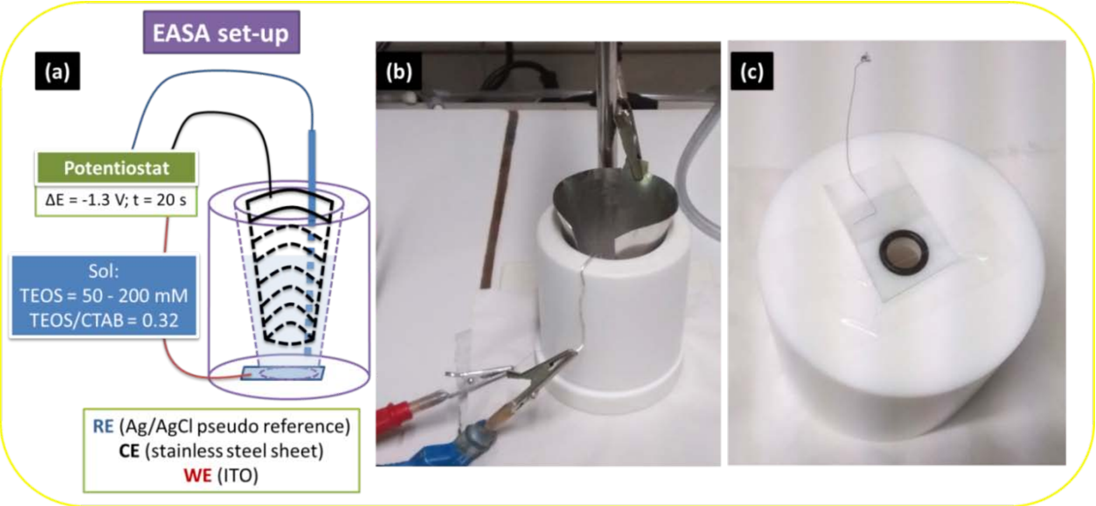

Figure 2.2 Electrochemically-assisted self-assembly (EASA) synthesis set-up representation (a) and photograph (b). Photograph of an ITO electrode fixed on the electrochemical cell completed with a 10 mm-diameter O-ring as the electrode surface delimitation (c).

2.3.3 Huisgen click reaction of azide-functionalized mesoporous silica films

Prior to the reaction, the surfactant template was removed from the aged azide-functionalized mesoporous silica films by extraction in 0.1 M HCl ethanolic solution for 10 minutes. These electrodes were further functionalized by Huisgen click coupling with ethynyl-bearing functional groups, for example ethynylFc, by immersion in the dark for 18-24h in a solution of DMF/H_2O (12/8 mL) of ethynylFc (5.0 mg), Cu(II)acetate (1.0 mg) and AA (2.5 mg) to get their ferrocene-functionalized form.

The films were firstly rinsed with water. Subsequently, they were immersed in an ethanolic solution of 0.1 M DDTC for 15 minutes to remove the traces of copper catalyst. Furthermore, the films were immersed in DMF for another 15 minutes to remove the possible unreacted ethynylFc and then rinsed thoroughly with distilled water.

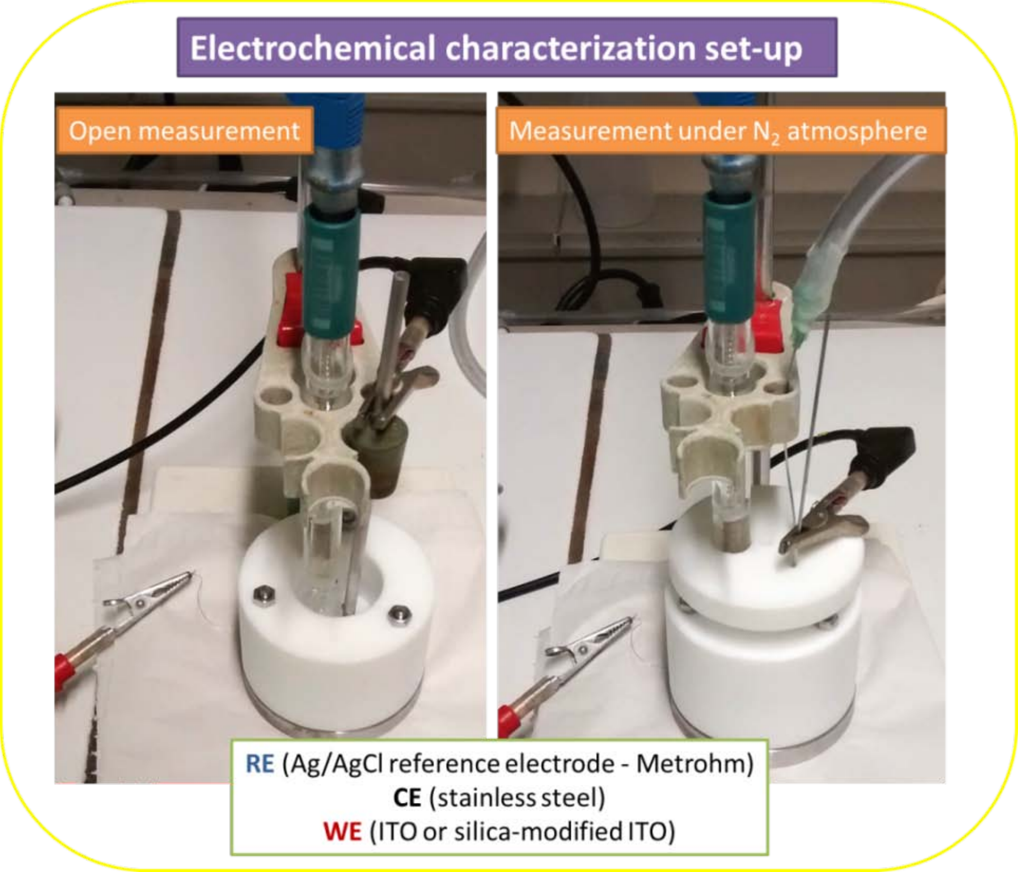

Figure 2.3 Set-ups for electrochemical characterizations of bare or modified ITO electrodes.

2.3.4 Electrochemical characterization

Characterization of silica modified ITO electrodes was generally conducted by cyclic voltammetry. Various redox probes, notably $Ru(NH_3)_6Cl_3$, $K_3Fe(CN)_6$, $K_4Fe(CN)_6$, $Fc(MeOH)_2$, were used mostly to confirm the quality of the deposited films (preferably present no-defects) and to study the mass and charge transport across the films. The experiments were conducted using a three-electrode electrochemical cell from Teflon, consists of Ag/AgCl reference electrode (Metrohm), stainless steel counter electrode, and ITO plates as working electrodes connected by a tinned copper wire.

Chapter III

Amplified Charge Transfer for Anionic Redox Probes through Oriented Mesoporous Silica Thin Films

3.1 Introduction

Transport phenomena involving small molecules/ions or macromolecules within nanopores have been largely studied using nanoporous membranes,[85,128–132] mainly because of their great interest for applications in separation,[133] sensing and biosensing,[99,134,135] or medical devices.[136] Compared to the widely-used organic functional polymer membranes,[137] inorganic nanoporous materials (such as zeolites,[138] porous silicon,[139] anodized alumina,[140,141] mesoporous silica and related organic-inorganic hybrids,[104,141,142] or some others[143]) offer the advantage of better control of the nanostructure and easier surface modification.[129,143,144]

As mentioned in **Chapter I**, mesoporous silica thin films on electrodes recently attracted considerable attention, notably in the field of electrochemical sensors and biosensors as well as energy conversion and storage,[15,115,145] especially thin films where the mesochannels are oriented perpendicularly to the electrode surface.[23,113,114] To date, oriented films have been mainly exploited for electroanalytical purposes,[105] and their performance is highly dependent on mass transport through the film.[86]

The presence of a mesoporous silica film onto an electrode surface affects significantly its response to redox probes in solution, and electrochemical techniques are good tools to characterize such diffusion-controlled phenomena.[84] Firstly, the mesoporous film induces some resistance to mass transport, with diffusion processes (and consequently voltammetric currents) strongly depending on the mesostructure type (e.g., hexagonal, cubic, or wormlike, with faster diffusion through well-ordered mesostructures containing many interconnections)[85,101,146] and pore orientation (fast transport across vertical mesopore channels whereas horizontal mesostructures were almost totally blocked).[85,113] The rate of mass transport through mesoporous silica is also affected by the pore diameter and the probe size,[147] even going to steric exclusion[148] or molecular sieving behaviour.[127] Secondly, charge permselectivity at mesoporous silica was also reported.[149–151] Actually, because of the negatively-charged mesopore walls (the silica surface is negative at pH above 2),[85] cations can easily diffuse through the mesochannels, being even accumulated owing to favourable electrostatic interactions,[113,151] whereas the ingress of anions is significantly restricted due to electrostatic repulsions, yielding respectively to enhanced and suppressed voltammetric currents.[84,105,149] Such charge effects are especially marked in ordered mesoporous materials exhibiting a regular spatial distribution of surface charges, generating stronger electric potential profile than in amorphous disordered silica gels.[152] The charge permselectivity can be regulated or tuned by ionic strength or pH changes,[150,153] or via grafting the silica walls with positively-charged functional groups[117,150,154] or redox polymers,[155] as otherwise pointed out for electrodes covered with organically-modified films of inorganic porous materials such as clays or opals.[156,157]

In this Chapter, we have investigated the possibility to amplify the voltammetric responses of anionic redox probes ($Fe(CN)_6^{3-}/^{4-}$), which are usually prevented/limited at mesoporous silica film modified electrodes, by using neutral or positively-charged solution-phase redox mediators ($Fc(MeOH)_2$ or $(Ru(NH_3)_6^{3+})$) that are likely to diffuse freely through the membrane to the electrode surface. To demonstrate such long-range electron shuttling, vertically oriented mesoporous silica films have been selected as they provide an almost ideal system (fast diffusion rates, only one dimensional pathway for mass transport, no pore interconnections). The effectiveness of the process has been monitored by cyclic voltammetry. It has been studied by varying the solution composition (probe and mediator concentrations, ionic strength) and the timescale of the experiments (potential scan rate).

3.2 Results and Discussion

3.2.1 Charge selectivity for transport of redox probes through oriented mesoporous silica thin films

Fig. 3.1 illustrates the typical responses of ITO electrodes covered with a vertically aligned mesoporous silica thin film to various redox probes ($Ru(NH_3)_6^{3+}$, $Fc(MeOH)_2$, $Fe(CN)_6^{4-}$ and $Fe(CN)_6^{3-}$). The absence of any noticeable signal for ionic species before extraction (see curves b in parts ACD of **Fig. 3.1**), compared to the well-defined reversible signals on bare ITO (see curves a in **Fig. 3.1**), confirms that the films covers uniformly the whole ITO surface, without cracks, and that neither cations nor anions are likely to cross the surfactant-templated layer. Only $Fc(MeOH)_2$ gives rise to a measurable signal because such neutral species are likely to solubilized in the surfactant phase and thus being able to reach the electrode surface. This behaviour is as expected from previous reports.[113,114]

After removal of the template, the film becomes permeable to the solution-phase redox probes, yet with significant differences depending on their charge (sees curves c in **Fig. 3.1**). While $Ru(NH_3)_6^{3+}$ and $Fc(MeOH)_2$ species can easily reach the ITO electrode surface (giving rise to voltammetric current of the same order of magnitude as on bare ITO, or even larger due to cations accumulation, **Figs. 3.1 A&B**), the responses of $Fe(CN)_6^{4-}$ and $Fe(CN)_6^{3-}$ anions are dramatically hampered (**Figs. 3.1 C&D**) and this is even worse in low ionic strength medium (**Figs. 3.1 E&F**). Such charge permselectivity at mesoporous silica films is well established,[85,149–151] and results from the negatively-charged silica surface over a wide pH range (pH_{iso}=2)[7], including in conditions used here (unbuffered $NaNO_3$ solutions), restricting the ingress of anions in the mesochannels because of electrostatic repulsions.[84,105,149] This yields to decreased voltammetric currents for $Fe(CN)_6^{4-}$ and $Fe(CN)_6^{3-}$, which are even suppressed when operating at low concentration of supporting electrolyte (i.e., 1 mM $NaNO_3$, see **Figs. 3.1 E&F**). Such suppression might be related to Donnan exclusion effects (which have been long recognized in membranes with fixed electric charges),[158,159] for which lower salt concentrations result in systems less open to permeation of species bringing the same charge as that of the membrane.[160]

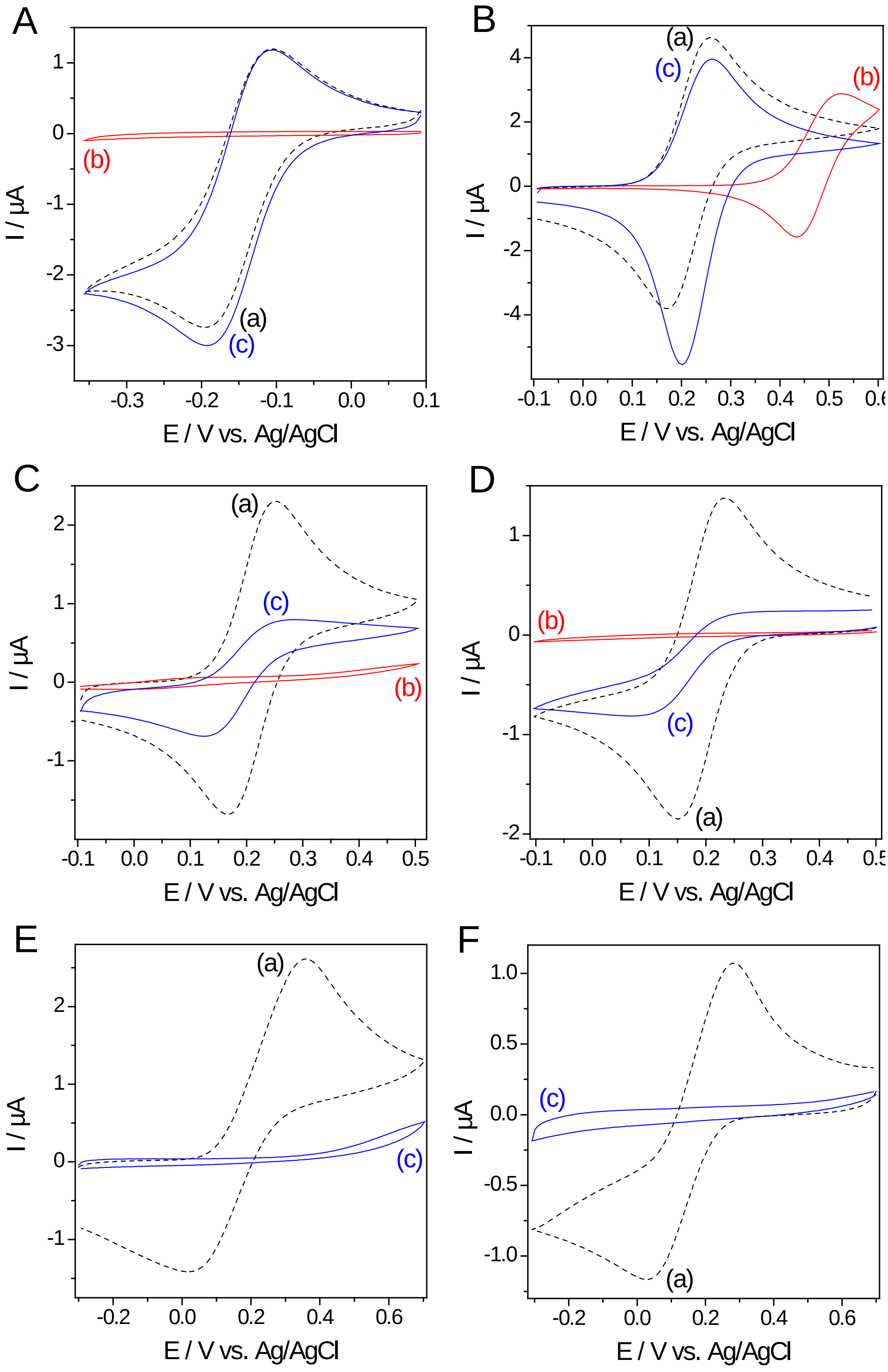

Figure 3.1 Cyclic voltammograms recorded in 0.1 mM solutions of (A) $Ru(NH_3)_6^{3+}$, (B) $Fc(MeOH)_2$, (C,E) $Fe(CN)_6^{4-}$, and (D,F) $Fe(CN)_6^{3-}$, using (a) bare ITO and (b-c) ITO electrodes modified with vertically aligned mesoporous silica films (b) before and (c) after surfactant extraction; supporting electrolyte solutions were either 0.1 M $NaNO_3$ (A-D) or 1 mM $NaNO_3$ (E and F); potential scan rate: 20 mV s^{-1}.

3.2.2 Amplification of $Fe(CN)_6^{4-}$ oxidation using 1,1'-ferrocene-dimethanol as mediator

On the basis of the above observations, a way to circumvent the limitations encountered for redox anions could involve the use of non-excluded redox species that would be able to shuttle electrons between the electrode surface and anionic redox probes in solution (i.e., long-range charge transport through the isolating film, which was not yet investigated at mesoporous silica film electrodes using mixtures of redox probes in solution). This is what we first demonstrate hereafter using $Fc(MeOH)_2$ to amplify $Fe(CN)_6^{4-}$ oxidation. Actually, these two probes undergo, reversible, one-electron redox reactions, and both couples ($Fc(MeOH)_2/Fc(MeOH)_2^+$ and $Fe(CN)_6^{4-}/Fe(CN)_6^{3-}$) are characterized by very similar standard potential values, as confirmed by cyclic voltammetry (see dashed curves on **Figs. 3.1 B&C**), yet with faster electron transfer kinetics for the ferrocene derivative (consistent with previous observations at unmodified electrodes[161,162]). When using the mesoporous silica film electrode, the rather low signal observed for $Fe(CN)_6^{4-}$ oxidation (see curve b in **Fig. 3.2**) is enhanced in the presence of a small amount of $Fc(MeOH)_2$ (0.1 mM) in the medium (see curve c in **Fig. 3.2**). The enhancement varies from dramatic to significant depending on the $Fe(CN)_6^{4-}$ concentration (respectively from 0.5 mM to 5 mM). The amplification of $Fe(CN)_6^{4-}$ oxidation is clearly due to the $Fc(MeOH)_2$ acting as redox mediator according to the **Eq. 3.1**:

$$Fc(MeOH)_2{}^{+} + Fe(CN)_6{}^{4-} \leftrightarrow Fc(MeOH)_2 + Fe(CN)_6{}^{3-} \qquad \textbf{Eq. 3.1}$$

In this reaction scheme, $Fc(MeOH)_2$ molecules that easily diffuse through the mesoporous silica film are oxidized onto the underlying ITO surface, into $Fc(MeOH)_2^+$ species, which can diffuse back through the film, becoming thus available for oxidizing the charge-excluded solution-phase $Fe(CN)_6^{4-}$ species. This explains the signal amplification for $Fe(CN)_6^{4-}$ oxidation. The redox shuttling resembles to that reported for amplified electron transfer at monolayer- or polymer-grafted electrodes,[163,164] being nevertheless conceptually different in the sense that long-range charge shuttling is involved here (film thickness = 100 nm) whereas previously reported amplification was purely based on electron transfer kinetic effects.

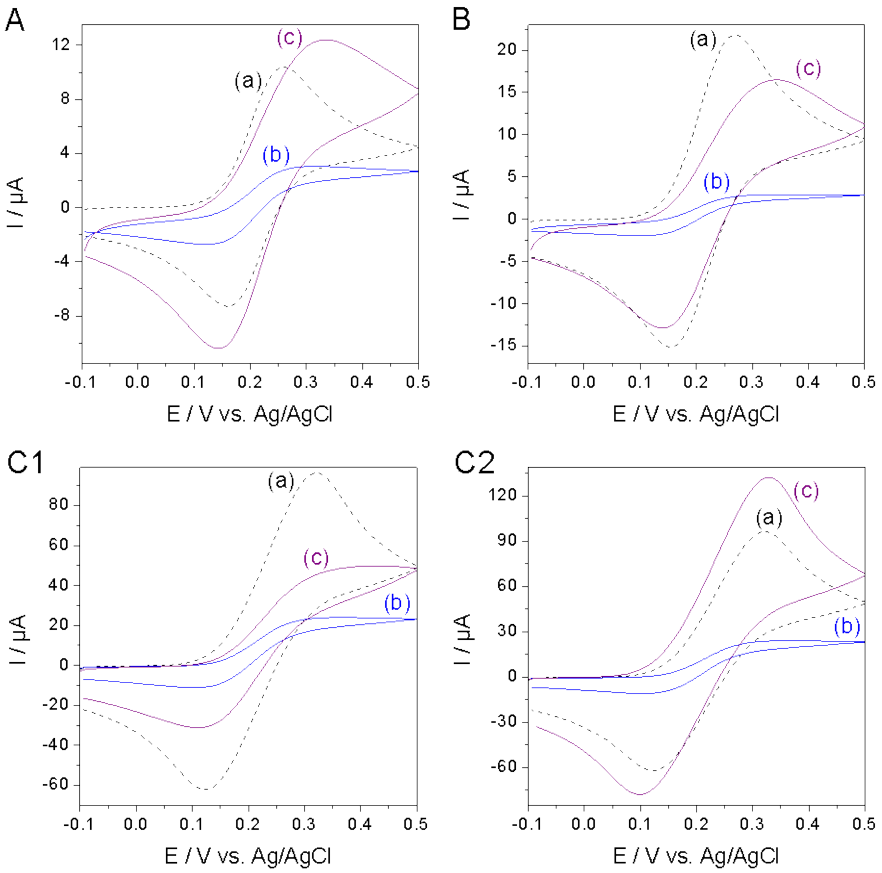

Figure 3.2 Cyclic voltammograms recorded in solutions containing (A) 0.5 mM, (B) 1 mM and (C) 5 mM Fe(CN)$_6^{4}$, using (a) bare ITO and (b-c) ITO electrodes modified with vertically aligned mesoporous silica films, respectively in the absence (b) and presence (c) of 0.1 mM (A-C1) or 1 mM (C2) Fc(MeOH)$_2$ in solution; supporting electrolyte: 0.1 M NaNO$_3$; potential scan rate: 20 mV s^{-1}.

As also shown on **Fig. 3.2**, the effectiveness of the process gradually decreases with increasing the Fe(CN)$_6^{4-}$ concentration. It is maximal at the [Fe(CN)$_6^{4-}$]/[Fc(MeOH)$_2$] (concentration ratio) = 5 (**Fig. 3.2A**) where the voltammetric response obtained at the film electrode (curve c) is almost similar as that of Fe(CN)$_6^{4-}$ on bare ITO (curve a), demonstrating that the mediator contributes to fully restore the electrochemical activity of the anionic probe in these conditions (contrary to restricted response in the absence of mediator, curve b). Note that the even larger peak currents observed at the film electrode (with respect to bare ITO) are due to the “simple” oxidation of Fc(MeOH)$_2$ (i.e., not involved in the mediated reaction [Eq. (1)]), consistent with current values sampled without Fe(CN)$_6^{4-}$ in the medium (**Fig. 3.1B**). Mediated amplification currents are stable upon successive potential cycling (see

Fig. 3.3). However, when using more concentrated $Fe(CN)_6^{4-}$ solutions, for instance corresponding to a concentration ratio $[Fe(CN)_6^{4-}]/[Fc(MeOH)_2]$ = 50 (**Fig. 3.2 C1**), the amplification of $Fe(CN)_6^{4-}$ oxidation is still clearly visible (compare curves b and c) but less overwhelming than for diluted solutions as it does not enable recovering the response at bare ITO (compare curves a and c). Actually, in this case, the rate-determining step becomes the mass transport of mediator species across the mesoporous film (not enough electrogenerated $Fc(MeOH)_2^+$ species to oxidize all $Fe(CN)_6^{4-}$ probes present at the film/solution interface). This limitation can be overcome and electrochemical activity of the anionic probe fully restored by using a more concentrated mediator solution (**Fig. 3.2 C2**, i.e., corresponding to $[Fe(CN)_6^{4-}]/[Fc(MeOH)_2]$ = 5).

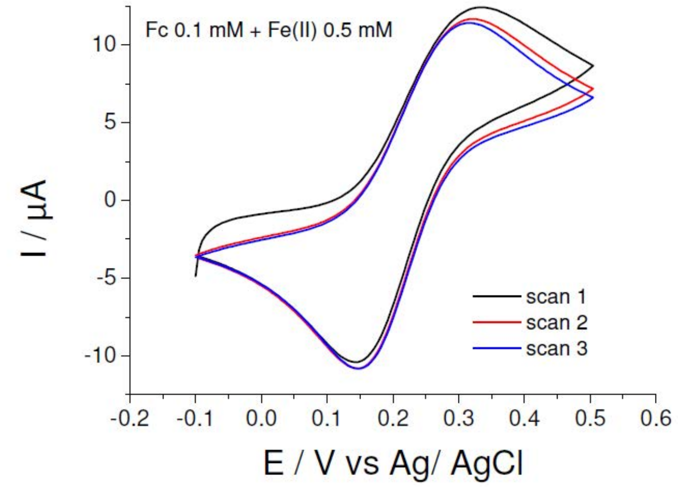

Figure 3.3 Three consecutive cyclic voltammograms recorded in solution containing 0.5 mM $Fe(CN)_6^{4-}$ and 0.1 mM $Fc(MeOH)_2$ using ITO electrodes modified with vertically aligned mesoporous silica films. Potential scan rate: 20 mV s^{-1}.

Even more impressive, the mediated electron shuttling can be also achieved through the non-extracted mesoporous silica films (**Fig. 3.4**). This takes advantage of the possibility for $Fc(MeOH)_2$ to solubilize to some extent into the liquid crystalline phase made by the CTAB template in the mesopore channels and to give rise to a noticeable electrochemical response (see curve a in **Fig. 3.4** or curve b in **Fig. 3.1 B**). The corresponding peak potentials are shifted towards more anodic values (by *ca*. 250 mV) than for bare ITO or surfactant-extracted film electrodes because $Fc(MeOH)_2$ species are stabilized in such hydrophobic environment and the electrogenerated $Fc(MeOH)_2^+$ cations are repelled by the cationic heads of the surfactant.[113] Anyway, these $Fc(MeOH)_2^+$ species can be formed and are likely to diffuse out of the film in order to electrocatalyze the oxidation of solution-phase $Fe(CN)_6^{4-}$ species (according to **Eq. 3.1**), as evidenced by gradual increase in anodic peak currents upon increasing the concentration of $Fe(CN)_6^{4-}$ (see curves b-d in **Fig. 3.4**) whereas only extremely limited non-mediated oxidation of $Fe(CN)_6^{4-}$ can be detected (see insert of **Fig. 3.4**). The extent of interfacial electron shuttling through surfactant-containing films is less than through the extracted mesopores (compare **Figs. 3.2** & **3.4**), as one can understand from slower mass transport processes in the former case (diffusion of ferrocene species into the surfactant phase is slower than in empty mesochannels, as also supported by voltammetric data : peak of curve b in **Fig. 3.4** is less intense than that of curve c in **Fig. 3.2A**)). One can also notice from **Fig. 3.4** a small decrease in the overpotential for $Fc(MeOH)_2$ oxidation in the presence of $Fe(CN)_6^{4-}$ (anodic peak shifting from 0.50 V to 0.48 V), confirming the role of the electrocatalytic reaction (**Eq. 3.1**).

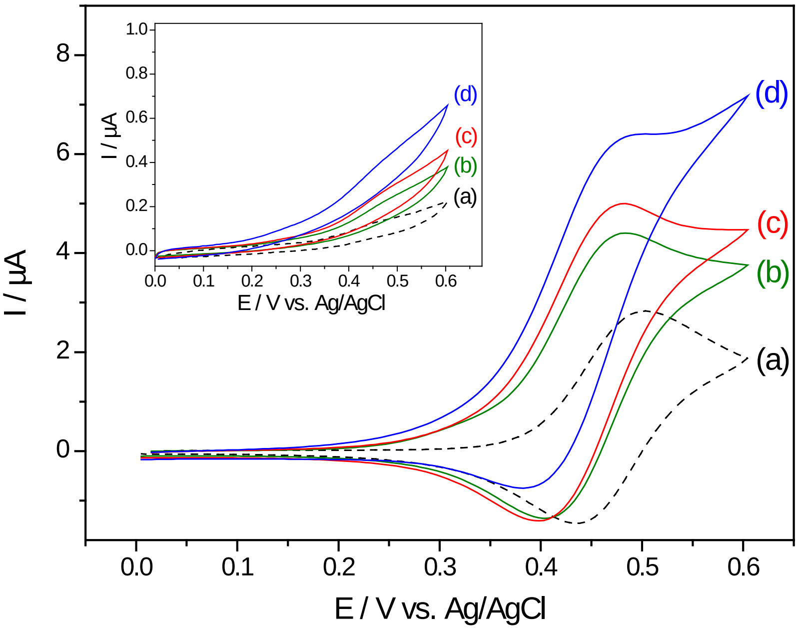

Figure 3.4 Cyclic voltammograms recorded in solutions containing 0.1 mM $Fc(MeOH)_2$, (a) alone, (b-d) with increasing concentrations of $Fe(CN)_6^{4-}$ ((b) 0.5 mM, (c) 1 mM and (d) 5 mM), using ITO electrodes modified with vertically aligned mesoporous silica films before surfactant extraction; supporting electrolyte: 0.1 M $NaNO_3$; potential scan rate: 20 mV s^{-1}. The insert shows the corresponding data without $Fc(MeOH)_2$ in solution.

3.2.3 Factors affecting the mediated amplification of $Fe(CN)_6^{3-/4-}$ charge transfer reactions

3.2.3.1 Preliminary remark on the effect of supporting electrolyte concentration

Before discussing the main factors affecting the amplification of $Fe(CN)_6^{4-}$ oxidation by $Fc(MeOH)_2$ mediator, one needs to remember that the ionic strength of the medium strongly affects the electrochemical response of anions at mesoporous silica film modified electrodes.[105,153] As shown in **Fig. 3.5**, the response of $Fe(CN)_6^{4-}$ is dramatically lowered by decreasing the electrolyte concentration, changing from well-defined peaks at 300 mM $NaNO_3$, to waves of less intense currents for concentrations 3-30 mM, and vanishing almost totally at 1 mM $NaNO_3$, although no significant modification is observed using bare ITO (only the effect of solution conductivity variations leading to somewhat less intense and more separated peaks, as shown in insert of **Fig. 3.5**).

As already briefly mentioned above (**Figs. 3.1 E&F**), this is due to electrostatic repulsion effects induced by the mesoporous silica film containing negative charges (silanolate groups) onto its mesopore walls. These charges are compensated by counter-ions from the electrolyte, forming an electrical double layer.

The thickness of such double layer is known to be dependent on electrolyte concentration and can be estimated from the Debye-Hückel length (i.e., respectively 10 nm, 3 nm, 1 nm and 0.3 nm for electrolyte concentrations of 1 mM, 10 mM, 100 mM and 1 M).[165] As a result, it is necessary to use rather concentrated electrolyte solutions (more than 10 mM) to avoid overlap of the electrical double layer in the mesopores (2-3 nm in diameter). This explains why almost no signal for direct oxidation of $Fe(CN)_6^{4-}$ is observed in 1 mM $NaNO_3$ (see curve a in **Fig. 3.5**). More quantitative analysis of the data (e.g., using Nernst-Planck or Poisson-Nernst-Planck equation) is prevented because one cannot accurately estimate the surface charge density and therefore the electric field in mesopore channels. Similar restrictions in low ionic strength media have been also reported for redox cations at electrodes covered with mesoporous silica films grafted with positively-charged groups.[117] Such conditions of low electrolyte concentrations, which induce the most drastic restrictions for direct oxidation of $Fe(CN)_6^{4-}$, are actually the best ones for investigating the mediated long-range charge transfer reactions as they would lead to the most clearly visible amplification processes. The following experiments will be thus performed in 1 mM $NaNO_3$. This also makes sense considering the poor chemical stability of amorphous silica in high ionic strength media, in particular when containing alkaline or alkaline-earth cations.[166–168]

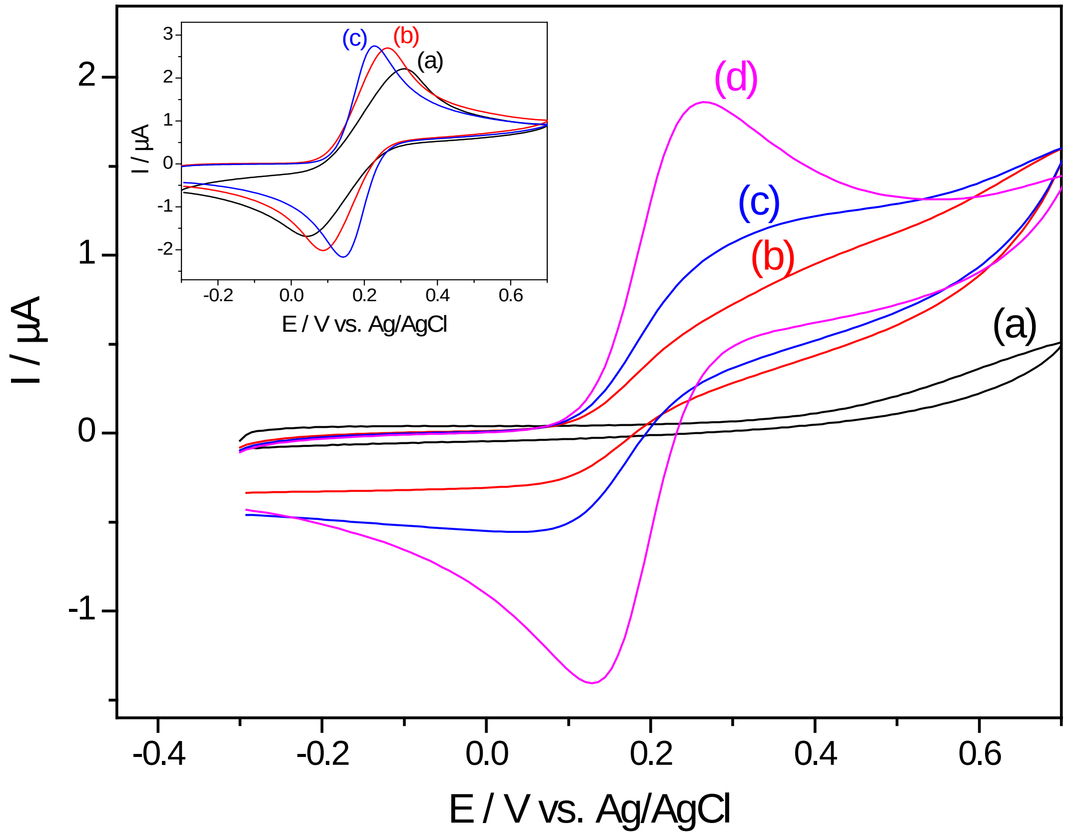

Figure 3.5 Cyclic voltammograms recorded using ITO electrodes modified with vertically aligned mesoporous silica films (after surfactant extraction), in solutions containing 0.1 mM $Fe(CN)_6^{4-}$ with increasing concentrations of supporting electrolyte: (a) 1 mM, (b) 3 mM, (c) 30 mM and (d) 300 mM $NaNO_3$; potential scan rate: 20 mV s^{-1}. The insert shows the corresponding data at bare ITO.

3.2.3.2 Effect of mediator concentration

Fig. 3.6 shows voltammetric responses obtained for 0.1 mM (**Fig. 3.6 A**) or 1.0 mM $Fe(CN)_6^{4-}$ (**Fig. 3.6 B**) and 0 to 100 µM $Fc(MeOH)_2$. In both cases, the mediated electron transfer is clearly observed, starting at $Fc(MeOH)_2$ concentrations above 1 µM and gradually increasing with the mediator content from 3 to 100 µM. The increase is slightly faster for 0.1 mM $Fe(CN)_6^{4-}$ (**Fig. 3.6 A**) than for 1.0 mM $Fe(CN)_6^{4-}$ (**Fig. 3.6 B**), as expected from the lower amounts of mediator species required to catalyze smaller amount of anionic probes at the film/solution interface.

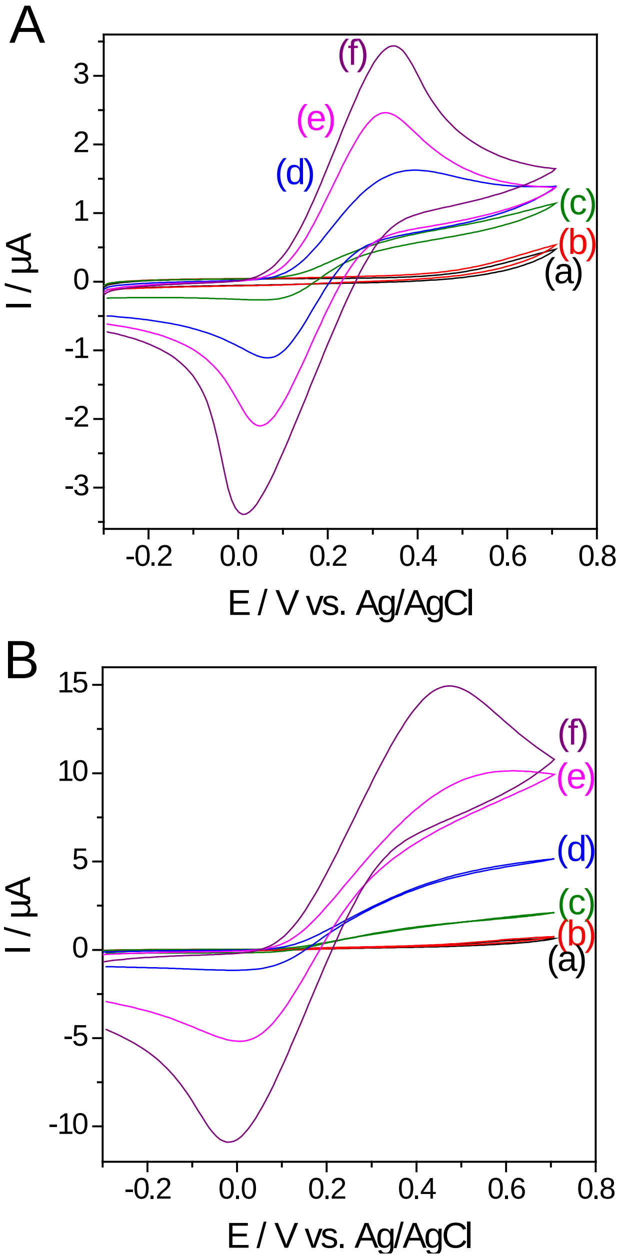

Figure 3.6 Cyclic voltammograms recorded in solutions containing (A) 0.1 mM and (B) 1 mM $Fe(CN)_6^{4-}$, using ITO electrodes modified with vertically aligned mesoporous silica films (after surfactant extraction), respectively in the absence (a) and presence (b-f) of increasing concentrations of $Fc(MeOH)_2$ in solution: (b) 1 µM, (c) 3 µM, (d) 10 µM, (e) 30 µM and (f) 100 µM; supporting electrolyte: 1 mM $NaNO_3$; potential scan rate: 20 mV s^{-1}.

The curves are wave-shaped at low $Fc(MeOH)_2$ concentrations, which indicates kinetically limited phenomena (not enough mediator to oxidize all $Fe(CN)_6^{4-}$ species present at the interface), but they turns to peak-shaped current responses in more concentrated mediator solutions, suggesting diffusion-controlled processes ($Fe(CN)_6^{4-}$ depletion at larger concentration of $Fc(MeOH)_2$). For a fixed concentration of 100 µM $Fc(MeOH)_2$ in solution, the voltammetric peak currents increase with the $Fe(CN)_6^{4-}$ content (see curves c in **Fig. 3.2**) but it is not directly proportional to the concentration (*i.e.*, anodic peak currents of 12.4, 16.5 & 49.8 µA, respectively for $Fe(CN)_6^{4-}$ concentrations of 0.5, 1.0 & 5.0 mM). This is consistent with the diffusion-limited mechanism suggested above, as a simple bimolecular mediation process would have resulted in a linear relationship.[164] One can also notice from the voltammetric data in **Fig. 3.6** that, once signals become peak-shaped (*i.e.*, at sufficiently high mediator concentration), the mediated redox process is likely to operate in both oxidation and reduction modes, thanks to the close proximity of standard potentials of redox systems ($Fc(MeOH)_2^{+/0}$ and $Fe(CN)_6^{3-/4-}$). For instance, the well-defined and intense reduction peaks for back conversion of $Fe(CN)_6^{3-}$ into $Fe(CN)_6^{4-}$ are indicative of successful mediated amplification in reduction using $Fc(MeOH)_2$ (as the direct reduction of $Fe(CN)_6^{3-}$ is not possible, see curve c in **Fig. 3.1 F**).

3.2.3.3 Effect of potential scan rate

Fig. 3.7 shows the evolution of cyclic voltammograms with potential scan rate for film electrodes in solutions containing 0.1 mM $Fc(MeOH)_2$ and $Fe(CN)_6^{4-}$ at two different concentrations (0.1 mM, **Fig. 3.7 A**, and 1 mM, **Fig. 3.7 B**). Due to the low electrolyte concentration (1 mM), significant shifts in anodic and cathodic peak potentials (respectively in positive and negative directions) are evidenced as a result of limited conductivity of the medium. In both cases, and consistent with above discussions, mediated oxidation of $Fe(CN)_6^{4-}$ and reduction of $Fe(CN)_6^{3-}$ based on the $Fc(MeOH)_2$ redox shuttle are observed. However, the effectiveness of the mediated reaction seems to decrease more rapidly with potential scan rate for the more concentrated $Fe(CN)_6^{4-}$ solution, in agreement with the above observations indicating more restrictive kinetic limitations in this case (not enough mediator to oxidize all $Fe(CN)_6^{4-}$ species at the interface).

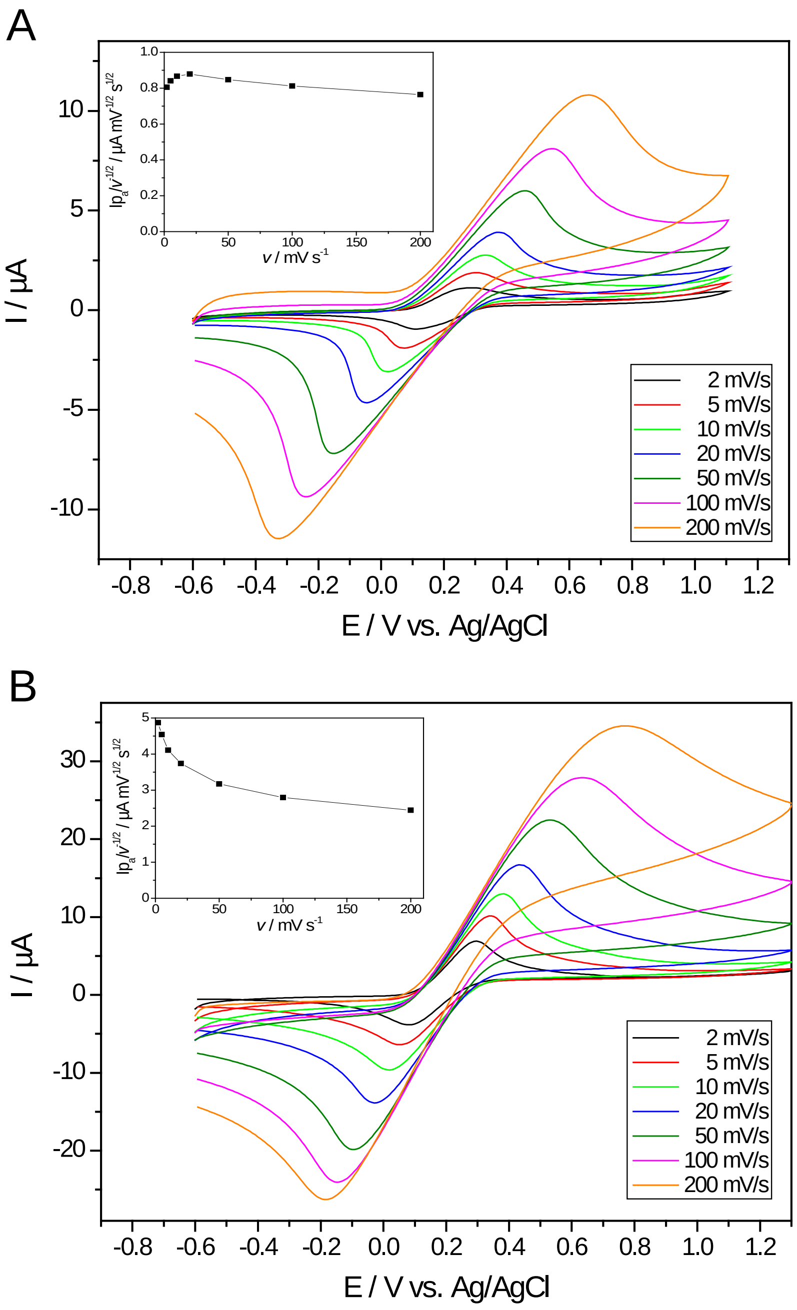

Figure 3.7 Cyclic voltammograms recorded in solutions containing (A) 0.1 mM and (B) 1 mM $Fe(CN)_6^{4-}$, in the presence of 0.1 mM $Fc(MeOH)_2$, using ITO electrodes modified with vertically aligned mesoporous silica films (after surfactant extraction), at various potential scan rates: 2, 5, 10, 20, 50, 100 and 200 mV s^{-1}; supporting electrolyte: 1 mM $NaNO_3$. The inserts show the variations of the ratio “anodic peak currents divided by the square root of potential scan rates” ($Ip_a/v^{1/2}$) with the potential scan rate (v).

Actually, the shape of the plot of the sweep-rate normalized current ($i_p/v^{1/2}$) *vs.* sweep rate (see inserts in **Fig. 3.7**) is typical of a regeneration mechanism (variation of the EC mechanism). The peak current function for this reaction is large at low scan rates and decreases to a constant value at higher scan rates. This is consistent with the diffusion-limited mediated reaction investigated here, for which optimal amplification efficiency is obtained at not too high $Fe(CN)_6^{4-}/Fc(MeOH)_2$ concentration ratios and quite large timescale of the experiments.

3.2.4 Extension to another system: enhanced $Fe(CN)_6^{3-}$ reduction using $Ru(NH_3)_6^{3+}$ as mediator

To point out the general aspect of long-range charge transfer by mediator shuttling through such mesoporous silica film modified electrodes, another system has been investigated. Typical results are shown in **Fig. 3.8** for mediated reduction of $Fe(CN)_6^{3-}$ by the $Ru(NH_3)_6^{3+/2+}$ redox system. In the absence of mediator, $Fe(CN)_6^{3-}$ cannot be directly reduced at the film electrode because of electrostatic repulsion while it gives a well-defined reversible signal on bare ITO with a midpoint potential E_{mid} = 0.20 V (see insert at the right bottom of **Fig. 3.8**). In the presence of 0.1 mM $Ru(NH_3)_6^{3+}$ in the medium (which is likely to be reduced into $Ru(NH_3)_6^{2+}$ with E_{mid} = -0.14 V at the silica film electrode, see **Fig. 3.1A**), the addition of increasing concentrations of $Fe(CN)_6^{3-}$ species in solution results in gradually increasing peak currents in the potential region corresponding to the $Ru(NH_3)_6^{3+/2+}$ redox system (**Fig. 3.8**). This is explained by the mediated reduction of $Fe(CN)_6^{3-}$ by the electrogenerated $Ru(NH_3)_6^{2+}$ species according to **Eq. 3.2**:

$$Ru(NH_3)_6{}^{2+} + Fe(CN)_6{}^{3-} \rightarrow Ru(NH_3)_6{}^{3+} + Fe(CN)_6{}^{4-} \qquad \textbf{Eq. 3.2}$$

This is made possible by the fact that the cationic mediator diffuses easily through the mesoporous silica film and can act as effective electron shuttle to reduce the solution-phase $Fe(CN)_6^{3-}$ species at the film/solution interface. **Eq. 3.2** is also consistent with the respective location of standard potentials of the two redox systems (no possibility for anodic mediation in this case).

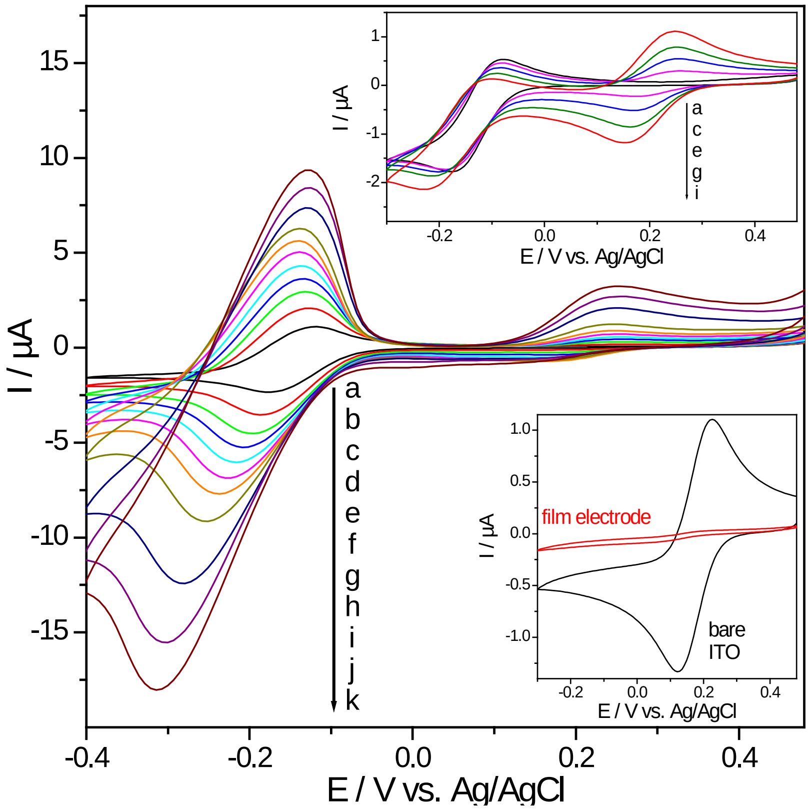

Figure 3.8 Cyclic voltammograms recorded at ITO electrodes modified with vertically aligned mesoporous silica films (after surfactant extraction) in solutions containing 0.1 mM $Ru(NH_3)_6^{3+}$ alone (a) and with increasing concentrations of $Fe(CN)_6^{3-}$: 0.02 mM (b); 0.04 mM (c); 0.06 mM (d); 0.08 mM (e); 0.1 mM (f); 0.13 mM (g); 0.16 mM (h); 0.2 mM (i); 0.25 mM (j); 0.3 mM (k). The upper insert shows some corresponding data (a, c, e, g, i) recorded at bare ITO electrode; supporting electrolyte: 10 mM $NaNO_3$; potential scan rate: 20 mV s^{-1}. The lower right insert shows cyclic voltammograms for 0.1 mM $Fe(CN)_6^{3-}$ alone at bare ITO and mesoporous silica film electrode.

The mediated amplified currents are stable upon successive cycling, yet with some intensity increase (see **Fig. 3.9**) resulting from the accumulation of the positively-charged $Ru(NH_3)_6^{3+}$ mediator on the negatively-charged silica surface,[32] which was not the case for neutral $Fc(MeOH)_2$ mediator. For the same reason of accumulation, studying the reduction of $Fe(CN)_6^{3-}$ with respect to increasing concentrations of $Ru(NH_3)_6^{3+}$ does not appear to be really relevant (as accumulation is concentration-dependent, the amount of mediator in the film would vary from one experiment to another one), but it was still possible to evidence the mediated enhancement (see **Fig. 3.10**), yet less important than for the $Fe(CN)_6^{4-}$/$Fc(MeOH)_2$ system (**Fig. 3.6**). The mediated reaction is only possible since the direct electrochemical reduction of $Fe(CN)_6^{3-}$ species is prevented due to the electrostatic barrier induced by the silica film blocking their access to the underlying ITO surface.

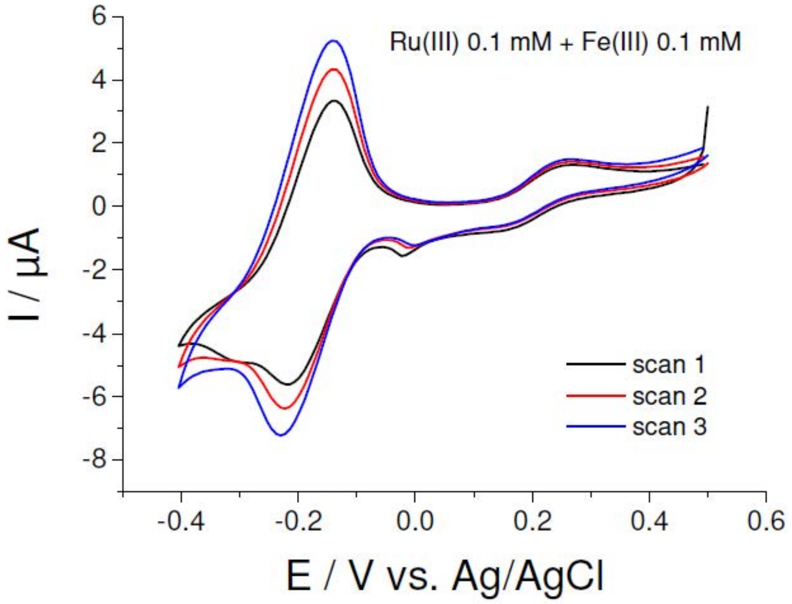

Figure 3.9 Three consecutive cyclic voltammograms recorded in solution containing 0.1 mM $Fe(CN)_6^{3-}$ and 0.1 mM $Ru(NH_3)_6^{3+}$ (in 10 mM $NaNO_3$) using ITO electrodes modified with vertically aligned mesoporous silica films. Potential scan rate: 20 mV s^{-1}.

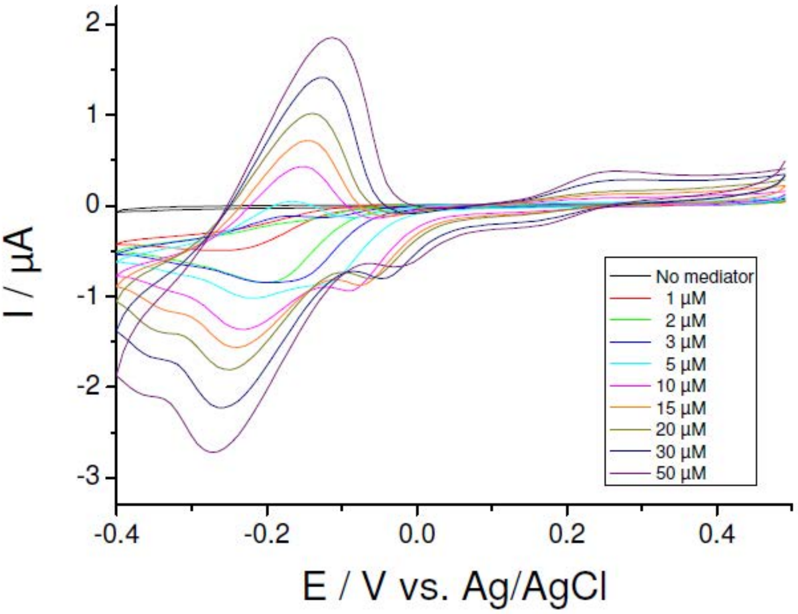

Figure 3.10 Cyclic voltammograms recorded on ITO electrode modified with a mesoporous silica film in a solution containing 5 µM $Fe(CN)_6^{3-}$ (in 1 mM $NaNO_3$) to which increasing concentrations of $Ru(NH_3)_6^{3+}$ have been added (from 1 µM to 50 µM). Potential scan rate: 20 mV s^{-1}.

As shown by the control experiment on bare ITO (see insert at the top right of **Fig. 3.8**), where the $Fe(CN)_6^{3-/4-}$ redox system undergoes its classical one-electron exchange, the addition of increasing concentrations of $Fe(CN)_6^{3-}$ species in solution results in gradually increasing peak currents only in the potential region corresponding to the $Fe(CN)_6^{3-/4-}$ couple, without affecting the response of the $Ru(NH_3)_6^{3+/2+}$ redox system.

3.3 Conclusions

Vertically-aligned mesoporous silica films on ITO electrodes are highly permeable to cationic and neutral redox probes while rejecting the anionic ones, especially at low ionic strength. Here we have shown that the electrochemical response of negatively charged redox probes such as $Fe(CN)_6^{4-}$ and $Fe(CN)_6^{3-}$ can be dramatically amplified at such nanostructured electrodes using neutral or cationic mediators ($Fc(MeOH)_2$ or $Ru(NH_3)_6^{3+}$). Thanks to their fast transport through the mesochannels, they act as effective electron shuttles between the underlying ITO electrode surface and $Fe(CN)_6^{4-}$ or $Fe(CN)_6^{3-}$ species blocked at the film/solution interface. The mediated long-range charge transfer reactions through such isolating porous membrane are affected by several parameters such as the relative concentrations of the redox probe species and the mediator, or the potential scan rate. The most effective amplification is achieved in conditions of not too high probe/mediator concentration ratios and not to fast scan rates, in order to enable the generation of enough mediator species that are likely to reach the film/solution interface (where the mediated reaction takes place) in the timescale of the experiment. This work also shows that permselective properties of mesoporous silica film electrodes can be modulated by using a suitable redox mediator. Associated to selective amplification of the electrode response, this feature is likely to open new perspectives in the field of electroanalysis, for instance.

Chapter IV

Indirect Amperometric Detection of non-Redox Ions Using a Ferrocene Functionalized and Oriented Mesoporous Silica Thin Film Electrode

4.1 Introduction

Potentiometry at ion-selective electrodes constitutes a well-established and efficient way of determining ionic species,[169,170] with applications notably in the field of clinical diagnostics[171] or environmental analysis.[172] However, the method highlights weak variations of concentration, because of their logarithmic response to the concentration, so that efforts have been made in the past to develop amperometric detection for non-redox ions.

The most generic approach is the electrochemistry at liquid-liquid interfaces, exploiting the fact that techniques commonly used for the measurement of electron transfer at solid electrode surfaces could be applied to study transfer processes through the interface between two immiscible electrolyte solutions.[173] This led to develop numerous amperometric ion sensors for inorganic, organic and biological ions.[174,175] In addition to liquid-liquid interfaces, such ion transfer voltammetry can be also applied to membrane or gel electrodes.[176,177]

The indirect amperometric detection of non-redox ions based on ion-to-electron transduction mechanisms constitutes another emphasized alternative to potentiometry at ion-selective electrodes[169,178,179], which have been notably applied after separation of ionic analytes by electrophoresis or liquid chromatography.[178,179] This can be achieved using electrodes modified with electroactive conducting polymers[178,180–186] or inorganic thin films,[187–189] for which the incorporation of ionic species is needed to counterbalance the electric charges generated by the electron transfer reactions. Examples are available for anions detection at oxidizable polymers such as polypyrrole,[180–183] polyaniline[178] or poly(o-phenylenediamine)[184] modified electrodes, and for cations detection using reducible polypyrrole-dodecylsulfate,[185] polydiphenylamine-dodecylsulfate,[186] metal hexacyanoferrates[187,188] or mixed-valent ruthenium iron cyanide[189] composite films. Linear and reproducible responses can be obtained in the best cases,[181] but sensitivity decrease upon successive analyses has been also reported,[183] possibly due to selectivity changes in relation with structural variations during the doping–undoping process.[190] Another approach relies on the use of electrodes modified with non-conductive ion-exchange materials (organic polymers[191] or inorganic zeolites[192–195]) filled with redox-active species. In this case, the electron transfer mechanism involves the exchange of the redox- active cations (or anions) by electrolyte cations (or anions) and the current response is directly related to the amount of exchanged mediators. In conditions of diffusion-controlled ion exchange processes, the recorded current signals can be proportional to the concentration of electroinactive ions in solution[191–195]. However, the progressive consumption of mediators from the material requires a chemical regeneration step (i.e. re-loading redox-active species) between each measurement to avoid sensitivity decrease.[193]

Electrodes modified with organic redox polymers constitute another category of electrochemical systems involving both electron transfer reactions and associated ion transport phenomena to maintain charge balance.[196–198] One can distinguish two kinds of such polymers depending on whether the redox moieties are immobilized either via weak or strong chemical bonds. The former family includes ion-exchange polymers incorporating redox ions that undergo charge transfer reactions according to two possible mechanisms, i.e., electron hopping between adjacent species or via molecular diffusion, or a combination of both, depending on the experimental conditions.[199–203] The second category consists in polymers to which the redox moieties have been covalently attached (resulting in intrinsically more durable immobilization), for which the electron transfer reactions involve electron hopping between redox centers with concomitant transport of electrolyte counterions for keeping electroneutrality.[204–209] Charge propagation is usually dominated by electron transport in such redox polymers,[207,209,210] except at very low ionic strengths where ion transport might become the rate-determining step.[208,209] Note that their electrochemical response can suffer from variations in case of prolonged use due to structural changes (e.g., segmental between polymer chains,[211] with mixed electron hopping and bounded diffusion during charge transport[212]). Such drawback can be circumvented to some extent by stiffening of the polymer structure (e.g., by cross-linking[213] or from designing block copolymer membranes with pendent redox moieties[212]), or by using mesoporous inorganic-organic hybrid materials which offer the advantage of a regular and rigid inorganic backbone ensuring good mechanical stability with the possibility to attach covalently electroactive functional groups on their internal mesopore walls.[112,116,118,123,125,214–216]

Ferrocene functionalized mesoporous silica films (prepared by a method described **in Section 1.3 and 2.3**) consisting of perpendicular pore channels, demonstrates an electrochemical response, occurring via an electron hopping mechanism, which is strongly influenced by the nature and concentration of the supporting electrolyte, as well as the ferrocene content in the material.[123] In this Chapter, we would like to exploit this behavior in which ferrocene oxidation into ferricinium cation requires the ingress of anions from the solution to maintain charge balance (see right part in **Scheme 4.1**), to investigate the indirect amperometric detection of electroinactive anions. The experiments will be performed by flow injection analysis using an electrolyte-free flowing stream, first by amperometry at constant potential and then in a square wave mode in order to regenerate the ferrocene moieties. The method will be also tested for the indirect amperometric detection of non-redox anions subsequent to chromatographic separation.

4.2 Experimental

4.2.1 Preparation of the mesoporous films

The ferrocene-functionalized silica films have been prepared on ITO electrode by combining the electro-assisted self-assembly (EASA) and co-condensation methods driven to form vertically-aligned mesoporous films, with click chemistry as described in **Section 2.3.2** and **2.3.3**.

It has been previously studied[123] and discussed in **Section 1.3.3** that the maximum ferrocene content able to be grafted into the mesochannels is 40%, yet at this level fast electron transfer within the very confined pores are not fully compensated by the diffusion-limited compensating anion ingress. Hence, for this Chapter we have chosen to work with 30% ferrocene functionalized silica films.

4.2.2 Indirect amperometric detection experiments

Flow injection analysis (FIA) of non-redox anions was made in either constant amperometry mode (optimized applied potential: +0.5 V) or by differential pulse (ΔE = 500-700 mV, frequency range = 0.4-10 Hz). In a conventional experiment, only based on the flow-injection cell as set-up (see **Scheme 4.1**), the continuous carrier solution is deionized water and an aliquot of electrolyte sample containing the desired anion is injected. The anion samples (concentration typically in the range of 10^{-5}-10^{-3} M) are injected through a 150 µL valve into the carrier solution which is pumped at an optimized rate of 1 mL/min (from 0.5-2 mL/min range). For analysis of several anions in mixture, the flow cell was mounted at the output of an ion chromatography system equipped with a suppressor and a conductivity detector (used for comparison purposes) and detection was made by differential pulse amperometry in conditions as above.

4.2.3 Apparatus

Flow injection amperometry (FIA) experiments involved the use of a flow-through cell (an electrochemical detection flow cell from BASi) operating mostly in a two-electrode configuration (ferrocene-functionalized silica film on ITO as working electrode and the stainless steel auxiliary electrode body also used as pseudo-reference, by replacing the reference electrode usually used in the BASi device by a stopper, **Scheme 4.1**) connected to a potentiostat. As also shown on **Scheme 4.1**, the ITO modified electrode was placed between the gasket defining the cell volume and the original electrode body (acting here just to secure the position of the working electrode; electrical contact provided by a Cu wire). The electrochemical cell was connected to either a FIA system (in which the high-purity water carrier was maintained at a constant flow rate of 1.0 mL min^{-1} by a peristaltic pump) or to the outlet of an ion chromatography apparatus.

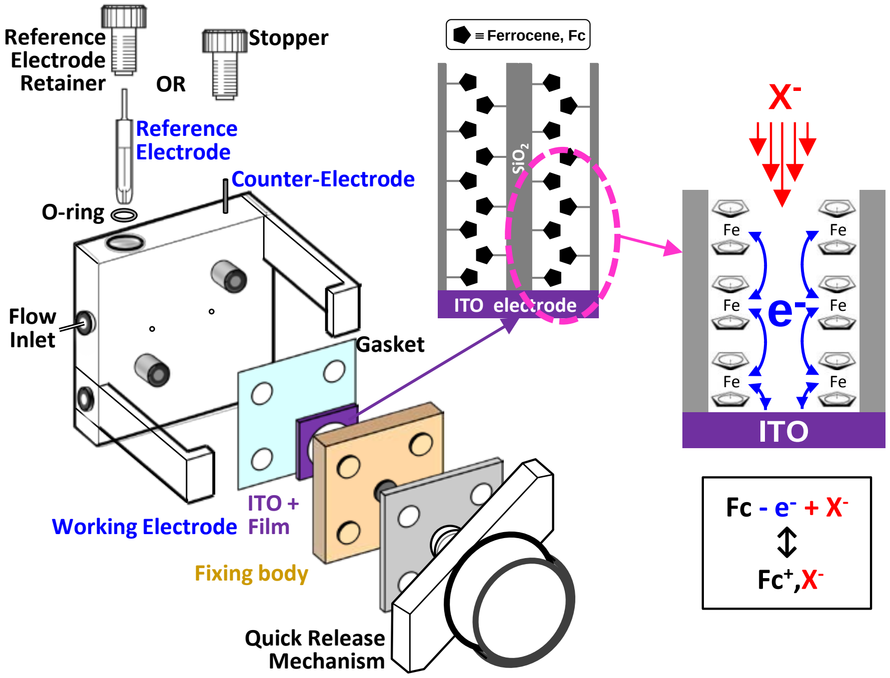

Scheme 4.1 Exploded view of the electrochemical flow cell (operating either with a reference electrode or using simply a stopper when working in a two-electrode configuration, with a schematic representation of the vertically-oriented, ferrocene-functionalized, mesoporous silica film on ITO electrode and, on the right a description of the electron transfer mechanism involving the ingress of the electrolyte anion (X^-) upon ferrocene oxidation into ferricinium ion.

Ion chromatography experiments were carried out using an apparatus described in **Section 2.2.4** with a mobile phase consisted of a mixture of 3.2 mM Na_2CO_3 and 1 mM $NaHCO_3$ in ultrapure water. The flow rate was 0.7 mL min^{-1} and the sample loop volume was 20 µL. Standard solutions were prepared from a commercial multi-element standard solution of 1000µg/mL of F^-, NO_3^-, Br^-, Cl^-, SO_4^{2-} and PO_4^{3-}.

4.3 Results and discussion

4.3.1 Practical considerations

In order to optimize the experiments, there are several practical considerations to be taken into account to avoid problems such as leakage, detection noise and cell resistance due to bubbles accumulation. Leakage through the compartment between the gasket and the ITO working electrode is prevented by flat fixation of the ITO plate in the system (hence, the position of Cu wire connection and the adhesive tape should be out of the tightening area shown in **Figs. 4.1 A** and **B**).

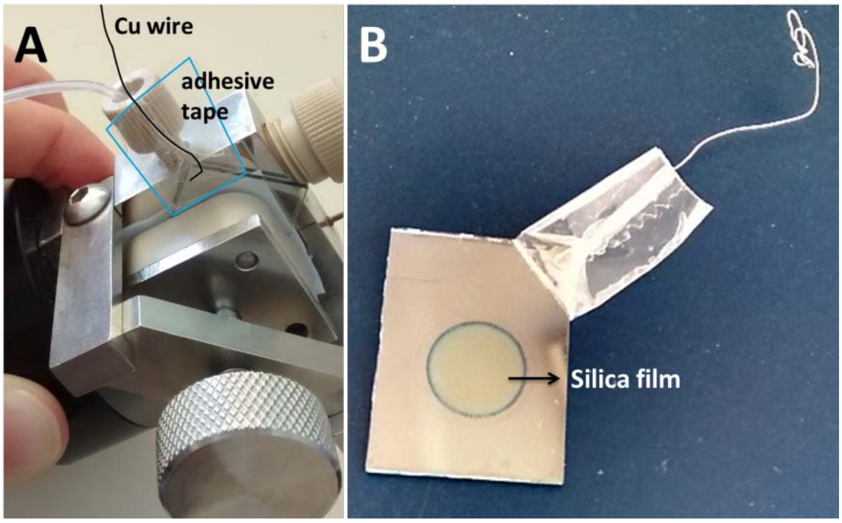

Figure 4.1 Working electrode positioning for fluid leakage prevention in the electrochemical flow cell (A) and top view of the Cu wire connection position on the ITO working electrode.

The presence of bubbles in the system creates resistance and so a decrease of current signals. Moreover, in the flow system, it produces also significant noise in the measurements. Several experimental conditions need to be conducted for bubbles formation prevention;

- Degassing of the water supply prior its supply into the flow system
- Flushing the flow system (tubes and flow cell) with ethanol to clean any dust or remaining salt before flowing the water
- Bubble-free injection sample and syringe

4.3.2 Preliminary observations and amperometric detection at constant potential

The electrochemistry of ferrocene-functionalized and vertically-aligned mesoporous silica films on ITO electrodes is known from our previous investigation.[123] Here, we have just checked how the cell geometry and/or configuration would affect the electrochemical behavior. **Fig. 4.2 A** shows that passing from a conventional batch electrochemical cell to the thin-layer flow cell (used without flow for this particular cyclic voltammetric study), both equipped with a real reference electrode, does not really affect the voltammetric response of the film (yet with some noticeable resistance increase). Nevertheless, as one intends to work in an electrolyte-free flow for FIA experiments later on, it is preferable to operate in a two-electrode configuration (using the auxiliary electrode as pseudo-reference) to avoid problems related to the presence of a resistive medium (i.e., deionized water) in the microchannel existing between the reference electrode and the thin layer cell in the BASi device. **Fig. 4.2 B** shows that it is indeed possible, yet with some distortion in the voltammetric signal, probably due to the poor features of the pseudo-reference (stainless steel) electrode.

As illustrated in the right part of **Scheme 4.1**, the redox transformation of ferrocene groups into ferricinium moieties operates by electron hopping, which is associated to the ingress of an anion from the electrolyte solution into the functionalized mesochannels (see **Eq. 4.1**)

$$\text{Fc} - 1\,e^- + X^-_{(sol)} \Leftrightarrow \text{Fc}^+, X^-_{(film)} \qquad \textbf{Eq. 4.1}$$

(with Fc = ferrocene; X^- = anion; sol = solution; Fc^+ = ferricinium ion)

As a consequence, if decreasing the electrolyte (and thus anion) concentration, this charge neutralization becomes rate-determining and peak currents decrease (see insert in **Fig. 4.2 B**). In such two-electrode configuration, the voltammetric peaks are however not defined well enough to evaluate clearly the corresponding E1/2 values and their shifts with respect to the electrolyte concentration (which is common for redox polymers involving counterions in the cycling of the redox centers to maintain electroneutrality).[202,208,209,217,218] Nevertheless, to demonstrate that counterions are also really involved in the cycling of ferrocene moieties in the silica film, we have made additional experiments with using the classical three-electrode batch electrochemical cell. The results indicate a positive shift in E1/2 values when decreasing the $NaNO_3$ concentration (i.e., from 0.35 V to 0.42 V when passing from 0.5 M to 10^{-2} M $NaNO_3$), proving that the oxidation/reduction of Fc is effectively associated to entrance/release of counter anions. Note that, compared to classical redox polymers, the permselective properties of mesoporous silica films are even more complicated by additional Donnan exclusion effects, as a result of the negatively-charged mesopore walls inducing charge selectivity behavior.[101] These effects and are also dependent on the electrolyte concentration[117,219] and they can be tuned notably by appropriate functionalization.[156]

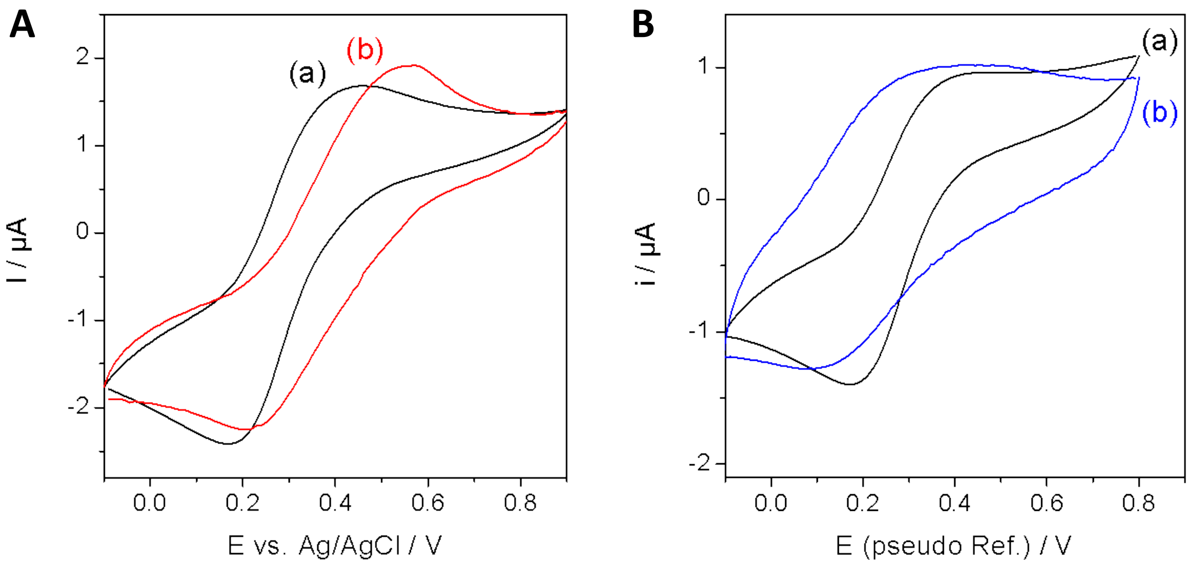

Figure 4.2 Cyclic voltammograms recorded in a conventional batch electrochemical cell (a) or in the thin layer flow cell (b, without flow), using the ferrocene-functionalized mesoporous silica film modified electrode, in a three-electrode (A) or two-electrode configuration (B); i.e. using the counter electrode as pseudo-reference; supporting electrolyte: 0.1 M $NaNO_3$; potential scan rate: 20 mV s^{-1}. The insert in part B represents the curve "b" recorded in various $NaNO_3$ concentrations: 0.1 M (b_1), 0.01 M (b_2) and 0.001 M (b_3).

Optimization of amperometric detection parameters, such as flow rate and applied potential difference, were determined using bare ITO electrode as working electrode, 0.1 M $NaNO_3$ solution as flowing mobile phase, and five consecutive injections of 1 mM ferrocene dimethanol ($FcMeOH_2$) solution. From these results, 1 mL/min was used as the optimized mobile phase flow rate and a minimum applied potential of 0.5 V was expected to obtain reasonable peak current signals.

Table 4.1 Optimization of (a) mobile phase flow rate and (b) applied constant potential of the amperometric detection. Mobile phase: 0.1 M $NaNO_3$; Injected solution: 1 mM $FcMeOH_2$.

(a) Flow rate optimization

E (V)	Flow rate (mL/min)	Average Peak Current (µA)
0.5	0.25	1.61
	0.5	2.24
	0.75	2.52
	1	**3.33**
	1.5	2.85
	2	2.16

(b) Applied potential optimization

Flow rate (mL/min)	E (V)	Average Peak Current (µA)
1	0.25	0
	0.3	1.46
	0.4	2.30
	0.5	**3.33**
	0.6	**3.55**
	0.7	**3.57**
	0.8	**3.40**
	0.9	**3.50**
	1	**3.47**

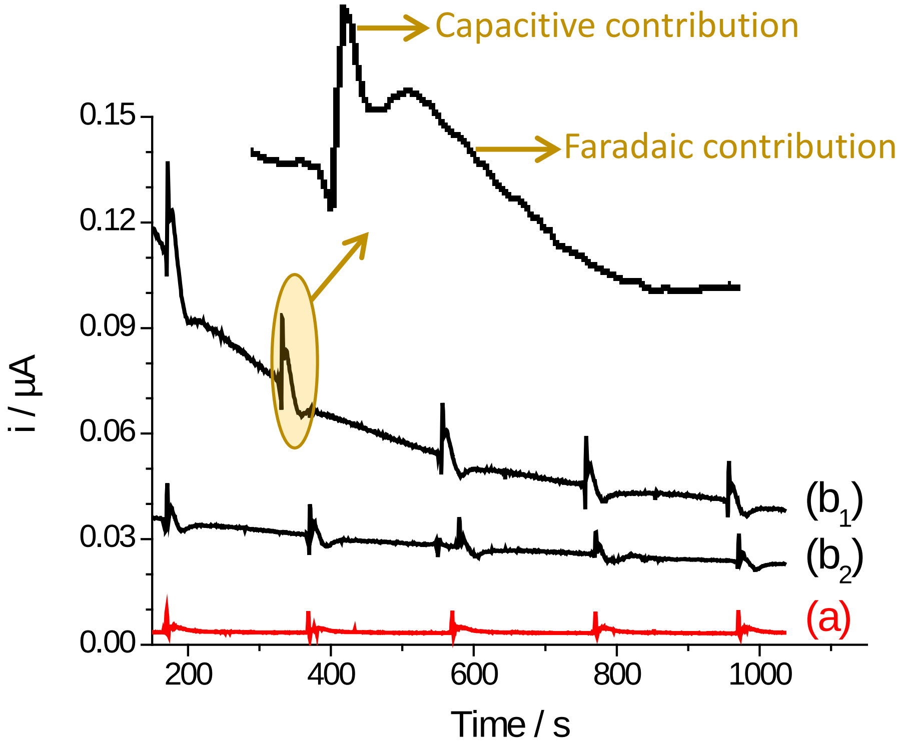

Figure 4.3 Typical amperometric curves recorded at unmodified ITO (a) or at the ferrocene-functionalized mesoporous silica film modified electrode (b) for five successive injections of 0.1 mM $NaNO_3$ in an electrolyte-free water flow (flow rate: 1 mL min^{-1}); flow cell with two-electrode configuration; applied potential: +0.5 V. For the modified electrode (b), the first experiment (b_1) was followed by a second series of measurements without regeneration (b_2).

The above characteristic is at the basis of the amperometric detection of non-redox anions at the ferrocene-functionalized film. If applying a positive potential to the electrode when operating in an electrolyte-free flow, no current could be generated as the medium is too resistive and no anion is available for charge compensation upon ferrocene oxidation. On the other hand, each time an aliquot of electrolyte (i.e., $NaNO_3$) is injected into the cell; it generates a significant current response due to ferrocene oxidation with concomitant charge balance by the electrolyte anion (**Fig. 4.3**). The shape of the current response (see insert in **Fig. 4.3**) reveals the presence of two contributions, a first sharp capacitive part associated to the change in conductivity of the flowing solution when the sample contacted the electrode surface, and a transient Faradaic signal originating from ferrocene oxidation into ferricinium moieties being compensated by the electrolyte anion (**Eq. 4.1**). After the electrolyte sample has left the flow cell, the current values goes back to its background value. When using the unmodified ITO electrode, only the capacitive component is visible (see curve “a” in **Fig. 4.3**).

As also shown on **Fig. 4.3**, background currents are quite large at the beginning of the experiments. When running a second experiment after five injections, without any additional treatment to the electrode (from b_1 to b_2 in **Fig. 4.3**), this effect is much less pronounced but still noticeable, with lower peak currents recorded upon successive injections of $NaNO_3$. This is explained by the “consumption” of ferrocene in the film, which are progressively oxidized into ferricinium moieties and thus less available for detection. The large background currents should be faradaic in nature (as they do not exist for unmodified ITO), resulting from ferrocene oxidation and charge balance by residual anions in the electrolyte-free water solution (taking into account water dissociation ensuring 10^{-7} M hydroxide ions (and protons) in the medium).

Peak currents are proportional to the anion concentration (**Fig. 4.4 A**), yet exhibiting sensitivity loss upon successive use, which was even more significant if repeating the experiment (**Fig. 4.4 B**). The sensitivity drop is due to the progressive oxidation of ferrocene groups and not to any leaching of them from the electrode material (as it was the case for zeolite modified electrodes doped with redox mediators, for instance, which needed to be re-filled between each series of experiment,[193] due to their ion exchange properties[62]). It is possible to restore partly the signal of the first run by reduction of the oxidized ferricinium species (**Fig. 4.4 C**), but it does not solve the problem of sensitivity decrease in successive FIA measurements (see curve b_1 in **Fig. 4.3** and curves A & C in **Fig. 4.4**). A more elegant way to operate should be regenerating ferrocene groups directly in the course of the amperometric detection process, which should be possible by working in the square wave mode.

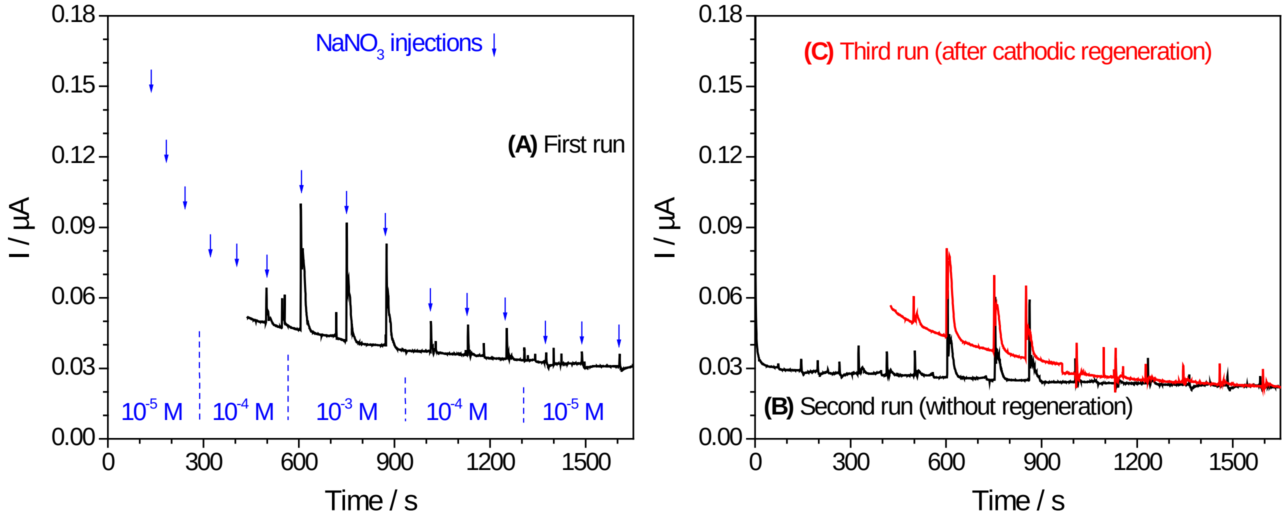

Figure 4.4 Amperometric curve recorded at the ferrocene-functionalized mesoporous silica film modified electrode for successive triplicate injections of $NaNO_3$ at various concentrations in an electrolyte-free water flow (flow rate: 1 mL min^{-1}); flow cell with two-electrode configuration; applied potential: +0.7 V. Left part of the figure (A) shows the first run of the experiment with a fresh electrode, while right part (B,C) shows the second and third runs respectively performed without (B) or with (C) cathodic regeneration (at 0.0 V for 25 min).

4.3.3 Square wave amperometric detection

Operating in the square wave mode implies the applications of successive potential pulses in the positive and negative directions, at a certain frequency, and plotting differences between anodic and cathodic currents (Di) as a function of time (current sampling done over the whole duration of potential pulse). Contrary to amperometry at constant potential (**Fig. 4.3**), square wave detection resulted in flat background and reproducible current responses upon multiple injections of 1 mM $NaNO_3$ (**Fig. 4.5**). This is due to the regeneration of ferrocene species, which are oxidized on the positive pulse and reduced on the negative one. If some capacitive contribution is noticeable at the base of the main peak (**Fig. 4.5 b**), the shape of the current response is a gaussian (corresponding to the passing of the $NaNO_3$ sample solution) and the detection is much more sensitive with the ferrocene-functionalized film than on bare ITO (compare parts a & b in **Fig. 4.5**). The square wave parameters have been optimized, giving the best results for pulse amplitude in the range 500–700 mV and frequency of 1.25 Hz. Long-term operational stability has been evaluated by 100 successive FIA measurements (see the last 30 signals on **Fig. 4.6 A**), suggesting an effective regeneration of ferrocene groups (as confirmed by cyclic voltammetry, **Fig. 4.6 B**).

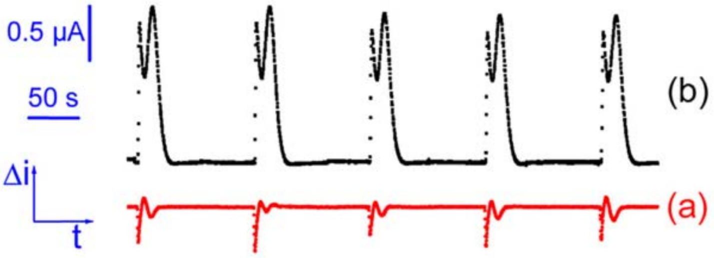

Figure 4.5 Differential pulse amperometric detection of 1 mM $NaNO_3$ (5 successive injections each 2 min in an electrolyte-free water flow at a rate of 1 mL min^{-1}) using the flow cell in two-electrode configuration (E_A = +0.5 V, E_C = 0.0 V, frequency = 1.25 Hz), respectively at unmodified ITO (a) and the ferrocene-functionalized mesoporous silica film electrode (b).

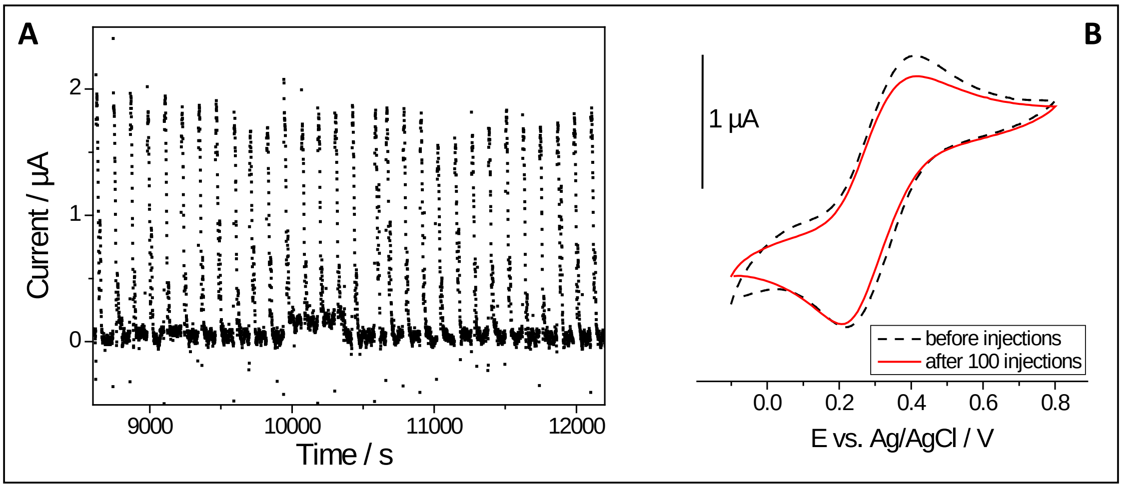

Figure 4.6 (A) 30 last signals (out of a series of 100 successive injections of 1 mM $NaNO_3$ in an electrolyte-free water flow) recorded at the ferrocene-functionalized mesoporous silica film electrode using the flow cell in two-electrode configuration (E_A = +0.5 V, E_C = 0.0 V, frequency = 1.25 Hz). (B) Cyclic voltammograms recorded in a conventional electrochemical cell for the film electrode, respectively before and after the series of measurements in (A).

4.3.4 Ion chromatography and anions in mixture

On the basis of the above results, one should be able to exploit the ferrocene-functionalized mesoporous silica film electrode for the amperometric detection of non-redox anions in suppressed ion chromatography (IC). The chemical suppressor is used to reduce dramatically the mobile phase conductivity, leading only the ionic analyte flowing through the electrochemical detector. **Fig. 4.7** confirms the sensitivity decrease of FIA detection at a constant potential, which imposed a crucial error in terms of detection of anions in mixture, as each anion has different retention time in the IC column. Hence, the latter anions entering the flow cell would suffer more the sensitivity decrease of this method. Therefore, the detection of multianions was further conducted by square wave amperometric detection.

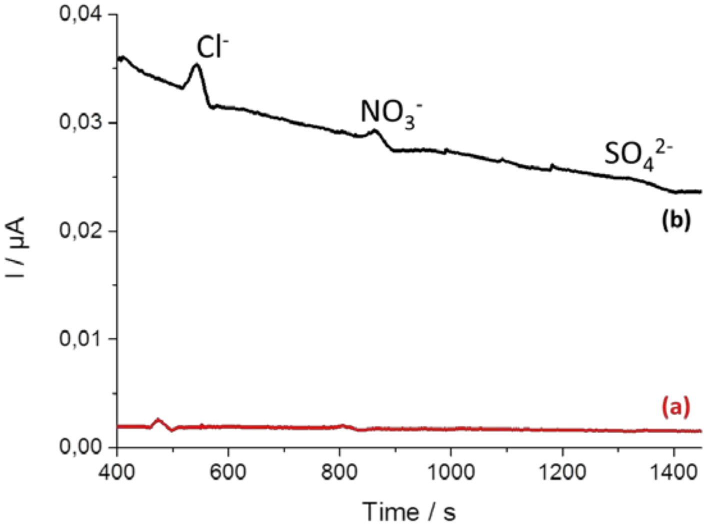

Figure 4.7 Amperograms recorded at a constant potential (+0.5 V) for a mixture of anions (Cl^-, NO_3^-, and SO_4^{2-}), previously separated in IC, at unmodified ITO (a) and at the ferrocene-functionalized mesoporous silica film modified electrode (b).

The feasibility of the indirect square wave amperometric detection subsequent to IC is demonstrated in **Fig. 4.8** for the analysis of nitrate samples at various concentrations, using the differential pulse detection mode. As expected from the presence of an ion exchange column between the injection loop and the amperometric cell, the analyte is somewhat retarded, its concentration profile is enlarged, and it passes the electrode surface during a period of time longer than that afforded by the direct FIA (compare **Fig. 4.5** and **Fig. 4.8 A**). The area under the peak is directly proportional to the anion concentration in the range between 10 and 100 µM, a value from which the sensitivity decreases and the signal intensity starts to level off at larger concentrations (see insert in **Fig. 4.8 A**). This is explained by additional resistance to mass transport in the small mesopore channels when filling them with huge amounts of anions compensating the ferricinium moieties, restricting thereby the ingress of more anions (less space available in channels containing more Fc$^+$, X$^-$ moieties), and thus leading to limited maximal current values. This observation is consistent with cyclic voltammetry data obtained for similar films as obtained at different supporting electrolyte concentrations.[123]

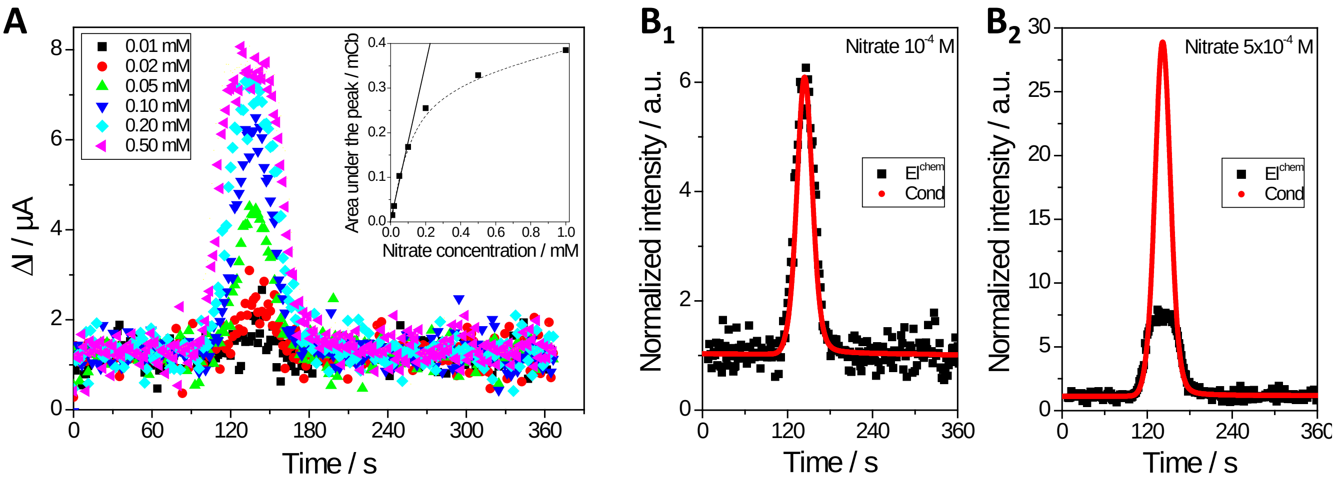

Figure 4.8 (A) Chromatograms obtained for NO$_3^-$ samples at various concentrations (from 0.01 mM to 0.50 mM) with differential pulse amperometric detection using the flow cell in two-electrode configuration (E_A = +0.5 V, E_C = 0.0 V, frequency = 1.25 Hz) at the ferrocene-functionalized mesoporous silica film electrode; the insert shows the corresponding variation of peak area with nitrate concentration. (B) Superimposition of amperometric data (El^{chem}) and classical conductivity signals (Cond) for the particular cases of (B$_1$) 1×10^{-4} M NO$_3^-$ and (B$_2$) 5×10^{-4} M NO$_3^-$ samples.

Surprisingly, current values are larger than those recorded in FIA, in spite of the dilution effect generated by the chromatographic column. One can rationalize this particular behavior again on the basis of the kinetically-limited indirect amperometric detection, which becomes less restricted for longer residence time of the analyte sample on the electrode surface (which is the case for IC compared to FIA). The superimposing of the amperometric data with those recorded using the classical conductivity detector, in a normalized way (**Fig. 4.8 B**), shows that no distortion has been induced by the electrochemical cell (same width at half maximum intensity, no tailing) in the linear part of the calibration curve, yet with just more noise (**Fig. 4.8 B_1**). For larger anion concentrations, the superimposing is still perfect in terms of peak width at the bottom, except that maximal current values are restricted at the top of the peak, for reasons of impeded mass transport / charge transfer in the film electrode as discussed above.

Fig. 4.9 depicts typical chromatograms obtained for mixtures of anions (fluoride, chloride, bromide, nitrate, sulfate, phosphate) at various concentrations, as recorded at both the indirect amperometry device developed here and the classical conductivity detector. The calibration plots corresponding to the electrochemical data (expressed with respect to ppm and molar concentrations) are shown in **Fig. 4.10**. The results indicate that the indirect amperometric detection of anions can be indeed performed and that the quality of the separation process (peak resolution/separation) is unaffected by the use of the electrochemical detector except the quite important noise in comparison to the conductivity detector (**Fig. 4.9**). This constitutes an improvement with respect to, e.g., the zeolite modified electrodes doped with redox-active ions and applied as detector in suppressed IC for which poorer resolution was reported in comparison to the conductivity detector.[203] Comparing amperometry and conductivity data also indicates some variation in sensitivity and linear range, which is especially noticeable for F^- and Cl^- anions. Actually, it is also visible on the calibration plot with concentration expressed in ppm (**Fig. 4.10 A**) for which the linear ranges seem to be strongly dependent on the anion type whereas the conductivity detector gives rise to linear responses for all anions in the whole concentration range (conductivity calibration plots not shown). The interpretation of this behavior is given by examining the calibration plots built on the basis of molar concentrations (**Fig. 4.10 B**). The investigated molar concentrations of F^- and Cl^- are actually much larger than the others and they correspond already to the situation of leveling off discussed above for nitrate (**Fig. 4.8**) for reasons of lowered mass transport rates. Also, for the monovalent anions, the peak current intensities are quite similar (**Fig. 4.10 B_1**), yet seeming to be inversely proportional to the size of hydrated anions (352 pm for F^-; 332 pm for Cl^-; 330 pm for Br^-; 340 pm for NO_3^-)[220], also consistent with a rate-determining process based on the diffusion of these anions in the small mesochannels (ingress of bulkier anions is expected to be slower than the smaller ones).

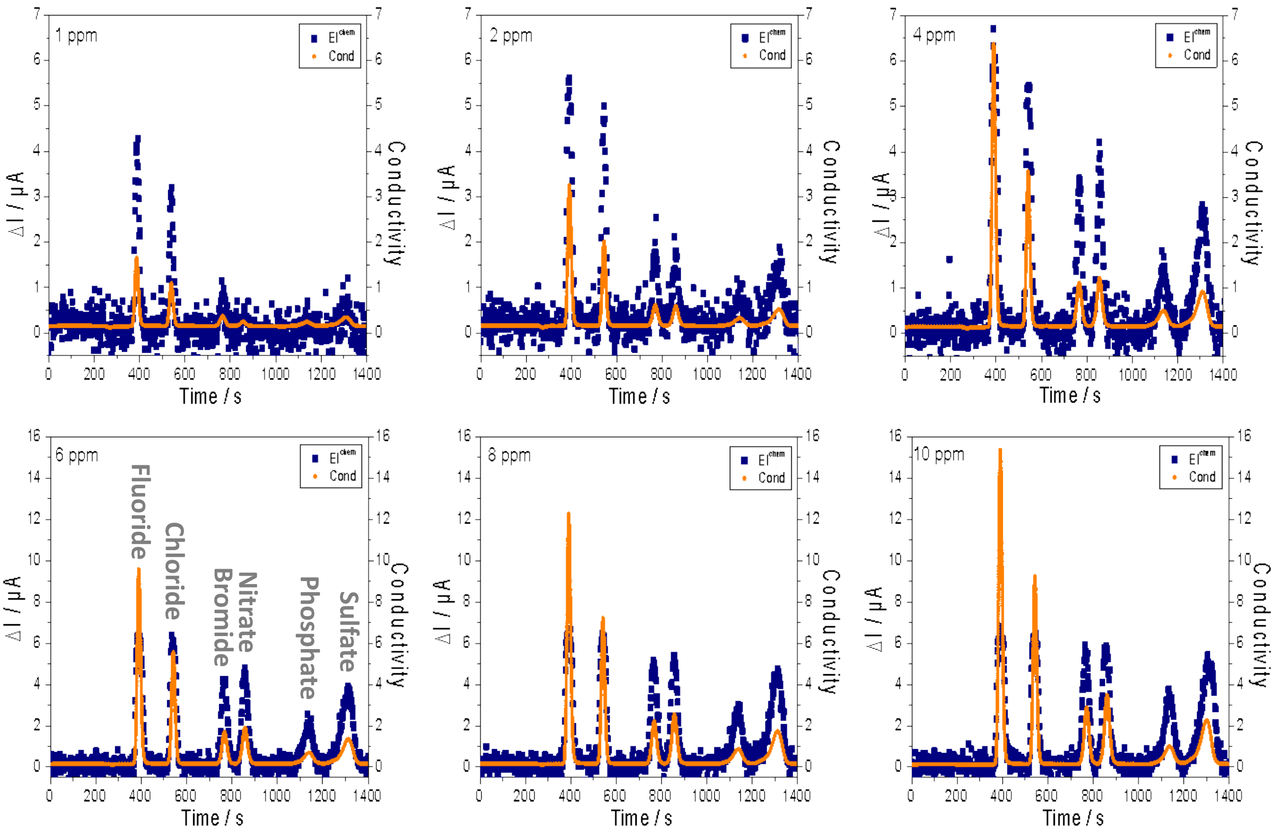

Figure 4.9 Chromatograms obtained for samples containing several anions (F^-, Cl^-, Br^-, NO_3^-, SO_4^{2-}, PO_4^{3-})in mixture,at various concentrations (from 1 to 10 ppm each), as recorded by differential pulse amperometry using the ferrocene-functionalized mesoporous silica film electrode (EI^{chem}) or the classical conductivity detector (Cond). Other conditions as in **Fig. 4.8**.

Note that phosphate species also belong to the monovalent series as they are in the form of $H_2PO_4^-$ after passing the suppressor. For the bivalent SO_4^{2-} anion, the situation is somewhat different, with a current response being *ca.* two times larger than for the monovalent anions (**Fig. 4.10 B$_2$**), which is explained by a greater capacity for more charged anions to compensate the positive charges generated by the oxidation of ferrocene groups into ferricinium cations.

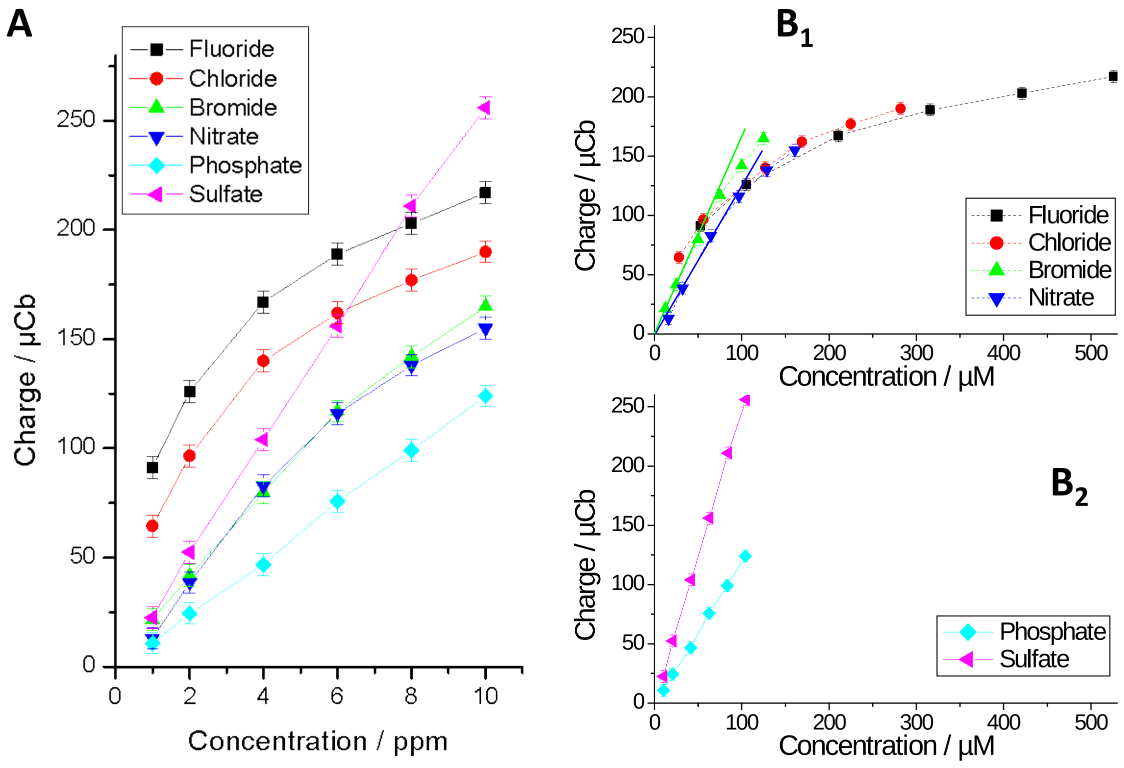

Figure 4.10 Calibration curves corresponding to the amperometric signals depicted in **Fig. 4.9**, with respect to the anion concentrationsrespectively expressed (A) in ppm and (B) in µM (monovalent ions in B_1 and multivalent in B_2).

4.4 Conclusions

A new procedure has been developed allowing the semi-continuous amperometric detection of non-electroactive anions using a simple flow injection cell working in a two-electrode configuration. The detection is based on the use of ferrocene-functionalized and vertically-aligned silica thin films on ITO as working electrode and using deionized water as carrier. Initial experiments have been performed in potentiostatic mode for which consecutive injections of anionic samples led to continuous decrease of the peak currents due to the progressive lack of available ferrocene groups, suggesting that their regeneration by reduction of the ferricinium ions formed is mandatory. Differential pulse amperometric detection has been then used to solve the problem of losing sensitivity since it allows the application of successive potential pulses alternatively in the anodic and cathodic potential ranges providing reproducible current responses that remain constant even after one hundred injections, thanks to the effective regeneration of ferrocene units. Furthermore, the feasibility of using such ferrocene-functionalized electrode for the amperometric detection of mixtures of anions subsequent to separation by ion chromatography (equipped with a suppressor) has been demonstrated. Although being much noisier than the commercially available conductivity detector, the amperometric flow cell gave rise to well-defined chromatograms without any noticeable peak distortion or enlargement, showing distinct sensitivity depending on their size and/or charge.

Chapter V

Immobilization of Ruthenium (II) Poly(bipyridyl) Complex in Vertically Oriented Mesoporous Silica Thin Films: Electrochemical and Photochemical Studies.

5.1 Introduction

The study of luminescent transition metal complexes started to emerge in the field of supramolecular photochemistry and electrochemistry since Paris and Brandt[221] reported in 1959 the metal-to-ligand charge transfer (MLCT) of ruthenium (II) (2,2'-bipyridyl) [$Ru(bpy)_3^{2+}$] complex's excited states. The study of $Ru(bpy)_3^{2+}$ luminescence furthermore continued by Lytle *et al*[222], Adamson *et al*[223] and Crosby *et al*[224–226] in the 1970s. The orbitals of transition metal complexes in general can be simplified by the molecular orbital (MO) diagram[227] shown in **Fig. 5.1**, which consists of two MO; metal (M) and ligand (L) orbitals. The electronic transitions can be classified depending on the localization of the MO[228];

1. Transitions between MOs localized on the metal center, called *metal-centered* (MC), *ligand field,* or *d-d transition*.
2. Transitions between MOs localized on the ligands, called *ligand-centered* (LC), *intra-ligand*, or *π-π* transitions*.
3. Transitions between MOs from different localization, called *charge transfer* (CT) *transitions*. These transitions cause the displacement of electronic charges from the metal to ligands or vice versa.
    a. *Ligand-to-metal* (LMCT) or *π-d transitions*.
    b. *Metal-to-ligand* (MLCT) or *d-π* transitions*.

The absorption and emission spectra of $Ru(bpy)_3^{2+}$ complex in aqueous solution is presented in **Fig. 5.2**, where the absorption bands can be assigned to the different excited states.[228]

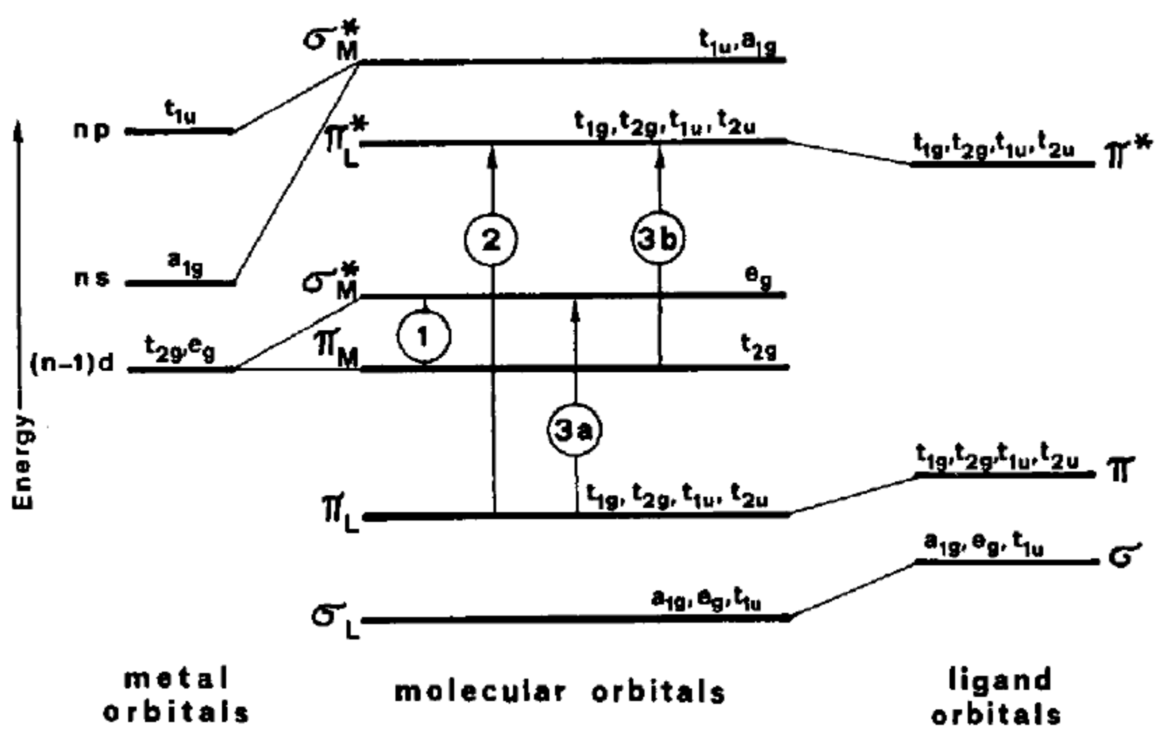

Figure 5.1 Molecular orbital (MO) energy diagram of octahedral metal complexes. Different types of electronic transitions are represented by numbers (1 – 3a/b); 1: metal centered (MC)transitions; 2: ligand centered (LC) transitions; 3a: ligand-to-metal charge transfer (LMCT) transitions; 3b: metal-to-ligand charge transfer (MLCT) transitions.[227]

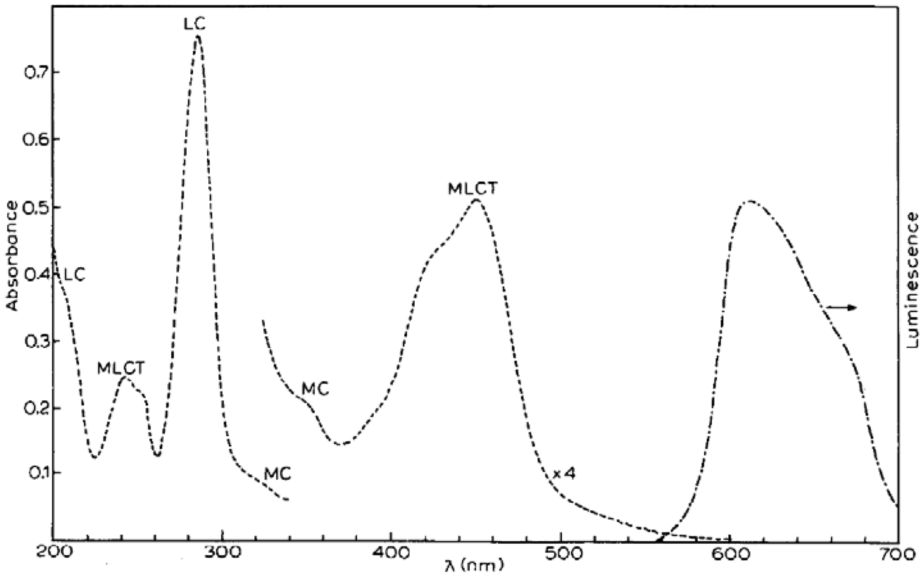

Figure 5.2 Typical absorption and emission spectra of $Ru(bpy)_3^{2+}$ dissolved in aqueous solution at room temperature.[228]

LC transitions are visible at λ = 208 and 285 nm. Weak absorption bands at 323 nm and at 345 nm are assigned to the MC transitions, whereas the broad and intense band centered at 452 nm is connected to the MLCT transition. Lastly, the orange-yellow emission band is located at around 600 nm, for $Ru(bpy)_3^{2+}$ solution at room temperature, originated from the Ru-centered triplet excited state shown in a simplified Jablonski diagram in **Fig. 5.3**.[229,230]

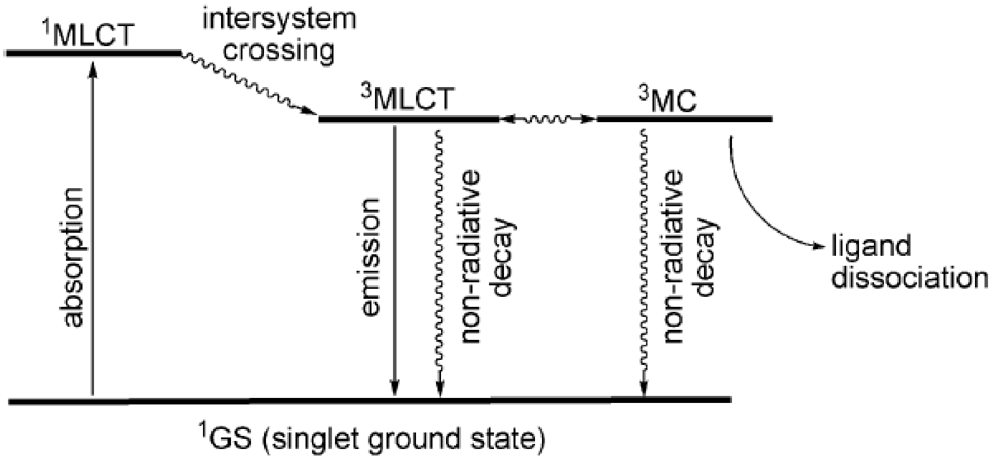

Figure 5.3 A simplified Jablonski diagram for ruthenium(II)polypyridine complexes, showing the emission of complexes resulting from triplet-state MLCT.[230]

The immobilization of these molecules directly onto electrode surfaces exists in the form of thin layer or film formed by self-assembly methods, such as coating and Langmuir Blodget (LB).[231–245] Ruthenium(II)bipyridyl thin films have received considerable attention owing to their rich photo- and electrochemical behavior, diversity of coordination forms and high thermal and chemical stability.[236,242,246] LB films of different ruthenium complexes have already successfully been applied in high-performance sensors,[243] although in some cases it suffers from chemical stability towards solvents, such as chloroform.[247] It has also been demonstrated that amphiphilic ruthenium complexes can be spin-coated as thin films for electronic devices.[244,245] One of the limitations of conventional device-manufacturing lies in the thickness of the emissive layer, since thin-layer devices, which could be brighter and more efficient obtained spin-coating or evaporation techniques show severe defects and malfunctioning when used in large area devices.[244]

Another form is by immobilizing ruthenium complexes in polymeric or inorganic matrices deposited on electrode surfaces. It can be carried out by several techniques, such as ion exchange[58,248–250], doping[251,252], and physical entrapment in polymer matrices[253–255]. Concerning $Ru(bpy)_3^{2+}$ immobilization in Nafion polymer via ion exchange or physical entrapment method, it gives disadvantages in the sensing application due to the slow mass transfer in the Nafion matrix.[256] Moreover, polymeric matrices often suffer from structural changes affecting the stability of the electron transfer of the immobilized species.[123]

Immobilization of luminescent ruthenium(II)polypyridyl complex and its derivatives has become an interesting field of research for its advantages compared to the applications in solution phase; such as minimizing the utilization of an expensive molecule, simplifying the experimental configuration and miniaturization of devices, as well as enhancing its properties, such as electrochemiluminescence (ECL) detection signal.[243] The most common applications of immobilized ruthenium(II)polypyrydyl complexes is ECL- based sensors.[247,251,254,257–266] The analytes which have been reported to be detected via ECL using immobilized $Ru(bpy)_3^{2+}$ complex are tripropylamine (TPA)[252,254,258,260,265], more complicated amines like biogenic polyamines (e.g. spermine and sperdimine)[262], and other substances such as 2-(dibutylamino)-ethanol (DBAE) and nicotinamide adenine dinucleotide (NADH)[257]. Another application in the field of analytical chemistry is the detection of oxygen based on the luminescence quenching of $Ru(bpy)_3^{2+}$ complex.[250,267–275] Furthermore, the electroluminescent properties of $Ru(bpy)_3^{2+}$ complex have been reported to be applied in light-emitting devices, especially organic light-emitting diodes (OLED).[243,245,276–283] Lastly, the derivatives of ruthenium(II)polypyrydyl complexes have been incorporated in semiconductor matrices (e.g. TiO_2 thin film) as a sensitizer of photoelectrochemical cells (PEC) or dye-sensitized solar cells (DSSC).[223,239,284–288]

This chapter deals with the preparation of ruthenium(II)bipyridyl based films in an organized and oriented silica matrices in order to investigate the effect of their confinement on the luminescence properties. Here, we are demonstrating the feasibility and optimization of ruthenium(2,2’-bipyridine)$_2$-(4-[(2-propyn-1-yloxy)methyl]-4’-methyl-2,2’-bipyridine); i.e. $[Ru(bpy)_2(bpy')]^{2+}$ species immobilization in the vertically-aligned mesoporous silica film using the combination between electro-assited self-assembly (EASA) and click chemistry, reported by Vilà *et al*[123] (see **Scheme 5.1**). Several levels of functionalization are controled by cyclic voltametry (CV). The electronic transitions of the grafted Ru complex moeities are monitored by UV-vis spectroscopy and the emission spectra with or without the presence of oxygen are tested using spectrofluorescence measurement.

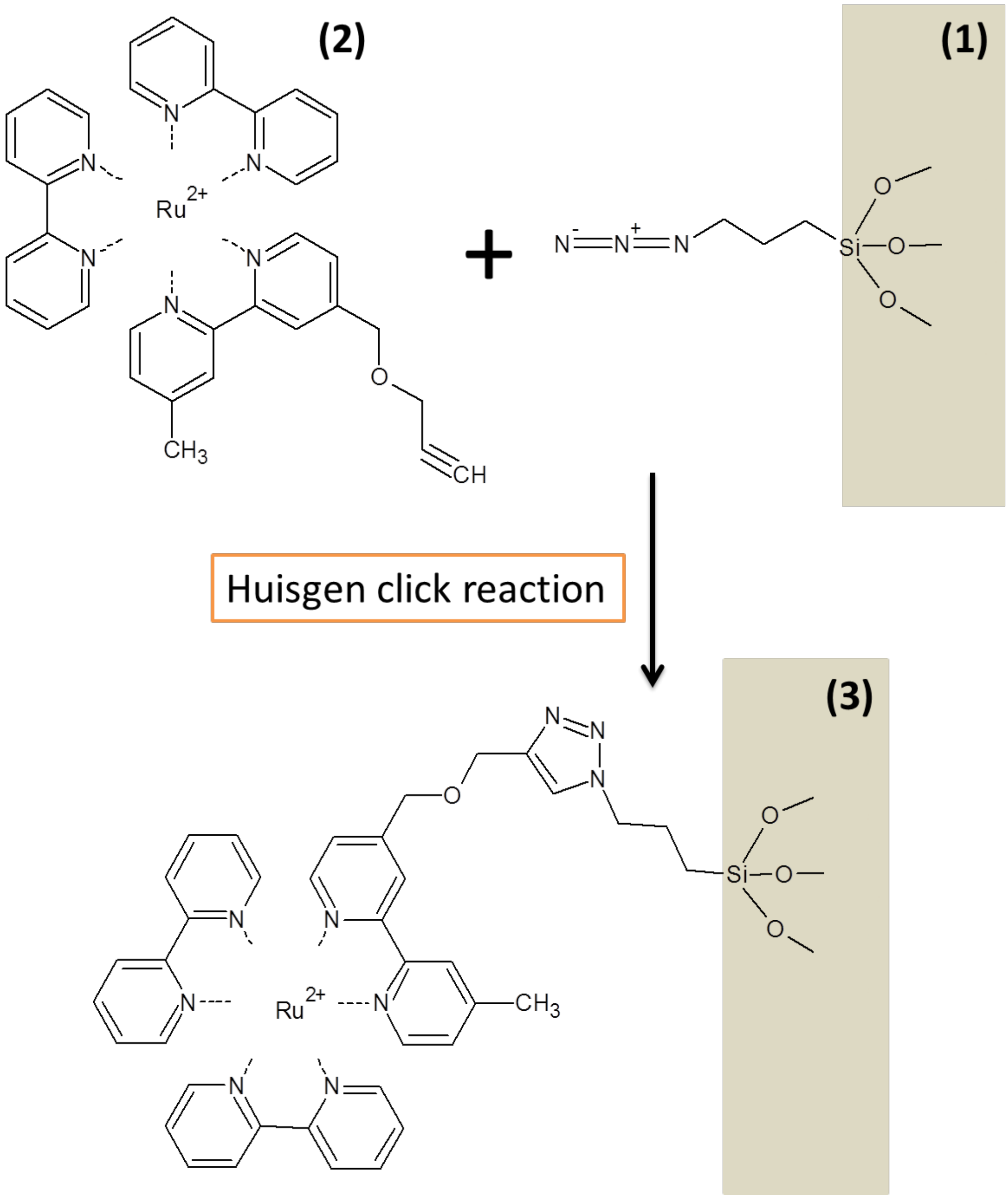

Scheme 5.1 Schematic representation of the click reaction of the azide-functionalized silica film **(1)** with ruthenium(2,2’-bipyridine)$_2$-(4-[(2-propyn-1-yloxy)methyl]-4’-methyl-2,2’-bipyridine); i.e. Ru(bpy)$_2$(bpy’) **(2)**, forming silica film grafted with [Ru(bpy)$_2$(bpy’)]$^{2+}$ moieties **(3)**.

5.2 Experimental

5.2.1 Synthesis of 4-[(2-propyn-1-yloxy)methyl]-4'-methyl-2,2'-bipyridine (bpy')

The synthesis of the bipyridine derivative was performed by following a procedure previously reported[289] starting from 4,4'-dimethyl-2,2'-dipyridyl and in three main steps:

a) Synthesis of 4-(carboxyaldehyde)-4'-methyl-2,2'-bipyridine

MS (CI, CH_4) m/z: 213 (100) [M+1]. ^1H NMR (400 MHz, $CDCl_3$) δ : 2.48 (s, 3H), 7.23 (d, J=5.0 Hz, 1H), 7.74-7.78 (m, 1H), 8.32 (s, 1H), 8.62 (d, J=4.9 Hz, 1H), 8.95 (d, J=4.9 Hz, 1H), 10.23 (s, 1H).

b) Synthesis of 4-(hydroxymethyl)-4'-methyl-2,2'-bipyridine.

MS (CI, CH_4) m/z: 201 (100) [M+1]. ^1H NMR (400 MHz, $CDCl_3$) δ : 2.49 (s, 3H), 5.03 (s, 2H), 7.18-7.25 (m, 1H), 7.41-7.48 (m, 1H), 8.30-8.35 (m, 1H), 8.40-8.42 (m, 1H), 8.59 (d, J=4.9 Hz, 1H), 8.72 (d, J=5.0 Hz, 1H).

c) Synthesis of 4-[2-propyn-1-yloxy)methyl]-4'-methyl-2,2'-bipyridine

MS (CI, CH_4) m/z: 239 (100) [M+1]. ^1H NMR (400 MHz, $CDCl_3$) δ : 2.36 (s, 3H), 2.40 (t, J=2.40 Hz, 2H), 4.23 (d, J=2.40 Hz, 2H), 4.67 (s, 2H), 7.15-7.18 (m, 1H), 7.19-7.20 (m, 1H), 8.24-8.28 (m, 1H), 8.30-8.33 (m, 1H), 8.49 (d, J=5.0 Hz, 1H), 8.68 (d, J=5.0 Hz, 1H).

5.2.2 Synthesis of $Ru(bpy)_2Cl_2$

$RuCl_3.3H_2O$ (1.0 g; 8.8 mmol), bipyridine (1.2 g; 7.6 mmol), and LiCl (1.1 g) were refluxed in reagent grade DMF (7 ml) for 8 h with magnetic stirring. The reaction mixture was cooled to room temperature, and reagent grade acetone (32 ml) was added. The reaction mixture was then cooled to 0°C overnight. The mixture was then filtered, yielding a red-violet filtrate and a black crystalline substance. The solid was washed three times with 10 ml of water followed by three 10 ml of diethyl ether, and was subsequently dried by suction (yield: 0.72 g; 39.1%).

5.2.3 Synthesis of $[Ru(bpy)_2(bpy')](PF_6)_2$

$Ru(bpy)_2.Cl_2$ (2 mmol), and 4-[2-propyn-1-yloxy)methyl]-4'-methyl-2,2'-bipyridine (1 mmol), and LiCl (1.077 g) were refluxed in reagent grade DMF (20 ml) for 24 h with magnetic stirring. The reaction mixture was cooled to room temperature, and reagent grade acetone (50 ml) was added. The mixture was then filtered, yielding a red-orange solid (0.3 g).

^1H NMR (400 MHz, $CDCl_3$) δ : 2.45 (s, 3H), 2.72 (s, J=2.60 Hz, 1H), 4.23 (d, J=2.40 Hz, 2H), 4.67 (s, 2H), 7.65-7.68 (m, 1H), 7.83-7.96 (m, 4H), 8.14-8.21 (m, 4H), 8.30-8.33 (m, 4H), 8.41 (d, J=5.0 Hz, 1H), 8.49 (d, J=5.0 Hz, 2H), 8.53 (m, J=5.0 Hz, 2H).8.72 (m, J=5.0 Hz, 4H).

5.2.4 Preparation of the mesoporous films

The $Ru(bpy)_2(bpy')$-functionalized silica films have been prepared on ITO electrode by the electro-assisted self-assembly (EASA) and co-condensation methods driven to form vertically-aligned mesoporous films described in **Section 2.3.2**, combined with Huisgen click chemistry with $Ru(bpy)_2(bpy')$. The click reaction was conducted for 18-24 hours, where the surfactant-extracted azide-functionalized films were immersed in the dark in a mixture solution of $Ru(bpy)_2(bpy')$ (20.0 mg) in DMF/H_2O (10/10 mL), Cu(II)acetate 1 M (20 µL) and AA 1 M (50 µL).

It has been previously studied[123] and discussed in **Section 1.3.3** that the maximum ferrocene content able to be grafted into the mesochannels is 40%, yet at this level fast electron transfer within the very confined pores are not fully compensated by the diffusion-limited compensating anion ingress. Hence, for this Chapter we have chosen to work with 30% ferrocene functionalized silica films.

5.2.5 Fluorescence measurements

For this experiment, $Ru(bpy)_2(bpy')$-functionalized films were deposited on a 5.5 x 1 cm ITO electrodes using an electrochemical cell completed with a 5 mm-diameter O-ring as the electrode surface delimitation. The fluorescence measurements (details about the apparatus described in **Section 2.2.2**) were conducted by immersing the modified electrode in a Quartz cuvette filled with either distilled water or acetonitrile as solvent.

Oxygen elimination was done by nitrogen purging using a needle insertion into the capped Quartz cuvette. Fluorescence was measured immediately after nitrogen purging.

5.2.6 Electrochemiluminescence (ECL) measurements

ECL measurements were conducted using Ru(bpy) $_2$(bpy')-functionalized films described in **Section 5.2.4** with spectrofluorometer apparatus described in **Section 2.2.2**. The ECL cell used for this experiment was completed with a 7 mm-diameter O-ring as the electrode surface delimitation, a silver wire reference electrode and platinum mesh as counter electrode.

5.3 Results and discussions

5.3.1 Preliminary considerations

It has been reported[112,123] before that the composition of the functionalized silica films was not able to be controlled by elemental analysis due to limited amount of matter used as samples. Nevertheless, the level of azide-functionalization can be estimated by XPS measurements, by the ratio between %-molar N and %-molar Si presented in **Table 5.1** for different AzPTMS/TEOS composition.

Table 5.1 Several properties obtained from different characterizations of azide- and $[Ru(bpy)_2(bpy')]^{2+}$-functionalized silica films ([total silica precursors] = 200 mM).

AzPTMS/TEOS (%)	Film Thickness (nm)[a] [112]	Incorporated azide[b] [112,123]	Click reaction yield[c]	Final $[Ru(bpy)_2(bpy')]^{2+}$ content[d]
5/95	136	80%	100%	4%
10/90	127	78%	100%	8%
20/80	112	74%	84%	12%
30/70	100	75%	9%	2%

[a]: Estimated from TEM.

[b]: Estimated from XPS by monitoring N/Si ratio (considering 3 N atoms per AzPTMS molecule).

[c]: Estimated from FTIR by monitoring the remaining unreacted fraction of azide groups.

[d]: Expressed with respect to the total silica amount in the film. Calculation was done by taking into account the incorporated azide functionalization and the click reaction yield.

Complementary to the XPS measurement, the functionalization of the silica film with azide-terminated groups can be also monitored by IR spectroscopy, which presents a strong stretching asymmetric band at 2095 cm^{-1}. The indirect quantitative analysis indicates that indeed, the rising AzPTMS/TEOS ratio in the starting sol gives increasing amount of azide groups grafted in the pores of the mesoporous silica. It has been demonstrated as well that the higher AzPTMS content promotes the generation of thinner azide-functionalized silica films (as represented in **Fig. 5.4** and listed in **Table 5.1**). According to these data, one can say that at higher functionalization level, there is an increase in spatial density between the azide groups. This is illustrated by smaller distances of adjacent azide groups at higher level of functionalization in **Fig. 5.4** ($d_4 < d_3 < d_2 < d_1$).

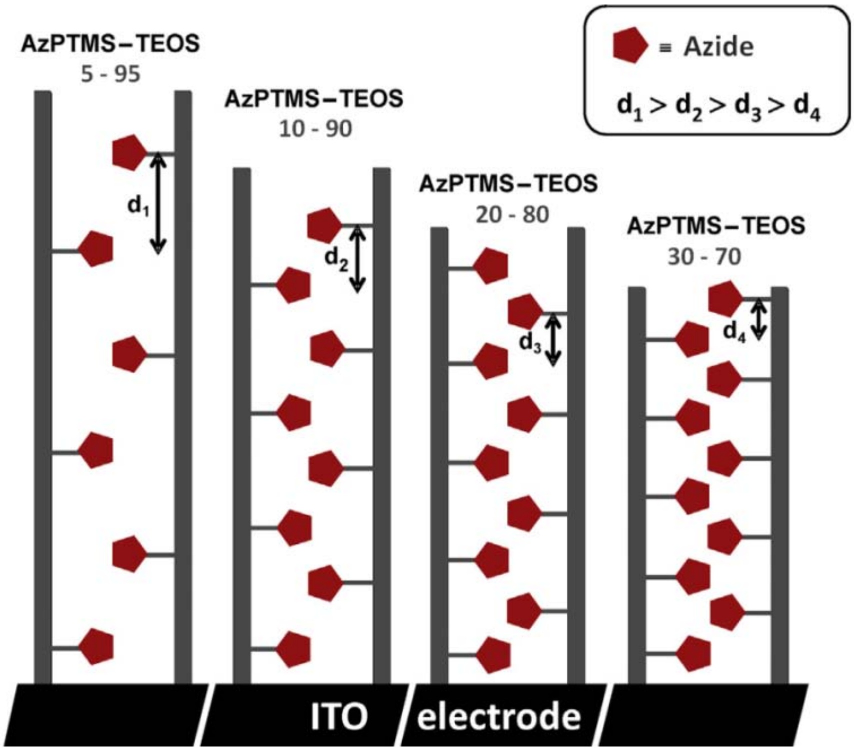

Figure 5.4 A schematic illustration of azide-functionalized vertically aligned silica mesochannels with different ratio of AzPTMS/TEOS in the starting sol solution. (adapted with permission from the report of Vilà et al.[123])

Furthermore, the efficiency of click reaction can also be followed by the disappearance of this characteristic asymmetric stretching band. The click reaction efficiencies for different ratio of AzPTMS/TEOS are presented in **Table 5.1**, as well as the theoretical final

$[Ru(bpy)_2(bpy')]^{2+}$ content in the film. At AzPTMS/TEOS 5/95 and 10/90 the yield of click reaction is 100% as presented by complete disappearance of the IR band (as presented in the blue box in **Fig. 5.5**). At the 20% azide-functionalized film, IR spectrum indicates some unreacted azide groups; i.e. ~16%. In this case, the film is denser ($d_3 < d_2$) so that the diffusion of $Ru(bpy)_2(bpy')$ reactant molecules starts to be more limited. For these three functionalization levels, the final amount of grafted $[Ru(bpy)_2(bpy')]^{2+}$ in the film increases linearly. In the case of 30% azide content, the yield of click reaction fell drastically (only 8.6%) and the final $[Ru(bpy)_2(bpy')]^{2+}$ content reaches even less than the one prepared from a film ratio of AzPTMS/TEOS 5/95. It can be regarded that at this level of functionalization, the mesochannels become so dense ($d_4 < d_3$), that there is very limited space for the click reaction and attachment of $Ru(bpy)_2(bpy')$ moeties.

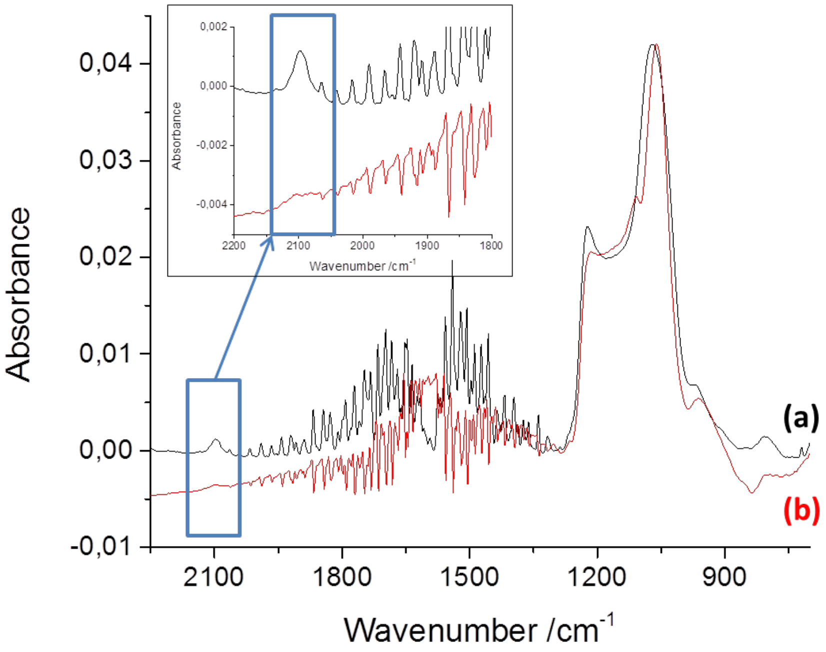

Figure 5.5 FTIR spectra of (a) azide-functionalized mesoporous silica thin films obtained from a sol containing AzPTMS:TEOS ratio of 10:90 and (b) the same film after click reaction with $Ru(bpy)_2(bpy')$. Blue box indicates the asymmetric stretching band of the azide group with its magnification presented in the inset.

The Huisgen click reaction between the azide-functionalized film and $Ru(bpy)_2(bpy')$ is illustrated in **Scheme 5.1**. The cyclic voltammograms of the resulting $Ru(bpy)_3$- functionalized silica films were recorded in a solution of $NaNO_3$ 0.1 M. The electrochemical response in **Fig. 5.6 (left)** shows the redox transformation of $Ru(bpy)_2(bpy')^{2+/3+}$ with E^o centered at 1.05 V, as published in other $Ru(bpy)_3$-encapsulated[252,258] or -doped[256,290] silica. As it was reported before[123] for the ferrocene-functionalized films, the redox reaction is governed by both electron hopping mechanism along the adjacent $Ru(bpy)_2(bpy')$ sites and the diffusion of counter anion from the electrolyte support (NO_3^- in this case) to compensate the extra positive charge formed upon oxidation of $Ru(bpy)_3^{2+}$ to $Ru(bpy)_3^{3+}$ (**Eq. 5.1**).

$$Ru(bpy)_2(bpy')^{2+} - 1\,e^- + X^-_{(sol)} \Leftrightarrow Ru(bpy)_2(bpy')^{3+}, X^-_{(film)}$$ **Eq. 5.1**

(with X^- = compensating anion; sol = solution)

Fig. 5.6 (right) demonstrate the correlation between AzPTMS content and both $[Ru(bpy)_2(bpy')]^{2+/3+}$ current intensity (black points) and theoretical content calculated and presented in **Table 5.1** (blue points). The ruthenium complex contents increase at the 5-20% azide-functionalized silica films, with the maximum response at AzPTMS/TEOS 20/80. The voltammogram also confirms the drop of current intensity as the click reaction yield declined significantly at 30% azide-functionalized film.

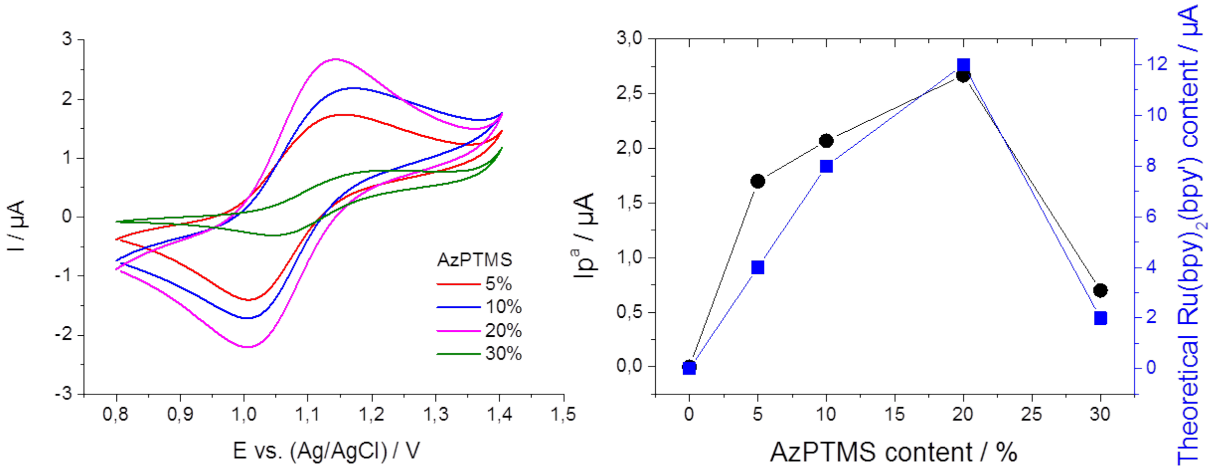

Figure 5.6 (Left) cyclic voltammograms of $[Ru(bpy)_2(bpy')]^{2+}$-functionalized silica film prepared from azide-functionalized silica film (5-30 % azide content) at v = 20 mV/s and (right) correlation between azide content in the silica film and both anodic peak current (black points) and the theoretical $[Ru(bpy)2(bpy')]^{2+}$ content (blue points).

5.3.2 Potential scan rate study

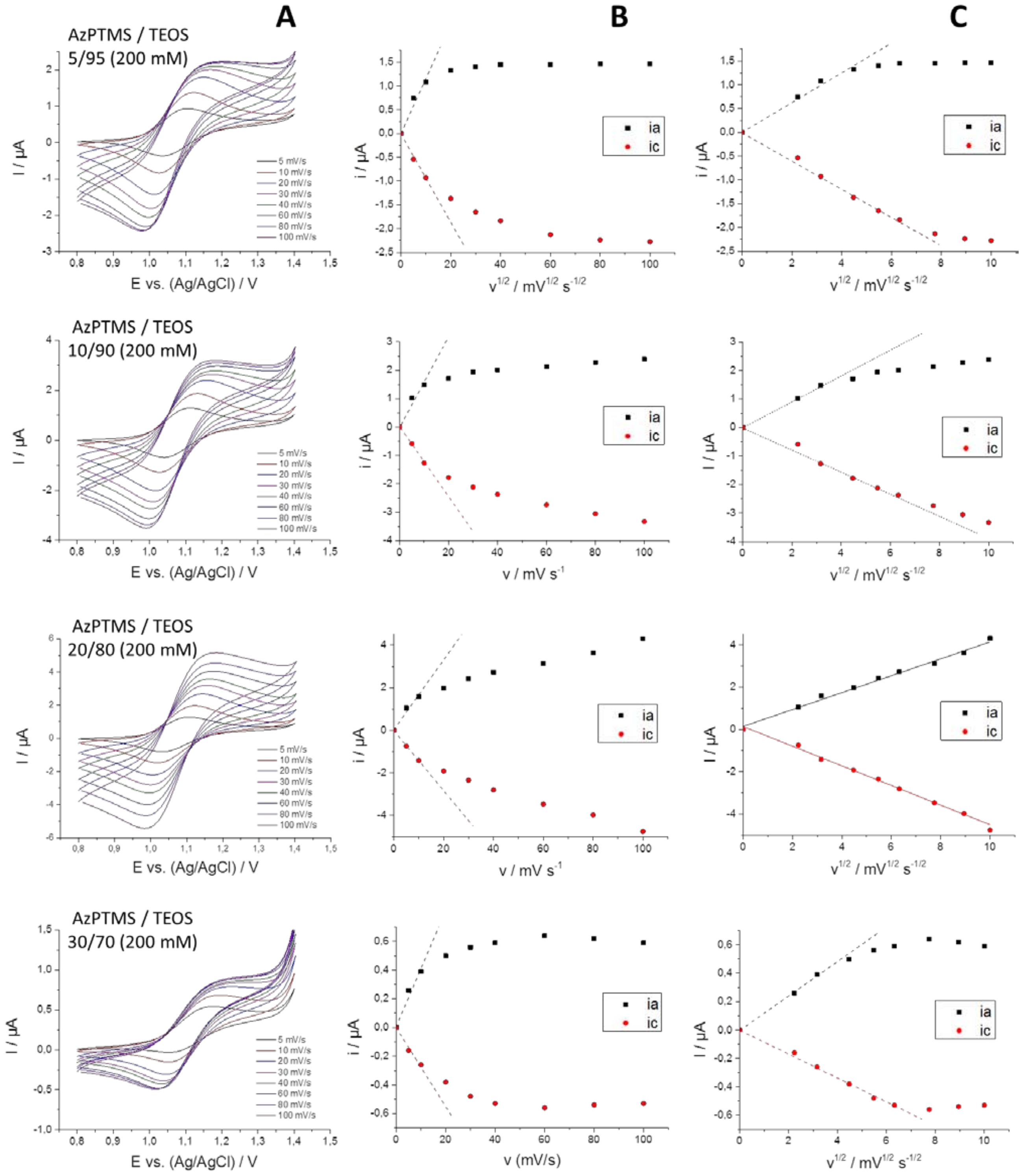

Figure 5.7 (A) Cyclic voltammograms of $[Ru(bpy)_2(bpy')]^{2+}$-functionalized films prepared from various AzPTMS/TEOS ratios and recorded at potential scan rates of 5-100 mV s^{-1}, in an electrolyte solution containing 0.1 M $NaNO_3$. Corresponding peak currents as a function of the scan rate (B) and its square root (C).

Electrochemical response of the $[Ru(bpy)_2(bpy')]^{2+}$-functionalized silica films, prepared from various AzPTMS/TEOS ratio, at different potential scan rates is studied using cyclic voltammetry shown in **Fig. 5.7 A**. At higher potential scan rates, the electrochemical response started to be limited as presented by the 'plateau' redox current and the wave shaped oxidation of $[Ru(bpy)_2(bpy')]^{2+}$ (except for the film prepared from AzPTMS/TEOS 20/80). This saturation can be more influenced by the different distance of the functionalization groups at the distinct samples. At 5 – 20% of functionalization, the higher the functionalization level, the thinner the silica film (see **Fig. 5.4**) and the more closely located are $Ru(bpy)_2(bpy')$ sites, hence the faster the electron hopping. Therefore, at 20% the current is no longer saturated and it gets saturated faster at 5% of functionalization level. For the case of 30% functionalization, the current is very quickly saturated which can be caused by both limited rate of e^- hopping (big distance between the adjacent $Ru(bpy)_2(bpy')$ sites) as well as slower counteranion diffusion (high density of the film, hence lower free space).

To further study about the electron and charge transfer through the films, the correlations of the peak currents, i_{pa} and i_{pc}, to both potential scan rate, ν (**Fig. 5.7 B**) and its square root, $\nu^{1/2}$ (**Fig. 5.7 C**) were considered. It is observed that the i_p is more linear to $\nu^{1/2}$, for ν = 5 – 100 mV/s of AzPTMS/TEOS 20/80 as well the other films at lower scan rate range before the saturation of the peak currents. This result indicates that the redox transformation of $[Ru(bpy)_2(bpy')]^{2+/3+}$ is more limited to the diffusion of the compensating anion from the electrolyte support to fulfill the electroneutrality of the system, rather than to the limitation of the pseudo e^- diffusion (e^- hopping) along the ruthenium complex sites.

5.3.3 UV-vis and fluorescence spectroscopy

Fig. 5.8 (left) presents the absorption spectrum obtained by UV-vis measurement of $Ru(bpy)_3$-functionalized films prepared from various AzPTMS/TEOS film ratios. The first broad absorption band centered at ~305 nm is assigned to the π-π* transition of bipyridyl ligand[222,228,229,244,291,292] and the one at ~450 nm is associated to the MLCT band[223,229,244,292,293]. Both of these absorption bands increase as the $Ru(bpy)_3$ content increases, with the same tendency as the electrochemical results, shown in **Fig. 5.8 (right)**.

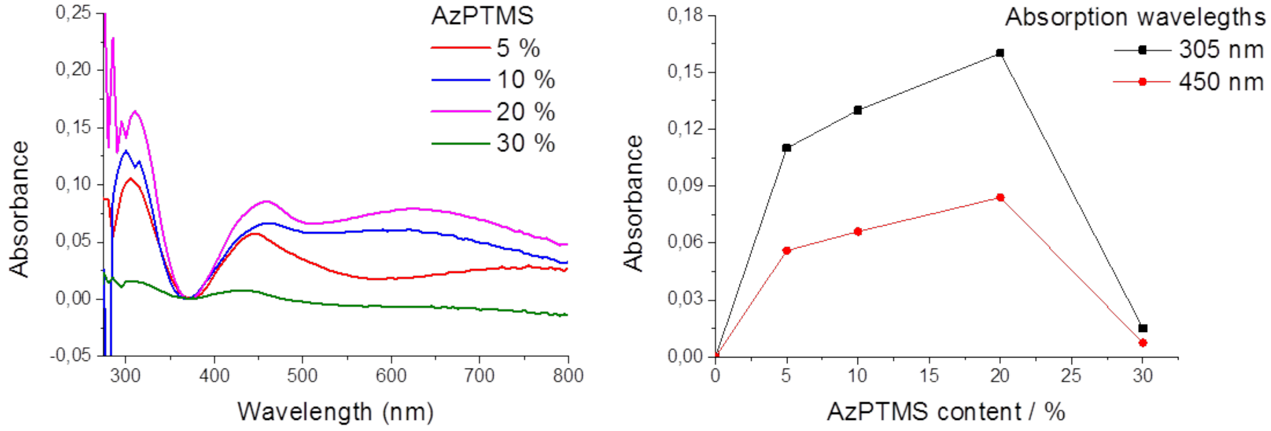

Figure 5.8 (Left) Absorption spectra of $[Ru(bpy)_2(bpy')]^{2+}$-functionalized silica films obtained from films containing 5-30% of azide functional group. (Right) correlation between absorbance at λ = 305 nm (black) and λ = 450 nm (black) and azide content in the silica film

Film prepared from AzPTMS/TEOS 30/70 contains the least $[Ru(bpy)_2(bpy')]^{2+}$ groups incorporated, followed by increase of the absorption bands from 5 to 20% azide-functionalized films. An additional band at ~620nm for some samples, probably due to imperfect positioning of the film modified ITO plates on the UV-vis apparatus.

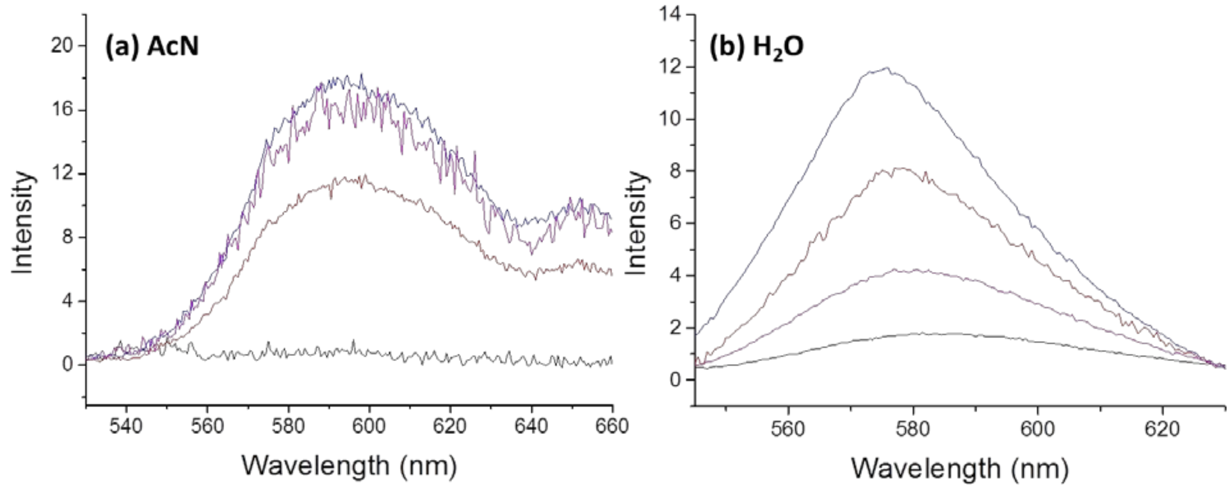

Figure 5.9 Emission spectra of $[Ru(bpy)_2(bpy')]^{2+}$-functionalized film prepared from AzPTMS/TEOS 20/80 in (a) acetonitrile and (b)water in the presence of dissolved O_2 in the solution (black curve) and after N_2 purging for 15 mins (red curve), 30 mins (blue curve), and 45 mins (magenta curve). Excitation wavelength = 450 nm.

Due to its optimum electrochemical and absorbance response, the emission of 20%-$[Ru(bpy)_2(bpy')]^{2+}$-functionalized film was measured using a spectrofuorometer by immersing the ITO glass slide modified with the functionalized film in a quartz cuvette containing solvents, such as acetonitrile (AcN) and distilled water (H_2O). The spectrums were obtained from an excitation wavelength of 450 nm (according to the recorded MLCT transition of the film obtained by the previous UV-vis measurements) and presented in **Fig. 5.9 (a)** and **(b)** for the different corresponding solvents. In AcN the emission maxima is around 595 nm, in accordance to some literatures[228,229,244,292–294] with a slight blue shift probably due to the triazole group attached to one of the bipyridine ligands. The emission optimum shifts to around 580 nm in aqueous media, following the same shifting tendency as octyl-modified silica gel doped with [4,4 -dimethyl-2,2′-bipyridine-bis(2,2′-bipyridine)] ruthenium(II) dichloride ($[Ru\text{-}mbpy]^{2+}$) reported by Ding *et al.*[295] It has also the tendency to follow the emission maxima of $Ru(bpy)_3$ in glassy solutions at low temperature (77 K)[228,229] or in water/ethylene glycol mixture at 105 K[292]. The intensity of emission is slightly lower in aqueous media due to higher oxygen solubility in water.[296,297]

The quenching of $[Ru(bpy)_2(bpy')]^{2+*}$ in the presence of oxygen[298] is clearly evidenced by flat or nearly-flat black curves in **Fig. 5.9**. Elimination of dissolved O_2 from the solution was done by N_2 purging for various length of time, with the optimum condition at 30 minutes for both acetonitrile and water based solvent. Longer period of N_2 bubbling promotes evaporation of the solvents and decrease of the emission peaks.

5.3.4 Electrochemiluminescence (ECL) properties of $Ru(bpy)_2(bpy')$ in the presence of tripropylamine (TPA)

The ECL properties of $Ru(bpy)_2(bpy')$-functionalized film prepared from AzPTMS/TEOS 20/80 sol solution was tested in the presence of a reducing agent. In general, one of the accepted mechanisms to explain the electrogenerated chemiluminescence of $Ru(bpy)_3^{2+}$ in the presence of tripropylamine was proposed by the group of Bard *et al*[234] and is based on the oxidation of both the $Ru(bpy)_3^{2+}$and the amine (**eq. 5.2 – 5.6)**.[258,259,299] Afterwards, the $TPA^{\bullet}$ reacts with electrogenerated $Ru(bpy)_3^{3+}$, producing luminescent $[Ru(bpy)_3^{2+}]^*$ state. TPA was chosen due to its well-known high ECL intensity of the $Ru(bpy)_3^{2+}$-TPA system.[258,263]

$$Ru(bpy)_3{}^{2+} \rightarrow Ru(bpy)_3{}^{3+} + 1e^- \qquad \textbf{(5.2)}$$

$$TPA \rightarrow [TPA]^{\bullet +} + 1e^- \qquad \textbf{(5.3)}$$

$$[TPA]^{\bullet +} \rightarrow TPA^{\bullet} + 1H^+ \qquad \textbf{(5.4)}$$

$$Ru(bpy)_3{}^{3+} + TPA\bullet \rightarrow [Ru(bpy)_3{}^{2+}]^* \qquad \textbf{(5.5)}$$

$$[Ru(bpy)_3{}^{2+}]^* \rightarrow Ru(bpy)_3{}^{2+} + h\nu \qquad \textbf{(5.6)}$$

Fig. 5.10 (left) exhibits good electrocatalytic activity of the $[Ru(bpy)_2(bpy')]^{2+}$-functionalized silica film towards 1 mM TPA, with an anodic current increase of more than 15 folds compared to the cyclic voltammogram (CV) in the absence of TPA in the solution (i.e. much more pronounced than the response of $Ru(bpy)_3Cl_2$ immobilized in silica nanoparticles towards 0.2 mM TPA[263]). Moreover, the ECL behavior between immobilized $[Ru(bpy)_2(bpy')]^{2+}$ species and TPA is shown in **Fig. 5.10 (right)** and presents comparable results and even more promising intensity compared to the behavior of $Ru(bpy)_3{}^{2+}$-doped in silica nanoparticles studied by Zhang *et al.*[251] and the one-step as-synthesized $Ru(bpy)_3Cl_2$-immobilized silica nanoparticles by Qian *et al.*[263], respectively.

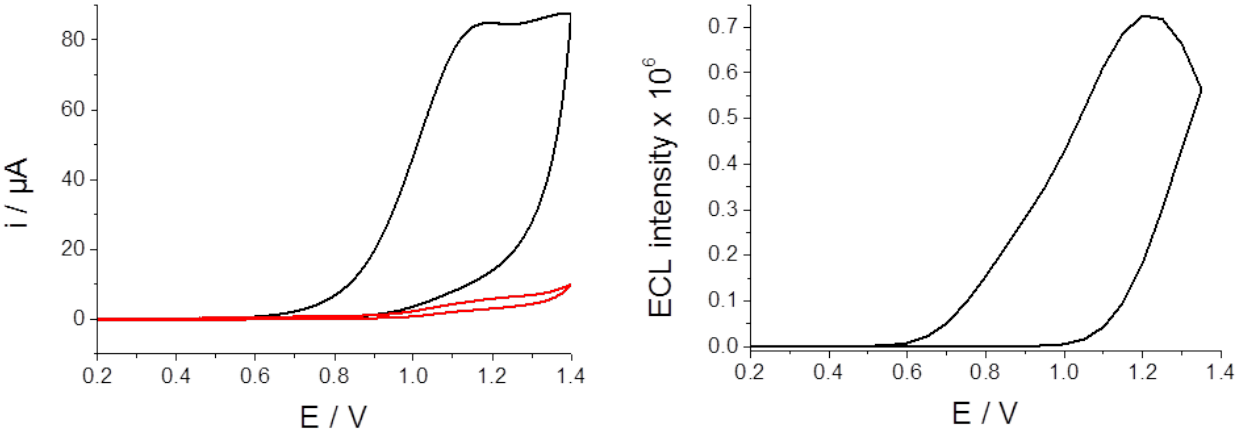

Figure 5.10 (Left) Cyclic voltammograms of $[Ru(bpy)_2(bpy')]^{2+}$-functionalized films prepared from 20/80 ratio of AzPTMS/TEOS and recorded at 50 mV s^{-1}, with (black curve) and without (red curve) the presence of 1 mM TPA; supporting electrolyte: 0.1 M KCl. (Right) ECL-potential curve of the corresponding film in the presence of 1 mM TPA and 0.1 M KCl.

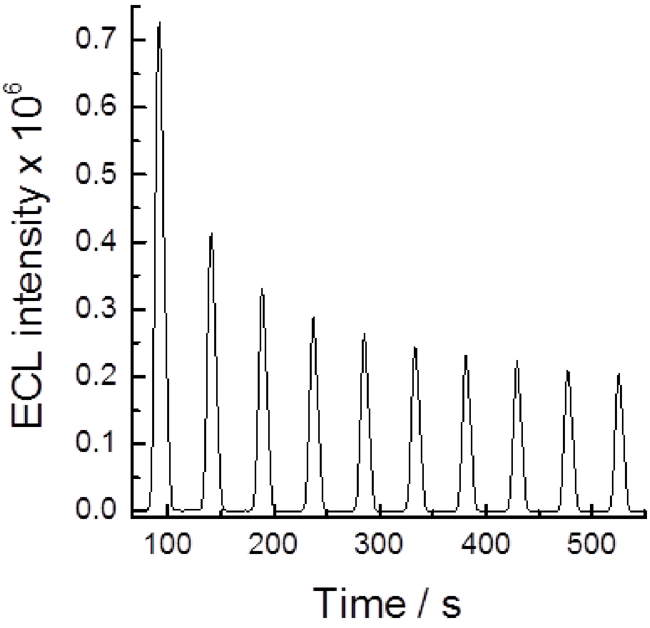

Figure 5.11 ECL response of the corresponding film presented in Fig. 5.10 under 10 consecutive cyclic voltammetric scans (potential scan rates: 50 mV s^{-1}).

However, the stability of the ECL intensity decreases upon continuous 10 CV scans, reaching stabilization around 2 x 10^5 cps (**Fig. 5.11**). This decrease was due to the decreased availability of TPA molecules near the electrode surface along the measurement time. Stopping the CV cycles and system stabilization for ~5 minutes (allowing the fresh TPA molecules to diffuse into the silica mesochannels) gives ECL intensity back to the initial 7 x 10^5 cps value (curve not shown).

5.4 Conclusions

The grafting of $[Ru(bpy)_2(bpy')]^{2+}$ in the pores of vertically-aligned mesoporous silica generated by EASA method was possible by the combination of AzPTMS/TEOS co-condensation followed by Huisgen click reaction with alkynyl-bearing $Ru(bpy)_2(bpy')$. The optimized level of functionalization was controlled by cyclic voltammetry in aqueous electrolytic solution and by UV-vis spectroscopy, which yield to the silica films prepared at AzPTMS/TEOS ratio of 20/80. At AzPTMS/TEOS 30/70, the click reaction was interrupted due to the high azide groups density in the mesochannels, leaving very limited space for functionalization.

Study of variation of potential scan rates shows that at all functionalization levels, $[Ru(bpy)_2(bpy')]^{2+/3+}$ redox reaction was generally more limited to the diffusion of compensating anion than to the e^- hopping process. Saturation of peak currents is found at higher potential scan rates (≥ 60 mV s^{-1}) except for the film prepared from AzPTMS/TEOS 20/80.

The electronic transitions of the grafted $[Ru(bpy)_2(bpy')]^{2+}$ in the silica films were evidenced using UV-vis spectroscopy showing the π-π* transition of the bipyrydyl ligands at 305 nm and the d- π* transition at 450 nm. The emission spectra of the optimized 20%-functionalized films was found to be centered at 595 nm in AcN as solvent and shifted to 580 nm in aqueous solution. The presence of oxygen was found to quench the emission of the corresponding film.

A preliminary ECL measurement confirms that $[Ru(bpy)_2(bpy')]^{2+}$-functionalized silica film presents an electrogenerated chemiluminescence towards the presence of TPA, in which the intensity is comparable to $Ru(bpy)_3^{2+}$ complex immobilized in silica nanoparticles.

Chapter VI

Controlling the Growth of Electropolymerized Polyaniline Nanofilaments through Vertically Oriented Silica Mesostructures

6.1 Introduction

6.1.1 Polyaniline

Intrinsically conducting polymers (CPs) are organic materials which exhibit electrical properties similar to metals and semiconductors.[300] They are polymers with highly π-conjugated chains, through which the motion of delocalized electrons occurs.[301] These conjugated polymers become conducting after doping. Previously, polymers were regarded as insulators, until the discovery of the conductivity of AsF_5-doped polyacetylene in 1977.[302] This important discovery was attributed to Alan MacDiarmid, Hideki Shirakawa, and Alan Heeger, who indeed received a Nobel Prize in Chemistry the upcoming 23 years.[302,303] Since then, many other types of CPs were reported (**Fig. 6.1** represents structures of some examples of the many CPs).

Polyaniline (PANI) is considered as the most promising CP because of its facile synthesis from low cost monomer, its tunable properties, good chemical stability, and strong interest for many applications.[300,304] Moreover, it has three different oxidation states which present associated color changes. **Scheme 6.1** shows the chemistry of reversible acid-base, doping-dedoping, oxidation-reduction of PANI. The fully reduced form, known as leucoemeraldine (L), presents yellow color which changes into green or dark blue when it is half oxidized or fully oxidized, respectively. The half-oxidized form is called emeraldine base (EB) and the fully oxidized is known as pernigraniline (P) state.[301,304–306]

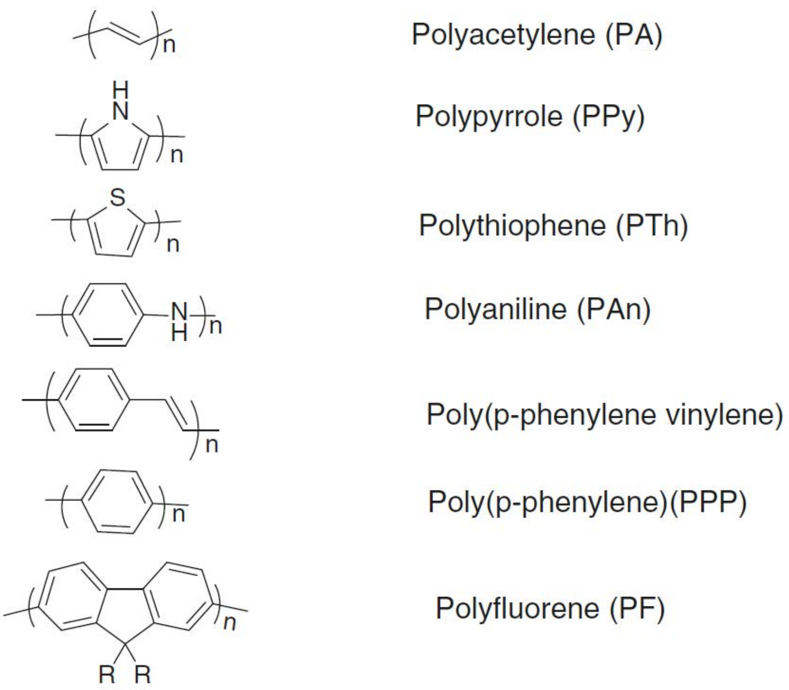

Figure 6.1 Chemical structures of several CPs[302]

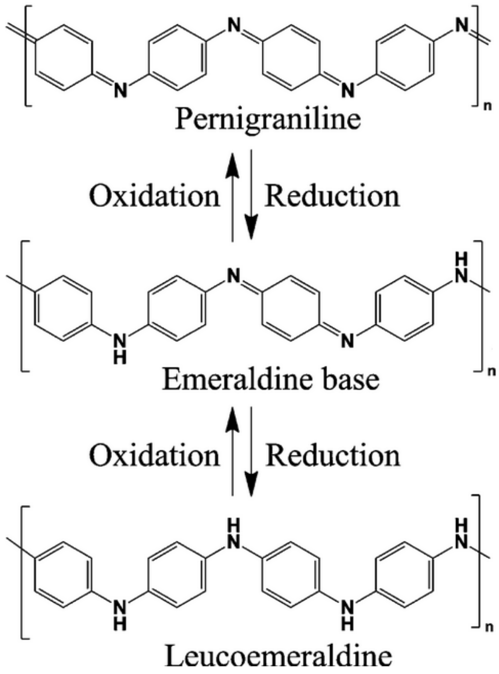

Scheme 6.1 Structures of the three oxidation states of PANI (fully reduced leucoemeraldine, half-oxidized emeraldine, and fully oxidized pernigraniline) and doping –dedoping process of emeraldine state.[305]

Conductivity of PANI occurs upon protonic acid doping of EB or oxidative doping of L, leading to the formation emeraldine salt (ES) polaron form which comprises of electron hole charge carriers and A^- counter anion to maintain the overall charge neutrality. This conductivity can be reversed by adding a strong base (dedoping of ES) or by electrochemical reduction of ES to L[301,304–306] (see **Scheme 6.2**). The electrical conduction along the polaron structure is due to the hopping of an electron from a neutral nitrogen site to the adjacent electron hole. Consequently, the hole moves towards one direction where another electron from neutral nitrogen site jumps into. This process continues and creates movements of electron hole and neutralizing electron towards an opposite direction.[304]

The synthesis of PANI can be done via oxidative polymerization of aniline monomers.[303,307,308] The polymerization method can differ depending on the type of oxidants, where chemical polymerization requires chemical oxidizing agent, such as ferric chloride or ammonium persulfate, and electrochemical synthesis applies an oxidative potential difference during the synthesis.[303] Electrochemical polymerization is considered to be an advantageous method because it is a straightforward process, it produces high purity PANI, and especially due to the ability to control the formation of thin films.[303,309]

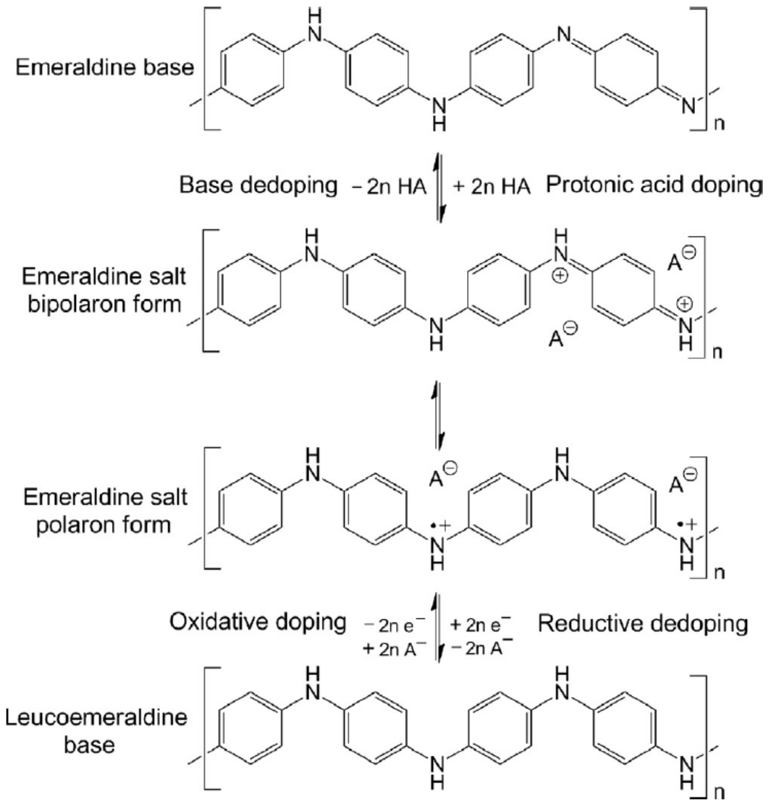

Scheme 6.2 Protonic acid doping of EB and oxidative doping of L.[306]

6.1.2 Nanostructured polyaniline

In the past two decades, a rise in the interdisciplinary study of PANI in parallel to nanosciences has led to major advances in conducting polymer nanostructures[303,306,310–313] or nanocomposites.[314–318] The main motivation for such enthusiasm is linked with potential advantages of polymeric conductors that exhibit low-dimensionality, uniform size or pore size distribution, high crystallinity and improved physical properties compared to their bulk counterparts, or enhanced performance due to the synergy between individual components in nanocomposites.[319,320]

Among the various nanostructure types (0D, *e.g.*, nanoparticles; 1D, *e.g.*, nanowires, nanotubes or nanofibers; 2D, *e.g.*, films and layers; 3D, *e.g.*, mesoporous or macroporous materials or polycrystals), one-dimensional (1D) nanostructures and nanomaterials have been given special attention, because they combine small dimensional structures with high aspects ratios and high degrees of flexibility, offering thereby attractive features for fast charge transfer and associated mass transport phenomena.[312,321,322] Moreover, aligned nanocomposites will allow to distinguish the roles of intrachain and interchain energy transfer in conjugated polymers, with possible enhanced performance of systems based on proper isolation of polymer chains.[323] A device based on electrical contact to single polymer chains encapsulated in mesoporous glass will have efficient charge transport since the current will not be limited by the hopping of carriers between chains, as in amorphous polymer films.

Main methods to prepare 1D nanostructures of PANI are based on the use of hard or soft templates through which the conducting polymers are grown along the usually cylindrical pores, or on template-free synthesis (supramolecular self-assembly in solution, electrospinning or nanolithography).[321,322,324–327] Conducting polymer nanowire arrays are of particular interest as superior electrode materials likely to be easily transferred to devices.[328,329] Such 1D PANI nanostructures or nanocomposites are attractive for applications in various fields, including energy,[322,324,328,330–333] sensors and biosensors,[314,334–337] photovoltaics,[338] nanophotonics, nanoelectronics, among others.[321]

The most regular PANI nanowire arrays are produced by the template route, using either hard templates such as particle track-etched membranes[339,340] or anodized aluminum oxide membranes,[341,342] or soft templates such as block copolymer assemblies or self-assembled surfactant phases,[343,344] associated to electroless polymerization or electrochemical growth. Template synthesis provides a route of reproducibly and predictably controlling the morphology (diameter, length) and geometry (*e.g.*, vertical alignment) of conjugated polymer films as they are endowed by the template itself. The lower limit of wire diameters remains however restricted to typically tens of nanometers.[329,344] A way to decrease the wire diameter, and consequently increasing their aspect ratios and the density of the array, would be using perpendicularly oriented mesoporous films with small pore diameters (few nm) as template. Actually, ordered mesoporous silica particles (MCM-41, KIT-6 or SBA-15) have been often proposed as hosts for confinement of PANI chains by chemical polymerization or gas-phase methods,[345–348] but mesoporous polyaniline films are less common,[349–351] and vertical control of the orientation of such nanowires generated through mesoporous templates is even more challenging.[352,353]

As thoroughly mentioned in **Chapter I**, perpendicularly oriented mesoporous silica thin films can be manufactured nowadays following two main approaches, *i.e.*, the electrochemically assisted self-assembly (EASA)[113,114] and a Stöber solution growth method[23], among some other underexplored strategies.[104,111] In particular, EASA is a versatile method leading to defect-free, perfectly-ordered, and uniformly deposited mesoporous silica films on electrodes, exhibiting hexagonally-packed and vertically-aligned mesochannels of *ca.* 100 nm length and pore diameters adjustable in the 2-3 nm range. Such oriented films on electrode are thus in principle ready for being used as one-dimensional hard template for generating redox-active nanofilaments. Some preliminary works have been indeed reported, notably for Prussian Blue,[153] Pd nanorod arrays,[354] polypyrrole[355] or polythiophene wires,[356] but most often without giving direct evidence of the presence of the guest species in the mesopores. For instance polythiophene wires were 5-6 nm thick (i.e., larger than the mesopore diameter 2-3 nm),[356] and the diameter of the Pd nanorods was even much larger (around 50 nm)[354], suggesting that these nano-objects were grown outside the mesoporous host. PANI nanostructures were also grown through oriented but wormlike mesoporous silica films[352,353] or using non ordered sol-gel films as template.[357,358]

In this Chapter, we describe the possible controlled growth of PANI nanofilaments generated by potentiostatic electropolymerization through well-ordered, hexagonally-packed and vertically-aligned silica mesochannels (2 nm in diameter) produced by EASA. Chronoamperometry and films with various thicknesses (100-200 nm) were used to distinguish the three stages associated to the process (induction period, filament growth, deposition outside the mesochannels). The obtained films have been characterized by electron microscopy and energy-dispersive spectroscopy, grazing-incidence X-ray diffraction, cyclic voltammetry, UV-vis spectroscopy, as well as capacitance studies.

6.2 Protocols

6.2.2 Preparation of the mesoporous silica hard template

Ordered and perpendicularly oriented mesoporous silica thin films were electrodeposited onto indium-tin oxide (ITO) plates as described in **Section 2.3.2**. Films with various thicknesses (controlled by varying TEOS concentration in the sol from 50 to 200 mM) were prepared. The resulting silica film is labeled as ITO/SiO_2-50, ITO/SiO_2-75, ITO/SiO_2-100 and ITO/SiO_2-200 in which the number indicates the TEOS concentration in the sol. After surfactant removal, ITO electrodes covered with mesoporous silica were stored at 130°C before use, in order to avoid prolonged contact with water molecules from the atmosphere which could lead to some degradation of the silica framework.

6.2.3 Electropolymerization of aniline

Mesoporous silica modified ITO electrodes, after being removed from the oven and let to cool down to room temperature, were inserted in the electrochemical cell (presented in **Fig. 2.3**) and the working electrode surface was delimited by a round seal (5 mm inner diameter). Electropolymerization took place by the application of a constant potential of +0.85 V (vs 3M Ag/AgCl) in a solution containing 0.1 M aniline in 0.5 M H_2SO_4 for selected periods of time: typically, the electropolymerization process was stopped after a certain amount of charge, Q, was passed ($0.4 \leq Q \leq 6$ mC). This experiment was conducted under nitrogen atmosphere.

6.2.4 Characterization procedures

The film thicknesses were evaluated by AFM contact-mode, being equal to 100, 120, and 200nm (±20nm), respectively for ITO/SiO_2-75, ITO/SiO_2-100, and ITO/SiO_2-200, consistent with previous studies indicating film thickness proportional to TEOS concentration.[114] The morphology/mesostructure of the films was characterized by Transmission Electron Microscopy, TEM (from silica samples carefully scratched from the ITO electrode and transferred to a TEM grid), using a CM20 microscope at an acceleration voltage of 200 kV equipped with an Energy Dispersive Spectroscopy (EDS) analyzer. Further control-experiments were carried out by scanning electron microscopy (SEM, JEOL JSM-840) and grazing incidence X-ray diffraction (GIXD, using a Nonius Kappa CCD diffractometer equipped with an ApexII CCD detector (copper cathode, $\lambda_{K\alpha}$=1.54184 Å)).

Electrochemical characterizations were performed in a separate, free of aniline home-made electrochemical cell (**Fig. 2.3**), under nitrogen atmosphere. Capacitance study was conducted in a solution containing 0.5 M HNO_3. The galvanostatic charge/discharge experiment was operated in a three-electrode cell configuration using chronopotentiometry technique with applied stepping currents of 5 and -5 µA corresponding respectively to the charging and discharging processes. Potential difference cut-offs were applied at 0.5 and -0.1 V to avoid degradation of the deposited PANI. The samples' electrochemical performance towards iron redox pair 1 mM (Fe^{2+}/Fe^{3+}) in acid media (0.5 M H_2SO_4) was evaluated by cyclic voltammetry.

6.3 Results and discussion

6.3.1 Silica film quality test

PANI electropolymerization is basically possible either through defects in the film, if any, or uniquely through the mesochannels. To rule out the possibility of PANI deposition through defects, mesoporous silica templates were checked before surfactant extraction by the use of ruthenium hexamine as redox probe (**Fig.6.2**). The absence of the redox signal before extraction indicated that mesoporous silica templates are covering the entire surface of the electrode and thus blocking entirely the access to the surface. Removal of the surfactant trapped inside the pore re-opened the access to the electrode through the mesochannels only. Based on these observations, PANI electropolymerization would only occur through the mesochannels. This is also consistent with a previous report on the perfect molecular sieving properties of EASA-based mesoporous silica films, with a threshold size of excluded species at 2.4 nm, confirming the absence of defects and structural integrity over the whole film area.[127]

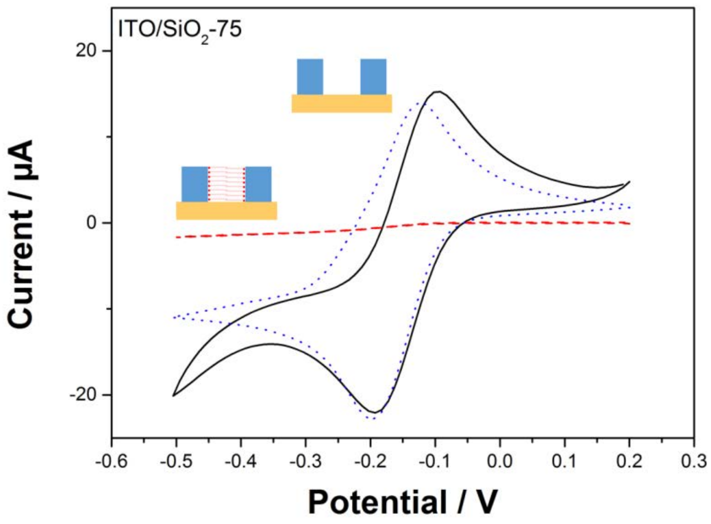

Figure 6.2 Cyclic voltammograms recorded in 0.1 mM solutions of $[Ru(NH_3)_6]^{3+}$ on bare ITO electrode (black curve) and ITO/SiO_2-75 before (red curve) and after (blue curve) surfactant removal. Supporting electrolyte solution: 0.1 M $NaNO_3$; potential scan rate: 20 mV s^{-1}.

6.3.2 Electropolymerization of aniline through mesoporous silica templates

The electropolymerization of aniline at constant potential through mesoporous silica templates is followed by chronoamperometry, shown in **Fig. 6.3**. There are three distinct stages observed and were defined more easily from the first derivative of the current transients of the electropolymerization of aniline on ITO/SiO_2 modified electrodes, shown in **Fig. 6.4**. The period before reaching the maximum plateau of the curve is related stage I. The region between the maximum and minimum points is attributed to stage II. After the minimum point of the curve, an onset of exponential current arises and defined stage III.

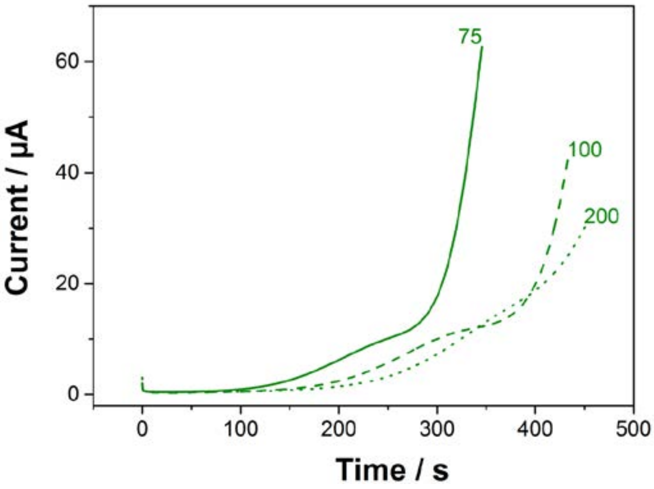

Figure 6.3 Potentiostatic electropolymerization of PANI at an ITO electrode modified with SiO_2 template with different thickness (up to Q = 3mC). Numbers on the curves represents the different silica film; i.e. SiO_2-75, SiO_2-100, and SiO_2-200.

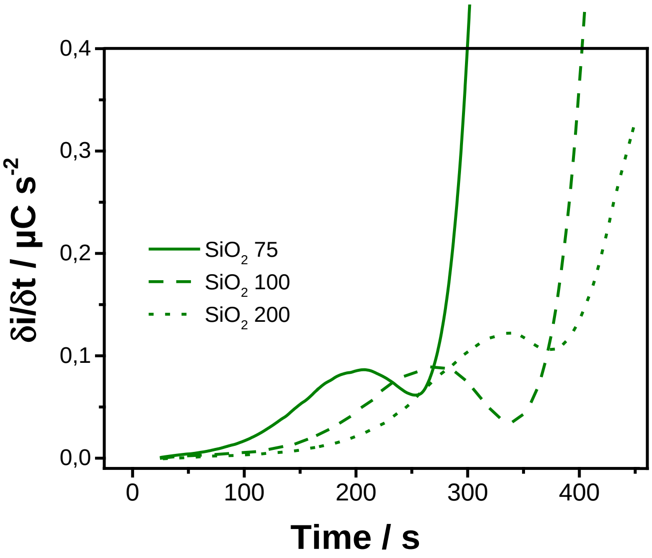

Figure 6.4 Derivatives of PANI electropolimerization current transients for ITO/SiO_2 75-200 electrodes.

The first stage shown in **Fig. 6.5** corresponds to an induction period during which aniline is oxidized at the electrode surface to form oligomers in agreement with a nucleation process (I).[307,308,357,359–363] After this induction period, oxidation current increases, due to the deposition of polymer on the electrode surface and concomitant growth of PANI nanofilaments in the mesochannels of the silica template (II). Finally, a PANI film is then grown electrochemically outside the mesochannels, leading to the formation of new electroactive sites available on the electrode surface, which are able to oxidize more aniline monomers, thus increasing the polymerization rate (III). Such exponential growth of the current is similar to that observed for aniline electropolymerization at a bare ITO electrode (inset of **Fig. 6.5**), a shape which is related to the autocatalytic effect of PANI (pernigraniline) for the monomer units.[364] At bare ITO, there is no stage II corresponding to the filling of the mesochannels so the induction period is directly followed by the 3D growth of PANI with instantaneous nucleation.[365] The induction period is longer in the presence of mesoporous silica template at the electrode surface, which can be explained by restricted mass/charge transfer phenomena in the confined environment of mesochannels.

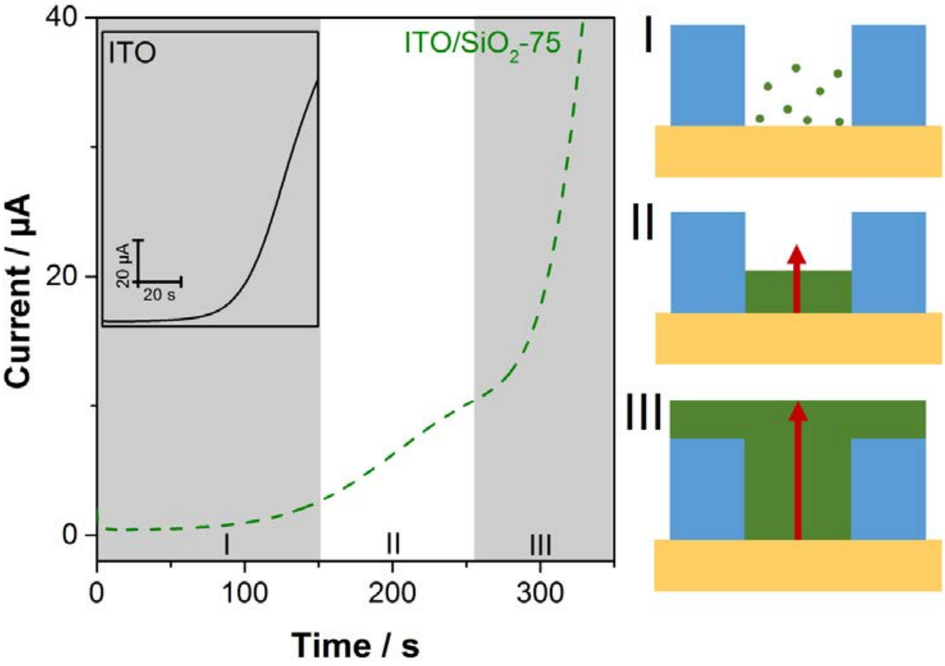

Figure 6.5 Potentiostatic electropolymerization of PANI at an ITO electrode modified with SiO$_2$-75 template (up to Q = 3mC). Inset: Electropolymerization at a bare ITO electrode (up to Q = 3 mC). (I) Induction and nucleation; (II) PANI nanowire formation within the mesochannels; (III) 3D PANI growth. The solution was made of 0.1 M aniline in 0.5 M H_2SO_4 and applied potential was +0.85 V.

For the same reason, the electropolymerization rate of the exponential region is much lower at the ITO electrode modified with mesoporous silica (region III) than at bare ITO (**Table 6.1**), in agreement with previous observations made for PANI generation through non-ordered sol-gel films.[357] The non-exponential rate of electropolymerization only observed at the mesoporous silica film modified electrode (region II) can be therefore related to the growth of isolated PANI nanofilaments across the oriented mesopore channels. Chronoamperometry is thus well-suited to both evidence and monitor the different growth regimes of PANI deposits, as discussed hereafter.

Table 6.1 Kinetic parameters associated to each stage of PANI electropolymerization (from **Figs. 6.5 and 6.6**).

Samples	**Stage I** α	**Stage II** ***Slope* / A s^{-1}**	**Stage III** ***k* / s^{-1}**
ITO	0.54	n/a	0.07
SiO_2-75	0.71	8.3×10^{-8}	0.04
SiO_2-100	0.71	8.5×10^{-8}	0.04
SiO_2-200	0.71	1.15×10^{-7}	0.02

These three-stage deposition processes were observed for different thicknesses of silica template although longer deposition times were required to transfer the same amount of charge through thicker films (**Fig. 6.3**). The effect of the presence of mesoporous silica template on the electropolymerization of PANI was investigated through an analysis of the chronoamperograms at the three different stages (**Fig. 6.5**). At the initial stage of polymerization, corresponding to 2D or 3D nucleation processes, the current transients can be described by $i = Kt^n$.[359,362,363] An analysis of the current transients at the initial stages of aniline electropolymerization indicates that they can be represented by **Eq. 6.1**:

$$i(t)= K_{ITO}\ (t-t_0)^3 \qquad \textbf{Eq. 6.1}$$

where K_{ITO} depends on the electrode potential and growth geometry and t_0 is an induction time needed before the current rises again. **Fig. 6.6 A** shows $i^{1/3} - t$ plots for PANI electropolymerization at both bare and modified electrodes. The slope observed for bare ITO are very different from those obtained using the mesoporous silica film modified ITO electrodes. These current-time relationships depend on both the kinetics of the nucleation process (instantaneous or progressive) and the geometry of the growing nuclei. In agreement with the literature, these linear trends for $i^{1/3} - t$ corresponds to a model with progressive appearance and 3D growth of PANI islands,[362,363,365] where a progressive nucleation is a process of nuclei creation at a low rate but on a large number of active sites. Such a model would correspond well to the mesoporous silica template where each mesochannel can be considered as an active site of polymerization.

K_{ITO} is usually assumed to be proportional to the anodic term $exp(\alpha zeE/kT)$ of the Butler-Volmer relation, where α is the charge transfer coefficient and z is the number of electrons involved in the electropolymerization reaction, e is the unit charge and k the Boltzmann's constant. Then this prefactor can be expressed by **Eq. 6.2**:

$$K_{ITO} \approx \exp(4\alpha zeE/kT) \qquad \textbf{Eq. 6.2}$$

From this relation the αz-values were estimated. In the case of a bare ITO electrode, this αz-value was equal to 0.54 which is in good agreement with previous results for initial stages of PANI growth on p-doped substrates.[363] Likewise, αz-value was estimated at 0.71 for all three types of mesoporous silica modified electrodes. This variation in the αz-value between bare and modified ITO electrodes indicates a possible change in the potential distribution at the phase boundary at early polymer film/electrode stages and it is attributed to the presence of the silica film. On the other hand, the fact that mesoporous silica modified electrodes have the same charge transfer coefficient values means that the thickness of silica films does not affect the early stage of aniline polymerization and the same polymerization mechanism is followed independently from the film thickness.

During stage II of electropolymerization, PANI nanofilaments are growing through the mesochannels. The current transients increase linearly with time (**Fig. 6.6 B**). It can be interpreted as a 1D growth forced in one direction by the small diameter of the mesochannels (ø = 2.5 nm), limited by the diffusion of monomers of aniline through the pores.[359] If we consider the slope obtained from the curves shown in **Fig. 6.6 B** as the rate (*di/dt*) of PANI chain growth inside of the mesochannels (**Table 6.1**), the thicker film (ITO/SiO_2-200) show a polymerization rate 1.5 times higher than thinner films (ITO/SiO_2-75 and -100). Previous studies have shown that polyaniline oligomers can remain inside an amorphous silica hydrogel.[357,358,366] Confined oligomers are then readily available for polymerization and may explain the improvements on the rates of polymerization for thicker mesostructured films.

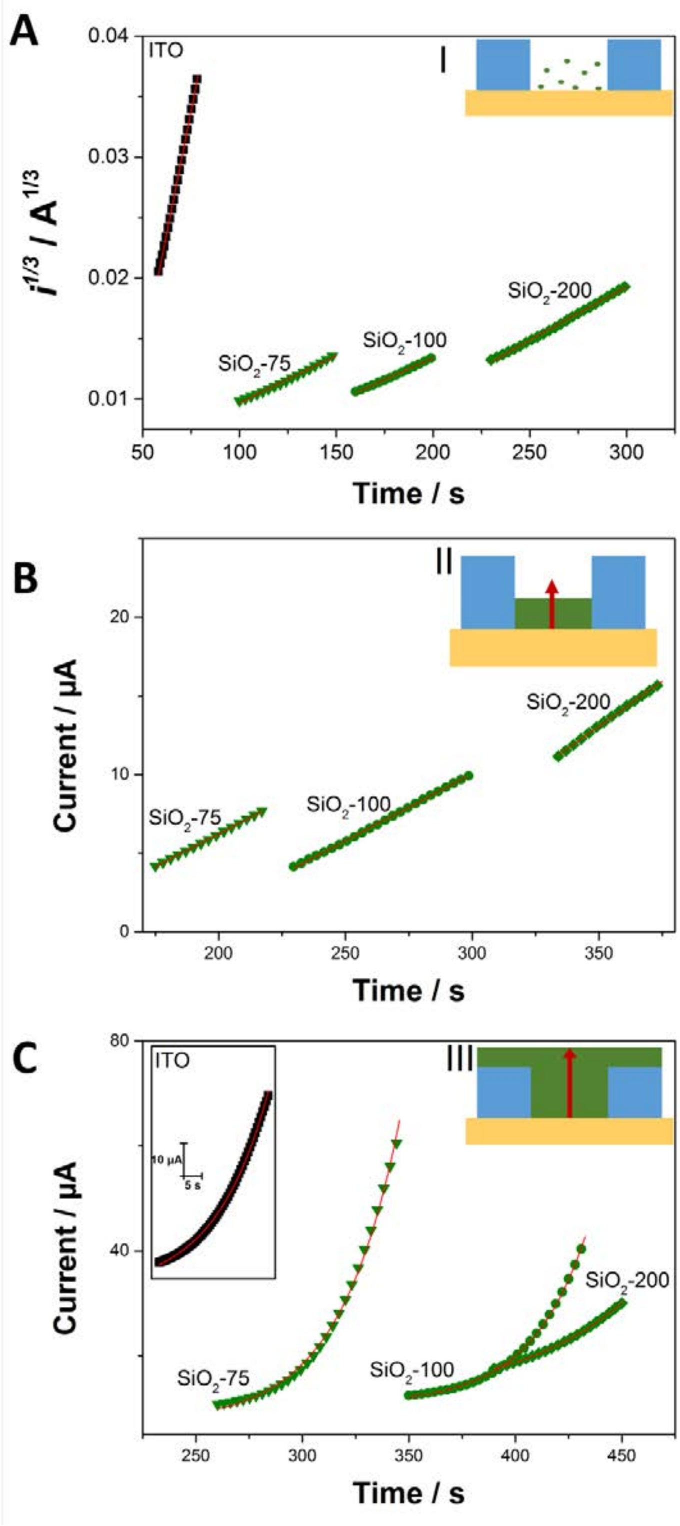

Figure 6.6 Analysis of the current transients for the three stages of the electropolymerization process through mesoporous silica templates. (A) Induction and nucleation; (B) PANI nanofilaments formation within the mesochannels; (C) 3D PANI growth outside the film. Black (bare ITO) and green (modified ITO) solid points are experimental data points whereas red curves are linear (stages I and II) and exponential (stage III) fittings. Insets: corresponding illustrative schemes.

Once the mesochannels are filled, PANI growth is not directed by the mesoporous template and it can happen in all directions as it is observed at bare electrodes (stage III). Monomers are directly incorporated into the already existing PANI chains and the current transients is following an exponential, characteristic of 1D growth in all directions.[301,362,363,367–371] Such exponential growth is observed at both bare and modified electrodes and is delayed as the thickness of mesoporous silica template increases. The time constant measured at the bare electrode was $0.07s^{-1}$, which is in agreement with the literature.[357,358,366] Then, the time constant decreases with the thickness of the template (**Table 6.1**), indicating that PANI nuclei emerging from the mesochannels have less surface density than PANI nuclei formed on ITO bare.

In conclusion, the various stages of the aniline electropolymerization through mesoporous silica template can be followed by chronoamperometry. The PANI formation can then be stopped at any stage of the electropolymerization process for structural and electrochemical characterization.

6.3.2.1 Special case of SiO_2-50

It is known that TEOS concentration is likely to influence the film thickness i.e. increasing TEOS contents from 50 to 200 mM and keeping the same CTAB/TEOS molar ratio as 0.32, has shown a linear relationship between the precursor concentration and the resulting film thickness. Furthermore, herein we have shown the relationship between silica thickness and PANI polymerization. However, ITO/ SiO_2-50 had shown a completely different electrochemical behavior than other modified electrodes ITO/SiO_2-75-200.

First of all, the current transient during the potentiostatic polymerization has significant differences (compared with for example ITO/SiO_2-100 in **Fig. 6.7**). In order to reach the same amount of charge transfer, i.e. 3 mC, this modified electrode has shown the longest time of polymerization close to 1120 s. The shape of the curve shows a constant rise of the current during the time period of 150 s to 300 s. However, after this period of time, a dramatic change on the current transient was observed, the current decrease with a negative slope until reach a minimum value at 600 s (see inset of **Fig. 6.7**). This current transient has similarities with the polymerization over metal substrates with small concentrations of aniline, wherein is reported a formation of non-conductive layers at initial stages of polymerization.[359,365,372,373] Secondly, kinetic studies at stage I of polymerization on ITO/SiO_2-50 have given a αz-value of 0.79, which is slightly different from the case of ITO-SiO_2-75-200 (i.e. 0.71). Stage III kinetic analysis has showed very slow PANI growth, given a time constant of only 003s^{-1}. The hypothesis of this particular behaviour of ITO/SiO_2-50 electrode might be due to partial vertical order of the mesoporous silica film, leading to limited accessibility of oligomers aggregation on the surface of the electrode which is further easily overoxidized by the electropolymerization over potential.

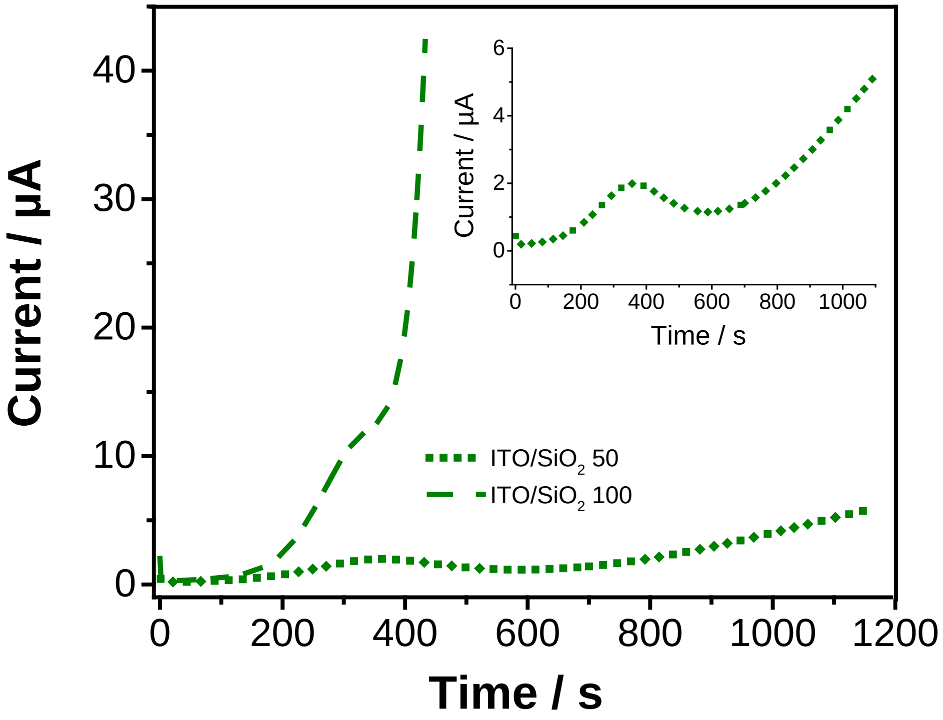

Figure 6.7 Comparison of PANI electropolymerization current transients at ITO/SiO_2-50 (dotted curve) and ITO/SiO_2-100 (dashed curve) electrodes. Inset: magnified current transient on ITO-SiO_2-50.

6.3.3 PANI nanofilaments characterization

6.3.3.1 General observations

PANI deposits obtained by electropolymerization through mesoporous silica films were characterized by SEM and cyclic voltammetry (**Fig. 6.8**). Before aniline electropolymerization, the mesoporous silica film is flat and uniform as observed by SEM and no redox response is measured because it does not contain any electroactive species (**Fig. 6.8, left**). After passing a charge of 1.5 mC to get electropolymerized PANI at the film modified electrode, some deposits appeared on the template surface and a redox signal is observed (**Fig. 6.8, middle**). A peak centered at 0.20 V is recorded during the forward scan. It is related to the oxidation process from leucoemeraldine (undoped-state) to emeraldine (doped-state). The corresponding counter-process is observed with a peak located at 0.14 V, giving a peak-to-peak separation (60 mV) close to a Nernstian behavior. This value is much lower than those usually reported for PANI (in the 120-160 mV range),[370,371,374] suggesting an influence of the mesoporous silica template on the polymerization of one-dimensional ordered polyaniline. The surface redox process (leucoemeraldine-emeraldine) is the consequence of phenomena which include the faradaic process (generation of charged electronic entities at the polymer chains near the electrode surface by the electron transfer to the metal), the transport of these species through the film and the ion exchange at the film/solution interface (to keep the overall electroneutrality, incoming-outcoming of counter-ions). The initial explanations for this hysteresis have been connected to the slow heterogeneous electron transfer, effects of local rearrangements of polymer chains, slow mutual transformations of various electronic species or insufficient conductivity of the film at the beginning of the anodic process.[304,367,375–377]

When more charge is consumed (Q = 2.7 mC), the mesoporous silica film surface is almost completely covered with PANI deposits (**Fig. 6.8, right**). As a consequence, the redox signal is much more prominent with the oxidation peak current increasing by nearly a factor 5 compared to the previous case (Q = 1.5 mC). In addition, the peak-to-peak separation increased to 90 mV.

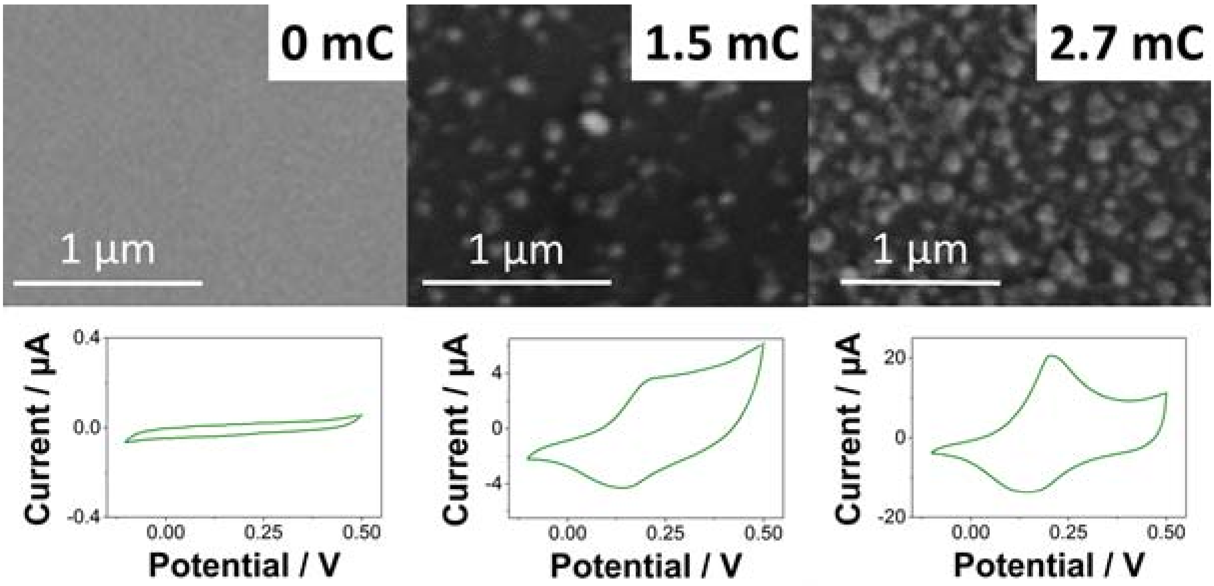

Figure 6.8 SEM (top) and CV (bottom) of ITO/SiO_2-100 electrodes before (0 mC) and after PANI electropolymerization (1.5 and 2.7 mC). CVs were run at 50 mV s^{-1} in 0.5 M H_2SO_4.

6.3.3.2 *Detailed electrochemical characterizations*

To investigate further the influence of the different PANI fillings of the mesochannels on the peak-to-peak separation, the electropolymerization charge has been varied from 0.4 to 6 mC for both ITO and ITO/SiO_2-100 electrodes (**Figure 6.9**). For both electrodes, the peak current increases with the charge passed during electropolymerization. However, as aforementioned, the main difference between ITO and ITO/SiO_2-100 resides in the peak-to-peak separation, ΔE. For an ITO electrode, the separation between the oxidation and the reduction peaks remains at *ca.* 130 mV, regardless of the amount of PANI electrodeposited. However, when PANI is electropolymerized through the mesoporous silica template, ΔE varies. For a low deposition charge (Q = 0.4 mC), ΔE is 120 mV. This could correspond to PANI being electropolymerized in a disorder manner onto the electrode surface at the bottom of the mesochannels and its short conjugation length at earlier stages.[340,378–380] When more PANI is electropolymerized (*i.e.*, $1 \leq Q \leq 2$ mC), ΔE is measured at about 60 mV. PANI polymer chains are grown along the mesochannels in a well-ordered fashion with the help of the silica template. At Q > 2 mC, ΔE increases with the thickness of PANI deposits over the silica film, reaching back the value 120 mV for Q = 6 mC. PANI grows outside the silica template and the electrochemical behavior tends back to the one of PANI electropolymerized directly on bare ITO.

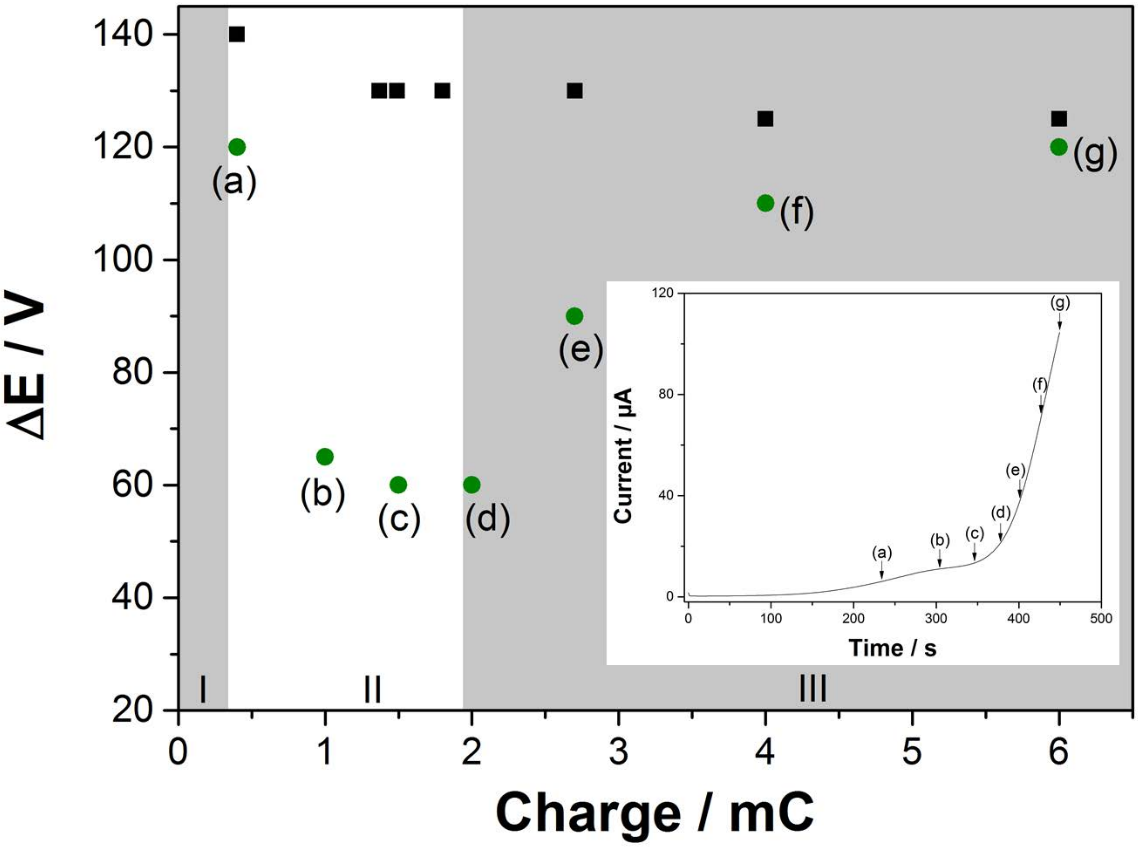

Figure 6.9 Peak-to-peak spearation, ΔE, for the redox signal of PANI grown at an ITO (black squares) and at an ITO/SiO_2-100 (green circles) electrode. Inset: corresponding chronoamperogram for PANI electropolymerization at ITO/SiO_2-100; the arrows mark the various times at which deposition was stopped, corresponding to charges of (a) 0.4, (b) 1, (c) 1.5, (d) 2, (e) 2.7, (f) 4, and (g) 6 mC. Other conditions as in **Fig. 6.5**.

If one considers PANI electropolymerization, by passing the same charge to reach beyond the silica template (Q = 2.7 mC) at different electrodes (ITO, ITO/SiO_2-75, -100 and -200), the shape of PANI oxidation signal from leucoemeraldine to emeraldine varies greatly (**Fig. 6.10**). For thinner films (ITO/SiO_2-75), the oxidation peak of PANI is sharp as for ITO/PANI electrodes (black curve on **Fig. 6.10**), indicating attractive interactions between PANI chains.[301] It supports the response of a 3D growth outside mesoporous silica template, suggesting that, for an electropolymerization charge of Q = 2.7 mC, the PANI has grown significantly on the top of the mesoporous silica film. For thicker films, the PANI oxidation peak grows broader with the film thickness and loses its intensity. The polymer is mainly grown within the mesochannels and the presence of the silica around the PANI filaments limits the interactions between PANI chains. This change on the peak shape is not observed on ITO/PANI modified electrodes wherein branching and electronic percolation occurs easily.[323,367,375] This is further supported by the evolution of the peak-to-peak separation at the different modified electrodes (**Fig. 6.10**). The decrease of the peak-to-peak separation with the template thickness indicates the improvement of the reversibility between the conducting and insulating states of PANI (*i.e.*, oxidized-state or reduced-state). Less energy is probably required for the diffusion of counter-ions in mesochannels than in PANI grown directly on ITO.[376,377,381,382]

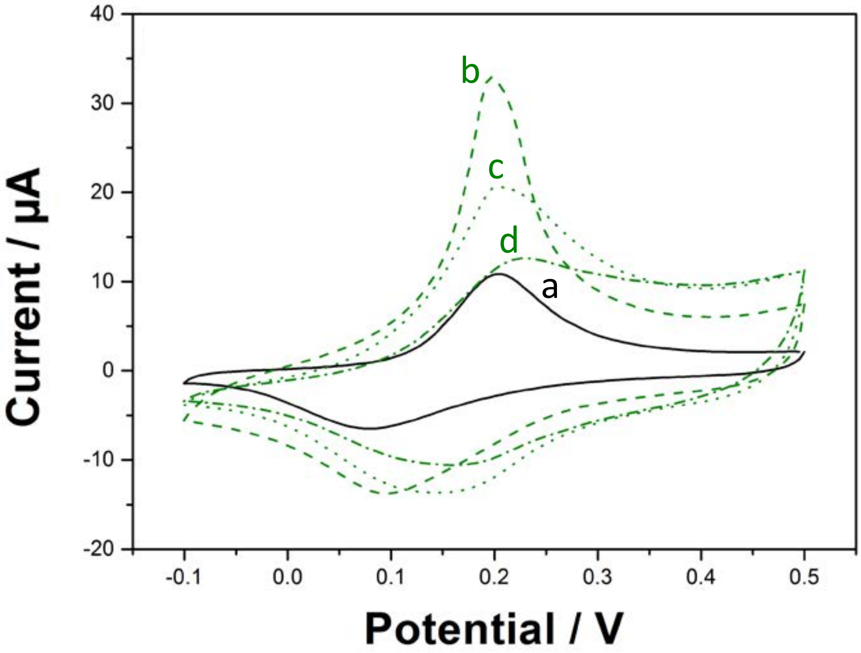

Figure 6.10 CVs of PANI electropolymerized (2.7 mC) at bare ITO (a, solid black line), at ITO/SiO_2-75 (b, dashed green line), ITO/SiO_2-100 (c, dotted green line) and ITO/SiO_2-200 (d, dash-dot green line). CVs were obtained in 0.5 M H_2SO_4 at 50 mV s^{-1}.

Regarding to PANI electropolymerization within the silica film (Q = 0.4 mC), their cyclic voltammograms on **Fig. 6.11 A** display better peak to peak separation between the half-oxidized and reduced state for silica modified electrodes. For instance, ITO/SiO_2-75 shows a peak to peak separation equal to 100 mV, compared to the one at bare ITO which is 130 mV. However, they display lower loads of PANI in contrast to the one at bare ITO electrode (the pseudo-capacitance of PANI obtained at ITO/SiO_2-75, for example, is 25.2 µF.cm^{-2} whereas at bare ITO is 37.8 µF.cm^{-2}. The yield of polymerization through the silica template also follows inverse relation with the silica thicknesses, i.e. less loads of PANI and lower capacitance values are obtained on thicker silica films, despite that same charge values were transferred during the electropolymerization on all the electrodes (0.4 mC). As mentioned before, at this early stage II of polymerization, PANI growth can exist in the form of short conjugated polymers or oligomers on the bottom of the mesochannels which possess yet low conductivity.[340,378–380]

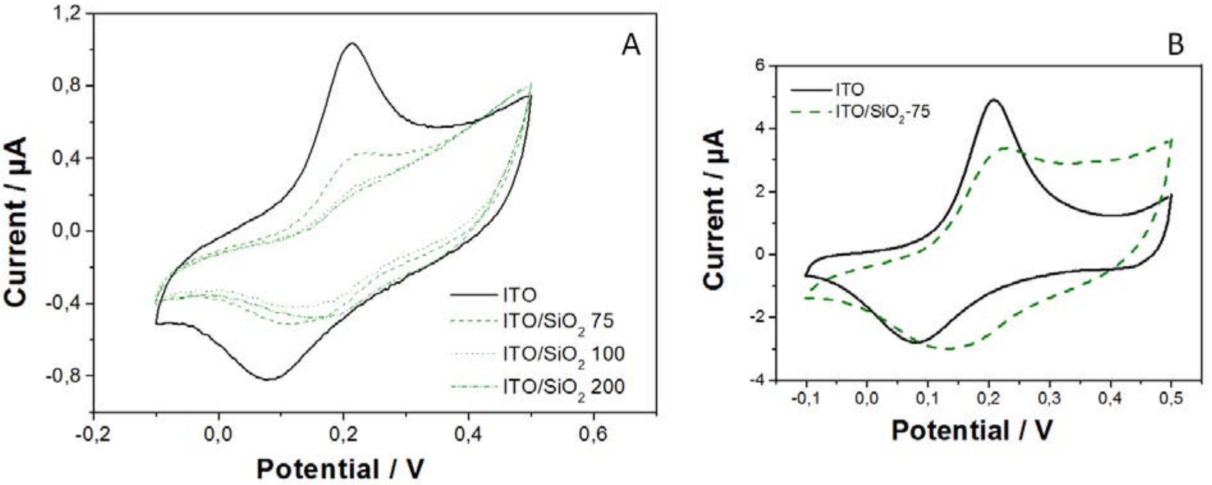

Figure 6.11 CVs of PANI electropolymerized (A) up to the middle of stage II (0.4 mC) at bare ITO (solid black line), at ITO/SiO_2-75 (dashed green line), ITO/SiO_2-100 (dotted green line) and ITO/SiO_2-200 (dash-dot green line) and (B) until the end of stage II (1.4 mC) at bare ITO (solid black line) and ITO/SiO_2-75 (dashed green line). CVs were obtained in 0.5 M H_2SO_4 at 50 mV s^{-1}.

For polymerization up to the amount of charge just enough to fulfill the mesochannels (Q = 1.4 mC), The pseudo-capacitance PANI nanofilaments in silica modified ITO display slight improvement than at bare ITO (**Fig. 6.11 B**), i.e. 2.37 x 10^2 µF cm^{-2} for ITO/SiO_2-75 electrode and 1.37 x 10^2 µF cm^{-2} for bare ITO. The broad peak of PANI nanofilaments shows that the filaments in each mesochannels are separated and does not present attraction between PANI chains.[301]

Taking into account an electropolymerization efficiency of 65%,[359] and 2.7 electrons per aniline monomer (the value reported for polyaniline electrogeneration),[359,383] the amount of PANI formed at a given charge can be evaluated. For instance, at Q = 1.5 mC, a polymer made of roughly 3 × 10^{15} aniline units is expected. Assuming that PANI nanofilaments have been generated only within the mesochannels, and taking into account the total number of mesochannel in the film used for electropolymerization (estimated as being 8 × 10^{12}), this would lead to about 375 aniline units by mesochannel. This value would correspond to a single PANI chain of about 250 nm length, which is in the order of magnitude of the template thickness considered here (ranging between 100 and 200 nm; with some PANI outgrown, see **Fig. 6.8**), suggesting that 1-2 individual PANI chain(s) per mesochannel were generated. With all the precautions imposed by the approximations made in the above calculations, electropolymerization of PANI through such oriented small-pore mesoporous silica templates seems to be a valuable method to generate isolated single chains of conducting polymer.

Regarding to the electrocatalytic behavior of the composites, **Fig. 6.12** shows the redox process of Fe^{2+}/Fe^{3+} couple over different electrodes, wherein, two peaks can be observed during the forward scan. For PANI on bare ITO (black solid line) the first peak appears at 0.20 V related to the leucoemeraldine-emeraldine transition, the second oxidation peak is centered at 0.56 V and is related with the oxidation of the iron (II), indeed the position of this peak is shifted markedly to less positive potentials after the PANI depostion. During the reverse scan the reduction Fe^{3+} species appears at 0.37 V. As a result, the peak to peak separation narrows to 190 mV. At silica modified electrodes, the Fe^{2+} oxidation peak is recorded at 0.49 and 0.54 V for an ITO/SiO_2-75 and -100, respectively. Regarding to the reduction of Fe^{3+}, this peak is shifted to 0.38 and 0.39 V. Hence, the peak potential differences are 110 mV and 150 mV, respectively. In terms of reversibility, the redox process for Fe^{2+}/Fe^{3+} couple is improved with PANI deposits within silica templates.

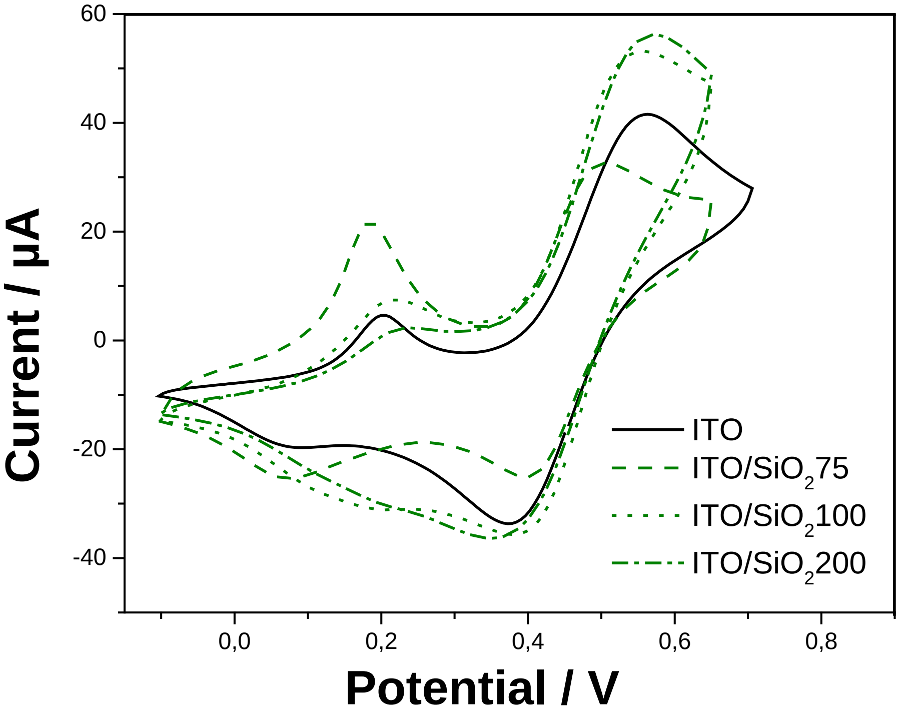

Figure 6.12 Electrochemical response of PANI (Q = 2.7 mC) electropolymerized on bare ITO (black solid line), ITO/SiO_2-75 (b, dashed green line), ITO/SiO_2-100 (c, dotted green line) and ITO/SiO_2-200 (d, dash-dot green line) in 0.5 M H_2SO_4 + 1 mM $FeSO_4/Fe_2(SO_4)_3$. Scan rate: 50 mV s^{-1}

In relation with peak current intensities, the voltammograms of PANI have shown that ITO/SiO_2-100 and -200 displayed higher peak heights than ITO/SiO_2-75. This result can be due to the thicker PANI deposit beyond the template that leads to the decrease of active sites in the polymer-solution interphase, or due to the fact that the active sites are in a limited depth of the polymer.[384,385] For instance, the best electrocatalytic response were recorded on ITO/SiO_2-100 and -200 with an apparent PANI film thickness of 265 and 147 nm, respectively, whereas for an ITO/SiO_2-75 with an apparent-thickness of 393nm has shown the lower current intensity, despite having the highest reversibility. The values of apparent PANI thicknesses were calculated using the Faraday`s law adapted by Genies *et al* for comparative purposes.[308,386]

6.3.3.3 Transmission electron microscopy and X-ray diffraction

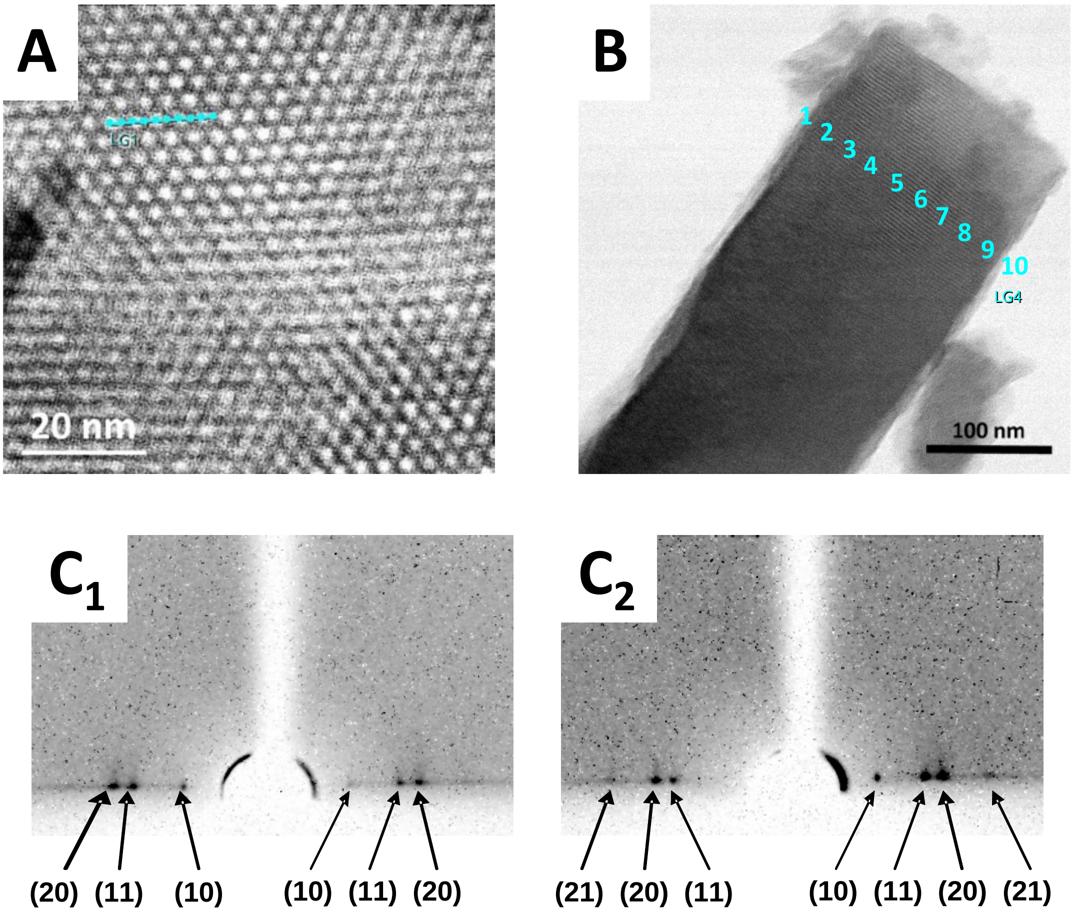

Figure 6.13 (A,B) STEM micrographs of mesoporous silica templates after PANI electropolymerization; (A) top view and (B) cross-section. (C) GIXD diffractograms of the film before (C_1) and after (C_2) PANI deposition. PANI was electropolymerized with Q = 2.7 mC at ITO/SiO_2-200 electrodes

The difficulty of directly visualizing such PANI nanofilaments, formed within templates made of oriented mesochannels of 2.0 nm in diameter for a length of 100-200 nm, arises from their small diameter. In addition to the above electrochemical characterizations (**Figs. 6.9 - 6.11**) suggesting no or few interactions between PANI chains when restricted the electropolymerization to the interior of mesochannels, Scanning Transmission Electron Microscopy (STEM) associated to EDS, Grazing-Incidence X-ray Diffraction (GIXD), as well as UV-vis spectroscopy analyses were undertaken to demonstrate the presence of PANI nanofilaments within the mesochannels. **Figs. 6.13 A-B** shows micrographs obtained by STEM from ITO electrodes modified with mesoporous silica films after electrodeposition of PANI (ITO/SiO_2-200, Q = 2.7 mC). Both the hexagonal arrangement and the orientation of mesochannels are preserved after PANI electropolymerization, as shown on the top-view (**Fig. 6.13 A**) and cross-section (**Fig. 6.13 B**). Furthermore, GIXD data obtained before (**Fig. 6.13 C_1**) and after PANI electrodeposition (**Fig. 6.13 C_2**) exhibit well-defined diffraction spots in the equatorial plane, indicating that long-range hexagonal order and perpendicularity of the mesochannels have not changed after polyaniline deposition through the mesoporous silica film. However, the presence of the polymer had a small effect on the diffraction angles, moving from 2.54° (before) to 2.47° (after electropolymerization), with lattice parameters shifting from 40.2 Å (before) to 42.4 Å (after electropolymerization). These variations do not indicate that the electropolymerization of PANI within the mesochannels is expanding the lattice but rather than the presence of PANI is changing the refraction index of the substrate and hence inducing small changes in the values determined.

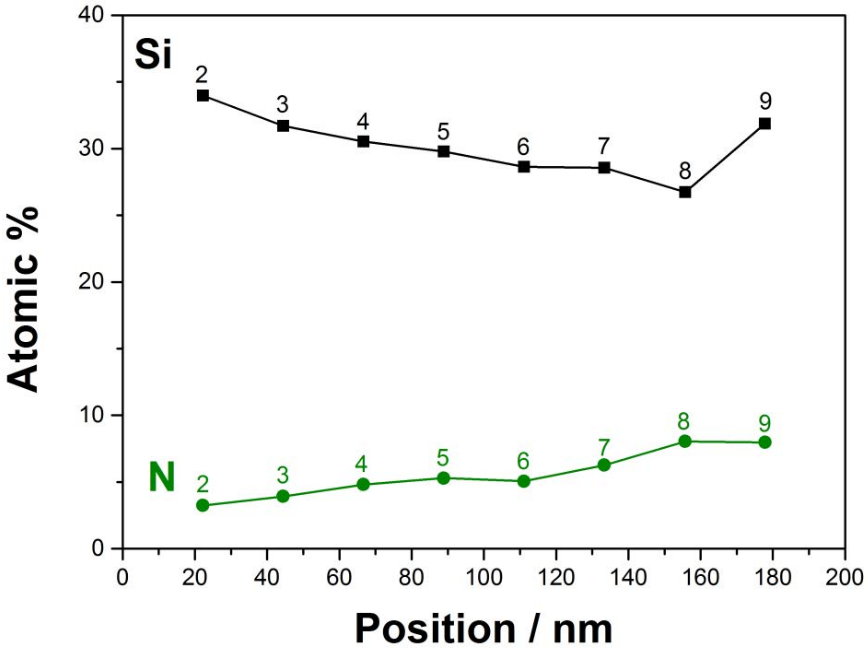

Figure 6.14 Atomic percentage for Si and N determined by EDS on cross-section of the mesoporous silica template modified with PANI (ITO/SiO_2-200, Q = 2.7 mC), at positions indicated on **Fig. 6.13 B**.

In order to further evidence the presence of PANI electropolymerized inside the mesochannels EDS spectra were taken along the whole width of the film, at locations symbolized by blue dots on the spectra (**Fig. 6.13 B**). The atomic % for Si and N is plotted as a function of the position within the mesochannel (**Fig. 6.14**). The number indicated beside the data point correspond to EDS spectra (see an example of EDS spectrum in Figure SI4). The silicon peak arises from the mesoporous silica template, whereas the N peak is coming from the electropolymerized PANI. For position $20 < x < 180$ nm, the EDS spectra reveal that both Si and N are present, confirming the existence of PANI nanofilaments in the mesopore channels. For $x >$ 180 nm and $x < 20$ nm, neither Si nor N are being detected in significant amount as EDS spectra are recorded outside the mesoporous silica template.

6.3.3.3 UV-vis spectroscopy

UV-vis spectroscopy is also able to distinguish between PANI electropolymerized at bare ITO and at electrodes modified with a mesoporous silica template (**Fig. 6.15**). Let us first consider the case of PANI electropolymerized at bare ITO (ITO/PANI). A first band at $\lambda = 315$ nm is visible in both reduced and oxidized forms of PANI, which is due to the π–π^* transition of the aromatic rings and present independently on the oxidation state of the polymer. Then, a second band recorded at $\lambda = 619$ nm in the oxidized form is characteristic of polarons, which is is shifted to $\lambda = 557$ nm for the reduced form of PANI. For a fully reduced form of PANI (leucoemeraldine) the disappearance of this band is expected[387] but it was not the case for ITO/PANI electrode (see left part of **Fig. 6.15**). This is possibly due to the fact that PANI electrodeposited in the absence of template forms cross-linked and intertwined polymeric chains, which result in a loss of conductivity, making electrochemical reduction incomplete. At ITO/SiO_2-100/ PANI, UV-vis spectrum for the oxidized form shows three peaks at $\lambda = 318$, 424 and 668 nm attributed to the π–π^* transition, the protonation of the polymeric backbone and the formation of polarons, respectively.[388] The polaron band for PANI at a silica mesoporous template is shifted to lower energies when compared to the polaron band obtained for PANI electropolymerized at bare ITO, confirming better conductivity of PANI within the mesochannels.[388]

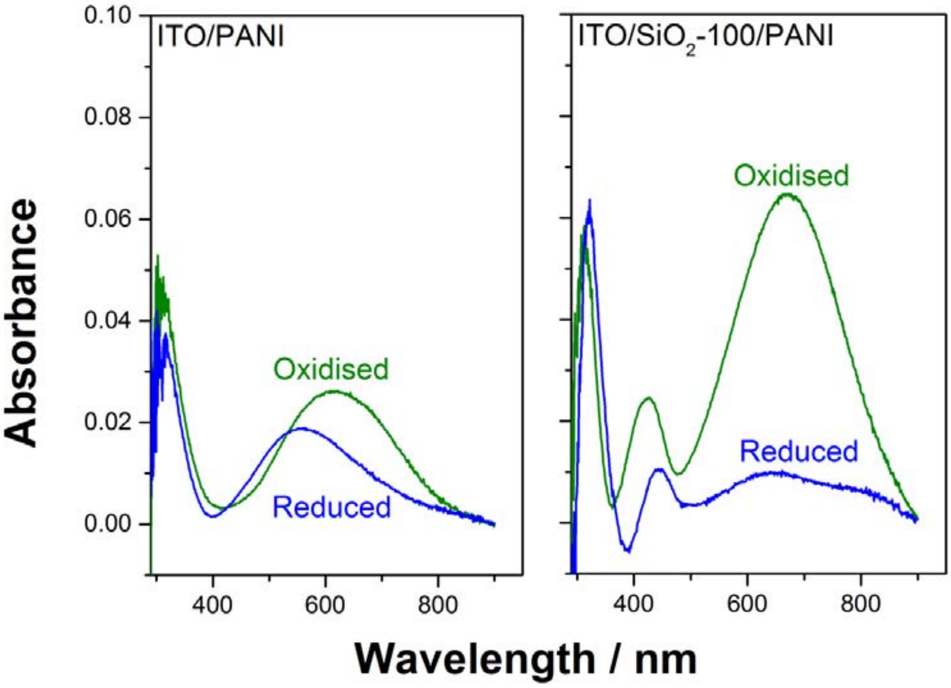

Figure 6.15 UV-vis. spectra of the oxidized (green curves) and reduced (blue curves) forms of PANI electropolymerized at ITO/PANI and ITO/SiO$_2$-100/PANI electrodes (Q = 3 mC). The oxidized form was obtained after linear sweep voltammetry stopped at +0.4 V. PANI was reduced by application of a potential of -0.1 V for 60 s.

After PANI electroreduction, the band at 668 nm has almost entirely disappeared, indicating that the polymer generated through the mesoporous silica film is fully reduced unlike PANI deposited at bare ITO electrodes. Polymeric chains grown within the mesochannels maintain a certain order and ensure almost complete electrochemical reduction of the PANI nanofilaments. The remaining signal for the reduced form at λ = 646 nm is probably due to the PANI that has grown outside the mesoporous silica template (as shown on top right of **Fig. 6.8**). Interestingly, such vanishing of the polarons band after reduction is much more marked than that observed for PANI electrodeposited through wormlike mesoporous films,[389] confirming the ability of the well-ordered, hexagonally packed and oriented mesoporous template to generate PANI nanofilaments that are well separated from each other.

6.3.4 Capacitance studies

Galvanostatic charge/discharge curves were recorded for PANI electropolymerised at a bare ITO electrode (**Fig. 6.16**, curve **a**) and through a mesoporous silica template (**Fig. 6.16**, curves **b** and **c**, corresponding to two different deposition charges). A constant current density of 25 µA cm^{-2} was applied using a three-electrode cell. For all types of electrodes, a typical pseudo-capacitance profile for conducting polymer nanowires was observed.[312] The charge and discharge parts of the curve were symmetrical. A change of slope was observed for all three electrodes at + 0.2 V due to the oxidation of PANI as it is expected from the voltammograms shown in **Fig. 6.8**. This transition from the insulating to the conducting form of PANI induced a faster potential variation. At an electrode modified with /PANI, a charge/discharge cycle lasted 72 s while it lasted only 26 s at an ITO electrode modified with the same charge of PANI (Q = 3 mC). Increasing the PANI electropolymerization charge to Q = 6 mC at an ITO/SiO_2-100 electrode resulted in longer charge/discharge cycles (249 s). This increase of the charge/discharge time obtained with mesoporous silica template results in higher energy than with PANI electropolymerized on ITO. The geometrical capacitance (C) was calculated using **Eq. 6.3**:

$$C = j/(dV/dt) \qquad \textbf{Eq. 6.3}$$

where j is the current density and dV/dt is the positive or negative slope of the curve obtained during charge or discharge experiments, respectively.

The capacitance at ITO/PANI (Q = 3 mC) was estimated at 1.10 ± 0.02 mF cm^{-2}, while the capacitance obtained from PANI nanowires grown through mesoporous silica template increased to 2.96 ± 0.03 mF cm^{-2}. The impact of different PANI morphology (nanowires *vs.* films) was already observed for nanowires grown through an anodic aluminium oxide template, but on the basis of much wider wires (in the range of 200 nm) and the capacitance enhancement with respect to bulk PANI film was only around 20%.[390,391] In the case of PANI grown through mesoporous silica template, yet with some PANI having outgrown the film, capacitance was increased by 269 %. Taking into account the amount of deposited PANI, the value of 2.96 mF cm^{-2} corresponds to about 600 F g^{-1}, *i.e.*, of the same order of magnitude as for other PANI nanostructures.[91] When the electropolymerization charge is further increased to 6 mC, the capacitance reached to 11.0 ± 0.2 mF cm^{-2} (1100 F g^{-1}) for ITO/SiO$_2$-100/PANI electrodes while the capacitance was 2.50 ± 0.02 mF cm^{-2} for ITO/PANI (*i.e.*, 4.4 times lower).

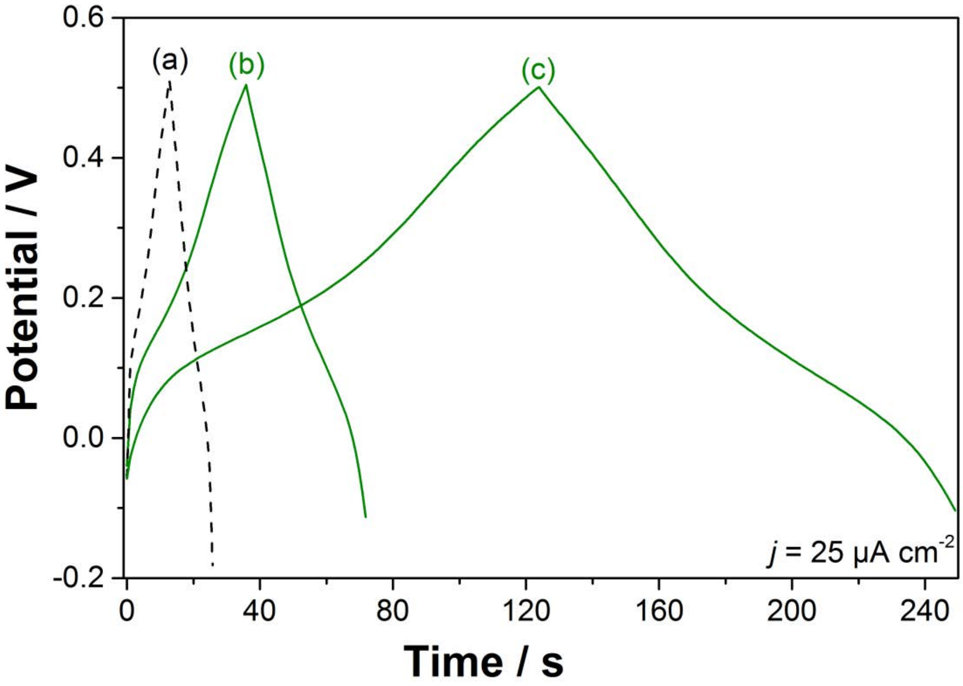

Figure 6.16 Galvanostatic charge/discharge curves for PANI at an ITO electrode (*Q* = 3 mC) (a), ITO/SiO$_2$-100 (*Q* = 3 mC) (b) and ITO/SiO$_2$-100 (*Q* = 6mC). The electrolyte solution was 0.5 M HNO$_3$.

6.4 Conclusions

Controlled growth of vertically-aligned polyaniline nanofilaments has been achieved by aniline electropolymerization through mesoporous silica templates. Operating at constant potential, the corresponding chronoamperometric transients indicate three regimes during the polymerization reaction (induction period, filament growth, subsequent deposition outside the mesochannels). The characterization of silica/PANI composites by STEM, EDS and GIXD confirmed the production of PANI nanofilaments inside the mesoporous channels, while PANI deposits outside the film were visible by SEM. Cyclic voltammetry studies have shown the influence of the mesoporous silica template on the polymerization of one-dimensional ordered polyaniline, wherein, a considerable improvement on the reversibility related to the emeraldine-lucomeraldine states (doped and undoped states) was pointed out. A faster counter-ions switching during the oxidation and reduction of the polymer chains is thus expected for such 1D isolated nanostructure. Electrochemical doping-dedoping experiments, as followed by UV-vis spectroscopy and charge-discharge measurements have shown that higher surface area of nanofilaments is in contact with the solution in comparison with conventional of bulk PANI deposits on ITO. Furthermore the capacitance displayed by mesoporous silica/PANI composites was several times higher than the capacitance of ITO/PANI synthesized in the same conditions. These results are indicative that well-ordered mesostructured silica avoids as much as possible contact and electric collapse between conducting PANI nanofilaments, in comparison with conventional ITO/PANI electrodes.

General Conclusion and Outlook

In this thesis, focus was drawn into a very specific type of electrode modification, i.e. vertically-aligned mesoporous silica thin film deposited on ITO by the electrochemically assisted self-assembly (EASA) method. Here, it was demonstrated that this type of thin film can attribute to three main functions, described below:

1. To study of mass transport and charge transfer through the negatively charged silica mesochannels. Generally, negatively charged species undergoes repulsion with the silica surface whereas the neutral ones can diffuse through. The positively charged ones can not only diffuse but also be adsorbed. Furthermore, a deeper study showed the possibility to mediate the charge transfer between the repulsed anions and the diffusing neutral and positively electroactive charged species
2. To become the host of functional species immobilization, by applying a versatile method called Huisgen click chemistry where as-deposited azide-functionalized silica films are reacted with ethynyl-bearing functional groups. Here, it was presented that the method was versatile and can be used for immobilizing different functional groups addressing different specific applications, such as:
   a. Ferrocene-functionalized silica film was proven to be able to detect non-electroactive anions in aqueous solution based on the diffusion of negatively

    charged species to compensate the positively charged ferrocinium species formed upon oxidation of the grafted ferrocene moeties.

    b. Ruthenium-trisbipyridyl-functionalized silica film presented the possibility to use the modified electrode for oxygen sensing or electrochemiluminescence-based detections.

3. To be used as a hard-template for the growth of a conducting polymer-based nanofilaments, notably polyaniline (PANI), which improves the redox properties (reversibility and capacitance) of the deposited nanosized PANI compared to bulk PANI deposit.

Lastly, the future outlook of this particular vertically-aligned mesoporous silica thin film can be towards the immobilization of other interesting functional groups displaying photo- and electrochrome properties (see Apendix II and III). Furthermore, it can be interesting to try to remove the silica template used for growing PANI nanofilaments, to produce a free-standing PANI nanofilaments modified electrode to improve further the capacitance of the system (see Apendix IV).

Conclusion Générale et Perspectives

Dans cette thèse, des électrodes modifiées par des films minces de silice présentant une orientation des canaux mésoporeux perpendiculaire au substrat ont été générés sur ITO par la méthode d'auto-assemblage assisté par électrochimie (EASA). Ce type de films a pu être utilisé dans trois principales directions décrites ci-dessous :

1. Étude du transport de matière ainsi que du transfert de charge au travers des mésopores de silice dont la surface est chargée négativement. Les interactions électrostatiques ayant lieu entre la surface négative et les espèces chargées sont responsables de la répulsion des anions (transport restreint/ralenti au travers des mésopores) ainsi que de l'accumulation des espèces cationiques au sein du matériau. Une étude plus approfondie a montré la possibilité de médiation du transfert de charge entre les espèces anioniques exclues, via le recours à des espèces neutres capables de diffuser librement au travers des films.
2. La méthode EASA a été utilisée avec succès pour l'obtention de films azoturés qui ont été ultérieurement fonctionnalisés par chimie click par réaction des groupes azoture avec des entités porteuses d'une fonction alcyne. La souplesse de cette méthode de fonctionnalisation a été démontrée selon deux voies :

    a. La préparation de films fonctionnalisés par des groupements électroactifs de type ferrocène, ce qui a permis la détection d'anions non-électroactifs par compensation de la charge positive générée suite à l'oxydation du ferrocène en ferricinium.
    b. La fonctionnalisation par des complexes de ruthenium tris-bipyridine a permis d'obtenir des résultats préliminaires vers le développement de capteurs pour la détection d'oxygène et de dispositifs électroluminescents.
3. Ces films minces de silice organisés ont été utilisés avec succès pour la croissance contrôlée de nanofilaments d'un polymère conducteur, la polyaniline (PANI). Leur confinement dans ce type de matériau a permis l'amélioration de leurs propriétés (réversibilité redox et capacitance).

L'immobilisation d'autres groupes fonctionnels d'intérêt est prévue pour essayer de faire croître des fils moléculaires avec des propriétés photo- et électrochromes (voir Appendix II et III). L'élimination de la matrice de silice pour l'obtention d'une électrode modifiée par des nanofilaments indépendants du polymère conducteur à base d'aniline est aussi envisagée (voir Appendix IV).

References

1. Zhao, D., Wan, Y. & Zhou, W. *Ordered mesoporous materials*. (Wiley-VCH Verlag & Co. KGaA, 2013).

2. Kresge, C. T. & Roth, W. J. The discovery of mesoporous molecular sieves from the twenty year perspective. *Chem. Soc. Rev.* **42,** 3663–3670 (2013).

3. Kresge, C. T., Leonowicz, M. E., Roth, W. J., Vartuli, J. C. & Beck, J. S. Ordered mesoporous molecular sieves synthesized by a liquid-crystal template mechanism. *Nature* **359,** 710–712 (1992).

4. Kresge, C. T., Leonowicz, M. E., Roth, W. J. & Vartuli, J. C. U.S. Patent 5098684: Synthetic Mesoporous Crystaline Material. (1992).

5. Kresge, C. T., Leonowicz, M. E., Roth, W. J. & Vartuli, J. C. U.S. Patent 5102643: Composition of Synthetic Porous Crystalline Material, Its Synthesis. (1992).

6. Beck, J. S., Vartuli, J. C., Roth, W. J., Leonowicz, M. E., Kresge, C. T., Schmitt, K. D., Chu, C. T-W., Olson, D. H., Sheppard, E. W., McCullen, S. B., Higgins, J. B. & Schlenkert, J. L. A New Family of Mesoporous Molecular Sieves Prepared with Liquid Crystal Templates. *J. Am. Chem. Soc.* **114,** 10834–10843 (1992).

7. C. Brinker & Scherer, G. *Sol-Gel Science: The Physics and Chemistry of Sol-Gel Processing*. (Academic Press, Inc., 1990).

8. Iler, R. K. *The Chemistry of Silica*. (John Wiley & Sons, 1979).

9. Brinker, C. J. Hydrolysis and Condensation of Silicates: Effects on Structure. *J. Non. Cryst. Solids* **100,** 31–50 (1988).

10. Lu, A. H. & Schüth, F. Nanocasting: A versatile strategy for creating nanostructured porous materials. *Adv. Mater.* **18,** 1793–1805 (2006).

11. Donk, V., Sander, Janssen, A. H., Bitter, J. H. & de Jong, K. P. Generation, Characterization, and Impact of Mesopores in Zeolite Catalysts. *Catal. Rev. Sci. Eng.* **45,** 297–319 (2003).

12. Hoffmann, F., Cornelius, M., Morell, J. & Fröba, M. Silica-based mesoporous organic-inorganic hybrid materials. *Angew. Chemie - Int. Ed.* **45,** 3216–3251 (2006).

13. Goltner, C. G. & Antonietti, M. Mesoporous materials by templating of liquid crystalline phases. *Adv. Mater.* **9,** 431–436 (1997).

14. Hoffmann, F. & Fröba, M. Vitalising porous inorganic silica networks with organic functions—PMOs and related hybrid materials. *Chem. Soc. Rev.* **40,** 608–620 (2011).

15. Walcarius, A. Mesoporous materials and electrochemistry. *Chem. Soc. Rev.* **42,** 4098–4140 (2013).

16. Zhu, G. Yang, Q., Jiang, D., Yang, J., Zhang, L., Li, Y. & Li, C. Synthesis of bifunctionalized mesoporous organosilica spheres for high-performance liquid chromatography. *J. Chromatogr. A* **1103,** 257–264 (2006).

17. Ma, Y., Qi, L., Ma, J., Wu, Y., Liu, O. & Cheng, H. Large-pore mesoporous silica spheres: Synthesis and application in HPLC. *Colloids Surfaces A Physicochem. Eng. Asp.* **229,** 1–8 (2003).

18. Katiyar, A., Yadav, S., Smirniotis, P. G. & Pinto, N. G. Synthesis of ordered large pore SBA-15 spherical particles for adsorption of biomolecules. *J. Chromatogr. A* **1122,** 13–20 (2006).

19. Huo, Q., Zhao, D., Feng, J., Weston, K., Buratto, S. K., Stucky, G. D., Scacht, S. & Shuth, F. Room temperature growth of mesoporous silica fibres: A new high-surface-area optical waveguide. *Adv. Mater.* **9,** 974–978 (1997).

20. Yao, B., Fleming, D., Morris, M. A. & Lawrence, S. E. Structural control of mesoporous silica nanowire arrays in porous alumina membranes. *Chem. Mater.* **16,** 4851–4855 (2004).

21. Che, S., Liu, Z., Ohsuna, T., Sakamoto, K., Terasaki, O. & Tatsumi, T. Synthesis and characterization of chiral mesoporous silica. *Nature* **429,** 281–285 (2004).

22. Yang, Y., Suzuki, M., Owa, S., Shirai, H. & Hanabusa, K. Control of helical silica nanostructures using a chiral surfactant. *J. Mater. Chem.* **16,** 1644 (2006).

23. Teng, Z., Zheng, G., Dou, Y., Li, W., Mou, C. Y., Zhang, X., Asiri, A. M. & Zhao, D. Highly ordered mesoporous silica films with perpendicular mesochannels by a simple stober-solution growth approach. *Angew. Chemie - Int. Ed.* **51,** 2173–2177 (2012).

24. Lu, Y., Fan, H., Stump, A., Ward, T. L., Rieker, T., Brinker, J. C. Aerosol-assisted self-assembly of mesostructured spherical nanoparticles. *Nature* **398,** 223–226 (1999).

25. Sen, T., Tiddy, G. J. T., Casci, J. L. & Anderson, M. W. Synthesis and characterization of hierarchically ordered porous silica materials. *Chem. Mater.* **16,** 2044–2054 (2004).

26. Yu, C., Tian, B., Fan, J., Stucky, G. D. & Zhao, D. Nonionic block copolymer synthesis of large-pore cubic mesoporous single crystals by use of inorganic salts. *J. Am. Chem. Soc.* **124,** 4556–4557 (2002).

27. Innocenzi, P. & Malfatti, L. Mesoporous thin films: Properties and applications. *Chem. Soc. Rev.* **42,** 4198–216 (2013).

28. Brinker, J. C., Lu, Y., Sellinger, A. & Fan, H. Evaporation-induced self-assembly: Nanostructures made easy. *Adv. Mater.* **11,** 579–585 (1999).

29. Yang, H., Coombs, N., Sokolov, I. & Ozin, G. a. Free-standing and oriented mesoporous silica films grown at the air-water interface. *Nature* **381,** 589–592 (1996).

30. Grosso, D., Cagnol, F., Soler-Illia, G. J. A. A., Crepaldi, E. L., Amenitsch, H., Brunet-Bruneau, A., Bourgeois, A. & Sanchez, C. Fundamentals of mesostructuring through evaporation-induced self-assembly. *Adv. Funct. Mater.* **14,** 309–322 (2004).

31. Murray, R. W. Chemically modified electrodes. *Acc. Chem. Res.* **117,** 135–141 (1980).

32. Bard, A. J., Faulkner, L. R., Swain, E. & Robey, C. *Fundamentals and Applications*.

33. Alkire, R. C., Kolb, D. M., Lipkowski, J. & Ross, P. N. *Chemically Modified Electrodes*. *Advances in Electrochemical Science and Engineering* (Wiley-VCH Verlag GmbH & Co. KGaA, 2009).

34. Bonaventura, J., Ignarro, L. & Dowling, David B. Dowling Spivack, A. J. U.S. Patent 6524466 Method and system of preventing fouling and corrosion of biomedical devices and structures. **US6524466,** 1–11 (2003).

35. Yen, H.-J., Lin, K.-Y. & Liou, G.-S. Transmissive to black electrochromic aramids with high near-infrared and multicolor electrochromism based on electroactive tetraphenylbenzidine units. *J. Mater. Chem.* **21,** 6230 (2011).

36. Murray, R. W. Chemically modified electrodes for electrocatalysis. *Phil. Trans. R. Soc. Lond. A* **A,** 253–265 (1981).

37. Li, T., Hauptmann, J. R., Wei, Z., Petersen, S., Bovet, N., Vosch, T., Nygãrd, J., Hu, W., Liu, Y., Bjørnholm, T., Nørgaard, K. & Laursen, B. W. Solution-processed ultrathin chemically derived graphene films as soft top contacts for solid-state molecular electronic junctions. *Adv. Mater.* **24,** 1333–1339 (2012).

38. Murugaiyan, S. B., Ramasamy, R., Gopal, N. & Kuzhandaivelu, V. Biosensors in clinical chemistry: An overview. *Adv. Biomed. Res.* **3,** 67 (2014).

39. Lenhard, J. R. & Royce, W. Coverage, decay kinetics , and solvent and interaction effects for ferrocenes covalently linked to platinum electrodes. *J. Am. Chem. Soc* **100,** 7870–7875 (1978).

40. Tse, D. C. S., Kuwana, T. & Royer, G. P. Stable attachment of redox groups for modified electrodes via cyanuric chloride. *J. Electroanal. Chem. Interfacial Electrochem.* **98,** 345–353 (1979).

41. Koval, C. A. & Anson, F. C. Electrochemistry of the ruthenium(3+, 2+) couple attached to graphite electrodes. *Anal. Chem.* **50,** 223–229 (1978).

42. Umana, M. & Waller, J. Protein-modified electrodes. The glucose oxidase/polypyrrole system. *Anal. Chem.* **58,** 2979–2983 (1986).

43. Gholamian, M., Sundaram, J. & Contractor, A. Q. Oxidation of formic acid at polyaniline-coated and modified-polyaniline-coated electrodes. *Langmuir* **3,** 741–744 (1987).

44. Leddy, J. & Bard, A. J. Polymer films on electrodes. Part XVIII. Determination of heterogeneous electron transfer kinetics at poly(vinylferrocene) and nafion/Ru(bpy)$^{2+/3+}$ polymer-modified electrodes by convolution voltammetry. *J. Electroanal. Chem.* **189,** 203–219 (1985).

45. White, H. S., Leddy, J. & Bard, A. J. Polymer films on electrodes. 8. Investigation of charge-transport mechanisms in Nafion polymer modified electrodes. *J. Am. Chem. Soc.* **104,** 4811–4817 (1982).

46. Calvo, E. J., Battaglini, F., Danilowicz, C., Wolosiuk, A. & Otero, M. Layer-by-layer electrostatic deposition of biomolecules on surfaces for molecular recognition, redox mediation and signal generation. *Faraday Discuss.* **116,** 47–65 (2000).

47. Masuda, H., Yada, K. & Osaka, A. Self-ordering of cell configuration of anodic porous alumina with large-size pores in phosphoric acid solution. *Jpn. J. Appl. Phys.* **37,** 1340–1342 (1998).

48. Balog, M., Schieber, M., Patai, S. & Michman, M. Thin films of metal oxides on silicon by chemical vapor deposition with organometallic compounds. I. *J. Cryst. Growth* **17,** 298–301 (1972).

49. Meyer, J., Hamwi, S., Kroger, M., Kowalsky, W., Riedl, T. & Kahn, A. Transition metal oxides for organic electronics: Energetics, device physics and applications. *Adv. Mater.* **24,** 5408–5427 (2012).

50. Connor, P., A, Dobson, K. D. & Mcquillan, A. J. Infrared spectroscopy of the TiO_2 / aqueous solution interface. *Langmuir* **15,** 2402–2408 (1999).

51. Zhang, Z., Liu, J., Gu, J., Su, L. & Cheng, L. An overview of metal oxide materials as electrocatalysts and supports for polymer electrolyte fuel cells. *Energy Environ. Sci.* **7,** 2535 (2014).

52. Melde, B. J., Johnson, B. J. & Charles, P. T. Mesoporous silicate materials in sensing. *Sensors* **8,** 5202–5228 (2008).

53. Walcarius, A. Electroanalytical applications of microporous zeolites and mesoporous (organo)silicas: Recent trends. *Electroanalysis* **20,** 711–738 (2008).

54. Walcarius, A. Analytical applications of silica-modified electrodes - A comprehensive review. *Electroanalysis* **10,** 1217–1235 (1998).

55. Švancara, I., Kalcher, K., Walcarius, A. & Vytřas, K. *Electroanalysis with carbon paste electrodes*. (CRC Press, 2012).

56. Boyer, A., Kalcher, K. & Pietsch, R. Voltammetric behavior of perborate on prussian blue modified carbon paste electrodes. *Electroanalysis* **2,** 155–161 (1990).

57. Ricci, F., Goncalves, C. & Amine, A. Electroanalytical study of Prussian Blue modified glassy carbon paste electrodes. *Electroanalysis* **15,** 1204–1211 (2003).

58. Wang, X. L., Wang, E. B., Lan, Y. & Hu, C. W. Renewable PMo12-based inorganic-organic hybrid material bulk-modified carbon paste electrode: Preparation, electrochemistry and electrocatalysis. *Electroanalysis* **14,** 1116–1121 (2002).

59. Han, Z., Zhao, Y., Peng, J., Feng, Y., Yin, J. & Liu, Q. The electrochemical behavior of keggin polyoxometalate modified by tricyclic, aromatic entity. *Electroanalysis* **17,** 1097–1102 (2005).

60. Navrátilová, Z. & Kula, P. Cation and anion exchange on clay modified electrodes. *J. Solid State Electrochem.* **4,** 342–347 (2000).

61. Xu, G., Fan, J. & Jiao, K. Immobilizing DNA on clay mineral modified carbon paste electrodes. *Appl. Clay Sci.* **40,** 119–123 (2008).

62. Walcarius, A., Barbaise, T. & Bessiere, J. Factors affecting the analytical applications of zeolite-modified electrodes preconcentration of electroactive species. *Anal. Chim. Acta* **340,** 61–76 (1997).

63. Walcarius, A. & Lamberts, L. Voltammetric response of the hexammino-ruthenium complex incorporated in zeolite-modified carbon paste electrode. *J. Electroanal. Chem.* **422,** 77–89 (1997).

64. Švancara, I., Walcarius, A., Kalcher, K. & Vytřas, K. Carbon paste electrodes in the new millennium. *Cent. Eur. J. Chem.* **7,** 598–656 (2009).

65. Wang, J. & Taha, Z. Catalytic oxidation and flow detection of carbohydrates at ruthenium dioxide modified electrodes. *Anal. Chem.* **62,** 1413–1416 (1990).

66. Cataldi, T. R. I. & Centonze, D. Development of a carbon composite electrode made from polyethylene and graphite powder modified with copper(I) oxide. *Anal. Chim. Acta* **326,** 107–115 (1996).

67. Schachl, K., Alemu, H., Kalcher, K., Jezkova, J., Švancara, I. & Vytras, K. Flow injection determination of hydrogen peroxide using a carbon paste electrode modified with a manganese dioxide film. *Anal. Lett.* **30,** 2655–2673 (1997).

68. Wang, J., Naser, N., Angnes, L., Wu, H. & Chen, L. Metal-dispersed carbon paste electrodes. *Anal. Chem.* **64,** 1285–1288 (1992).

69. Wang, J., Rivas, G. & Chicharro, M. Iridium dispersed carbon paste enzyme electrodes. *Electroanalysis* **8,** 434–437 (1996).

70. Liu, J., Lu, F. & Wang, J. Metal-alloy-dispersed carbon-paste enzyme electrodes for amperometric biosensing of glucose. *Electrochem. commun.* **1,** 341–344 (1999).

71. Švancara, I., Vytřas, K., Kalcher, K., Walcarius, A. & Wang, J. Carbon paste electrodes in facts, numbers, and notes: A review on the occasion of the 50-years jubilee of carbon paste in electrochemistry and electroanalysis. *Electroanalysis* **21,** 7–28 (2009).

72. Ravichandran, K. & Baldwin, R. P. Chemically modified carbon paste electrodes. *J. Electroanal. Chem* **126,** 293–300 (1981).

73. Erdem, A., Kerman, K., Meric, B., Akarca, U. S. & Ozsoz, M. Novel hybridization indicator methylene blue for the electrochemical detection of short DNA sequences related to the hepatitis B virus. *Anal. Chim. Acta* **422,** 139–149 (2000).

74. Mullor, G. S. ., Sanchez-Cabezudo, M. ., Ordieres, M. A. J. . & Ruiz, B. L. Alcohol biosensor based on the immobilization of meldola blue and alcohol dehydrogenase into a carbon nanotube paste electrode. *Talanta* **43,** 779–784 (1996).

75. Wang, J., Mo, J.-W., Li, S. & Porter, J. Comparison of oxygen-rich and mediator-based glucose-oxidase carbon-paste electrodes. *Anal. Chim. Acta* **441,** 183–189 (2001).

76. Huang, X. & Kok, W. T. Conductive carbon cement as electrode matrix for cobalt phthalocyanine modified electrodes for detection in flowing solutions. *Anal. Chim. Acta* **273,** 245–253 (1993).

77. Wang, L. & Tseng, S. Direct determination of d -panthenol and salt of pantothenic acid in cosmetic and pharmaceutical preparations by differential pulse voltammetry. *Anal. Chim. Acta* **432,** 39–48 (2001).

78. Ormonde, D. E. & O'Neill, R. D. Altered response of carbon paste electrodes after contact with brain tissue. Implications for modified electrode use in vivo. *J. Electroanal. Chem.* **261,** 463–469 (1989).

79. Escribano, M. T. S., Procopio, J. R., Macias, J. M. P. & Hernandez, L. H. Determination of Lead with a Carbon Paste Electrode Modified with a Chelating Resin in Rainwater and Human Urine. *Int. J. Environ. Anal. Chem.* **37,** 107–115 (1989).

80. Wang, J., Geene, B. & Morgan, C. Carbon paste electrodes modified with cation-exchange resin in differential pulse voltammetry. *Anal. Chim. Acta* **158,** 15–22 (1984).

81. Andrieux, C. P., Audebert, P., Bacchi, P. & Divisia-Blohorn, B. Kinetic behaviour of an amperometric biosensor made of an enzymatic carbon paste and a Nafion® gel investigated by rotating electrode studies. *J. Electroanal. Chem.* **394,** 141–148 (1995).

82. Bu, H. Z., Mikkelsen, S. R. & English, A. M. NAD(P)H sensors based on enzyme entrapment in ferrocene- containing polyacrylamide-based redox gels. *Anal. Chem.* **70,** 4320–4325 (1998).

83. Lvova, L., Kim, S. S., Legin, A., Vlasov, Y., Yang, J. S., Cha, G. S. & Nam, H. All-solid-state electronic tongue and its application for beverage analysis. *Anal. Chim. Acta* **468,** 303–314 (2002).

84. Etienne, M., Guillemin, Y., Grosso, D. & Walcarius, A. Electrochemical approaches for the fabrication and/or characterization of pure and hybrid templated mesoporous oxide thin films: A review. *Anal. Bioanal. Chem.* **405,** 1497–1512 (2013).

85. Etienne, M., Quach, A., Grosso, D., Nicole, L., Sanchez, C. & Walcarius, A. Molecular transport into mesostructured silica thin films: Electrochemical monitoring and comparison between p6m , P63/mmc , and Pm3n structures. *Chem. Mater.* **19,** 844–856 (2007).

86. Etienne, M., Goux, A., Sibottier, E. & Walcarius, A. Oriented mesoporous organosilica films on electrode: A new class of nanomaterials for sensing. *J. Nanosci. Nanotechnol.* **9,** 2398–406 (2009).

87. Guillemin, Y., Etienne, M., Aubert, E. & Walcarius, A. Electrogeneration of highly methylated mesoporous silica thin films with vertically-aligned mesochannels and electrochemical monitoring of mass transport issues. *J. Mater. Chem.* **20,** 6799 (2010).

88. Yu, J.-J., Lu, S., Li, J.-W., Zhao, F.-Q. & Zeng, B.-Z. Characterization of gold nanoparticles electrochemically deposited on amine-functioned mesoporous silica films and electrocatalytic oxidation of glucose. *J. Solid State Electrochem.* **11,** 1211–1219 (2007).

89. Vinoba, M., Jeong, S.-K., Bhagiyalakshmi, M. & Alagar, M. Electrocatalytic reduction of hydrogen peroxide on silver nanoparticles stabilized by amine grafted mesoporous SBA-15. *Bull. Korean Chem. Soc.* **31,** 3668–3674 (2010).

90. Walcarius, A., Etienne, M., Sayen, S. & Lebeau, B. Grafted silicas in electroanalysis: Amorphous versus ordered mesoporous materials. *Electroanalysis* **15,** 414–421 (2003).

91. Goubert-Renaudin, S., Etienne, M., Rousselin, Y., Denat, F., Lebeau, B &, Walcarius, A. Cyclam-functionalized silica-modified electrodes for selective determination of Cu(II). *Electroanalysis* **21,** 280–289 (2009).

92. Goubert-Renaudin, S., Moreau, M., Despas, C., Meyer, M., Denat, F., Lebeau, B. & Walcarius, A. Voltammetric detection of lead(II) using amide-cyclam-functionalized silica-modified carbon paste electrodes. *Electroanalysis* **21,** 1731–1742 (2009).

93. Dai, Z. H., Ni, J., Huang, X. H., Lu, G. F. & Bao, J. C. Direct electrochemistry of glucose oxidase immobilized on a hexagonal mesoporous silica-MCM-41 matrix. *Bioelectrochemistry* **70,** 250–256 (2007).

94. Dai, Z., Ju, H. & Chen, H. Mesoporous materials promoting direct electrochemistry and electrocatalysis of horseradish peroxidase. *Electroanalysis* **17,** 862–868 (2005).

95. Zhang, L., Zhang, Q. & Li, J. Direct electrochemistry and electrocatalysis of hemoglobin immobilized in bimodal mesoporous silica and chitosan inorganic-organic hybrid film. *Electrochem. commun.* **9,** 1530–1535 (2007).

96. Li, J., Xiong, Z., Zhou, L., Han, X. & Liu, H. Effects of pore structure of mesoporous silicas on the electrochemical properties of hemoglobin. *Microporous Mesoporous Mater.* **130,** 333–337 (2010).

97. Font, J., De March, P., Busqué, F., Casas, E., Benitez, M., Teruel, L. & García, H. Periodic mesoporous silica having covalently attached tris(bipyridine) ruthenium complex: Synthesis, photovoltaic and electrochemiluminescent properties. *J. Mater. Chem.* **17,** 2336–2343 (2007).

98. Innocenzi, P., Martucci, A., Guglielmi, M., Bearzotti, A. & Traversa, E. Electrical and structural characterisation of mesoporous silica thin films as humidity sensors. *Sensors Actuators B* **76,** 299–303 (2001).

99. Walcarius, A. & Kuhn, A. Ordered porous thin films in electrochemical analysis. *TrAC - Trends Anal. Chem.* **27,** 593–603 (2008).

100. Walcarius, A. Template-directed porous electrodes in electroanalysis. *Anal. Bioanal. Chem.* **396,** 261–272 (2010).

101. Etienne, M. & Walcarius, A. Evaporation induced self-assembly of templated silica and organosilica thin films on various electrode surfaces. *Electrochem. commun.* **7,** 1449–1456 (2005).

102. Wei, T. C. & Hillhouse, H. W. Mass transport and electrode accessibility through periodic self-assembled nanoporous silica thin films. *Langmuir* **23,** 5689–5699 (2007).

103. Bearzotti, A., Bertolo, J. M., Innocenzi, P., Falcaro, P. & Traversa, E. Humidity sensors based on mesoporous silica thin films synthesised by block copolymers. *J. Eur. Ceram. Soc.* **24,** 1969–1972 (2004).

104. Urbanova, V. & Walcarius, A. Vertically-aligned mesoporous silica films. *Z. Anorg. Allg. Chem.* **640,** 537–546 (2014).

105. Yan, F., Lin, X. & Su, B. Vertically ordered silica mesochannel films: electrochemistry and analytical applications. *Analyst* **141,** 3482–3495 (2016).

106. Zhao, D., Yang, P., Margolese, D. I. & Stucky, G. D. Synthesis of continuous mesoporous silica thin films with three-dimensional accessible pore structures. *Chem. Commun.* **1,** 2499–2500 (1998).

107. Richman, E. K., Brezesinski, T. & Tolbert, S. H. Vertically oriented hexagonal mesoporous films formed through nanometre-scale epitaxy. *Nat. Mater.* **7,** 712–717 (2008).

108. Guillemin, Y., Etienne, M., Sibottier, E. & Walcarius, A. Microscale controlled electrogeneration of patterned mesoporous silica thin films. *Chem. Mater.* **23,** 5313–5322 (2011).

109. Ariga, K., Ajayan, V., Yamauchi, Y., Ji, Q. & Hill, J. P. Nanoarchitectonics for Mesoporous Materials. *Bull. Chem. Soc. Jpn.* **85,** 1–32 (2012).

110. Otomo, J., Wang, S., Takahashi, H. & Nagamoto, H. Microstructure development of mesoporous silica thin films with pore channels aligned perpendicularly to electrode surfaces and application to proton conducting composite electrolyte membranes. *J. Memb. Sci.* **279,** 256–265 (2006).

111. Kao, K. C., Lin, C. H., Chen, T. Y., Liu, Y. H. & Mou, C. Y. A General Method for Growing Large Area Mesoporous Silica Thin Films on Flat Substrates with Perpendicular Nanochannels. *J. Am. Chem. Soc.* **137,** 3779–3782 (2015).

112. Vilà, N., Ghanbaja, J., Aubert, E. & Walcarius, A. Electrochemically assisted generation of highly ordered azide-functionalized mesoporous silica for oriented hybrid films. *Angew. Chemie - Int. Ed.* **53,** 2945–2950 (2014).

113. Walcarius, A., Sibottier, E., Etienne, M. & Ghanbaja, J. Electrochemically assisted self-assembly of mesoporous silica thin films. *Nat. Mater.* **6,** 602–608 (2007).

114. Goux, A., Etienne, M., Aubert, E., Lecomte, C., Ghanbaja, J. & Walcarius, A. Oriented mesoporous silica films obtained by electro-assisted self-assembly (EASA). *Chem. Mater.* **21,** 731–741 (2009).

115. Walcarius, A. Mesoporous Materials-Based Electrochemical Sensors. *Electroanalysis* **27,** 1303–1340 (2015).

116. Rafiee, M., Karimi, B., Farrokhzadeh, S. & Vali, H. Hydroquinone functionalized oriented MCM-41 mesochannels at the electrode surface. *Electrochim. Acta* **94,** 198–205 (2013).

117. Li, W., Ding, L., Wang, Q. & Su, B. Differential pulse voltammetry detection of dopamine and ascorbic acid by permselective silica mesochannels vertically attached to the electrode surface. *Analyst* **139,** 3926–31 (2014).

118. Audebert, P. Vilà, N., Allain, C., Maisonneuve, F., Walcarius, A. & Hapiot, P. Highly Organized Ferrocene-Functionalized Nanoporous Silica films with an extremely fast electron-transfer rate for an intrinsically nonconducting oxide-modified electrode. *ChemElectroChem* **2,** 1695–1698 (2015).

119. Despas, C., Vodolazkaya, N. A., Ghanbaja, J. & Walcarius, A. Preparation of ordered and oriented mesoporous silica thin films bearing octyl or hexadecyl groups by electrochemically assisted self-assembly and evaluation of their transport properties. *J. Solid State Electrochem.* **19,** 2075–2085 (2015).

120. Herzog, G., Sibottier, E., Etienne, M. & Walcarius, A. Electrochemically assisted self-assembly of ordered and functionalized mesoporous silica films: impact of the electrode geometry and size on film formation and properties. *Faraday Discuss.* **164,** 259 (2013).

121. Herzog, G., Vodolazkaya, N. A. & Walcarius, A. Platinum ultramicroelectrodes modified with electrogenerated surfactant-templated mesoporous organosilica films: Effect of film formation conditions on its performance in preconcentration electroanalysis. *Electroanalysis* **25,** 2595–2603 (2013).

122. Rafiee, M., Karimi, B., Asl, Y. A. & Vali, H. Electrochemical fabrication of electroactive ordered mesoporous electrode. *Analyst* **138,** 1740–4 (2013).

123. Vilà, N. & Walcarius, A. Electrochemical response of vertically-aligned, ferrocene-functionalized mesoporous silica films: Effect of the supporting electrolyte. *Electrochim. Acta* **179,** 304–314 (2015).

124. Vilà, N., Allain, C., Audebert, P. & Walcarius, A. Tetrazine-functionalized and vertically-aligned mesoporous silica films with electrochemical activity and fluorescence properties. *Electrochem. commun.* **59,** 9–12 (2015).

125. Vilà, N., Ghanbaja, J. & Walcarius, A. Clickable Bifunctional and Vertically Aligned Mesoporous Silica Films. *Adv. Mater. Interfaces* **3,** 1–11 (2016).

126. Millar, S. Tips and tricks for the Lab: Air-sensitive techniques (3). *Chemistry Views* (2013).

127. Vilà, N., André, E., Ciganda, R., Ruiz, J., Astruc, D. & Walcarius, A. Molecular Sieving with Vertically Aligned Mesoporous Silica Films and Electronic Wiring through Isolating Nanochannels. *Chem. Mater.* **28,** 2511–2514 (2016).

128. Small, L. J., Wheeler, D. R. & Spoerke, E. D. Nanoporous membranes with electrochemically switchable, chemically stabilized ionic selectivity. *Nanoscale* **7,** 16909–20 (2015).

129. Zharov, I. & Khabibullin, A. Surface-modified silica colloidal crystals: Nanoporous films and membranes with controlled ionic and molecular transport. *Acc. Chem. Res.* **47,** 440–449 (2014).

130. Gong, M. M., Zhang, P., Macdonald, B. D. & Sinton, D. Nanoporous Membranes Enable Concentration and Transport in Fully Wet Paper-Based Assays. *Anal Chem* **86,** 8090–8097 (2014).

131. Brunsen, A., Calvo, A., Williams, F. J., Soler-Illia, G. J. A. A. & Azzaroni, O. Manipulation of molecular transport into mesoporous silica thin films by the infiltration of polyelectrolytes. *Langmuir* **27,** 4328–4333 (2011).

132. Jackson, E. A. & Hillmyer, M. A. Nanoporous membranes derived from block copolymers: From drug delivery to water filtration. *ACS Nano* **4,** 3548–3553 (2010).

133. Kim, W. G. & Nair, S. Membranes from nanoporous 1D and 2D materials: A review of opportunities, developments, and challenges. *Chem. Eng. Sci.* **104,** 908–924 (2013).

134. Mo, Y. & Fei, T. Nanoporous Membrane for Biosensing Applications. *Nano Life* **02,** 1230003 (2012).

135. Ito, T. & Perera, D. M. N. T. Trace Analysis with Nanomaterials. in *Trace Analysis with Nanomaterials* (eds. Pierce, D. T. & Zhao, J. X.) 341–358 (Wiley-VCH Verlag & Co. KGaA, 2010).

136. Adiga, S. P., Jin, C., Curtiss, L. A., Monteiro-riviere, N. A. & Narayan, R. J. Nanoporous Membranes for Medical and Biological Applications. *WIREs Nanomedicine and Nanobiotechnology* **1,** 568–581 (2009).

137. Ulbricht, M. Advanced functional polymer membranes. *Polymer* **47,** 2217–2262 (2006).

138. Rangnekar, N., Mittal, N., Elyassi, B., Caro, J. & Tsapatsis, M. Zeolite membranes - a review and comparison with MOFs. *Chem. Soc. Rev.* **44,** 7128–7154 (2015).

139. Bassous, E. Anisotropic etching of silicon for 3-D microstructure fabrication - a review. *Proc. Electrochem. Soc.* **88-23,** 619–645 (1988).

140. Singh, M. & Das, G. Highly ordered anodic porous alumina membrane and its surface modification approaches for biomedical application\n. *IOSR J. Appl. Chem.* **7,** 17–34 (2014).

141. Platschek, B., Keilbach, A. & Bein, T. Mesoporous structures confined in anodic alumina membranes. *Adv. Mater.* **23,** 2395–2412 (2011).

142. Feng, D., Wei, J., Wang, M., Yue, Q., Deng, Y., Asiri, A. M. & Zhao, D. Advances in mesoporous thin films via self-assembly process. *Adv. Porous Mater.* **1,** 164–186 (2013).

143. Liu, J. & Cao, G. Solution-based synthesis of oriented one-dimensional nanomaterials. *Annu. Rev. Nano Res.* **640,** 537–546 (2014).

144. Liu, N., Dunphy, D. R., Atanassov, P., Bunge, S. D., Chen, Z., Lo, G. P., Boyle, T. J. & Brinker, C. J. Photoregulation of mass transport through a photoresponsive membrane. *Nano Lett.* **4,** 551–554 (2004).

145. Etienne, M., Zhang, L., Vilà, N. & Walcarius, A. Mesoporous materials-based electrochemical enzymatic biosensors. *Electroanalysis* **27,** 2028–2054 (2015).

146. Etienne, M., Sallard, S., Schröder, M., Guillemin, Y., Mascotto, S., Smarsly, B. M. & Walcarius, A. Electrochemical generation of thin silica films with hierarchical porosity. *Chem. Mater.* **22,** 3426–3432 (2010).

147. Delacôte, C., Gaslain, F. O. M., Lebeau, B. & Walcarius, A. Factors affecting the reactivity of thiol-functionalized mesoporous silica adsorbents toward mercury(II). *Talanta* **79,** 877–886 (2009).

148. Serrano, M. B., Despas, C., Herzog, G. & Walcarius, A. Mesoporous silica thin films for molecular sieving and electrode surface protection against biofouling. *Electrochem. commun.* **52,** 34–36 (2015).

149. Etienne, M., Cortot, J. & Walcarius, A. Preconcentration electroanalysis at surfactant-templated thiol-functionalized silica thin films. *Electroanalysis* **19,** 129–138 (2007).

150. Fattakhova-Rohlfing, D., Wark, M. & Rathouský, J. Ion-permselective pH-switchable mesoporous silica thin layers. *Chem. Mater.* **19,** 1640–1647 (2007).

151. Zhou, Z., Guo, W., Xu, L., Yang, Q. & Su, B. Two orders-of-magnitude enhancement in the electrochemiluminescence of $Ru(bpy)_3^{2+}$ by vertically ordered silica mesochannels. *Anal. Chim. Acta* **886,** 48–55 (2015).

152. Walcarius, A., Etienne, M. & Lebeau, B. Rate of access to the binding sites in organically modified silicates. 2. Ordered mesoporous silicas grafted with amine or thiol groups. *Chem. Mater.* **15,** 4181–4192 (2003).

153. Goux, A., Ghanbaja, J. & Walcarius, A. Prussian Blue electrodeposition within an oriented mesoporous silica film: Preliminary observations. *J. Mater. Sci.* **44,** 6601–6607 (2009).

154. Chen, F., Jiang, X., Kuang, T., Chang, L., Fu, D., Yang, J., Fan, P. & Zhong, M. Polyelectrolyte/mesoporous silica hybrid materials for the high performance multiple-detection of pH value and temperature. *Polym. Chem.* **6,** 3529–3536 (2015).

155. Elbert, J., Krohm, F., Rüttiger, C., Kienle, S., Didzoleit, H., Balzer, B. N., Hugel, T., Stühn, B., Gallei, M. & Brunsen, A. Polymer-modified mesoporous silica thin films for redox-mediated selective membrane gating. *Adv. Funct. Mater.* **24,** 1591–1601 (2014).

156. Tonle, I. K., Ngameni, E. & Walcarius, A. From clay- to organoclay-film modified electrodes: Tuning charge selectivity in ion exchange voltammetry. *Electrochim. Acta* **49,** 3435–3443 (2004).

157. Newton, M. R., Bohaty, A. K., White, H. S. & Zharov, I. Chemically modified opals as thin permselective nanoporous membranes. *J. Am. Chem. Soc.* **127,** 7268–7269 (2005).

158. Yaroshchuk, A. E. Dielectric exclusion of ions from membranes. *Adv. Colloid Interface Sci.* **85,** 193–230 (2000).

159. Helfferich, F. *Ion Exchange*. (McGraw-Hill, 1962).

160. De Grooth, J., Oborný, R., Potreck, J., Nijmeijer, K. & de Vos, W. M. The role of ionic strength and odd-even effects on the properties of polyelectrolyte multilayer nanofiltration membranes. *J. Memb. Sci.* **475,** 311–319 (2015).

161. Cannes, C., Kanoufi, F. & Bard, A. J. Cyclic voltammetry and scanning electrochemical microscopy of ferrocenemethanol at monolayer and bilayer-modified gold electrodes. *J. Electroanal. Chem.* **547,** 83–91 (2003).

162. Zevenbergen, M. A. G., Wolfrum, B. L., Goluch, E. D., Singh, P. S. & Lemay, S. G. Fast Electron-Transfer Kinetics Probed in Nanofluidic Channels. *J. Am. Chem. Soc.* **131,** 11471–11477 (2009).

163. Nekoueian, K., Hotchen, C. E., Amiri, M., Sillanpää, M., Nelson, G. W., Foord, J. S., Holdway, P., Buchard, A., Parker, S. C. & Marken, F. Interfacial Electron-Shuttling Processes across KolliphorEL Monolayer Grafted Electrodes. *ACS Appl. Mater. Interfaces* **7,** 15464–15465 (2015).

164. Hotchen, C. E., Maybury, I. J., Nelson, G. W., Foord, J. S., Holdway, P. & Marken, F. Amplified electron transfer at poly-ethylene-glycol (PEG) grafted electrodes. *Phys. Chem. Chem. Phys.* **17,** 11260–8 (2015).

165. Stojek, Z. *Electroanalytical methods*. (Springer, 2010).

166. Icenhower, J. P. & Dove, P. M. The dissolution kinetics of amorphous silica into sodium chloride solutions: Effects of temperature and ionic strength. *Geochim. Cosmochim. Acta* **64,** 4193–4203 (2000).

167. Dove, P. M., Han, N. & De Yoreo, J. J. Mechanisms of classical crystal growth theory explain quartz and silicate dissolution behavior. *Proc. Natl. Acad. Sci.* **102,** 15357–15362 (2005).

168. Dove, P. M., Han, N., Wallace, A. F. & De Yoreo, J. J. Kinetics of amorphous silica dissolution and the paradox of the silica polymorphs. *Proc. Natl. Acad. Sci. U. S. A.* **105,** 9903–9908 (2008).

169. Hu, J., Stein, A. & Bühlmann, P. Rational design of all-solid-state ion-selective electrodes and reference electrodes. *Trends Anal. Chem.* **76,** 102–114 (2016).

170. Michalska, A. All-solid-state ion selective and all-solid-state reference electrodes. *Electroanalysis* **24,** 1253–1265 (2012).

171. Pawlak, M. & Bakker, E. Chemical Modification of Polymer Ion-Selective Membrane Electrode Surfaces. *Electroanalysis* **26,** 1121–1131 (2014).

172. Radu, A., Radu, T., McGraw, C., Dillingham, P., Anastasova-Ivanova, S. & Diamond, D. Ion selective electrodes in environmental analysis. *J. Serbian Chem. Soc.* **78,** 1729–1761 (2013).

173. Girault, H. H. *Electroanalytical chemistry*. **23,** (CRC Press, 2010).

174. Arrigan, D. W. M. *Electrochemical Strategies in Detection Science*. (RSC Publishing, 2015).

175. Arrigan, D. W. M., Herzog, G., Scanlon, M. D. & Strutwolf, J. *Electroanalytical chemistry*. **25,** (CRC Press, 2014).

176. Bakker, E. Electroanalysis with Membrane Electrodes and Liquid–Liquid Interfaces. *Anal Chem* **88,** 395–413 (2016).

177. Lee, H. J. & Girault, H. H. Amperometric Ion Detector for Ion Chromatography. *Anal. Chem.* **70,** 4280–4285 (1998).

178. Ye, J., Baldwin, R. P. Flow injection analysis of electroinactive anions at a polyaniline electrode. *Anal Chem* **60,** 1979–1982 (1988).

179. Xu, J. J., Peng, Y., Bao, N., Xia, X.-H. & Chen, H. Y. In-channel indirect amperometric detection of heavy metal ions for electrophoresis on a poly(dimethylsiloxane) microchip. *Electrophoresis* **26,** 3615–3621 (2005).

180. Ikariyama, Y. . & Heineman, W. R. Polypyrrole electrode as a detector for electroinactive anions by flow injection analysis. *Anal Chem* **58,** 1803–1806 (1986).

181. Sadik, O. A. & Wallace, G. G. Effect of Polymer Composition on the Detection of Electroinactive Species Using Conductive Polymers. *Electroanalysis* **5,** 555–563 (1993).

182. Barisci, J. N., Wallace, G. G. & Clarke, a. Amperometric Detection of Electroinactive Anions Using Conducting Polymer Electrodes Subsequent to Chromatographic Separation. *Electroanalysis* **9,** 461–467 (1997).

183. Staes, E. & Nagels, L. J. Determination of electroinactive organic acids with LC and amperometric detection, using a PPy coated electrode. *Talanta* **52,** 277–284 (2000).

184. Xu, Q., Xu, C., Wang, Y., Zhang, W., Jin, L., Tanaka, K., Haraguchi, H. & Itoh, A. Amperometric detection studies of Nafion / indium hexacyanoferrate film for the determination of electroinactive cations in ion chromatography. *Analyst* **125,** 241–245 (2000).

185. Carabias Martínez, R., Becerro Domínguez, F., Martín González, F., Hernández Méndez, J. & Córdova Orellana, R. Polypyrrole-dodecyl sulphate electrode as a microsensor for electroinactive cations in flow-injection analysis and ion chromatography. *Anal. Chim. Acta* **279,** 299–307 (1993).

186. Xu, Q., Xu, C., Wang, Q., Tanaka, K., Toada, H., Zhang, W. & Jin, L. Application of a single electrode, modified with polydiphenylamine and dodecyl sulfate, for the simultaneous amperometric determination of electro-inactive anions and cations in ion chromatography. *J. Chromatogr. A* **997,** 65–71 (2003).

187. Thomsen, K. N. & Baldwin, R. P. Amperometric detection of nonelectroactive cations in flow systems at a cupric hexacyanoferrate electrode. *Anal. Chem.* **61,** 2594–2598 (1989).

188. Byrd, H., Chapman, B. E. & Talley, C. L. Prussian Blue coated electrode as a sensor for electroinactive cations in aqueous solutions. *J. Chem. Educ.* **90,** 775–777 (2013).

189. Fu, C., Wang, L. & Fang, Y. Determination of nonelectroactive cations by capillary electrophoresis with amperometric detection at a graphite electrode modified with a thin film of mixed-valent ruthenium-iron cyanide. *Anal. Chim. Acta* **391,** 29–34 (1999).

190. Ge, H. & Wallace, G. G. Ion exchange properties of polypyrrole. *React. Polym.* **18,** 133–140 (1992).

191. Mariaulle, P., Sinapi, F., Lamberts, L. & Walcarius, A. Application of electrodes modified with ion-exchange polymers for the amperometric detection of non-redox cations and anions in combination to ion chromatography. *Electrochim. Acta* **46,** 3543–3553 (2001).

192. Walcarius, A., Lumberts, L. & Derouane, E. G. Cation determination in aqueous solution using the methyl viologen-doped zeolite-modified carbon paste electrode. *Electroanalysis* **7,** 120–128 (1995).

193. Walcarius, A. Factors affecting the analytical applications of zeolite modified electrodes: Indirect detection of nonelectroactive cations. *Anal. Chim. Acta* **388,** 79–91 (1999).

194. Walcarius, A., Vromman, V. & Bessiere, J. Flow injection indirect amperometric detection of ammonium ions using a clinoptilolite-modified electrode. *Sensors Actuators, B Chem.* **56,** 136–143 (1999).

195. Walcarius, A., Mariaulle, P., Louis, C., Lamberts, L. & Nancy, Â. I. Amperometric detection of nonelectroactive cations in electrolyte-free flow systems at zeolite modified electrodes. *Electroanalysis* **11,** 393–400 (1999).

196. Ikeda, S. & Oyama, N. Investigation of electrochemical behavior and mass-transfer process of ferrocene-siloxane polymer film using quartz crystal electrode method. *Anal. Chem.* **65,** 1910–1915 (1993).

197. Hillman, A. R., Loveday, D. C., Glidle, A., Vos, J. G., Clarke, A. P., Kelly, D. & Bruckenstein, S. Electrochemical quartz crystal microbalance studies of redox polymer films. *Macromol. Symp.* **80,** 323–335 (1994).

198. Wang, B., Brown, S. & Rusling, J. F. Electrolyte effects on charge transport behavior of $[Os(bpy)_2$ (PVP)10Cl]Cl and $[Ru(bpy)_2(PVP)10Cl]Cl$ redox polymers in ultra-thin films of polyions. *Electroanalysis* **17,** 1601–1608 (2005).

199. Buttry, D. A. & Anson, F. C. Electron hopping vs. molecular diffusion as charge transfer mechanisms in redox polymer films. *J. Electroanal. Chem. Interfacial Electrochem.* **130,** 333–338 (1981).

200. Anson, F. C. Self-exchange reactions at redox polymer electrodes. A kinetic model and theory for stationary voltammetric techniques. *J. Phys. Chem.* **87,** 214–219 (1983).

201. Naegeli, R., Redepenning, J. & Anson, F. C. Influence of supporting electrolyte concentration and composition on formal potentials and entropies of redox couples incorporated in Nafion coatings on electrodes. *J. Phys. Chem.* **90,** 6227–6232 (1986).

202. Blauch, D. N. & Saveant, J. M. Dynamics of electron hopping in assemblies of redox centers. Percolation and diffusion. *J. Am. Chem. Soc.* **114,** 3323–3332 (1992).

203. Watanabe, M., Nagasaka, H., Sanui, K., Ogata, N. & Murray, R. W. Ion/electron mixed conductors based on polymer electrolytes. *Electrochim. Acta* **37,** 1521–1523 (1992).

204. Surridge, N. A., Sosnoff, C. S., Schmehl, R., Facci, J. S. & Murray, R. W. Electron and counterion diffusion constants in mixed-valent polymeric osmium bipyridine films. *J. Phys. Chem.* **98,** 917–923 (1994).

205. Jernigan, J. C. & Murray, R. W. Consequences of restricted ion mobility in electron transport through films of a polymeric osmium-polypyridine complex. *J. Phys. Chem.* **91,** 2030–2032 (1987).

206. Mathias, M. F. & Haas, O. Effect of counterion type on charge transport at redox polymer-modified electrodes. *J. Phys. Chem.* **97,** 9217–9225 (1993).

207. Nieto, F. J. R., Posadas, D. & Tucceri, R. I. Effect of the bathing electrolyte concentration on the charge transport process at poly (o-aminophenol) modified electrodes . An ac impedance study. *Electroanal. Chem.* **434,** 83–91 (1997).

208. Tagliazucchi, M. & Calvo, E. J. Charge transport in redox polyelectrolyte multilayer films: The dramatic effects of outmost layer and solution ionic strength. *ChemPhysChem* **11,** 2957–2968 (2010).

209. Majda, M. Molecular Design of Electrode Surfaces. in *Techniques of Chemistry Series* (ed. Murray, R. W.) **22,** 159–206 (Wiley Interscience, 1992).

210. Gerstl, M., Joksch, M. & Fafilek, G. The dissolution of palladium as a function of glucose concentration in chloride containing solutions of acidic pH. *J. Electroanal. Chem.* **741,** 1–7 (2015).

211. Aoki, A., Rajagopalan, R. & Heller, A. Effect of Quaternization on Electron Diffusion Coefficients for Redox Hydrogels Based on. *J. Phys. Chem.* **99,** 5102–5110 (1995).

212. Akhoury, A., Bromberg, L. & Hatton, T. A. Interplay of electron hopping and bounded diffusion during charge transport in redox polymer electrodes. *J. Phys. Chem. B* **117,** 333–342 (2013).

213. Pöller, S., Koster, D. & Schuhmann, W. Stabilizing redox polymer films by electrochemically induced crosslinking. *Electrochem. commun.* **34,** 327–330 (2013).

214. Rohlfing, D. F., Rohlfing, Y., Bartels, O. & Wark, M. Functionalized Mesoporous Silica Films as a Matrix for Anchoring Electrochemically Active Guests. *Langmuir* **21,** 11320–11329 (2005).

215. Delacote, C., Bouillon, J. P. & Walcarius, A. Voltammetric response of ferrocene-grafted mesoporous silica. *Electrochim. Acta* **51,** 6373–6383 (2006).

216. Zhou, Z., Franz, A. W., Bay, S., Sarkar, B., Seifert, A., Yang, P., Wagener, A., Ernst, S., Pagels, M., Muller, T. J. J. & Thiel, W. R. Redox active mesoporous hybrid materials by in situ syntheses with urea-linked triethoxysilylated phenothiazines. *Chem. - An Asian J.* **5,** 2001–2015 (2010).

217. Ugo, P. & Anson, F. C. Poly(2-vinylpyrazine) as a soluble polymeric ligand and as an electrode coating. Reactions with pentacyanoferrate(II). *Anal. Chem.* **61,** 1799–1805 (1989).

218. Toniolo, R. & Schiavon, G. Potential Shifts at Electrodes Coated with Ion-Exchange Polymeric Films. *Talanta* **41,** 473–478 (1994).

219. Karman, C., Vilà, N. & Walcarius, A. Amplified charge transfer for anionic redox probes through oriented mesoporous silica thin films. *Chem. Electro. Chem.* **3,** 2130–2137 (2016).

220. Volkov, A. G., Paula, S. & Deamer, D. W. Two mechanisms of permeation of small neutral molecules and hydrated ions across phospholipid bilayers. *Bioelectrochemistry Bioenerg.* **42,** 153–160 (1997).

221. Paris, J. P. & Brandt, W. W. Charge transfer luminescence of a ruthenium(II) chelate. *J. Am. Chem. Soc.* **81,** 5001–5002 (1959).

222. Lytle, F. E. & Hercules, D. M. The luminescence of tris(2,2'-bipyridine)ruthenium(II) dichloride. *J. Am. Chem. Soc.* **91,** 253–257 (1969).

223. Adamson, A. W. & Demas, J. N. A new photosensitizer. Tris(2,2'-bipyridine)ruthenium(II) chloride. *J. Am. Chem. Soc.* **93,** 1800–1801 (1971).

224. Harrigan, R. W. & Crosby, G. A. Symmetry assignments of the lowest CT excited states of ruthenium (II) complexes via a proposed electronic coupling model. *J. Chem. Phys.* **59,** 3468–3476 (1973).

225. Harrigan, R. W., Hager, G. D. & Crosby, G. A. Evidence for multiple-state emission from ruthenium(II) complexes. *Chem. Phys. Lett.* **21,** 487–490 (1973).

226. Baker, D. C. & Crosby, G. A. Spectroscopic and magnetic evidence for multiple-state emission from tris(2,2'-bipyridine)ruthenium(II) sulfate. *Chem. Phys.* **4,** 428–433 (1974).

227. Balzani, V., Bouetta, F., Gandolfi, M. T. & Maestri, M. Bimolecular electron transfer reactions of the excited states of transition metal complexes. *Top. In Curr. Chem.* **75**, 1–64 (1978).

228. Kalyanasundaram, K. Photophysics, photochemistry and solar energy conversion with tris(bipyridyl)ruthenium(II) and its analogues. *Coord. Chem. Rev.* **46,** 159–244 (1982).

229. Juris, A., Balzani, V., Barigelletti, F., Campagna, S., Belser, P. & von Zelewsky, A. Ru(II) polypyridine complexes: photophysics, photochemistry, eletrochemistry, and chemiluminescence. *Coord. Chem. Rev.* **84,** 85–277 (1988).

230. Dixon, I. M., Lebon, E., Sutra, P. & Igau, A. Luminescent ruthenium-polypyridine complexes & phosphorus ligands: anything but a simple story. *Chem. Soc. Rev.* **38,** 1621–34 (2009).

231. Lee, J., Lee, S-H., Kim, M., Kim, H., Kim, D-H., Lee, W-Y. Organosilicate thin film containing $Ru(bpy)_3^{2+}$ for an electrogenerated chemiluminescence (ECL) sensor. *Chem. Commun.* 1602–1603 (2003).

232. Greenway, G. M., Greenwood, A., Watts, P. & Wiles, C. Solid-supported chemiluminescence and electrogenerated chemiluminescence based on a tris(2,2'-bipyridylruthenium(II) derivative. *Chem. Commun.* 85–87 (2006).

233. Wei, H., Du, Y., Kang, J.-Z., Xu, G.-B. & Wang, E.-K. Tris(2,2'- bipyridyl) ruthenium(II) doped silica film modified indium tin oxide electrode and its electrochemiluminescent properties. *Chinese J. Chem.* **25,** 159–163 (2007).

234. Miao, W., Choi, J. & Bard, A. J. Electrogenerated Chemiluminescence 69: The Tri -n-propylamine (TPrA) System Revisited s A New Route Involving TPrA • + Cation Radicals. *J. Am. Chem. Soc.* **124**, 14478–14485 (2002).

235. Sprintschnik, G., Sprintschnik, H. W., Kirsch, P. P. & Whitten, D. G. Preparation and photochemical reactivity of surfactant ruthenium(II) complexes in monolayer assemblies and at water-solid interfaces. *J. Am. Chem. Soc.* **99,** 4947–4954 (1977).

236. Miller, C. J., McCord, P. & Bard, A. J. Study of Langmuir monolayers of ruthenium complexes and their aggregation by electrogenerated chemiluminescence. *Langmuir* **7,** 2781–2787 (1991).

237. Bertoncello, P., Kefalas, E. T., Pikramenou, Z., Unwin, P. R. & Forster, R. J. Adsorption dynamics and electrochemical and photophysical properties of thiolated. *J. Phys* **110,** 10063–10069 (2006).

238. Keith Dearmond, M. & Fried, G. A. *Langmuir-blodgett films of transition metal complexes*. *Progress in Inorganic Chemistry* **44,** (1996).

239. Walsh, J. J., Zhu, J., Bond, A. M., Forster, R. J. & Keyes, T. E. Visible light sensitized photocurrent generation from electrostatically assembled thin films of [Ru(bpy)3]2+ and the polyoxometalate gamma-[W18O54(SO4)2]4- : Optimizing performance in a low electrolyte medium. *J. Electroanal. Chem.* **706,** 93–101 (2013).

240. Valenty, S., Behnken, D. & Jr, G. G. Preparation and monolayer properties of surfactant tris (2, 2′-bipyridine) ruthenium (II) derivatives. *Inorg. Chem.* **18,** 2160–2164 (1979).

241. Pazinato, J. Hoffmeister, D. M., Naidek, K. P., Westphal, E., Gallardo, H. & Winnischofer, H. Amphiphilic ruthenium bipyridine complex containing long-chain azopyridine group and the mechanism of electron transfer in Langmuir-Blodgett films. *Electrochim. Acta* **153,** 574–582 (2015).

242. Taniguchi, T., Fukasawa, Y. & Miyashita, T. Photoelectrochemical response of polymer Langmuir-Blodgett films containing tris (2,2′bipyridine) ruthenium (II) complex. *J. Phys. Chem. B* **103,** 1920–1924 (1999).

243. Wei, H. & Wang, E. Solid-state electrochemiluminescence of tris (2,2′-bipyridyl) ruthenium. *Trends Anal. Chem.* **27,** 447–459 (2008).

244. Ishida, H., Tobita, S., Hasegawa, Y., Katoh, R. & Nozaki, K. Recent advances in instrumentation for absolute emission quantum yield measurements. *Coord. Chem. Rev.* **254,** 2449–2458 (2010).

245. Kalyuzhny, G., Buda, M., Mcneill, J., Barbara, P. & Bard, A. J. Stability of thin-film solid-state electroluminescent devices based on tris(2′,2 -bipyridine) ruthenium (II) complexes. *J. Am. Chem. Soc.* **125,** 6272–6283 (2003).

246. Zhang, X. & Bard, A. J. Electrogenerated chemiluminescent emission from an organized (L-B) monolayer of a tris(2,2′-bipyridine)ruthenium(2+)-based surfactant on semiconductor and metal electrodes. *J. Phys. Chem.* **92,** 5566–5569 (1988).

247. Wang, H., Xu, G. & Dong, S. Electrochemiluminescence of tris(2,2′-bipyridine)ruthenium(II) immobilized in poly(p-styrenesulfonate)–silica–Triton X-100 composite thin-films. *Analyst* **126,** 1095–1099 (2001).

248. Mori, K., Kagohara, K. & Yamashita, H. Synthesis of tris(2,2 ′-bipyridine)iron(II) complexes in zeolite Y cages: Influence of exchanged alkali metal cations on physicochemical properties and catalytic activity. *J. Phys. Chem. C* **112,** 2593–2600 (2008).

249. Martin, C. R., Rubinstein, I. & Bard, A. J. Polymer films on electrodes. 9. Electron and mass transfer in nafion films containing $Ru(bpy)_3^{2+}$. *J. Am. Chem. Soc* **104,** 4817–4824 (1982).

250. Ruda-Eberenz, T. A., Nagy, A., Waldman, W. J. & Dutta, P. K. Entrapment of Ionic Tris (2,2 -Bipyridyl) Ruthenium (II) in Hydrophobic Siliceous Zeolite : O_2 Sensing in Biological Environments. *Environments* **29,** 9140–9147 (2008).

251. Zhang, L. & Dong, S. Electrogenerated chemiluminescence sensors using Ru(bpy)32+ doped in silica nanoparticles. *Anal. Chem.* **78,** 5119–5123 (2006).

252. Collinson, M. M., Taussig, J. & Martin, S. A. Solid-state electrogenerated chemiluminescence from gel-entrapped ruthenium (II) tris (bipyridine) and tripropylamine. *Chem. Mater.* **11,** 2594–2599 (1999).

253. Dennany, L., Forster, R. J. & Rusling, J. F. Simultaneous direct electrochemiluminescence and catalytic voltammetry detection of DNA in ultrathin films. *J. Am. Chem. Soc.* **125,** 5213–5218 (2003).

254. Dennany, L., Hogan, C. F., Keyes, T. E. & Forster, R. J. Effect of surface immobilization on the electrochemiluminescence of ruthenium-containing metallopolymers. *Anal. Chem.* **78,** 1412–1417 (2006).

255. Lu, M. & Whang, C. The role of direct oxalate oxidation in electrogenerated chemiluminescence of poly(4-vinylpyridine)-bound $Ru(bpy)_2Cl^+$/oxalate system on indium tin oxide electrodes. *Anal. Chim. Acta* **522,** 25–33 (2004).

256. Wang, H., Xu, G. & Dong, S. Electrochemiluminescence of tris(2,2'-bipyridyl)ruthenium(II) ion-exchanged in polyelectrolyte-silica composite thin-films. *Electroanalysis* **14,** 853–857 (2002).

257. Delaney, J. L., Hogan, C. F., Tian, J. & Shen, W. Electrogenerated chemiluminescence detection in paper-based microfluidic sensors. *Anal. Chem.* **83,** 1300–1306 (2011).

258. Collinson, M. M., Novak, B., Martin, S. A. & Taussig, J. S. Electrochemiluminescence of ruthenium(II) tris(bipyridine) encapsulated in sol-gel glasses. *Anal. Chem.* **72,** 2914–2918 (2000).

259. Collinson, M. M., Taussig, J. & Martin, S. A. Solid-State Electrogenerated Chemiluminescence from Gel-Entrapped Ruthenium(II) Tris(bipyridine) and Tripropylamine. *Chem. Mater.* **11,** 2594–2599 (1999).

260. Zanarini, S. Rampazzo, E., Ciana, L. D., Marcaccio, M., Marzocchi, E., Montalti, M., Paolucci, F. & Prodi, L. Ru(bpy) Covalently Doped Silica Nanoparticles as Multicenter Tunable Structures for Electrochemiluminescence Amplification $Ru(bpy)_3$ Covalently Doped Silica Nanoparticles as Multicenter Tunable Structures for Electrochemiluminescence. *J. Am. Chem. Soc.* **131,** 2260–2267 (2009).

261. Bertoncello, P. & Forster, R. J. Nanostructured materials for electrochemiluminescence (ECL)-based detection methods: Recent advances and future perspectives. *Biosens. Bioelectron.* **24,** 3191–3200 (2009).

262. Spehar-Délèze, A.-M., Almadaghi, S. & O'Sullivan, C. Development of Solid-State Electrochemiluminescence (ECL) Sensor Based on $Ru(bpy)_3^{2+}$-Encapsulated Silica Nanoparticles for the Detection of Biogenic Polyamines. *Chemosensors* **3,** 178–189 (2015).

263. Qian, L. & Yang, X. One-step synthesis of Ru(2,2 -Bipyridine)3Cl2-immobilized silica nanoparticles for use in electrogenerated chemiluminescence detection. *Adv. Funct. Mater.* **17,** 1353–1358 (2007).

264. Yin, X., Dong, S. & Wang, E. Analytical applications of the electrochemiluminescence of tris (2,2′-bipyridyl) ruthenium and its derivatives. *Trends Anal. Chem.* **23,** 432–441 (2004).

265. Guo, Z., Shen, Y., Wang, M., Zhao, F. & Dong, S. Electrochemistry and electrogenerated chemiluminescence of SiO_2 nanoparticles/tris (2,2′bipyridyl) ruthenium (II) multilayer films on indium tin oxide electrodes. *Anal. Chem.* **76,** 184–191 (2004).

266. Wang, H., Xu, G. & Dong, S. Electrochemiluminescence sensor using Eastman-AQ55D – silica composite thin-films. *Anal. Chim. Acta* **480,** 285–290 (2003).

267. Xiong, Y., Xu, J., Zhu, D. Q., Duan, C. F. & Guan, Y. F. Fiber-optic fluorescence sensor for dissolved oxygen detection based on fluorinated xerogel immobilized with ruthenium (II) complex. *J. Sol-Gel Sci. Technol.* **53,** 441–447 (2010).

268. Payra, P. & Dutta, P. K. Development of a dissolved oxygen sensor using tris(bipyridyl) ruthenium (II) complexes entrapped in highly siliceous zeolites. *Microporous Mesoporous Mater.* **64,** 109–118 (2003).

269. Meier, B., Werner, T., Klimant, I. & Wolfbeis, O. S. Novel oxygen sensor material based on a ruthenium bipyridyl complex encapsulated in zeolite Y: dramatic differences in the efficiency of luminescence quenching by oxygen on going from surface-adsorbed to zeolite-encapsulated fluorophores. *Sensors Actuators B. Chem.* **29,** 240–245 (1995).

270. Coutant, M. A., Payra, P. P. & Dutta, P. K. Oxygen transport in zeolite Y measured by quenching of encapsulated tris(bipyridyl)ruthenium. *Microporous Mesoporous Mater.* **60,** 79–90 (2003).

271. Grant, P. S. & McShane, M. J. Development of multilayer fluorescent thin film chemical sensors using electrostatic self-assembly. *IEEE Sens. J.* **3,** 139–146 (2003).

272. MacCraith, B. D., McDonagh, C. M., O'Keeffe, G., Keyes, E. T., Vos, J. G., O'Kelly, B. & McGilp, J. F. Fibre optic oxygen sensor based on fluorescence quenching of evanescent-wave excited ruthenium complexes in sol-gel derived porous coatings. *Analyst* **118,** 385–388 (1993).

273. Xiong, X., Xiao, D. & Choi, M. M. F. Dissolved oxygen sensor based on fluorescence quenching of oxygen-sensitive ruthenium complex immobilized on silica-Ni-P composite coating. *Sensors Actuators B* **117,** 172–176 (2006).

274. DeGraff, B. A. & Demas, J. N. Luminescence-based oxygen sensors. in *Reviews in Fluoresce 2005* (eds. Geddes, C. D. & Lakowicz, J. R.) 125–147 (Springer, 2005).

275. Zheng, L., Chi, Y., Shu, Q., Dong, Y., Zhang, L. & Chen, G. Electrochemiluminescent reaction between $Ru(bpy)_3^{2+}$ and oxygen in Nafion film. *J. Phys. Chem.* **113,** 20316–20321 (2009).

276. Bernhard, S. Barron, J. A., Houston, P. L., Abruña, H. D., Ruglovksy, J. L., Gao, X. & Malliaras, G. G. Electroluminescence in ruthenium (II) complexes. *J. Am. Chem. Soc.* **124,** 13624–13628 (2002).

277. Buda, M., Kalyuzhny, G. & Bard, A. J. Thin-film solid-state electroluminescent devices based On tris(2,2′-bipyridine) ruthenium (II) complexes. *J. Am. Chem. Soc.* **3,** 6090–6098 (2002).

278. Rudmann, H., Shimada, S. & Rubner, M. F. Solid-state light-emitting devices based on the tris-chelated ruthenium (II) complex. 4. High-efficiency light-emitting devices based on derivatives of the tris (2,2′bipyridyl) ruthenium (II) complex. *J. Am. Chem. Soc.* **124,** 4918–4921 (2002).

279. Lyons, C. H., Abbas, E. D., Lee, J. & Rubner, M. F. Solid-state light-emitting Devices Based on the trischelated ruthenium (II) complex . 1 . Thin film blends with poly (ethylene oxide). *J. Am. Chem. Soc.* **120,** 12100–12107 (1998).

280. Wu, A., Yoo, D., Lee, J. & Rubner, M. F. Solid-state light-emitting devices based on the tris-chelated ruthenium (II) complex: 3 . High efficiency devices via a layer-by-layer molecular-level blending approach. *J. Am. Chem. Soc.* **121,** 4883–4891 (1999).

281. Handy, E. S., Pal, A. J. & Rubner, M. F. Solid-state light-emitting devices based on the tris-chelated ruthenium (II) complex. 2 . Tris (bipyridyl) ruthenium (II) as a high-brightness emitter. *J. Am. Chem. Soc.* **121,** 3525–3528 (1999).

282. Gao, F. G. & Bard, A. J. Solid-state organic light-emitting diodes based on tris (2,2′ -bipyridine) ruthenium (II) complexes. *J. Am. Chem. Soc.* **122,** 7426–7427 (2000).

283. Lee, J. K., Yoo, D. S., Handy, E. S. & Rubner, M. F. Thin film light emitting devices from an electroluminescent ruthenium complex. *Appl. Phys. Lett.* **69,** 55–58 (1996).

284. Zhu, J., Zeng, Q., O'Carroll, S., Bond, A., Keyes, T. E. & Forster, R. J. Photocurrent generation from thin films of ruthenium metallopolymer: Polyoxometalate adducts using visible excitation. *Electrochem. commun.* **13,** 899–902 (2011).

285. Schwarz, O., van Loyen, D., Jockusch, S., J. Turro, N. & Dürr, H. Preparation and application of new ruthenium(II) polypyridyl complexes as sensitizers for nanocrystalline TiO_2. *J. Photochem. Photobiol. A Chem.* **132,** 91–98 (2000).

286. Bedja, I., Kamat, P. V., Hua, X., Lappin, a. G. & Hotchandani, S. Photosensitization of nanocrystalline ZnO films by Bis(2,2‘-bipyridine)(2,2‘-bipyridine-4,4‘-dicarboxylic acid)ruthenium(II). *Langmuir* **13,** 2398–2403 (1997).

287. Alibabaei, L., Brennaman, M. K., Norris, M. R., Kalanyan, B., Song, W., Losego, M. D., Concepcion, J. J., Binstead, R. A., Parsons, G. N. & Meyer, T. J. Solar Water Splitting in a Molecular Photoelectrochemical Cell. *Proc. Nat. Acad. Sci. USA* **110,** 20008–20013 (2013).

288. Chen, C., Wang, M., Li, J-Y., Pootrakulchote, N., Alibabaei, L., Ngoc-le, C-H., Decoppet, J-D., Tsai, J-H., Gratzel, C., Wu, C-G., Zakeeruddin, S. M. & Gratzel, M. Highly efficient light-harvesting ruthenium sensitizer for thin-film dye-sensitized solar cells. *ACS Nano* **3,** 3103–3109 (2009).

289. Walcarius, A., Nasraoui, R., Wang, Z., Qu, F., Urbanova, V., Etienne, M., Göllü, M., Demir, A. S., Gajdzik, J. & Hempelmann, R. Factors affecting the electrochemical regeneration of NADH by (2,2’-bipyridyl) (pentamethylcyclopentadienyl)-rhodium complexes: Impact on their immobilization onto electrode surfaces. *Bioelectrochemistry* **82,** 46–54 (2011).

290. Collinson, M. M., Rausch, C. G. & Voigt, A. Electroactivity of redox probes encapsulated within sol-gel- derived silicate films. *Langmuir* **13,** 7245–7251 (1997).

291. Harriman, A. Photophysics of 2,2’-bipyridyl. *J. Photochem.* **8,** 205–209 (1978).

292. Felix, F., Ferguson, J., Giidel, H. U. & Ludilc, A. The electronic spectrum of $Ru(bpy)_3^{2+}$. *J. Am. Chem. Soc,* **12,** 4096–4102 (1980).

293. Durham, B., Caspar, J. V, Nagle, J. K. & Meyer, T. J. Photochemistry of tris(2,2’-bipyridine)ruthenium(2+) ion. *J. Am. Chem. Soc.* **104,** 4803–4810 (1982).

294. Bhasikuttan, A. C., Suzuki, M., Nakashima, S. & Okada, T. Ultrafast fluorescence detection in tris (2,2′-bipyridine) ruthenium (II) complex in solution: relaxation dynamics involving higher excited states. *J. Am. Chem. Soc.* **124,** 8398–8405 (2002).

295. Ding, J., Li, B., Zhang, H., Lei, B. & Li, W. Oxygen-sensing properties of ormosil hybrid materials doped with ruthenium(II) complexes via a sol-gel process. *Mater. Lett.* **61,** 3374–3377 (2007).

296. Franco, C. & Olmsted, J. Photochemical determination of the solubility of oxygen in various media. *Talanta* **37,** 905–909 (1990).

297. Truesdale, G. A., Downing, A. L. & Lowden, G. F. The solubility of oxygen in pure water and sea-water. *J. Appl. Chem.* **5,** 53–62 (1955).

298. Demas, J. N., Harris, E. W. & McBride, R. P. Energy transfer from luminescent transition metal complexes to oxygen. *J. Am. Chem. Soc.* **99,** 3547–3551 (1977).

299. Noffsinger, J. B. & Danielson, N. D. Generation of chemiluminescence upon reaction of aliphatic amines with tris(2,2′-bipyridine)ruthenium(III). *Anal. Chem.* **59,** 865–868 (1987).

300. Baker, C. O., Huang, X. & Kaner, R. B. Polyaniline nanofibers: broadening applications for conducting polymers. *Chem. Soc. Rev.* **46**, 1510-1525 (2017).

301. Inzelt, G. *Conducting Polymers: A new Era in Electrochemistry*. (Springer, 2012).

302. Li, Y. *Organic optoelectronic materials*. (Springer, 2015).

303. Nguyen, D. & Yoon, H. Recent Advances in Nanostructured Conducting Polymers: from Synthesis to Practical Applications. *Polymers* **8,** 118 (2016).

304. Bhadra, S., Khastgir, D., Singha, N. K. & Lee, J. H. Progress in preparation, processing and applications of polyaniline. *Prog. Polym. Sci.* **34,** 783–810 (2009).

305. Wang, Y., Tran, H. D., Liao, L., Duan, X. & Kaner, R. B. Nanoscale morphology, dimensional control, and electrical properties of oligoanilines. *J. Am. Chem. Soc.* **132,** 10365–10373 (2010).

306. Ciric-Marjanovic, G. Recent advances in polyaniline research: Polymerization mechanisms, structural aspects, properties and applications. *Synth. Met.* **177,** 1–47 (2013).

307. Gospodinova, N. & Terlemezyan, L. Conducting polymers prepared by oxidative polymerization: polyaniline. *Prog. Polym. Sci.* **23,** 1443–1484 (1998).

308. Geniès, E. M., Boyle, A., Lapkowski, M. & Tsintavis, C. Polyaniline: A historical survey. *Synth. Met.* **36,** 139–182 (1990).

309. Guimard, N. K., Gomez, N. & Schmidt, C. E. Conducting polymers in biomedical engineering. *Prog. Polym. Sci.* **32,** 876–921 (2007).

310. Dallas, P. & Georgakilas, V. Interfacial polymerization of conductive polymers: Generation of polymeric nanostructures in a 2-D space. *Adv. Colloid Interface Sci.* **224,** 46–61 (2015).

311. Tian, Z., Yu, H., Wang, L., Saleem, M., Ren, F., Ren, P., Chen, Y., Sun, R., Sun, Y. & Huang, L. Recent progress in the preparation of polyaniline nanostructures and their applications in anticorrosive coatings. *RSC Adv.* **4,** 28195 (2014).

312. Cho, S. I. & Lee, S. B. Fast electrochemistry of conductive polymer nanotubes: synthesis, mechanism, and application. *Acc Chem Res* **41,** 699–707 (2008).

313. Vlad, A., Dutu, C. A., Guillet, P., Jedrasik, P., Fustin, C. A., Sodervall, U., Gohy, J. F., Melinte, S. Highly Ordered Conjugated Polymer Nanoarchitectures with Three-Dimensional Structural Control. *Nano Lett.* **9,** 2838–2843 (2009).

314. Sen, T., Mishra, S. & Shimpi, N. G. Synthesis and sensing applications of polyaniline nanocomposites: a review. *RSC Adv.* **6,** 42196–42222 (2016).

315. Kaur, A., Kaur, A. & Saini, D. A Review on Synthesis of Silica Nanocomposites With Conducting Polymers : Polyaniline. *Res. Cell Int. J. Eng. Sci.* **6913,** 40–53 (2016).

316. Abdelhamid, M. E., Snook, G. A. & O'Mullane, A. P. Electrochemical tailoring of fibrous polyaniline and electroless decoration with gold and platinum nanoparticles. *Langmuir* **32,** 8834–8842 (2016).

317. Zhang, Z., Wang, G., Li, Y., Zhang, X., Qiao, N., Wang, J., Zhou, J., Liu, Z. & Hao, Z. A new type of ordered mesoporous carbon/polyaniline composites prepared by a two-step nanocasting method for high performance supercapacitor applications. *J. Mater. Chem. A* **2,** 16715–16722 (2014).

318. Lahav, M., Weiss, E. A., Xu, Q. & Whitesides, G. M. Core-shell and segmented polymer-metal composite nanostructures. *Nano Lett.* **6,** 2166–2171 (2006).

319. Shi, Y. & Yu, G. Designing Hierarchically Nanostructured Conductive Polymer Gels for Electrochemical Energy Storage and Conversion. *Chem. Mater.* **28,** 2466–2477 (2016).

320. Niu, Z., Yang, Z., Hu, Z., Lu, Y. & Han, C. C. Polyaniline-Silica Composite Conductive Capsules and Hollow Spheres. *Adv. Funct. Mater.* **13,** 949–954 (2003).

321. Kim, F. S., Ren, G. & Jenekhe, S. A. One-dimensional nanostructures of pi-conjugated molecular systems: Assembly, properties, and applications from photovoltaics, sensors, and nanophotonics to nanoelectronics. *Chem. Mater.* **23,** 682–732 (2011).

322. Yin, Z. & Zheng, Q. Controlled synthesis and energy applications of one-dimensional conducting polymer nanostructures: An overview. *Adv. Energy Mater.* **2,** 179–218 (2012).

323. Nguyen, T. Q., Wu, J., Tolbert, S. H. & Schwartz, B. J. Control of energy transport in conjugated polymers using an ordered mesoporous silica matrix. *Adv. Mater.* **13,** 609 (2001).

324. Wang, J. & Zhang, D. One-Dimensional Nanostructured Polyaniline: Syntheses, Morphology Controlling, Formation Mechanisms, New Features, and Applications. *Adv. Polym. Technol.* **32,** E323–E368 (2013).

325. Choi, W., An, T. & Lim, G. Fabrication of Conducting Polymer Nanowires. in *Nanowires - Implementations and Applications* 440–454 (Intechopen, 2011).

326. Kim, N. J., Kwon, J. H. & Kim, M. Highly oriented self-assembly of conducting polymer chains: Extended-chain crystallization during long-range polymerization. *J. Phys. Chem. C* **117,** 15402–15408 (2013).

327. Li, G., Jiang, L. & Peng, H. One-dimensional polyaniline nanostructures with controllable surfaces and diameters using vanadic acid as the oxidant. *Macromolecules* **40,** 7890–7894 (2007).

328. Wang, K., Wu, H., Meng, Y. & Wei, Z. Conducting polymer nanowire arrays for high performance supercapacitors. *Small* **10,** 14–31 (2014).

329. Chiou, N.-R., Lu, C., Guan, J., Lee, L. J. & Epstein, A. J. Growth and alignment of polyaniline nanofibres with superhydrophobic, superhydrophilic and other properties. *Nat. Nanotechnol.* **2,** 354–7 (2007).

330. Shi, Y., Peng, L., Ding, Y., Zhao, Y. & Yu, G. Nanostructured conductive polymers for advanced energy storage. *Chem. Soc. Rev.* **44,** 6684–6696 (2015).

331. Ghosh, S., Thandavarayan, M. & Basu, R. N. Nanostructured Conducting Polymers for Energy Applications: Towards a Sustainable Platform. *Nanoscale* **8,** 6921–6947 (2016).

332. Hui, N., Chai, F., Lin, P., Song, Z., Sun, X., Li, Y., Niu, S. & Luo, X. Electrodeposited Conducting Polyaniline Nanowire Arrays Aligned on Carbon Nanotubes Network for High Performance Supercapacitors and Sensors. *Electrochim. Acta* **199,** 234–241 (2016).

333. Gupta, V. & Miura, N. High performance electrochemical supercapacitor from electrochemically synthesized nanostructured polyaniline. *Mater. Lett.* **60,** 1466–1469 (2006).

334. Song, E. & Choi, J.-W. Conducting Polyaniline Nanowire and Its Applications in Chemiresistive Sensing. *Nanomaterials* **3,** 498–523 (2013).

335. Travas-Sejdic, J., Aydemir, N., Kannan, B., Williams, D. E. & Malmstrom, J. Intrinsically conducting polymer nanowires for biosensing. *J. Mater. Chem. B* **2,** 4593–4609 (2014).

336. Fratoddi, I., Venditti, I., Cametti, C. & Russo, M. V. Chemiresistive polyaniline-based gas sensors: A mini review. *Sensors Actuators, B Chem.* **220,** 534–548 (2015).

337. Huang, J., Virji, S., Weiller, B. H. & Kaner, R. B. Nanostructured polyaniline sensors. *Chemistry* **10,** 1314–1319 (2004).

338. Wang, H., Feng, Q., Gong, F., Li, Y., Zhou, G. & Wang, Z-S. In situ growth of oriented polyaniline nanowires array for efficient cathode of Co(iii)/Co(ii) mediated dye-sensitized solar cell. *J. Mater. Chem. A* **1,** 97 (2013).

339. Parthasarathy, R. V & Martin, C. R. Template-synthesized polyaniline microtubules. *Chem. Mater.* **6,** 1627–1632 (1994).

340. Delvaux, M., Duchet, J., Stavaux, P. Y., Legras, R. & Demoustier-Champagne, S. Chemical and electrochemical synthesis of polyaniline micro- and nano-tubules. *Synth. Met.* **113,** 275–280 (2000).

341. Kim, B. H., Park, D. H., Joo, J., Yu, S. G. & Lee, S. H. Synthesis, characteristics, and field emission of doped and de-doped polypyrrole, polyaniline, poly(3,4-ethylenedioxythiophene) nanotubes and nanowires. *Synth. Met.* **150,** 279–284 (2005).

342. Silva, C. P., Santander-Nelli, M., Vera-Oyarce, C., Silva, J. F., Gómez, A., Muñoz, L. A., Zagal, J. H., Gulppi, M. & Pavez, J. Polyaniline nanostructure electrode: morphological control by a hybrid template. *J. Solid State Electrochem.* **20,** 1175–1180 (2016).

343. Li, X., Tian, S., Ping, Y., Kim, D. H. & Knoll, W. One-step route to the fabrication of highly porous polyaniline nanofiber films by using PS-b-PVP diblock copolymers as templates. *Langmuir* **21,** 9393–9397 (2005).

344. Zhong, W., Deng, J., Yang, Y. & Yang, W. Synthesis of large-area three-dimensional polyaniline nanowire networks using a 'soft template'. *Macromol. Rapid Commun.* **26,** 395–400 (2005).

345. Wu, C. & Bein, T. Conducting Polyaniline Filaments in a Mesoporous Channel Host. *Science* **264,** 1757–1759 (1994).

346. Choi, H. J., Cho, M. S. & Ahn, W. S. Synthesis of polyaniline/MCM-41 nanocomposite and its electrorheological property. *Synth. Met.* **135-136,** 711–712 (2003).

347. Dou, Y. Q., Zhai, Y. Zeng, F., Liu, X. X., Tu, B. & Zhao, D. Encapsulation of polyaniline in 3-D interconnected mesopores of silica KIT-6. *J. Colloid Interface Sci.* **341,** 353–358 (2010).

348. Zeng, C., Han, S., Yan, X., Yu, X., Che, H. & Zhao, X. Ordered mesoporous silica materials. *Prog. Chem.* **20,** 26–32 (2008).

349. Nandi, M., Gangopadhyay, R. & Bhaumik, A. Mesoporous polyaniline having high conductivity at room temperature. *Microporous Mesoporous Mater.* **109,** 239–247 (2008).

350. Khdary, N. H., Abdesalam, M. E. & El Enany, G. Mesoporous Polyaniline Films for High Performance Supercapacitors. *J. Electrochem. Soc.* **161,** G63–G68 (2014).

351. Wang, Q. Yan, J., Fan, Z., Wei, T., Zhang, M. & Jing, X. Mesoporous polyaniline film on ultra-thin graphene sheets for high performance supercapacitors. *J. Power Sources* **247,** 197–203 (2014).

352. Ding, L., Li, W., Wang, Q., Sun, Q., He, Y. & Su, B. Vertically oriented silica mesochannels as the template for electrodeposition of polyaniline nanostructures and their electrocatalytic and electroanalytical applications. *Chem. Eur. J.* **20,** 1829–33 (2014).

353. Ding, L. & Su, B. A non-enzymatic hydrogen peroxide sensor based on platinum nanoparticle–polyaniline nanocomposites hosted in mesoporous silica film. *J. Electroanal. Chem.* **736,** 83–87 (2015).

354. Qu, F., Sun, H., Zhang, Y., Lu, H. & Yang, M. Electrochemically deposited Pd nanorod array/sol-gel silica thin film for the fabrication of electrochemical sensors. *Sensors Actuators, B Chem.* **166-167,** 837–841 (2012).

355. Kang, H.-S., Lee, H.-C. & Kwak, J.-H. Electrodeposition of Polypyrrole Nanowires within Vertically Oriented Mesoporous Silica Template. *J. Korean Electrochem. Soc.* **14,** 22–26 (2011).

356. Del Valle, M. A., Gacitúa, M., Díaz, F. R., Armijo, F. & Río, R. Del. Electrosynthesis of polythiophene nanowires via mesoporous silica thin film templates. *Electrochem. commun.* **11,** 2117–2120 (2009).

357. Montilla, F., Cotarelo, M. A. & Morallón, E. Hybrid sol–gel–conducting polymer synthesised by electrochemical insertion: tailoring the capacitance of polyaniline. *J. Mater. Chem.* **19,** 305–310 (2009).

358. Salinas-Torres, D., Montilla, F., Huerta, F. & Morallón, E. All electrochemical synthesis of polyaniline/silica sol-gel materials. *Electrochim. Acta* **56,** 3620–3625 (2011).

359. Schultze, J. W. & Thyssen, A. The Kinetics of Electropolymerization. *Synth. Met.* **43,** 2825–2830 (1991).

360. Wei, Y., Sun, Y. & Tang, X. Autoacceleration and Kinetics of Electrochemical Polymerization of Aniline. *J. Phys. Chem.* **04,** 4878–4881 (1989).

361. Yang, H. & Bard, A. J. The application of fast scan cyclic voltammetry. Mechanistic study of the initial stage of electropolymerization of aniline in aqueous solutions. *Electroanalysis* **339,** 423–449 (1992).

362. Bade, K., Tsakova, V. & Schultze, J. W. Nucleation, growth and branching of polyaniline from microelectrode experiments. *Electrochim. Acta* **37,** 2255–2261 (1992).

363. Komsiyska, L., Tsakova, V. & Staikov, G. Electrochemical formation and properties of thin polyaniline films on Au(111) and p-Si(111). *Appl. Phys. A Mater. Sci. Process.* **87,** 405–409 (2007).

364. Mu, S. & Kan, J. Evidence for the autocatalytic polymerization of aniline. *Electrochim. Acta* **41,** 1593–1599 (1996).

365. Mandić, Z., Duić, L. & Kovačiček, F. The influence of counter-ions on nucleation and growth of electrochemically synthesized polyaniline film. *Electrochim. Acta* **42,** 1389–1402 (1997).

366. Gamero-Quijano, A., Huerta, F., Salinas-Torres, D., Morallón, E. & Montilla, F. Enhancement of the Electrochemical Performance of SWCNT dispersed in a Silica Sol-gel Matrix by Reactive Insertion of a Conducting Polymer. *Electrochim. Acta* **135,** 114–120 (2014).

367. Inzelt, G., Pineri, M., Schultze, J. W. & Vorotyntsev, M. A. Electron and proton conducting polymers : recent developments and prospects. *Electrochim. Acta* **45,** 2403–2421 (2000).

368. Mandić, Z. & Duić, L. Polyaniline as an electrocatalytic material. *J. Electroanal. Chem.* **403,** 133–141 (1996).

369. Nam, D.-H., Kim, M.-J., Lim, S.-J., Song, I.-S. & Kwon, H.-S. Single-step synthesis of polypyrrole nanowires by cathodic electropolymerization. *J. Mater. Chem. A* **1,** 8061 (2013).

370. Okamoto, H., Okamoto, M. & Kotaka, T. Structure development in polyaniline films during electrochemical polymerization. II: Structure and properties of polyaniline films prepared via electrochemical polymerization. *Polymer* **39,** 4359–4367 (1998).

371. Wang, Z., Li, C., Scherr, E. & Epstein, A. Three dimensionality of metallic states in conducting polymers: Polyaniline. *Phys. Rev. Lett.* **66,** 1745–1748 (1991).

372. Thyssen, A., Borgerding, A. & Schultze, J. W. Formation and Electronic Conductivity of Polyaniline. *Macromol. Symp.* **8,** 143–157 (1987).

373. Thyssen, A., Hochfeld, A., Kessel, R., Meyer, A. & Schultze, W. Anodic Polymerisation of Aniline and Methysubstituted derivatives: Orto and Para couplings. *Synth. Met.* **29,** 357–362 (1989).

374. Gawli, Y., Banerjee, A., Dhakras, D., Deo, M., Bulani, D., Wadgaonkar, P., Shelke, M. & Ogale, S. 3D Polyaniline Architecture by Concurrent Inorganic and Organic Acid Doping for Superior and Robust High Rate Supercapacitor Performance. *Sci. Rep.* **6,** 21002 (2016).

375. Aoki, K., Cao, J. & Hoshino, Y. Coulombic irreversibility at polyaniline-coated electrodes by electrochemical switching. *Electrochim. Acta* **38,** 1711–1716 (1993).

376. Gottesfeld, S., Redondo, A., Rubinstein, I. & Feldberg, S. W. Resistance-induced peaks in cyclic voltammograms of systems that can be switched electrochemically between an insulating and conductive state. *J. Electroanal. Chem.* **265,** 15–22 (1989).

377. Feldberg, S. W. & Rubinstein, I. Unusual Quasi-Reversibility (UQR) or Apparent Non-Kinetic Hysteresis in Cyclic Voltammetry. An Elaboration upon the Implications of N-Shaped Free Energy Relationships as Explanation. *J. Electroanal. Chem.* **240,** 1–15 (1988).

378. Baughman, R. H. & Shacklette, L. W. The Dependence of Electronic Conductivity Upon Conjugation Length for Conducting Polymers. *Synth. Met.* **17,** 173–181 (1987).

379. Garnier, F., Horowitz, G., Peng, X. Z. & Fichou, D. Structural basis for high carrier mobility in conjugated oligomers. *Synth. Met.* **45,** 163–171 (1991).

380. Zade, S. S., Zamoshchik, N. & Bendikov, M. From short conjugated oligomers to conjugated polymers. Lessons from studies on long conjugated oligomers. *Acc. Chem. Res.* **44,** 14–24 (2011).

381. Grande, H., Otero, T. F. & Cantero, I. Conformational relaxation in conducting polymers: effect of polymer–solvent interactions. *J. Non. Cryst. Solids* **235-237,** 619–622 (1998).

382. Nateghi, M. R. & Savabieh, B. Study of polyaniline oxidation kinetics and conformational relaxation in aqueous acidic solutions. *Electrochim. Acta* **121,** 128–135 (2014).

383. Choi, S.-J. & Park, S.-M. Electrochemistry of Conductive Polymers. XXVI. Effects of Electrolytes and Growth Methods on Polyaniline Morphology. *J. Electrochem. Soc.* **149,** E26 (2002).

384. Malinauskas, A. & Holze, R. A UV-vis spectroelectrochemical study of redox reactions of solution species at a polyaniline electrode in the conducting and the reduced state. *J. Electroanal. Chem.* **461,** 184–193 (1999).

385. Chi, H. & Lin, S. The mediation effect of a polyaniline-coated electrode on the reduction of Iron (III) ions. *J. Chinese Chem. Soc.* **39,** 213–216 (1992).

386. Geniès, E. M. & Tsintavis, C. Electrochemical behaviour, chronocoulometric and kinetic study of the redox mechanism of polyaniline deposits. *J. Electroanal. Chem.* **200,** 127–145 (1986).

387. Masters, J. G., Sun, Y., MacDiarmid, A. G. & Epstein, A. J. Polyaniline: Allowed oxidation states. *Synth. Met.* **41,** 715–718 (1991).

388. Stejskal, J., Kratochvíl, P. & Radhakrishnan, N. Polyaniline dispersions 2. UV-Vis absorption spectra. *Synth. Met.* **61,** 225–231 (1993).

389. Liu, J., He, D., Liu, Q., He, X., Wang, K., Yang, X., Shangguan, J., Tang, J. & Mao, Y. Vertically Ordered Mesoporous Silica Film-Assisted Label-Free and Universal Electrochemiluminescence Aptasensor Platform. *Anal. Chem.* **88**, 11707-11713 (2016).

390. Cao, Y. & Mallouk, T. E. Morphology of template-grown polyaniline nanowires and its effect on the electrochemical capacitance of nanowire arrays. *Chem. Mater.* **20,** 5260–5265 (2008).

391. Kumar, S. & Sharma, S. K. Large scale synthesis of polyaniline nanowires and their characterization. *J. Mater. Sci. Mater. Electron.* **23,** 1260–1262 (2012).

392. Wu, S. H., Burkhardt, S. E., Zhong, Y. W. & Abruña, H. D. Cyclometalated ruthenium oligomers with 2,3-di(2-pyridyl)-5,6- diphenylpyrazine: A combined experimental, computational, and comparison study with noncyclometalated analogous. *Inorg. Chem.* **51,** 13312–13320 (2012).

393. Zhong, Y. W., Wu, S. H., Burkhardt, S. E., Yao, C. J. & Abruña, H. D. Mononuclear and dinuclear ruthenium complexes of 2,3-Di-2-pyridyl-5,6- diphenylpyrazine: Synthesis and spectroscopic and electrochemical studies. *Inorg. Chem.* **50,** 517–524 (2011).

394. Vilà, N., Zhong, Y. W., Henderson, J. C. & Abruña, H. D. Anthracene-bridged binuclear ruthenium complexes: Electrochemical and spectroscopic evidence of electronic communication through the pi system. *Inorg. Chem.* **49,** 796–804 (2010).

395. Zhong, Y., Vilà, N., Henderson, J. C. & Abruña, H. D. Dithienylcyclopentenes-containing transition metal bisterpyridine complexes directed toward molecular electronic applications. *Inorg. Chem.* **48,** 991–999 (2009).

396. Vilà, N., Royal, G., Loiseau, F. & Deronzier, A. Photochromic and redox properties of bisterpyridine ruthenium complexes based on dimethyldihydropyrene units as bridging ligands. *Inorg. Chem.* **50,** 10581–10591 (2011).

397. Zhang, W. Z., Kan, X. W., Jiao, S. F., Sun, J. G., Yang, D. S., Bin, F. Electrochemical characteristics and catalytic activity of polyaniline doped with ferrocene perchlorate. *J. Appl. Polym. Sci.* **102,** 5633–5639 (2006).

Appendix I

Amplified charge transfer for anionic redox probes through ferrocene-functionalized mesoporous silica thin films

In **Chapter 3**, it was shown that the charge transfer of the electrostatically repulsed anionic redox probes [i.e. $Fe(CN)_6^{3-/4-}$] can be amplified in the presence of $Fc(MeOH)_2$ redox mediator in the mixture solution. A set of trials was intended to show the corresponding charge transfer amplification by using 30% ferrocene-functionalized mesoporous silica film (prepared by the method mentioned in **Section 2.2**). The resulting ferrocene-functionalized film is electroactive in a solution containing electrolyte support (i.e. 0.1 M $NaNO_3$) and shown in the voltammogram in **Fig. A1.1**.

$$Fc - 1\,e^{-} + X^{-}_{(sol)} \Leftrightarrow Fc^{+}, X^{-}_{(film)} \qquad \textbf{Eq. A1.1}$$

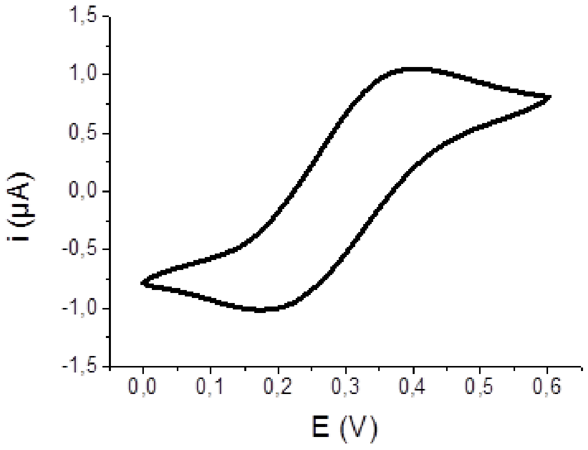

Figure A1.1 Cyclic voltammogram of ferrocene-functionalized vertically-aligned silica film prepared from 30% azide-functionalized silica film, recorded in a solution containing $NaNO_3$ 0.1 M. Potential scan rate: 20 mV s^{-1}.

Fig. A1.2 shows the feasibility of charge transfer amplification at two different concentrations of $Fe(CN)_6^{4-}$, notably 0.1 and 0.5 mM, using ferrocene-functionalized silica film in the presence of $NaNO_3$ 0.1 M as supporting electrolyte. A similar tendency is presented at the ferrocene-functionalized film, as demonstrated before in the case of $Fc(MeOH)_2$ in solution, that the effectiveness of redox mediating reaction gets lower at higher $Fe(CN)_6^{4-}$ concentration (compare the red-to-black current intensity ratios in **Figs A1.2 A** and **B**). Moreover, at higher $Fe(CN)_6^{4-}$ concentration, the amplified current starts to be shifted from peak- to wave-like shape, showing signs of $Fe(CN)_6^{4-}$ anion acting as compensating counteranion together with NO_3^- upon constant oxidation of Fc forming Fc^+ (**eq. A1.2**), where a more voluminous anions occupy more and more space and therefore restricting the rate of the reaction. The same tendency was reported before by Vilà *et al*[123] in the case of big p-toluenesulfonate as well as multivalent sulfate and citrate anions.

$$Fc(MeOH)_2{}^{+} + Fe(CN)_6{}^{4-} \leftrightarrow Fc(MeOH)_2 + Fe(CN)_6{}^{3-} \qquad \textbf{Eq. A1.2}$$

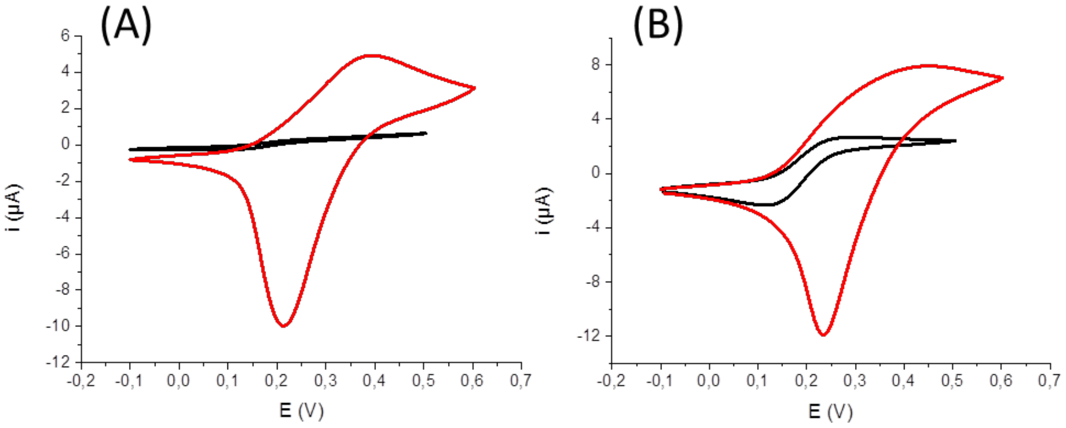

Figure A1.2 Cyclic voltammograms recorded in solutions containing (A) 0.1 mM and (B) 0.5 mM $Fe(CN)_6^{4-}$ using non-functionalized (black curve) and ferrocene-functionalized (red curve) silica modified ITO electrodes; supporting electrolyte: 0.1 M $NaNO_3$; potential scan rate: 20 mV s^{-1}.

Furthermore, at low $Fe(CN)_6^{4-}$ concentration (i.e. 0.1 mM) and at higher potential scan rate (shown in **Fig. A1.3**) wave-shaped anodic curve is also observed, confirming the mass transfer restriction of bigger and multivalent anions reported by Vilà *et al.*[123]

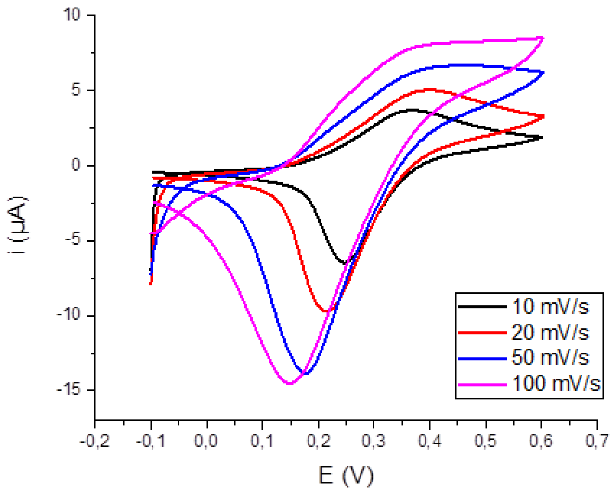

Figure A1.3 Cyclic voltammograms at different potential scan rate, recorded in a solution containing 0.1 mM Fe(CN)$_6^{4-}$ using ferrocene-functionalized (red curve) silica modified ITO electrodes; supporting electrolyte: 0.1 M NaNO$_3$; potential scan rate: 20 mV s^{-1}.

Finally, as the purpose of this set of experiment was to observe the charge amplification of repulsed Fe(CN)$_6^{4-}$ anions, it is preferable that only the NO$_3^-$ anion diffuse into the silica mesochannels to compensate the positively charged ferrocinium species. However, such selectivity is not possible. Therefore, a more applicable study of ferrocene-functionalized films was conducted for the field of electroanalysis reported in **Chapter 4**.

Appendix II

Immobilization of other metal polypyridyl complexes: $Fe(bpy)_3^{2+}$

Attempts to immobilized polypyridyl complexes was conducted prior to immobilization of $Ru(bpy)_2(bpy')^{2+}$ described in **Chapter 5**, notably $Fe(bpy)_3^{2+}$ species. The grafting was done in three steps;

1. Electro-assisted self-assembly of azide-functionalized mesoporous silica film on ITO electrode (see **Chapter 2**)
2. Huisgen click reaction of the azide-functionalized film with ethynyl-bipyridine, using the protocol explained in **Chapter 2**
3. Complexation reaction with Fe^{2+} cation by immersion in 1 mM $FeSO_4$ solution for 2 hours, continued by immersion in 1 mM 2,2'-bipyridine solution for another 2 hours.

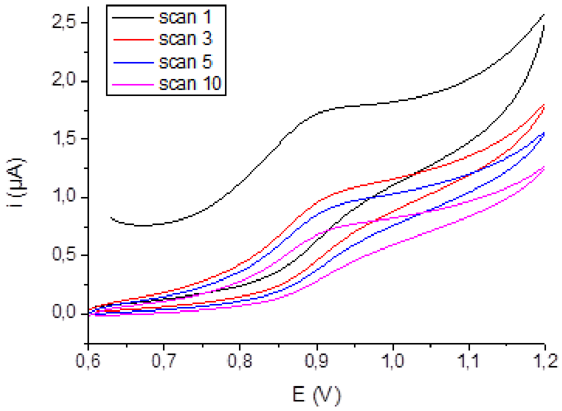

Figure A2.1 Cyclic voltammograms (CV) of $Fe(bpy)_3^{2+}$-functionalized mesoporous silica film at consecutive number of scans, recorded in 0.1 M $NaNO_3$; potential scan rate: 20 mV s^{-1}.

Fig. A2.1 shows the electrochemical response of the functionalized silica modified electrode over consecutive CV scans which indicate signs of instability of the signal (i.e. decreasing current intensity and smaller reduction peak compared to the oxidation curve). The non-reversibility of the

CV is more pronounced in the functionalized film prepared from 30% azide-functionalized silica film (**Fig. A2.2**).

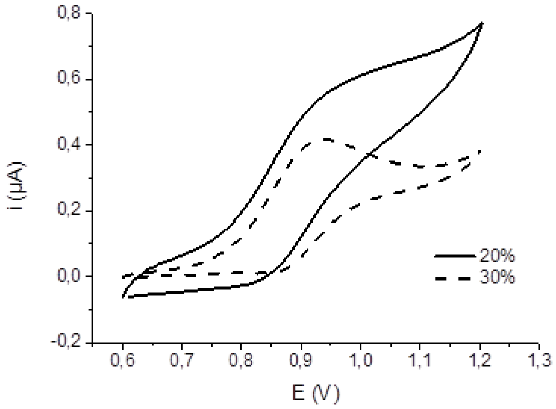

Figure A2.2 Cyclic voltammograms (10th scan) of $Fe(bpy)_3^{2+}$-functionalized mesoporous silica film prepared from 20% (solid line) and 30% azide functionalized silica films, recorded in 0.1 M $NaNO_3$; potential scan rate: 20 mV s^{-1}.

To determine the nature of the functionalization instability, CVs of $Fe(bpy)_3SO_4$ complex in aqueous solution was tested at both bare ITO and silica-modified ITO electrodes. **Fig A2.3** presents the similar instability of the electrochemical response over consecutive scans. This proves that the complex itself is not stable in solution.

The same response was observed for Cobalt-based complex (figures not shown). This has led to the decision to immobilize Ruthenium-based complex due to its stability in solution.

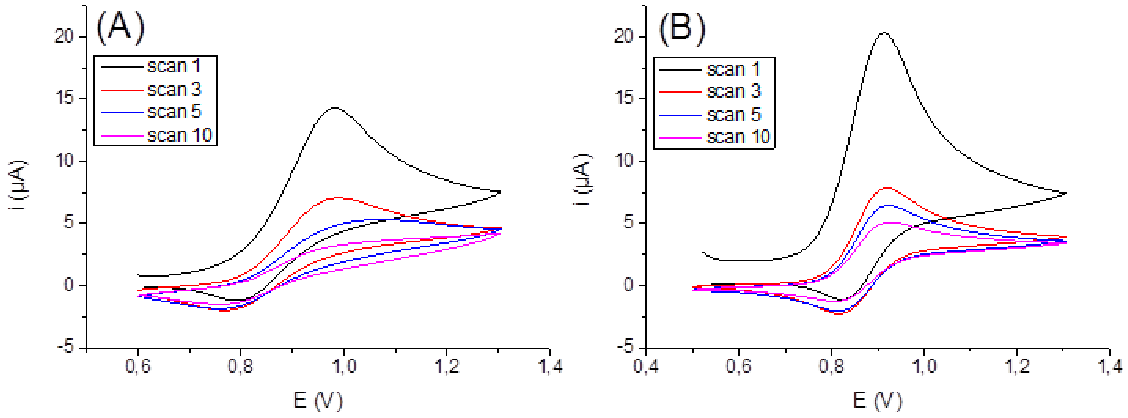

Figure A2.3 Consecutive 10 scans voltammograms of 1 mM $Fe(bpy)_3SO_4$ solution recorded at (A) bare ITO and (B) vertically-aligned mesoporous silica modified ITO electrodes. Electrolyte support: 0.1 M $NaNO_3$; potential scan rate: 20 mV s^{-1}.

Appendix III

Bridging ruthenium bipyridyl complexes grafted in the vertically-aligned mesoporous silica film

It has been reported by the group of Abruña[392–395], that bridging metal complexes using bridging ligands can form significantly rigid molecular wires which show enhanced absorptivity and red-shitted absorption maximum, hence narrower energy gaps and lower electrochemical formal potential. These results are very promising in the field of molecular electronics.[394–396]

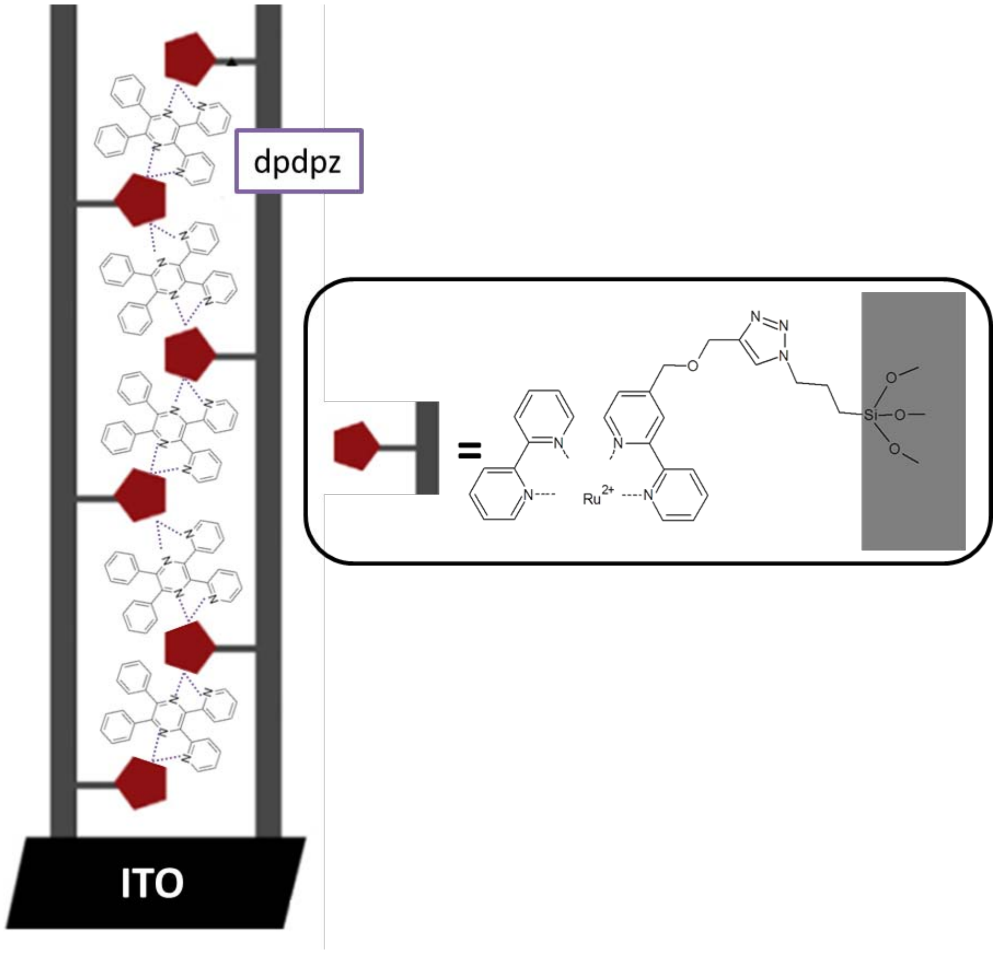

Figure A3.1 Schematic representation of molecular wiring of grafted Ru(bpy)$_2$ complexes using dpdpz bridging ligand.

Attempts were therefore conducted to bridge the grafted $Ru(bpy)_2^{2+}$ by the same method executed in **Chapter 5** by using 2,3-di-2-pyridyl-5,6-diphenylpyrazine (dpdpz) bridging ligand to form an immobilized ruthenium based molecular wire presented in **Fig. A3.1**. Trials were done for 10% azide-functionalized leaving more space between the functionalization sites for the bridging ligand. The yield of click reaction between the azide film and ethynyl-$Ru(bpy)_2$ were evidenced at ~67% by the reduction of the typical strong assymetric band of the azide compound at FTIR measurement shown in **Fig. A3.2**. There is also an additional band appeared at 1100 cm^{-1} after the click reaction. Afterwards, the $Ru(bpy)_2$-functionalized film was left to react in a 1 mM dpdpz/DMF solution on reflux for 8 - 10 hours.

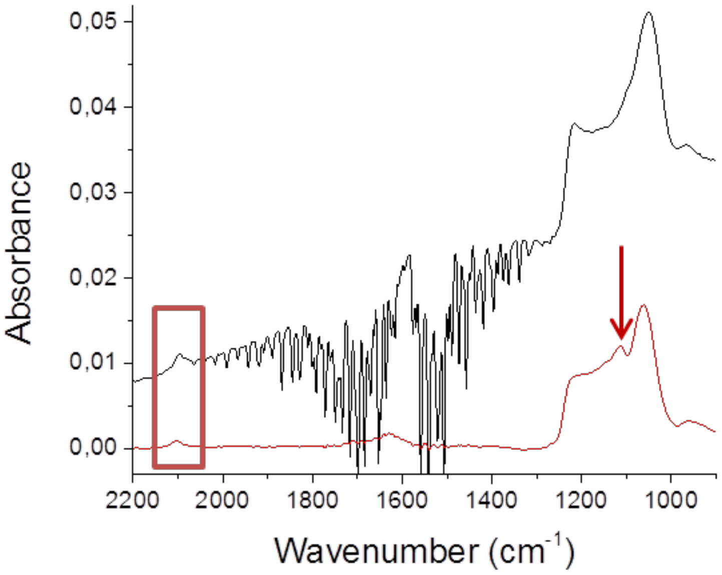

Figure A3.2 FTIR spectra of (a) azide-functionalized mesoporous silica thin films obtained from a sol containing AzPTMS:TEOS ratio of 10:90 and (b) the corresponding film after click reaction with ethynyl-$Ru(bpy)_2$. Red box indicates the asymmetric stretching band of the azide group.

After the reaction with dpdpz ligand, the absorbance and electrochemical activity of the films were recorded by UV-vis spectroscopy and cyclic voltammetry respectively. The UV-vis spectra in **Fig. A3.3A** clearly showed a change of absorbance subsequent to the reaction, leading to appearance of band maximums at 270 nm, 310 nm, as well as broad absorbance between 350 and 650 nm. However, the resulting film doesn't seem to show electroactivity at the expected potential window, both in aqueous and organic electrolytic solution shown in **Fig. A3.3B**. Hence, the formation of ruthenium-polypyridyl-based molecular wire in the pores of the silica film was not clearly evidenced. The trial was repeated for films with 5% and 20% of azide functionalization (figures not shown) and resulted in the same electrochemical behavior.

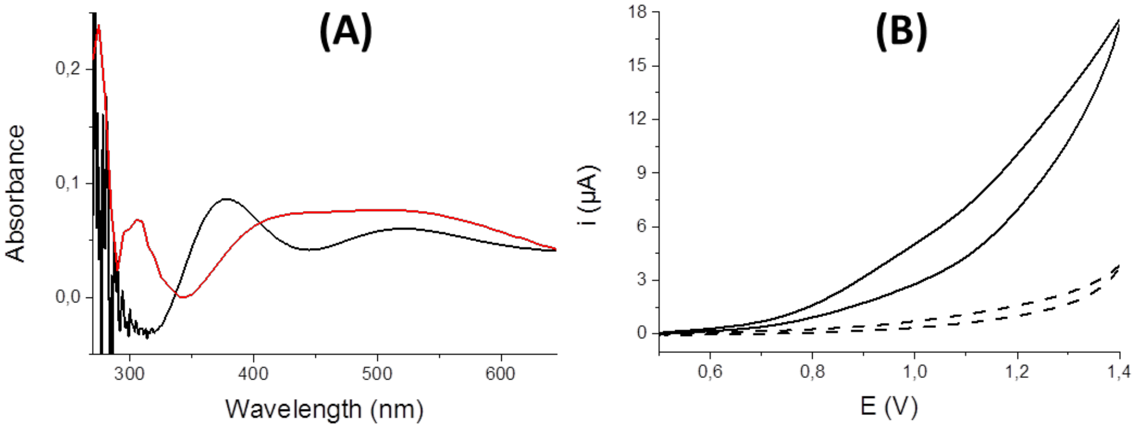

Figure A3.3 (A) UV-vis spectra of Ru(bpy)$_2$-functionalized mesoporous silica thin films obtained from a sol containing AzPTMS:TEOS ratio of 10:90 before (black line) and after (red line) complexation reaction with dpdpz bridging ligand. (B) Cyclic voltammetry of the film after complexation reaction, in aqueous (0.1 M NaNO$_3$) and organic (0.1 M TBABF$_4$/AcN) solutions; potential scan rate: 50 mV s^{-1}.

The feasibility of high temperature complexation reaction in such narrow silica mesochannels was checked by reacting the Ru(bpy)$_2$-functionalized films (AzPTMS/TEOS = 5/95 and 10/90) in a 1 mM 2,2'-bipyridyl/DMF solution on reflux for 8 - 10 hours, in order to form Ru(bpy)$_3$-functionalized films. After complexation, the UV-vis spectras (red lines in Figs. A3.4 A and B) show higher band maximum intensity at 300 nm (π-π* transition of bipyridyl ligand), showing indirect evidence of more bipyridine species incorporated. At, AzPTMS/TEOS : 5/95 the MLCT band at ~400 nm also improved, however at AzPTMS/TEOS : 10/90 the MLCT bad maximum decreases. The electrochemical activity in the expected potential window also did not show the presence of Ru(bpy)$_3$ species. Hence, it seems that the reaction was not successful.

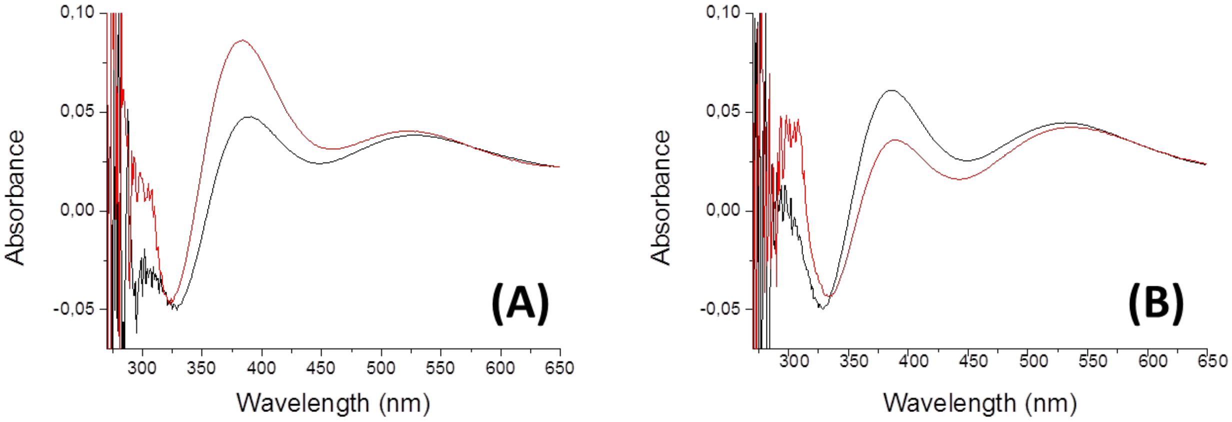

Figure A3.4 UV-vis spectra of Ru(bpy)$_3$-functionalized mesoporous silica thin films obtained from a sol containing AzPTMS:TEOS ratio of 5:95 (A) and 10:90 (B), before (black line) and after (red line) complexation reaction with 2,2'-bipyridine.

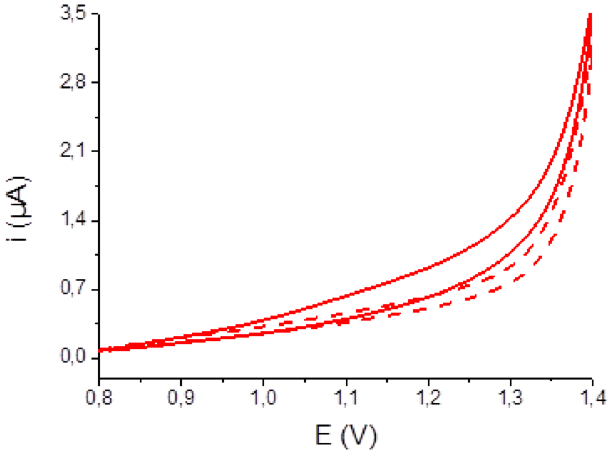

Figure A3.5 Cyclic voltammograms of Ru(bpy)$_3$-functionalized mesoporous silica thin films obtained from a sol containing AzPTMS:TEOS ratio of 5:95 (solid line) and 10:90 (dashed line), after the complexation reaction with 2,2'-bipyridine.

Another experiment pathway was taken to try to immobilize the Ru-based molecular wire, i.e. by click reaction of azide-functionalized films with ethynyl- and dpdpz-bearing ruthenium complex, shown in **Fig. A3.6**.

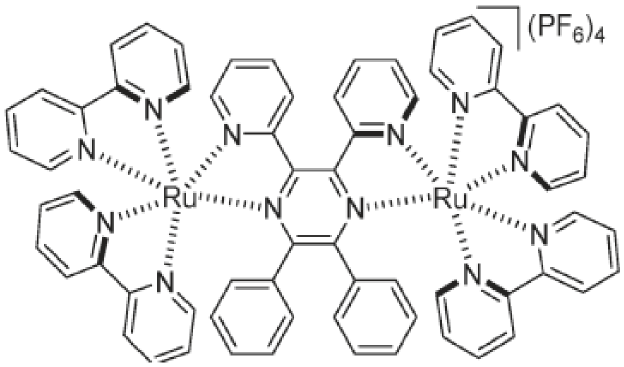

Figure A3.6 Ru(bpy)$_2$-dpdpz compound structure.

The resulting films, although they show MLCT band maximum of the ruthenium complex at ~380 nm (**Fig. A3.7A**) for both 5 and 10% of functionalization levels, don't present significant electroactivity (**Fig. A3.7B**) at the expected potential window is not clearly evident.

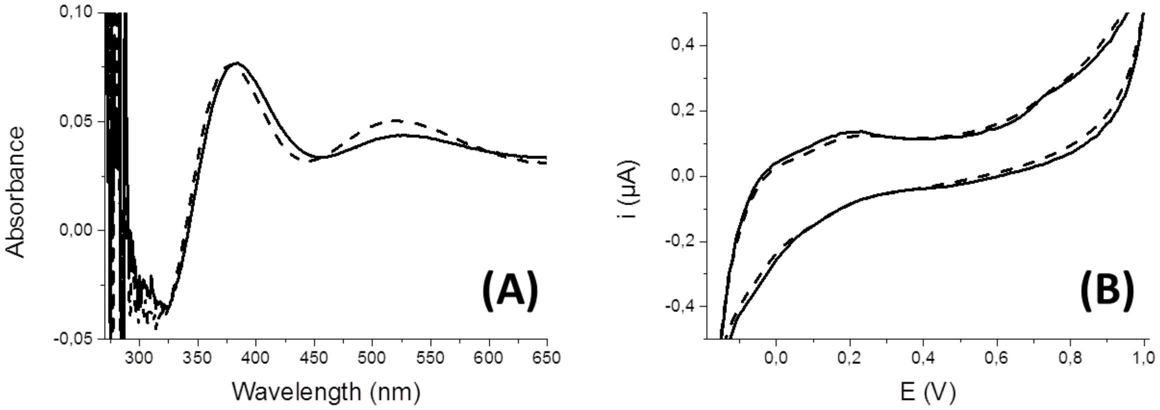

Figure A3.7 (A) UV-vis spectra of Ru(bpy)$_2$dpdpz-functionalized mesoporous silica thin films obtained from a sol containing AzPTMS:TEOS ratio of 5:95 (solid line) and 10:90 (dashed line). (B) Cyclic voltammetry of the corresponding films, in aqueous (0.1 M $NaNO_3$) media; potential scan rate: 50 mV s^{-1}.

From these experiments, it was slightly indicated that it might be possible to immobilize ruthenium-polypyridyl- based molecular wire in the vertically-aligned mesoporous silica film, however many more tests should be conducted to clearly proof the feasibility of the objective.

Appendix IV

Anchored growth of PANI nanofilaments

Free-standing nanomaterials have been considered as interesting structured materials for its large surface area. In **Chapter 6**, we have demonstrated the possibility to grow polyaniline (PANI) nanofilaments through the vertically-aligned mesoporous silica films as a hard template. Further challenge will be to be able to remove the silica template in order to achieve free-standing PANI nanofilaments on ITO electrode, increasing even the surface area and hence improving even more the redox reversibility, capacitance, and electrocatalytic properties of the material.

During the removal of the silica template, it is important that the PANI nanofilaments are well anchored on the ITO surface. Here, the idea is to attach aniline monomer on ITO surface prior the polymerization so that PANI growth preferably from the anchor upwards. In this appendix, we are showing preliminary results on control experiment on bare ITO electrodes. The aniline attachment was conducted in two steps;

1. Drop casting of (3-bromopropyl)trichlorosilane on ITO surface for 30 seconds, then washing in ethanol
2. Bromo - aniline substitution reaction by immersion of the electrodes in 1 M aniline/chloroform solution in stirring for 17 hours.

Here, we are comparing three different electrodes (bare ITO, bromo-functionalized ITO, and aniline-functionalized ITO electrodes) of their three aspects; i.e. PANI electropolymerization growth behavior, cyclic voltammetry of the resulting PANI deposit, and its electrocatalytic behavior towards $Fe^{2+/3+}$ redox probe.

Fig. A4.1 shows that for different amount of PANI, its growth on both modified ITO electrodes is slower that bare ITO due to the additional resistance of the modifying layer. The interesting result is that, at the modified electrodes after bromo-aniline substitution reaction, PANI growth is faster compared to the one before the reaction, indicating indirect proof of presence of aniline species on the electrode surface as nucleation points for PANI polymerization.

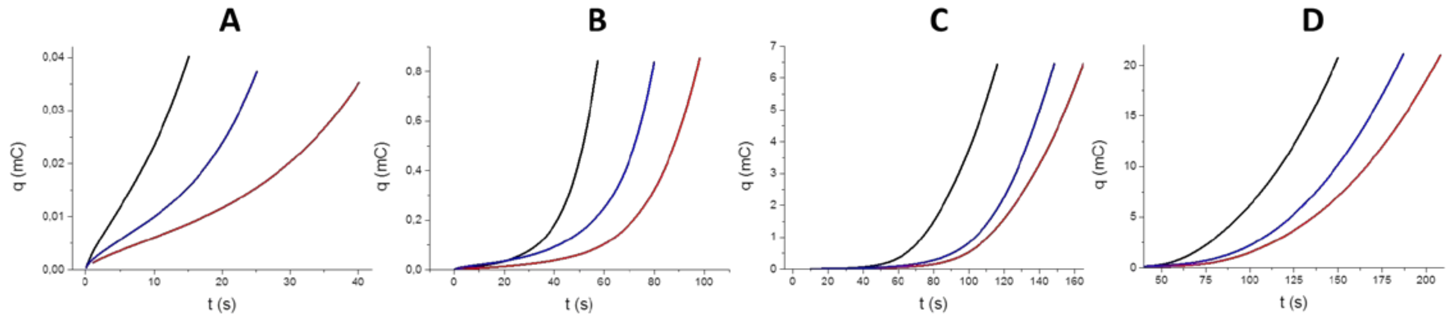

Figure A4.1 Chronocoulometry of PANI potentiostatic electropolymerization (E = 0.85 V) on bare ITO (black curve), bromo-modified ITO (red curve), and aniline-modified ITO (blue curve) electrodes, at various polymerization stages; 0.04 mC (A), 0.8 mC (B), 6.5 mC (C), and 21 mC (D).

Another indication is that the resulting PANI grown on aniline-modified ITO show higher current intensity of the leucoemeraldine/emeraldine redox activity compared to the other two electrodes (**Fig. A4.2**) and hence slightly better electrocatalysis towards $Fe^{2+/3+}$ probe (**Fig. A4.3**).

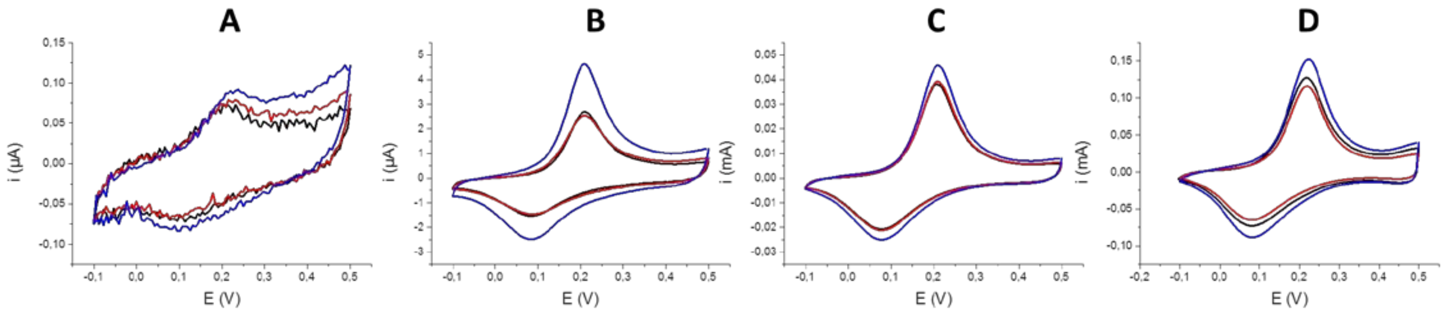

Figure A4.3 Cyclic voltammograms of the resulting PANI grown on bare ITO (black curve), bromo-modified ITO (red curve), and aniline-modified ITO (blue curve) electrodes, recorded in 0.5 M H_2SO_4. Polymerization stages: 0.04 mC (A), 0.8 mC (B), 6.5 mC (C), and 21 mC (D). Potential scan rate: 50 mV s^{-1}.

Despite the indirect evidence of aniline attachment on ITO surface, a more direct proof needs to be obtained. XPS measurement of the bromo-based thin layer before and after reacting with aniline needs to be conducted.

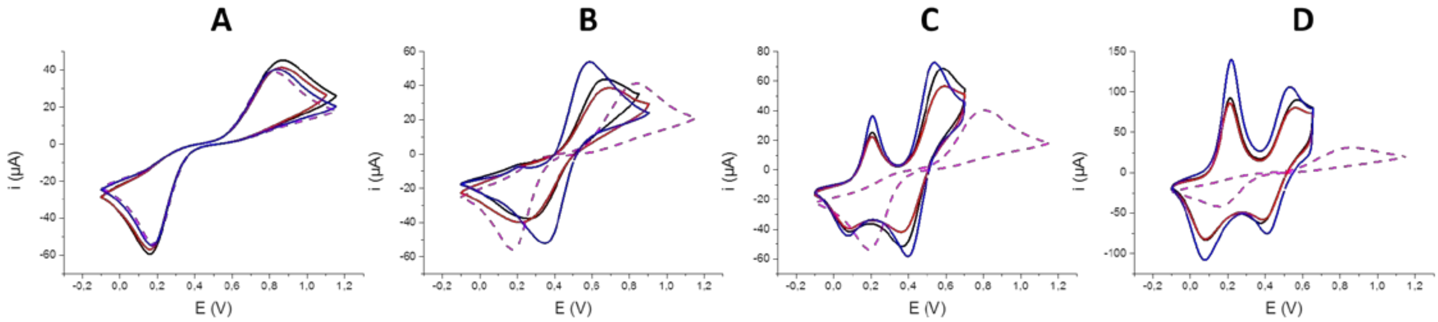

Figure A4.3 Voltammetric response various electrodes (bare ITO electrode (dashed magenta), and PANI grown on bare ITO (black curve), bromo-modified ITO (red curve), and aniline-modified ITO (blue curve) electrodes) towards $Fe^{2+/3+}$ redox probes (supporting electrolyte: 0.5 M H_2SO_4). Polymerization stages: 0.04 mC (A), 0.8 mC (B), 6.5 mC (C), and 21 mC (D). Potential scan rate: 50 mV s^{-1}.

Lastly, once this set of experiments is clearly controlled, it is interesting to conduct the same set of experiments for the silica modified electrodes and further try to remove the silica template to obtaine the free-standing PANI nanofilaments.

Appendix V

Growth of PANI nanofilaments through the vertically-aligned and ferrocene-functionalized mesoporous silica modified ITO electrodes

It has been reported before that in the presence of ferrocene perchlorate as the doping agent in electrochemical polymerization of polyaniline (PANI) improves the electroactivity of the conducting polymer in pH>4, as well as the electrocatalysis of ascorbic acid (AA) at high pH.[397]

As we have successfully immobilized ferrocene species (**Chapter 2**) as well as controlled the electropolymerization of PANI (**Chapter 6**) in a vertically-aligned silica film modified electrode, experiments were conducted to see the growth of PANI in the ferrocene-functionalized film, and the electrocatalysis of the resulting film towards ascorbic acid at high pH.

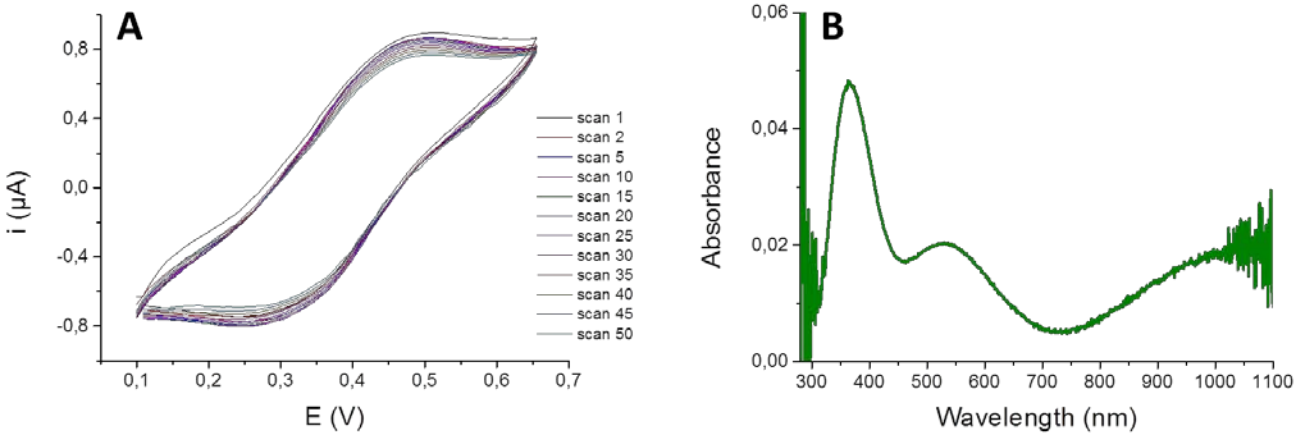

Figure A5.1 (A) Stability test of ferrocene-functionalized film prepared from 30%-azide-functionalized silica film, through consecutive 50 cyclic voltammetry recorded in 0.5 M H_2SO_4 (pH 0); potential scan rate: 50 mV/s. (B) UV-vis spectra of the corresponding ferrocene-functionalized silica film.

First step was to check the stability of grafted ferrocene species in acid medium (pH 0) needed for electropolymerization of PANI (see **Fig. A5.1A**). It was found to be considerably stable during 50 consecutive cyclic voltammetric scans. Furthermore, the growth of PANI was compared by potentiostatic electropolymerization i-t curve shown in **Fig. A5.2 A**, where the presence of ferrocene seems to slow down the process which was probably due to the less space available in the mesochannels for the monomers and oligomers to diffuse into.

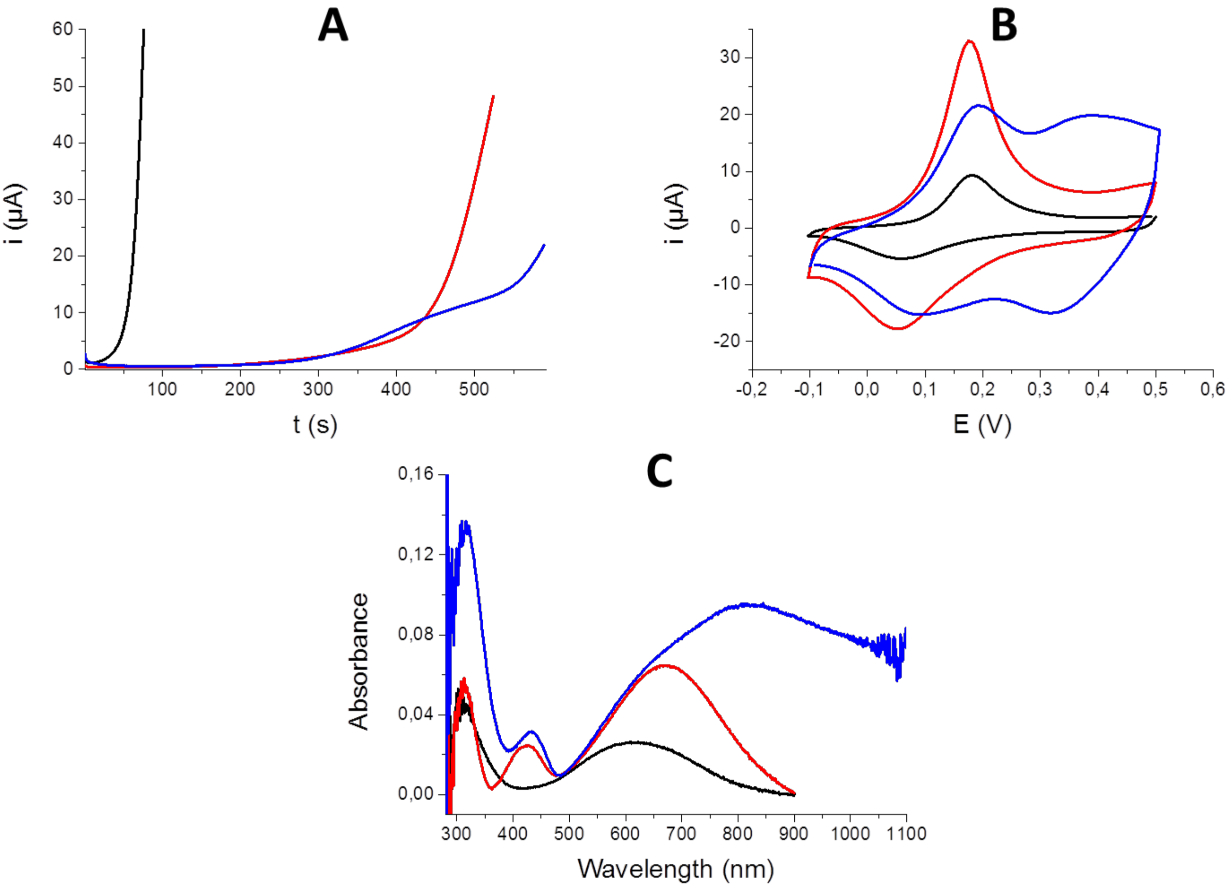

Figure A5.2 (A) i-t curve of PANI potentiostatic (E = +0.85 V, in 0.5 M H_2SO_4 + 0.1 M aniline solution) electropolymerization at bare ITO (black curve), silica-modified ITO prepared from 100 mM TEOS sol solution (red curve), and ferrocene-functionalized silica film prepared from AzPTMS/TEOS 30/70 sol solution (blue curve). The stable cyclic voltammograms as recorded in H_2SO_4 0.5 M (B) and the UV-vis spectra (C) of of the resulting polymerized PANI on the corresponding electrodes (total charge transfered: 3 mC).

The redox activity of PANI deposited on each electrode was recorded by cyclic voltammetry in 0.5 M H_2SO_4 solution, shown in **Fig. A5.2 B**. As presented in **Chapter 6**, PANI grown through silica template has higher capacitance. PANI at ferrocene-functionalized silica film seems to have additional reversible redox couple centered at 0.35 V, which can be due to the mediated ferrocene redox species by the emeraldine form of polyaniline oxidized at ~0.2 V. To test this hypothesis, it is important to further conduct more experiments on different ferrocene content in the silica film.

The UV-vis monitoring of each PANI deposit on different electrodes was conducted using different blank samples accordingly, so that only the spectra of PANI was recorded; i.e. bare ITO, silica modified ITO (TEOS 100 mM), and ferrocene-functionalized silica modified ITO (AzPTMS/TEOS 30/70) as blanks for PANI deposited on the corresponding electrodes. PANI spectra for each sample are presented in **Fig. A5.2 C**. Compared to the one grown in non-functionalized silica template, the presence of ferrocene functionalization resulted in higher amount of PANI deposit (indicated by the higher absorbance maximum at λ = 315 nm and the broad band between 500 and 1000 nm, attributed to the π–π* transition of the aromatic rings and the polarons respectively). Again, to complete the study, various levels of ferrocene functionalization have to be checked to see their effects on the deposited PANI absorbance.

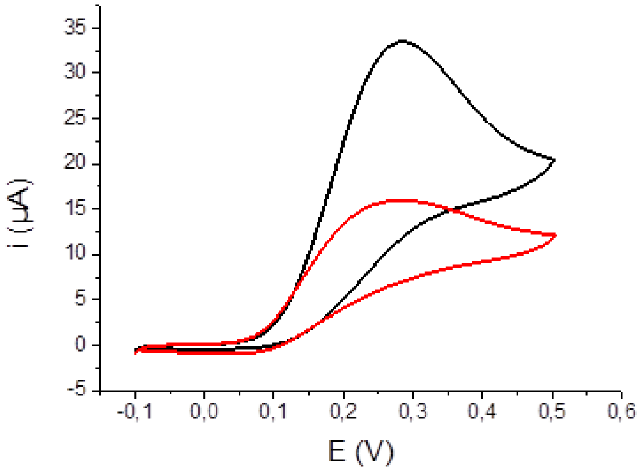

Figure A5.3 Cyclic voltammetric response of 1 mM Ascorbic Acid (AA) at pH 5, at different modified electrodes; i.e. PANI deposits (Q = 3 mC) on silica-modified ITO [TEOS = 100 mM] (black curve) and ferrocene-functionalized silica-modified ITO [AzPTMS/TEOS = 30/70] (red curve). Potential scan rate: 50 mV/s, supporting electrolyte: 0.1 M Na_2SO_4.

Lastly, the electrocatalysis of PANI deposited on both non- and ferrocene-functionalized silica films towards 1 mM AA at pH 5 was compared by cyclic voltammetry, showing not really improved electrocatalytic performance of the latter, in contrary to the previously reported improvement of simple ferrocene perchlorate doping in PANI.[397]

Although these preliminary tests have shown significant difference of PANI deposited through the vertically-aligned silica template containing ferrocene species, a lot more control experiments need to be done to have a clear conclusion; such as varying the ferrocene content of the film.